UNIVERSITY OF
BIRMINGHAM

MEASUREMENT AND IDENTIFICATION OF AMBIENT ATMOSPHERIC METALLIC NANOPARTICLES

By

PAUL SANDERSON

A thesis submitted to the University of Birmingham for the degree of

DOCTOR OF PHILOSOPHY

Division of Environmental Health and Risk Management

School of Geography, Earth and Environmental Sciences

University of Birmingham

June 2015

ABSTRACT

Physico-chemical characterisation of particles collected at six roadside, background and rural sites has been undertaken by multiple methods to improve knowledge of the size distributions and morphology of atmospheric metals in the ultrafine size range. Gravimetric analysis of filters has produced mass-size distributions of total PM mass enabling comparison between multiple sites and calculation of roadside increments in Birmingham, which are found to occur in the size ranges 100-180 nm, 320-560 nm and >1000 nm. Rural distributions are dominated by coarse particles, but roadside sites have high contributions from fine and ultrafine particles. Size distributions of individual elements and ions have been plotted and comparisons between different sites been made. Good correlations are observed between Ba, Cu and Fe, but some divergence of sources is evident in small particles. Single-particle analysis by TEM-X-EDS and EELS has classified Fe-dominated particles into two main groups; those with Fe content >90%/wt and Fe-Mn alloys (Fe ~75%/wt). Both classes are mainly γ-Fe_2O_3 and α-Fe_2O_3. Pb-dominated particles divide into three types, two with high Zn content and one with around 25% Sb/wt. Ce particles have been found in the form of nanoparticles attached to large soot agglomerates. TEM and ICP-MS samples have also been taken from a static brake test rig, showing changes in mass distributions at different braking forces and differences in the behaviour of different elements, in particular between Ba, Cu, Fe, Ni and Al.Data from TEM samples of diesel exhaust imply that particles containing Fe, Cr and Ni together may be indicative of this source and that engines are a possible source of submicrometre Cu. Furthermore, use of Al-alloys in engine design contributes Al-dominated particles to the emitted exhaust. Significant progress has been made in characterising the concentrations and size distributions of several metals and ions in ultrafine particulate matter both at the bulk and single particle level in ambient air in several environments as well as the key sources in brake wear and diesel soot.

ACKNOWLEDGEMENTS

Funding of the project by the UK Natural Environment Research Council is gratefully acknowledged (grant reference number NERC NE/I008314/1).

My supervisors, Professor Roy Harrison, Dr Juana Mari Delgado-Saborit and Professor John Ayres have supported and advised me throughout the project and without their invaluable guidance and feedback I could not possibly have succeeded. I am immensely grateful for all they have done for me in the last four years.

Dr Steve Baker has gone beyond the call of duty in carrying out the ICP-MS analyses upon which much of this thesis is based and I am deeply indebted to him for his hard work. Similarly, lab managers Gillian Kingston, Eimear Orgill and Maria Thompson have provided invaluable assistance in the laboratory. Richard Johnson and Jamie Peart have helped on many occasions in fieldwork. Dr Salim Alam, Dr Jianxin Yin and Christopher Stark have also provided assistance in practical work and data analysis. I am very grateful to Dr Shei Su and Dr Ralf Weber for crucial assistance in carrying out electron microscopy and analysing the data from these experiments. Thanks also to Dr Demie Kepaptsoglou and Dr Quentin Ramasse at SuperSTEM, without whom I would not have any of the EELS data. Dr Angeliki Karanasiou and Dr Fulvio Amato carried out the sampling in Barcelona upon which much of Chapters 5 and 6 is based.

Fellow students Lami Abdullahi, Nick Davidson, Ian Keyte, Jenny Kirby, Max Mascelloni, Barbara Macias-Hernandez, Adobi Okam and Pallavi Pant have all offered advice and support throughout.

Finally, my parents John and Jane Sanderson, and my brother David. I could not have completed my PhD without the unstinting support and understanding of my family.

CONTENTS

CHAPTER 1: INTRODUCTION AND LITERATURE REVIEW

CHAPTER 5: GRAVIMETRIC ANALYSIS OF FILTERS AT UK URBAN AND RURAL SITES AND AT ROADSIDE AND BACKGROUND SITES IN BARCELONA

CHAPTER 6: BULK CHEMICAL ANALYSIS OF FILTERS USING INDUCTIVELY COUPLED PLASMA MASS SPECTROMETRY AND ANION CHROMATOGRAPHY

LEGEND OF FIGURES AND TABLES

FIGURES

TABLES

CHAPTER 1: INTRODUCTION AND LITERATURE REVIEW

Explanatory notes on terminology

Airborne particulates are a highly complex mixture of different particle types, derived from many different sources and with considerable heterogeneity of composition. There is surprisingly little consistency in terminology and definitions between published works, due to different sampling protocols and different size divisions imposed by different instruments which lead to particles being classified differently. This can make direct comparisons of published measurements difficult.

The term nanoparticle (NP) is used to refer to a wide range of particles, and definitions vary considerably between different studies, depending on the context of the study and the technique of measurement. It is most frequently used as a specific size description (usually < 100 nm, though sometimes < 50 nm) and this study will use the term nanoparticle to refer to particles of < 100 nm, interchangeably with the term ultrafine particle (UFP) (taken to mean $PM_{0.1}$). If the study being referred to defines these terms differently this will be stated. Likewise, the terms atmospheric, airborne and ambient will be used interchangeably, and refer to outdoor and indoor non-occupational environments. Many sources also refer to particle modes – nuclei, Aitken, accumulation, coarse – and definitions of these modes also vary greatly. This subject is discussed at length in a review of atmospheric nanoparticles (Kumar et al., 2010). Some recent studies of UFP have included larger particles up to 180 or even 250 nm aerodynamic diameter (Daher et al., 2013; Ntziachristos et al., 2007; Saffari et al., 2013). The cut-off point between ultrafine and accumulation modes is not clear; a large fraction of accumulation mode particles are sourced from UFP, and due to the fractal structures of soot particles, particles with measured diameter > 100 nm may be comprised of small sub-particles within the nanoparticle size range. Some studies refer to particles up to 180 or 250 nm as ‘pseudo-ultrafine’. Where the use of MOUDI instruments makes the lowest

size fraction $PM_{0.18}$ (or for Barcelona background data, $PM_{0.22}$) this convention is followed in the thesis.

1. REASONS FOR STUDY OF METALLIC NANOPARTICLES

1.1 Possible health implications relating to personal exposure

It is well established that suspended particulate matter in the atmosphere can have serious implications, both long and short term, for human health. Generally, the finer the particle the more severe the effect, since particles with a smaller atmospheric diameter can penetrate further into the respiratory system. Air pollution exposure estimated from central monitoring data has been repeatedly associated with mortality. Moreover there is a stronger association between mortality and exposure to fine PM than with total suspended particulates(Dockery et al., 1993).

The impact of particulate exposure, both acute and chronic, has been studied extensively; strong evidence links PM exposure to detrimental effects on respiratory and cardiovascular systems, for instance reducing lung function, exacerbating asthma and bronchitis, and possible impacts on lung development in childhood. Associations of both chronic and acute exposure on cardiopulmonary health are strong in the cases of ischemic heart disease and possible for cerebrovascular disease and cardiac arrhythmia and arrest (Kelly and Fussell, 2012a). A connection between PM exposure and increased frequency, size and vulnerability of atherosclerotic plaques offers another route by which PM exposure could increase cardiovascular mortality (Kelly and Fussell, 2012a). Connections between exposure to fine and ultrafine particulate matter and DNA damage through strand breaks and oxidation of guanine to mutagenic 8-oxoguanine have been reported (Bräuner et al., 2007); the study reported an increase in strand breaks and formamidopyrimidine DNA glycolase sites after subjects were exposed to nonfiltered urban air compared to filtered air. A significant dose-response relationship was observed with the 57 nm mean particle diameter mode having the main contribution to these effects. They also reported, in contrast to previous work, that

expression of repair activity was unaffected within the 24hr exposure time. The impacts both of air pollution generally and various PM components specifically on the brain is also an area of intense research. Evidence for effects on the central nervous system related to air pollution exposure is accumulating (Block et al., 2012) although in many areas is not currently well understood. Evidence has been presented to show that ambient PM and diesel exposure are associated with elevated cytokine expression and oxidative stress in the brain; it is suggested that excessive, chronic activation of microglia may be an important mechanism, as this has been shown to lead to neuronal damage and be associated with neurodegenerative diseases such as Parkinson's and Alzheimer's. However, the connection between PM exposure and neuroinflammation is not fully understood and could be exposure specific.

In the case of nanoscale particles (<100 nm), particles can be transported within the body from the typical entry routes such as the gastrointestinal tract and the lungs via the circulatory and lymphatic systems to enter into organs and tissues (Buzea et al., 2007). As such, there is increasing research interest in the health impacts of airborne particulates in the nanoparticulate size range. Ultrafine (smaller than 100 nm in diameter) aerosols form, by particle number, the largest share of the total ambient aerosol loading (Bzdek et al., 2012a). Translocation of nanoparticles to different systems and organs within the body is important and much progress has been made in understanding the movement of nanoparticles in biological systems. Ultrafine particulates deposited in the olfactory epithelium can be distributed via olfactory transport throughout the brain; the mechanisms for this process remain unclear although metal-binding carrier molecules and proteins have been implicated, following results showing that several metals including Mn, Fe, Cd, Th, Hg, Co and Zn can move into the brain following inhalation and exposures in the intranasal and tracheal regions (Block et al., 2012).

Particulate matter is a heterogenous mixture of particles varying greatly in morphology and chemical composition depending on a wide range of contributing factors. At present it is difficult to quantify health effects from different sources or components, this being complicated further by the interactions between components to act on different physiological mechanisms (Kelly and Fussell, 2012b). Lung epithelial cells co-exposed to iron oxide nanoparticles and carbon black showed much greater oxidative stress than if exposed to either pollutant on its own (Guo et al., 2009). The authors attributed this effect to reduction of Fe^{3+} by carbon black nanoparticles inside the cells, and suggest that it is not valid to assume elemental carbon materials are inert in particle toxicology studies. Studies revealing that metals and carbon can exert synergistic effects have important implications, given that a study in California determined ultrafine particles to be formed by mass of 9% carbon black and 14% transition metal oxides (Cass et al., 2000).

As well as the difficulties in assessing the actual causes of particulate related health impacts, there are also problems in accurately measuring the biologically effective dose (BED) resulting from a specific exposure. It is being recognised that the traditional metrics of ambient particulate matter mass (PM_{10} and $PM_{2.5}$) are not a good indicator of BED as much of the harmful material may be biologically inaccessible, for instance located in the bulk of a carbonaceous particle. This is particularly important in the case of ultrafine and nanoparticles, owing to their increased reactivity due to higher surface area/volume ratio which is crucial for nanobiological interactions. The surface properties, both in physical morphology and chemical composition, of nanoparticles are known to be more important than the bulk composition in interactions with biological systems making it important to accurately characterise the distribution of metals within particles (Elsaesser and Howard, 2012).

Nanoparticle exposure is associated with asthma, bronchitis, emphysema and lung cancer, as well as neurodegenerative diseases, from inhaled particles (Buzea et al., 2007). Entry into the

bloodstream is associated with increased instances of heart disease and cardiac arrhythmia. As well as the effects on the cardiopulmonary system, nanoparticle entry into the bloodstream has also been linked with enhanced neuroinflammation and changes to the blood-brain barrier in young people living in areas with high air pollution levels (Cassee et al., 2011). Various likely mechanisms of nanoparticle toxicology have been proposed, including the generation of reactive oxygen species, protein misfolding, perturbation of membranes and direct physical damage (Elsaesser and Howard, 2012). The authors pointed out the importance and the difficulty of characterising nanomaterials, because variations in particle size, roughness, shape, charge and chemical composition, especially of the surface, with which biological systems primarily interact, make characterisation more complex than for larger materials. Estimation of dose is also deemed to be complicated, with the authors noting that it remains a subject of debate whether mass, number or surface area is the most important parameter when estimating doses; furthermore, there is a clear requirement for estimation of dose to be based on real-life exposure levels, but existing models of chronic low-level exposure in rodents are not adequate for this purpose. Chemical and physical properties of nanoparticles lead to a number of processes in response on and inside cells, such as physical and chemical damage to the stability of cell membranes, interference with cell signalling processes and proteins, and since it has been reported that some nanoparticles can enter the nuclear envelope, the potential for DNA damage. This could also be induced by other effects of nanoparticles on cells such as an increase in reactive oxygen species, rather than requiring the direct involvement of the nanoparticles.

A number of metals are known to be toxic by inhalation and/or ingestion, and furthermore may have somewhat different effects in the nanoparticle phase, owing to the differences in reactivity and surface chemistry resulting from the small particle size (Buzea et al., 2007). Atmospheric trace metals occur largely within this size fraction, with a number of trace

elements emitted from hydrocarbon combustion and other traffic related sources such as brake wear and material originating from catalytic converters and engine components. While mass concentrations are not high, trace metals are ubiquitous in urban environment atmospheres (Querol et al., 2007) meaning that exposures to trace metals in ambient air are a concern for public health. Once deposited within tissues, metallic particles are known to cause damage through oxidative stress and pulmonary inflammation and can lead to heart attacks and cardiac arrhythmia, though biological effects are highly dependent on particle size, structure and composition (Adachi and Buseck, 2010).

It is thought possible that vanadium and nickel, both markers for fuel oil combustion and therefore important in urban atmospheres, may interact to produce adverse health effects (Tolocka et al., 2004). Iron, emitted by incinerators, boilers and smelters and also brake wear, is known to cause elevated hydroxyl radical levels in the lung. Existing evidence for the health effects of cerium oxide is limited – the Health Effect Institute reported that even in a worst case scenario of 1.2 ug/m^{-3}, the public health risk appears small, though they qualified this by noting that there was insufficient evidence to assess the risk of long-term exposure. Park et al. (2008) concluded that exposure to nano-ceria in ambient air as a result of the use of the ceria fuel additive Envirox was not harmful at then-current levels of exposure (Park et al., 2008a). A recent in vivo study of exposure to ceria-doped diesel fuels in mice concluded that the only cause for concern from the use of ceria-doped fuels was a raised level of cytokines in part of the nervous system. This study concluded that ceria-doped fuels posed less of a risk of atherosclerosis – while a trend towards increased size and complexity of atherosclerotic plaques was observed from exposure to ordinary fuel this did not happen when ceria was added(Cassee et al., 2012). Steiner et al. (2012) have reported on an in-vitro 3D co-culture study which found that although combined exposure to diesel exhaust particles and CeO_2 nanoparticles did not result in cytotoxic effects, either at low (20 µg/ml) or high

(60 µg/ml) doses, there was a significant loss in the reduced intracellular glutathione level. High exposure also led to an increase in gene expression and protein release of tumour necrosis factor-alpha. The study concluded that this demonstrated the ability of CeO_2 nanoparticles in conjunction with diesel exhaust to interfere with cell machinery, indicating a possibly adverse role for CeO_2 nanoparticles in the biological response to exposure to diesel exhaust (Steiner et al., 2012). Chuang et al. (2012), used MOUDI instruments to collect PM in a range of size fractions at a coach station in Taipei, and found that trace metal concentrations were positively correlated with increased production of the vasoactive regulators NO and endothelin-1 and the proinflammatory interleukin-6, demonstrating that trace metals in PM can alter regulation in the endothelium and cause inflammatory effects (Chuang et al., 2012).

The World Health Organisation upgraded diesel exhaust from a possible carcinogen to known carcinogen in June 2012 (http://press.iarc.fr/pr213_E.pdf), based on a range of evidence connecting long-term exposure to diesel to an increased risk of lung cancer and bladder cancer. Diesel had been listed as a possible carcinogen by the WHO since 1989. A long term study investigating cancer in miners exposed to diesel exhaust concluded that there was a causal relationship between exposure and lung cancer mortality. They also concluded that exposures to elemental carbon levels of around 2-6 $\mu g/m^3$ (similar to some highly polluted cities) were similar to cumulative exposures experienced by underground miners with lower exposures in the terms of the study. These subjects experienced a 50% increase in lung cancer risk, implying that the public health problem posed by diesel inhalation among urban populations and workers in high exposure scenarios could be significant (Attfield et al., 2012). McClellan et al. (2012) have argued that the composition of exhaust particles emitted from new technology diesel engines is significantly different to that of traditional diesel

engines (much lower PM mass) and therefore should not be classed as a carcinogen (McClellan et al., 2012).

Nanoparticles from brake wear, a known source but not extensively studied at this time, are concerning because despite limited knowledge of physical and chemical characteristics of such particles, there is minimal regulation and manufacturers are not obliged to work towards formulations posing less health or environmental risks (Kukutschová et al., 2011).

Therefore there are good grounds to be concerned about the potential health impacts of atmospheric metallic nanoparticles, and any assessment of such health problems requires detailed characterisation of the ambient concentrations, compositions and forms of metallic particles in order to determine which components are present and begin to assess which will be most hazardous. Addressing the characterisation questions was the main aim of this project.

1.2 Roles in atmospheric and bio/geochemical cycles.

Trace metals in ultrafine particles, including Fe, Mn and Pb, are now known to exert an important role in many atmospheric chemical reactions. For instance, Fe(III) and Mn(II) are known to participate in the oxidation of S(IV) compounds such as SO_2 to S(VI) compounds such as H_2SO_4 by O_2 in aqueous aerosol (Kerminen et al., 2000). This is known to be a complex cycle, because of the complicated equilibria between the different Fe states. At low initial pH conditions Fe(III) is most important but at higher pH Fe(II) dominates (Grgić et al., 1993). Both are present in ultrafine particles. Grgic et al. focused on Fe leaching from soot from coal burning in this study, but many possible Fe and Mn sources may exert an influence on this process. There is also a synergism between Fe and Mn at low S(IV) concentrations which markedly increases the oxidation rate (Martin and Good, 1991).

Iron has also been shown to influence marine productivity and therefore has a marked influence on the global carbon cycle (Mahowald et al., 2005).

1.3 ORIGIN AND SOURCES OF METALLIC NANOPARTICLES

There are a wide range of known sources of metallic particles in the ultrafine size range, contributing many different elements to the particulate mass in a number of different chemical or physical forms. Among the more commonly observed metals in ultrafine aerosol are Na, Ca, K, Al, Fe, Pb, Ni, Cr, Ti, V and Zn, but a number of less abundant elements such as U and Ce have also been observed (Bzdek et al., 2012b).

In recent years there has been growing appreciation of the significance of metallic nanoparticles in the atmosphere. In particular, the nanoparticle fraction of metals produced by road traffic appears to be increasing as a proportion of the total particulate matter emitted by motor vehicles, owing to the increasing use of metallic fuel additives, catalysts and diesel particulate filters (Liati et al., 2012) and additives in lubricating oil (Miller et al., 2007b). Particularly important are metallic fuel borne catalysts (Gidney et al., 2010; Jung et al., 2005; Lahaye et al., 1996; Nash et al., 2012; Park et al., 2008a), the aim of which is to reduce the total inhalable particulate matter fraction. In doing so they fundamentally change the morphology and distribution of emitted particles, decreasing the size of soot particles (Morawska et al., 2009).

It has been reported that 50% of metal-containing nanoparticles contain more than one metal (Adachi and Buseck, 2010). Fe, Zn, Ni, Cr and Ti are often found in particles containing two or more metals. Particular combinations of multiple elements have sometimes been found to be specific to particular sources or processes, enabling these particle classes to be used as markers (Bzdek et al., 2012b) or to demonstrate common emission sources. A study in Baltimore discovered that Fe particles were detected under certain wind conditions, and 62%

of these particles also contained Pb. They were able to assign these particles to emissions from a medical waste incinerator near to the sampling site (Tolocka et al., 2004).

Source Type	Associated Elements	Reference
Diesel	Al, Ca, Cu, Fe, Mg, Mn, V, Zn	Liati et al., 2012; Patel et al., 2012
Gasoline (emissions)	Sr, Cu, Mn	Lin et al., 2005
Lubricating oil	Fe, Ca, P, Zn, Mg	Gidney et al., 2010
Fuel-borne catalysts	Fe, Mn, Ce	Park et al., 2008a; Casee et al., 2011
Diesel Fuel (Marine engines)	Al, Ca, Fe, Ni, V, Zn	Lyyrannen et al., 1999; Moldanava et al., 2009; Kumar et al., 2012
Non-exhaust traffic sources:		
Brakes	Fe, Cu, Sn, Zn	Kukutschová et al., 2011
Tyres	Cd, Co, Cr, Cu, Fe, Mn, Pb	Adachi and Tainosho, 2004
Road dust	Zn, Al, K, Fe, Na, Mn	Saffari et al., 2013; Daher et al. 2013
Industrial sources:		
Metalworking	Fe, K, Na, Pb, Zn	Reinard et al., 2007
Power generation	Ce, Fe, La, Na, K, V,	Reinard et al., 2007; Linak et al., 2007;
Incinerators	Cd, Pb, Sb, Zn	Tolocka et al., 2005

Table 1. Metals in ultrafine particles associated with known sources.

1.3.1 Crustal Origin

Studies of the Si/Al relationship in ambient aerosols have revealed an extremely close correlation between the concentrations of the two elements, thereby demonstrating that the main source is likely to be crustal (Kenneth A, 1976). This study also suggests, however, that fly ash and anthropogenic dust may affect the Si/Al ratios in urban areas. However, while the diagnostic use of the ratio is considered to be useful for $PM_{2.5}$ or PM_{10}, it is less likely to be valid for the ultrafine size fraction, due to the presence of Al in diesel exhaust particles (Bérubé et al., 1999). Since such particles are prime contributors to urban ultrafine aerosol, this will skew the Si/Al ratio compared to crustal reference materials. Furthermore, Lin et al.

(2005) reported that Al, Si, Ca and Fe all exhibited ultrafine Aitken modes (below 100 nm), which implies that local combustion sources are responsible for most particles of these elements in this size range (Lin et al., 2005). This has clear – but so far little discussed - implications for the validity of using these elements as crustal tracers in the ultrafine size range.

Many studies have used concentrations normalised to aluminium for other metal concentrations in order to calculate enrichment factors (Dodd et al., 1991; Ntziachristos et al., 2007). Ntziachristos et al. (2007) reported that although it was not possible to rule out an anthropogenic contribution to roadside Al, Al abundance did not exceed its upper continental crust enrichment level in any of the samples they collected. Park et al. (2008b) have also found that Ca concentrations in ultrafine particles collected in Gwangju, Korea were significantly enriched during an Asian dust event, although the total UFP mass did not increase (Park et al., 2008b).

1.3.2 Industrial Processes

Waste incinerators are known to be a source of trace metals in atmospheric particulates, although abatement technology on modern incinerators is designed to limit their emissions to low levels ((Buonanno et al., 2009). $ZnCl_2$ is a prominent component, while Sb, Cd and Pb are also known to be emitted by incinerators. These three metals in combination have been used as a marker for incinerator emissions (Tolocka et al., 2005). A previous study reported that number size distributions of particles containing V, Fe, As and Pb peaked at 150 nm in Baltimore (Tolocka et al., 2004), indicative of combustion and incineration sources.. Cernuschi et al. (2012) reported that metals accounted for 17% of total PM mass below 50 nm and 22% below 100 nm emitted from four waste to energy plants, and observed that particle formation mechanisms are similar to solid fuels such as coal. The main metals in

ultrafine and nanoparticle emissions (100 nm and 50 nm respectively) were Cr, Fe, Ni, Pb and Zn. Traces of Ti, V, Mn and Co were also detected (Cernuschi et al., 2012). Buonanno et al. (2011) measured metal content in particles of 50, 100, 150 and 200 nm. Concentrations of metals with boiling points below 1200C (As, Cd, Zn) were found to decrease with increasing particle size and metals with higher boiling points (Co, Cr, Fe, Sb, Sc, Sm, Th, Eu, Yb) to increase with particle size, as the more volatile elements boiled and then nucleated during cooling. The less volatile elements remained in solid phase (Buonanno et al., 2011). However, modern energy from waste plants have extremely low nanoparticle emissions (Buonanno et al., 2009; Ragazzi et al., 2013).

Many metals are also emitted by coal combustion, such as in power generation. Linak et al. (2007) reported that fly ash particles below 500 nm contained elevated concentrations of more volatile metals such as Na, K and V. Iron is the most important metal and is reported to occur quite uniformly in all size fractions, with nanoparticulate γ-Fe_2O_3 being especially prominent below 500 nm (Linak et al., 2007).

Zn and Ni concentrations measured in ultrafine particulate matter in Gwangju, Korea, were found to exhibit a strong wind direction dependence which tied them to a nearby industrial complex, from which the main sources were metallurgical processes (Park et al., 2008b).

1.3.3 Traffic: Exhaust and Non-Exhaust Sources

Emissions from road vehicles are the primary source of metallic nanoparticles to the atmosphere. These can include combustion derived material from internal combustion engines, the metallic content being derived from lubricating oils, fuel additives and trace amounts in gasoline and diesel fuels, particles from brake wear (Gietl et al., 2010), and from resuspended tyre dust.

1.3.4 Exhaust sources

Miller et al. (2007b) attempted to isolate the effects of lubricating oil additives by using TEM-X-EDS to analyse particles generated in a hydrogen-fuelled engine. It was found that soot agglomerates were rare, while four types of metal-bearing particle were common. High density metallic spheres formed of Fe, Ca, P, Zn and Mg were seen across a wide size range (30-300 nm; such particles tend to be at the smaller end of this range in diesel and become associated with soot) and probably originate from self-nucleation of dense elements like Fe and Ca coated with more volatile components, which condense onto the surface during cooling. Less dense spheres, containing less Ca, were also seen. In some cases the volatile components formed shells around metals. Spherical nanoparticles, mainly composed of Fe, were observed and likely formed immediately after combustion by self-nucleation. Some carbonaceous particles were attributed to homogenous nucleation of hydrocarbon vapours (Miller et al., 2007b). Aluminium and vanadium are both associated with combustion processes. Al is most likely to derive from wear to mechanical parts in the engine itself, while vanadium is naturally present in oil and is often used as a marker for fuel oil burning (Tolocka et al., 2004).

Diesel exhaust is the most important traffic-related nanoparticle source. A study in Mexico City (Adachi and Buseck, 2010) discovered that around 70% of metal nanoparticles were embedded in or attached to particles containing soot with 13% in particles of organic and sulphate compounds, but only around 1% were in soot particles not associated with organics and sulphate. The authors proposed that condensation involving organics and sulphate led to this association in polluted air. However, a lack of obvious correlation between metallic nanoparticle composition and the presence of soot implies that many metallic NPs are incorporated during atmospheric transport. Diesel soot, being formed by high temperature

combustion or pyrolysis of hydrocarbons, consists primarily of carbon, with small amounts of oxygen and hydrogen. However, other elements can become associated with it through interactions with lubricating oils. Among these components are phosphorus, sulphur, calcium and zinc (Patel et al., 2012). Liati et al. (2012) investigated the inorganic ash components of diesel emissions deposited in the diesel particulate filter of a light truck using TEM-X-EDS. They found the inorganic particles to be highly variable in size (7-12 to 170 nm) and to consist mainly of Ca, Mg, P, Zn, S and O with some Al and Fe. Some metallic material reached the ambient air, some but not all associated with soot. These findings were similar in a passenger car using Fe-doped fuel, but in this case the typical particle size was smaller; from 4-40 nm (Liati et al., 2012).

Fewer data are available concerning gasoline engine exhaust; however, Lin et al. (2005) reported that relative abundances (normalised to upper continental crust) of several metals (Sr, Cu and Mn) in ambient samples in the 56-100 nm size range were similar to those in gasoline exhaust, and strikingly different to those in diesel soot. By contrast, Ba, Pb and Zn showed similar relative abundance in the 56-100 nm range to diesel soot (Lin et al., 2005) . It has been reported that metallic additives (Mn, Fe, Pb) cause significant changes to particle size distributions from gasoline engines. While untreated fuel exhibited a unimodal distribution with only an accumulation mode which was attributed to hydrocarbon removal by the three-way catalyst, metallic species increased number concentrations in the ultrafine mode. Treatment with a catalytic stripper demonstrated that the nucleation mode particles were largely composed of inorganic material. Furthermore, iron and manganese, which are able to condense at around 1250°C, were present in much higher amounts than lead, which remains in the gas phase down to 650°C (Gidney et al., 2010). Kittelson et al. (2006) carried out a detailed investigation of on-road number distributions from spark-ignition gasoline engines and determined that emissions were low under cruise conditions but under heavy

acceleration, distributions similar to diesel engines were produced. Source apportionment showed that number concentration was dominated by heavy duty diesels, except at weekends when light duty gasoline engines became more important (Kittelson et al., 2006).

1.3.5 Fuel additives

The increasing use of fuel-borne oxidation catalysts to improve engine performance is currently a cause for concern as these can add species and quantities of potentially harmful metals to the ultrafine particulate burden which would not otherwise be present.

Recent studies (Cassee et al., 2011; Park et al., 2008a) have shown that nanoparticulate CeO_2 is present in ambient air, resulting from use as an additive in diesel fuels. Ceria is generally added to diesel as nanoparticles resuspended in an organic matrix to make them miscible with diesel fuel. For example, the nanoparticulate ceria additive Envirox is suspended in a hydrocarbon carrier at 2% w/v, and diluted with diesel at 1:4000 for a concentration of 5 mg dm^{-3} in fuel. This approach is considered superior to coating particulate filters in the catalyst, an approach which suffers from catalytic poisoning by combustion gases (Lahaye et al., 1996). Functioning as an oxygen donating catalyst, it can improve and extend fuel burn and enhances the performance of particulate filters by oxidising deposited material, such as hard carbon deposits. While particulate emissions as a whole are found to decrease if CeO_2 is used (by approximately 15%, according to Park et al. (2008a) emissions in the nanoparticle range are found to increase (Park et al., 2008a). Jung et al. (2005) tested the impact of adding Ce to a medium duty diesel engine, discovering that the number of accumulation mode particles decreased while the number of nucleation mode particles increased; they attributed this to the reduction in the available surface area reducing the scavenging of particle precursors, thereby leading to more homogenous nucleation and reduced coagulation of nucleation mode particles with particles in the accumulation mode (Jung et al., 2005).

Metallic additives using other metals are also available. Optimax 4804, tested in diesel at 200 ppm by Song et al. (2006), contains a 4:1 ratio of Fe:Sr. Especially at light loads, this additive yielded a significant reduction in total soot especially at lower engines loads, but led to metal oxides being detected in the soot aggregates (Song et al., 2006). Ferrocene has also been tested as a fuel borne catalyst (Lee et al., 2006), introduced into the fuel by dissolving ferrocene powder in a small volume of diesel then blending with the bulk fuel to the desired concentration. Ferrocene doping was found to produce iron-rich nanoparticles, whose size and concentration increase with doping level.

Lenin et al. (2013) recently tested additives prepared from MnO and CuO, MnO being found to be the more effective of the two. As in the ferrocene and ceria studies, soot production was found to be reduced but to include metal oxides from the catalyst in inhalable particles (Lenin et al., 2013).

1.3.6 Non-exhaust traffic sources

Material derived from brake wear can originate either from abrasive processes (which tend to produce particles in the fine and coarse modes) or from volatilisation of metals due to heating, which tends to produce ultrafine particles. Ba, Sb, Mg, Cu, Fe and Zn are all present in brake materials and therefore associated with PM derived from this source (Gietl et al., 2010). Metal silicates and mineral fibres have also been associated with brake linings (Hays et al., 2011). Composition of brake discs and linings varies considerably between manufacturers and applications, however, so wide ranges of composition are possible in emitted particles from this source. At sites where traffic emission predominates, brake wear appears to be the main source of these elements. Ba, which is unlikely to have many other sources, can be used as a tracer for brake wear in fine PM (Gietl et al., 2010). Evidence from

roadside studies suggests this is also possible for ultafine PM. For example, Ntziachristos et al. (2007) found that Sb, Fe, Ba and Cu, all associated with brake wear by earlier studies, showed significantly higher concentrations at a roadside site both in $PM_{0.18}$ and $PM_{2.5}$, illustrating both abrasive and volatilising processes contributing these elements, with the enrichment being more significant in the accumulation mode than the ultrafine mode. Evidence of nanoscale wear particles being produced has been found in laboratory tests. Garg et al. (2000) found that between 26-44% of the total mass of emitted brake particles were 100 nm or less (Garg et al., 2000). Kukutschová et al. (2011) reported that the nanoscale particles differed considerably in chemical composition from larger wear particles and from the bulk composition of the brake material, owing to the high temperatures and pressures at the friction interface. Cu, Fe, Sn and Zn were confirmed in nanoscale particles, but although Mo, Al and Pb were found in the bulk material they were not confirmed in the smallest wear particles (Kukutschová et al., 2011). These elements have been detected in ambient $PM_{0.25}$, associated with the road dust fraction at urban sites and separate from it at rural ones, probably due to the dominance of traffic sources making apportionment at urban sites more difficult (Saffari et al., 2013).

Tyre dust contributes metallic particles to aerosol from a number of sources (Adachi and Tainosho, 2004). Zinc oxide is particularly important but other metals including Mn, Fe, Co, Ni, Cu, Cd and Pb are also emitted. While tyre wear is often associated with coarse particles, Dahl et al. (2006) present evidence showing that nanoparticles are also emitted. Mean particle number diameters were found to be between 15-50 nm, with emission factors increasing with speed. Compared to an emission study assuming a light-duty vehicle fleet of 95% gasoline and 5% diesel vehicles, the emission factors corresponded to 0.1-1% of tailpipe emissions (Dahl et al., 2006). Gustafsson et al. (2008) also reported nanoparticle generation from tyre-surface interfaces (Gustafsson et al., 2008).

Tyre dust is known to include particles which are not originated from the tread, but from brake dust, paint and abraded asphalt, each of which has distinct chemical and morphological characteristics (Adachi and Tainosho, 2004). Aggregate oval particles of $PbCrO_4$ are particularly associated with abraded particles of yellow paint, high levels of iron and Cu/Sb ratios of 4.6 +/- 2.3 with brake wear particles and multi-angular ZnO containing particles with tyre tread, although the ZnO content of tread can vary significantly. So far, the determination of tracer elements and/or diagnostic ratios for tyre dust have proven unsuccessful. Zinc has several other sources and there are no other metals associated only with tyre wear in the way barium appears to be for brake material (Thorpe and Harrison, 2008). These authors suggest that while it may be possible to assign tracer elements through experimental measurements, the results would only be specific to that site (Thorpe and Harrison, 2008). Elements associated with road dust resuspension such as Al, K, Fe, Na and Mn have been reported in ambient samples below 250 nm by Saffari et al. (2013) and Daher et al. (2013). Furthermore, these have been found to correlate with organic carbon concentrations, linking them to motor vehicle emissions.

1.3.7 Emissions from residual oil fuel – marine diesel engines

In or near ports, nanoparticle pollution from heavy duty marine diesels will also be relevant. The physico-chemical characteristics of emissions from engines using low-grade residual fuel oils are quite different to automobile diesel engines, owing to the higher ash and aromatic content, the high air to fuel ratio which should produce less carbon soot, and the more variable conditions inside the cylinders (Lyyränen et al., 1999). Existing data regarding medium duty marine diesels show bimodal particle size distributions, in which the modes are found at 60-90 nm and 7000-10000 nm. The primary particles have been determined to be spherules, formed by nucleation of ash from metallic contaminants – V and Ni are

particularly prominent, but Al, Ca, Zn and Na were also observed (Lyyränen et al., 1999). The mass distributions of these elements generally follow the bimodal structure of the PM distribution, but compared to V and Ni, Ca and Zn have larger coarse modes. Moldanava et al. (2009) found three main metal-bearing morphologies in emissions from residual oil fuels: soot aggregates of carbon containing V, Ni and S, dominating $PM_{1.0}$; char and char mineral particles (200-5000 nm) consisting of carbonaceous spheres, in some cases quite pure but in others high in V, Ni, Ca and Fe; mineral ash of prismatic crystals (CaO, $CaSO_4$, $CaCO_3$, NiS and V_2O_3 were all identified), which were often found embedded in carbonaceous matrices. They also found carbon based particles originating from uncombusted fuel and lubricating oils. The authors concluded that morphological and composition structures in ship-exhaust residuals are very different from typical soot-like particles associated with emissions from other sources (Kumar et al., 2012; Moldanová et al., 2009). Saffari et al. (2013) detected a class of V-La-S particles in samples collected at Long Beach, directly affected by ship emissions, but found that this class could not be resolved by Principal Component Analysis at receptor sites inland (Saffari et al., 2013).

1.3.8 Biomass Burning and Wood Fuels

Evidence for metals in ultrafine particle emissions from these sources has been reported. Different fuel types and combustion conditions produce very different particle types and composition, so it is not thought possible to suggest universally applicable tracer elements, although it is possible to distinguish between softwood and hardwood particle emissions (Kleeman et al., 1999). Tissari et al. (2008) reported that combustion of birch wood produced ultrafine ash particles. Metallic content was dominated by K and Zn, with Ca, Fe, Mg and Na also observed in some particles. These particles were found to be formed under ideal combustion conditions. Under incomplete combustion, carbonaceous particles dominated

(Tissari et al., 2008). Kleeman et al.(1999) reported that particle mass distributions from wood smoke from pine, oak and eucalyptus exhibited a single mode peaking between 100 and 200 nm aerodynamic diameter, determined gravimetrically from samples collected by MOUDI. Several metals were observed in these samples. K showed similar distributions in emissions from all three fuels, while other trace metals varied more, probably due to differences in the soil composition and climate conditions the woods grew in. Pine particles were associated with Fe, Rb and Ti, oak with trace levels of Al, Ba, Fe and Zn and eucalyptus with Al, Ba, Fe, Rb, Sr and Ti (Kleeman et al., 1999).

1.3.9 Summary

The complexity of source profiles, with many elements attributable to multiple sources, is a major challenge but also offers the possibility of attributing certain elemental combinations and physical forms to sources as a way of discriminating between them. It also makes composition of ambient particles highly site-specific and dependent on local conditions, and therefore variable even at single sites.

1.4 CONCENTRATIONS AND EXPOSURES

1.4.1 Mass Concentration of Metals in Ultrafine and Quasi-Ultrafine Particles

Table 2 contains mass concentration data for metals in size fractions below 250 nm diameter. These field measurements indicate a remarkable diversity of metal concentrations in the ultrafine and pseudo-ultrafine size fractions, both in absolute terms and relative to other elements.

Study	**Chuang et al., 2012**	**Lu et al., 2012**	**Nztiachristos et al., 2007**	**Hughes et al., 1998**	**Pakennen et al., 2001**		**Cass et al., 2000**	**Park et al., 2008b**	**Saffari et al., 2013**			
Instrument	MOUDI	nanoMOUDI	nanoMOUDI	MOUDI	Berner Low-pressure Impactor		MOUDI	4-stage LPI	SPCI			
Metric	$PM_{0.1}$	$PM_{0.1}$	$PM_{0.18}$	$PM_{0.097}$	$PM_{0.1}$		$PM_{0.056\text{-}0.1}$	$PM_{0.132}$	$PM_{0.25}$			
Location	Coach station, central Taipei City, Taiwan	Xujiahui, Shanghai, China (urban rooftop site)	Nr I-710 freeway, South Gate, CA	Pasadena, California winter	Urban: Vallila, Helsinki, Finland	Rural: Luukki, Espoo, Finland	Central Los Angeles	Rooftop urban background site, Gwangju	Long Beach	Los Angeles	Riverside	Lancaster
Season	Sept – Nov	Dec – Jan	Feb - Apr	Jan – Feb	Annual mean		Aug - Sept	Annual mean	Annual mean			
Element												
					urban	**rural**						
Ag					3.70×10^{-3}	5.90×10^{-3}			0.04	0.01	0.04	0.02
Al			~6		0.51	0.44			24.7	4.58	13.1	17.8
As	0.76 ± 0.53	2.16			0.016	0.01		0.6	0.04	0.01	0.02	0.01
Ba			~1-2	1.04	0.058	0.031	19					
Be								<0.01				
Bi					1.90×10^{-3}	1.70×10^{-3}						
Ca		6.23	~6		2.2	1.9		200	23.8	5.36	12.7	11.6
Cd	0.12 ± 0.03			0.061	3.50×10^{-3}	2.40×10^{-3}	0.19	0.06	0.01	0.01	0.03	0
Ce				0.19			1.2					
Co	0.07 ± 0.08				0.024	0.023			0.02	0	0.01	0.02
Cr	0.52 ± 0.49	0.69		7.32			6.7		0.35	0.17	0.51	0.11
Cs				0.016			0.1					
Cu	7.24 ± 8.38	7.34	~1-2		0.14	0.17			1.71	1.2	1.15	0.57

Eu				0.013			0.2					
Fe	9.49 ± 12.57	14.38	35	67.5	1.8	0.73	186	150	37.8	10.9	17.5	27.2
Hg				5.20×10^{-3}			0.09					
K					0.86	1.3	88	300	14.4	4.36	9.32	23.2
La				0.11			0.021		0.02	0.01	0.01	0.01
Li					2.50×10^{-3}	1.60×10^{-3}			0.03	0.01	0.03	0.03
Lu				3.80×10^{-4}			0.014					
Mg					0.26	0.27		3	6.01	1.22	3.61	5.12
Mn	0.96 ± 0.95	0.48		0.74	0.035	0.014		~1	0.79	0.17	0.42	0.78
Mo	2.25 ± 0.24			7.20×10^{-2}	0.015	0.013	0.48		0.18	0.03	0.06	0.02
Na			~6	27	2.9	1.3	85		10.6	2.67	5.24	16.3
Ni	4.57 ± 1.33	0.61			0.24	0.24			0.27	0.11	0.23	0.08
Pb	7.89 ± 4.36	4.88						8	0.46	0.13	0.32	0.13
Rb		0.14			2.80×10^{-3}	6.60×10^{-3}			0.04	0.01	0.02	0.05
Sb					0.022	6.00×10^{-3}		4	0.25	0.12	0.12	0.07
Sc							0.028					
Se	0.62 ± 0.53	0.08			0.032	0.035		0.6				
Sm				0.015			0.012					
Sn									0.24	0.74	0.09	8.77
Sr	1.41 ± 1.40	0.03			0.01	9.00×10^{-3}			0.26	0.08	0.11	0.15
Th				6.50×10^{-3}	1.90×10^{-4}	9.60×10^{-4}						
Ti	1.56 ± 1.63	0.43	~1-2	7.65	0.04	0.034	43		3.09	0.69	1.1	3.26
Tl					2.20×10^{-4}	2.00×10^{-4}						
U												
V	5.65 ± 3.65	4		0.059	0.16	0.092		0.2	0.87	0.19	0.18	0.16
Yb		2.06		2.80×10^{-3}			0.26					
Zn	54.71 ± 66.61		~1-2	3.68	0.81	0.7	3.8	50	3.09	0.89	1.07	1.48

Table 2. Reported concentrations of trace elements in ultrafine particles (all ng m^{-3}).

A recent study by Boogard et al. (2011) in the Netherlands demonstrated that there were particularly strong contrasts in the concentrations of a number of substances indicative of traffic emissions measured at roadside and background sites. Cu, Fe, Cr and black carbon were significantly elevated at roadside sites. Similarly, particle number concentrations in the 30-100 nm range were also elevated at roadsides. (Boogaard et al., 2011).

Lough et al. (2004) also found that Zn, Ba and Sb (wear elements) exhibited size distributions similar to crustal elements due to being sourced from resuspended road dust. They reported submicrometre modes indicative of combustion processes and/or high temperatures for Fe, Cu, Pb and Ca, with lead and copper also possessing an ultrafine mode suggestive of a source in non-mechanical processes (brake surface vaporisation, combustion of fuel and lubricating oil). Some elements, such as Cu, Sb, Zn and Ba, associated with road dust were observed at times when more heavy duty traffic was present during weekdays, correlating with a greater mass of coarse particles from resuspension (Lough et al., 2004).

Ntziachristos et al. (2007) found that the road traffic influence in $PM_{0.18}$ became more pronounced at the higher end of this size range, as the ratio of heavy-duty to light duty vehicle emission factors increases. Such emissions contain a greater proportion of fractal soot agglomerates in the upper end of the ultrafine size range; many of these particles have large mobility diameters even though their aerodynamic diameters are relatively small, owing to their low density (Ntziachristos et al., 2007). Their measurements at a California traffic roadside with around 20% heavy-duty diesel traffic found Fe to be the most abundant metal in $PM_{0.18}$ followed by Ca, Al and Na and lower levels of Ba, Cu, Zn and Ti. They also determined that most metals fell into two concentration profiles. Some elements including V, Fe, Sn and Ba showed monotonic distributions (a uniform increase in concentration with size)

and originated primarily from abrasive mechanical processes or represented crustal materials. However, Mg, Al, Ca, Cu, Zn and Pb revealed similar concentrations across the lower size range, resulting in a flatter distribution. They found that Ca, Cu and Pb had similar absolute concentrations in the size ranges 18-32 nm, 32-56 nm, 56-100 nm and 100-180 nm, even though total PM concentration and total trace element concentration rose significantly over this range. The mode 18-32 nm had elevated concentrations of a range of metals, which showed a formation pathway by condensation onto metallic particles and shows that per unit mass, this size range makes a larger contribution to heavy and transition metals.

A study using a MOUDI to collect samples at a coach station in Taipei found that the bulk of the metallic mass below 1 µm occurs in the $PM_{0.1\text{-}1}$ size range, with about one third of that mass in the $PM_{0.1}$ range. Zinc was by far the most abundant metal in the $PM_{0.1}$ size range, followed by Fe, Cu, Pb, V and Ni (Chuang et al., 2012).

The results published by Hughes et al. (1998) form an interesting comparison to Ntzaichristos et al. (2007) in that there are similar trends within this group of elements but the actual mass concentrations are in many cases around twice as high. Hughes et al. (1998) also reported that they were unable to identify 23-40% of the total ultrafine particle mass, the large range being caused by the small masses available for analysis. In central Los Angeles, Cass et al. (2000) reported much higher concentrations of Ba, Cd and Ti than Hughes along with nearly three times as much Fe. UFP were found to be of similar composition to bulk $PM_{2.5}$.

More recent measurements in the Los Angeles area have been performed by Saffari et al. (2013) using Sioutas personal cascade impactors at 10 sites. This study extends the analysis to all particles below 250 nm aerodynamic diameter (quasi-ultrafine). The most abundant

elements at all sites were Al, Ca, Fe, K and Na whose mass concentrations ranges ranged from 50 ng/m^3 – 200 ng/m^3, while trace element concentrations were in the range below 10 ng/m^3 (Saffari et al., 2013). Concentrations of elements related to shipping such as V and La were found to decrease with distance from the source, to the extent that this component was not identifiable by PCA in the data from inland receptor sites.

The near-highway study by Hays et al. (2011) differs in the selection of a road with an extremely high proportion of light-duty gasoline fuelled vehicles (95% of the total 125,000 vehicles per day). In this case, inorganic material was found to account for ~7% of total mass in $PM_{0.1}$. The dominant metals in $PM_{0.1}$ were found to be K and Ca. The next most important elements were Zn and Al followed by Ti and Fe. Ni, Cr, Pb, Sb and Cu were all observed around an order of magnitude below these elements along with Ce. Zn and Ca were found to correlate in $PM_{0.1}$ implying a common source in lubricating oil. Fe, Ba, Cu and Sb – the brake wear elements – were seen to correlate closely throughout all three size ranges ($PM_{0.1}$, $PM_{2.5}$ and PM_{10}), though the correlations with Zn were not as good due to excess Zn, arising from tyre wear in the higher size fractions and lubricating oil in $PM_{0.1}$. Despite its complex source profiles, Zn concentrations were found to be quite consistent from day to day. The platinum-group elements Pt, Pd and Rh were not reported in $PM_{0.1}$ (Hays et al., 2011).

Pennanen et al. (2007) compared the water soluble metal fraction of $PM_{0.2}$ in six European cities. Levels of some trace elements such as Pb and Cd were found to be consistently low, but highly elevated levels of Ni and V were found in Helsinki and Barcelona, which is likely to reflect a shipping source. Elevated concentrations of several metals (Cr, Mn, Zn) were found in Duisberg, a city associated with metal industries (Pennanen et al., 2007).

The measurements of Lu et al. (2012) at an urban site in central Shanghai showed that Fe, Cu and Ca were the most abundant metals in ultrafine particles, followed by V, Pb, Zn and As, with traces of Ti, Cr, Mn, Se and Rb. Of these element, only V and Cr showed ultrafine modes, although all appeared in the combined ultrafine samples. V, Cr and Ni also showed very high enrichment factors over crustal material in fine and ultrafine particles, but lower enrichments in coarse particles (Lü et al., 2012)

In an earlier paper, Lu et al. (2011) determined that metals in Shanghai aerosol could be divided into crustal/marine (Al, Ca, Fe, K, Mg and Na) and anthropogenic (As, Ba, Cd, Cr, Cu, Mn, Ni, Pb, Se, Sr and Zn) classes. Total metal mass was found to be highest in the coarse fraction for crustal elements and the fine fraction for anthropogenic elements. Iron showed the highest concentrations in the ultrafine, followed by copper and calcium. The authors also hypothesised that since calcium showed high mass concentrations and varied little between the size fractions, it was primarily crustal in source and participated in atmospheric reactions forming secondary mineral particles in the fine and ultrafine ranges (Lu et al., 2011).

Ultrafine chemical composition data for metals at rural sites is not extensive, but some useful data have been published. Dodd et al. (1991) calculated modal diameters and enrichment factors of a number of metals relative to crustal aluminium in a study in rural Western Maryland. The aerosol fine structure in the submicron size fraction was found to be highly complex with most elements exhibiting more than one mode. Na, Ga, Ti, Al, La, Ce, and Fe all exhibited a narrow peak at 100 nm. The authors took such modes as representative of sources in high temperature combustion processes. Pakkanen et al. (2001) used low-pressure impactors to measure UFP composition at urban and rural sites in the Helsinki area and found

that chemical composition was similar at both sites; in each case the most important metals in $PM_{0.1}$ were Ca, Na, Fe, K and Zn, concentrations varying between 0.7-5 ng/m^3. The metals Ni, V, Pb and Cu were reported at concentrations in the 0.1-0.2 ng/m^3 range. Total ultrafine particle mass was reported to be 490 ng/m^3 at the urban site and 520 ng/m^3 at the rural site. The authors also stated that while the number of samples was too small to be certain of this, it appeared that concentrations were higher in summer at the rural site and no clear seasonal pattern could be seen at the urban site (Pakkanen et al., 2001). Daher el al. (2013) found that crustal metals (Al, Fe, K, Ca, Mg and Ti) were proportionally more important contributors to annually averaged $PM_{0.25}$ at a remote rural site than at heavily polluted urban sites (13-17% of total mass), while the remaining trace elements accounted for less than 1% of total mass. Furthermore, metals related to specific industrial sources such as Ni, and with shipping such as V and La, were present in much smaller concentrations than at urban sites. By comparison, concentrations of Fe and Al were much more similar between urban and rural sites (Daher et al., 2013; Saffari et al., 2013).

1.4.2 Temporal and Spatial Variability

A great deal of work has been published concerning this issue and has been summarised by other reviews (Morawska et al., 2008), but primarily refers to number distributions of total particles and not mass, as the longer collection times necessary for mass measurements tend to average out short-term variability. For mass data, the field is very limited at the present time.

Park et al. (2008c) reported that little variation in ultrafine particle concentration and composition was observed in Gwangju despite significant variation in PM_{10} (Park et al., 2008c). By comparison, Tolocka et al. (2005) reported significant differences in particle composition in Baltimore in the short term, influenced by local meteorology determining the

impact of local sources on the receptor site, but not much seasonal or diurnal variation (Tolocka et al., 2005).

Saffari et al. (2013) have reported data showing that winter-time concentrations at a remote receptor site near Los Angeles were lowest, but were higher at near-source sites. This was thought to reflect decreased mixing heights in cold weather. It was found that the highest summertime concentrations were recorded at the inland receptor sites, with metals peaking at urban sites in winter and downwind receptor sites in summer. Total $PM_{0.25}$ mass has been found to be rather uniform across the Los Angeles basin, but significant variations in the distribution of several toxic metals were observed, so that population exposures will be considerably different even across quite small spatial scales (Daher et al., 2013).

1.4.3 Summary

The available literature on metallic ultrafine PM composition makes it very clear that there is enormous variation from site to site, and that concentration and composition of particles are subject to many influences. Location and duration of sampling, local weather conditions during sampling and the types of local source mean that it is hard to obtain truly representative results; rather characterisations will be specific to time and site.

1.5 INSTRUMENTAL TECHNIQUES

1.5.1 Sampling Instruments

Instrument	Metric	Analysis	Size Range (Aerodynamic Diameter)
MOUDI	Mass	Off-line	Model 100 (10-stage): 0.18, 0.32, 0.56, 1.0, 1.8, 3.2, 5.6, 10, 18 μm Model 110 (12-stage): also 0.056, 0.1 μm Models 115 and 116 include nano-stages: 0.01, 0.018, 0.032 μm
nanoMOUDI	Mass	Off-line	0.01, 0.018, 0.032 0.056, 0.1, 0.18, 0.32, 0.56, 1.0, 1.8, 3.2, 5.6, 10 μm
ELPI	Mass	Off-line and on-line	0.007 μm Filter stage, 0.03, 0.06, 0.108, 0.17, 0.26, 0.4, 0.65, 1, 1.6, 2.5, 4.4, 6.8, 10
PCIS	Mass	Off-line	<0.25, 0.25–0.5, 0.5–1.0, 1.0–2.5 and 2.5 μm
BLPI	Mass	Off-line	0.035, 0.067, 0.093, 0.16, 0.32, 0.53, 0.94, 1.8, 3.5, 7.5 μm

Table 3. Outline of sampling techniques.

Various forms of impactor-type instruments have been widely used in particulate matter sample collection, including Micro and nano-Micro Orifice Uniform Deposit Impactors (MOUDI and nanoMOUDI, manufactured by MSP corporation) and Low Pressure Impactors, their purpose being to collect size segregated particulate matter samples (see Table 3). The nanoMOUDI-ii 125 instrument has thirteen stages with nominal 50% cut-points of 10000, 5600, 3200, 1800, 1000, 560, 320, 180, 100, 56, 32, 18 and 10 nm when operated at an inlet flow rate of 10.0 L/min. The instrument separates particles into a series of logarithmically equal size fractions based on aerodynamic diameter. Cascade impactor instruments such as the nanoMOUDI-ii can require long sampling times to collect sufficiently high masses of nanoparticulate material for accurate quantification of mass and chemical composition. Lu et al. (2011) found that it was necessary to combine the ultrafine filters for extraction and analysis, as one was persistently below limits of detection (Lu et al., 2011). The length of sampling periods have to be decided based on the limits of detection established for the

analytical processes and the likely range of sampled concentrations, but in most published work using nanoMOUDIs, sampling times of several days are typical. One method of overcoming this problem is to set up the nanoMOUDI downstream of an aerosol concentrator; Ntziachristos et al. (2007). employed this method when sampling for 35 hours (Ntziachristos et al., 2007) and Geller et al. (2002) also used a similar set-up in a study designed to investigate mass size distributions over relatively short (< 24 hr) timescales, which would preclude using such an instrument normally (Geller et al., 2002). The operation of such systems is described in more detail elsewhere (Geller et al., 2002; Kim et al., 2001), but in brief it enriches ultrafine particle concentrations by drawing in air at 220 L/min and growing particles to 2-3 μm by a saturation-condensation system and then passes the particles through diffusion dryers in order to return them to the original size distribution. The system is capable of up to 40-fold enrichment, although this depends on output flow rate; Geller et al. (2002) employed two parallel sampling lines, at an input rate of 110 L/min and output rate of 5 L/min, giving an enrichment factor of 22.

The MOUDI in its 10- and 12- stage forms has also been used for ultrafine particle collection (Cass et al., 2000), although it provides less resolution below 100 nm aerodynamic diameter than the nanoMOUDI. Currently available models have cut-points beginning at 180 nm in the standard 10-stage Model 100 but extra stages to give better size distribution data in the ultrafine size range are also available; the model 110 has 56 nm and a 100 nm cut-points below the 180 nm stage . The MOUDI samples at 30 L/min, allowing faster sample collection than the nanoMOUDI.

Other impactor designs available include the Personal Cascade Impactor Sampler (PCIS), a miniaturised 4 stage design operating at 9L/min which is more easily portable than MOUDI/

nanoMOUDI type instruments but offers no size segregation below 250 nm aerodynamic diameter (Misra et al., 2002b). Agreement with SMPS sizing data is reported to be good. Total mass concentration agrees well with MOUDI measurements even at below 250 nm, although the MOUDI underestimates slightly in this range compared to PCIS (PCIS:MOUDI = 1.09) (Singh et al., 2003). This underestimate is thought to be caused by higher evaporative losses from the MOUDI afterfilter owing to the lower pressure, demonstrated by the PCIS:MOUDI ratio for nitrate in $PM_{0.25}$ being ~2.7 (Singh et al., 2003). The instrument has been successfully used in collecting quasi-ultrafine samples in ambient conditions (Daher et al., 2013; Saffari et al., 2013).

The development of an ultrafine separator to allow separation of particles below 150 nm in the High Volume Cascade Impactor was reported by Misra et al. (2002a). This instrument operates at 550 L/min and the authors reported that tests with monodisperse aerosol showed agreements with MOUDI data which were within 10% (Misra et al., 2002a). A further study by Sillanpää et al. (2003) compared three different configurations of the HVCI with a virtual impactor and a low-pressure impactor and concluded that the most effective set-up for aerosol configuration using this instrument was to use three HVCI stages with cutpoints of 2400, 900 and 200 nm with an Andersen PM_{10} inlet to remove material above 10 µm (Sillanpää et al., 2003). The HVCI has been used for ambient sampling of $PM_{0.2}$ in several European cities by Pennanen et al. (2007), along with the Berner low pressure impactor (BLPI). Good results were obtained although the water soluble metal samples extracted from the HVCI samples were found to be underestimated by comparison to BLPI (Pennanen et al., 2007). The method is clearly viable and the high sampling rate would be ideal for exposure studies, the major limitation being the lack of size segregation in the ultrafine size range. Another type of high volume sampler is the High Capacity Particle Size Classifier (HCPSC),

an inertial impactor operating at 850 L/min and capable of collecting $PM_{0.15}$ (Chang et al., 2000). A field evaluation comparing the HCPSC to the MOUDI found that total mass, chloride, nitrate and sulphate all agreed within 10%, but also found that approximately 15% of fine mode particles are carried over to the ultrafine due to imperfect collection characteristics caused by the rectangular nozzle shape (Chang et al., 2001). The instrument has been used for ultrafine particle collection by Hetland et al. (2004) , though not specifically for metals, (Hetland et al., 2004).

The Compact Multistage Cascade Impactor (CCI) developed at Harvard could also be used for sampling ultrafine/pseudo-ultrafine particulates. This instrument operates at 30 L/min and is designed to reduce particle bounce and re-entrainment loss by using inert polyurethane substrates. Particle losses per stage below 7,000 nm have been reported to be below 10%. In comparison with the MOUDI, tests with artificially generated aerosol showed mass concentrations measuring persistently higher using CCI (MOUDI:CCI = 0.86). The size distributions were closer than MOUDI distributions to those calculated from real-time methods such as SMPS and APS; the comparative results were consistent with particle bounce in the MOUDI (Demokritou et al., 2004). The Harvard CCI has been used with success to collect UPF in an exposure study measuring metals, ions and total PM mass associated with welding activities (Chang et al., 2013).

Berner-type low pressure impactors have also been widely used in many environmental research applications (Hughes et al., 1998; Pakkanen et al., 2001; Pennanen et al., 2007) and are capable, depending on the model (several instruments based on the same principle have been produced) of separations of particles down to aerodynamic diameters around 10 nm. The development of the commonest type was reported by Berner and Lurzer (1980) and the collection characteristics of the instrument have been well characterised (Hillamo and

Kauppinen, 1991; Wang and John, 1988). Pakkanen et al. (2001) collected the following cut-points: 7500, 3500, 1800, 940, 530, 320, 160, 93, 67 and 35 nm equivalent aerodynamic diameter, based on the calculations of Hillamo and Kauppinen (1991), which differed slightly from the original 50% cut-points quoted by the manufacturer (Hauke).

The Electrical Low Pressure Impactor (ELPI) is now a widely used and well characterised system (Keskinen et al., 1992), capable of measuring particle mass distributions and particle number distributions depending on the mode of operation. Unlike MOUDI/nanoMOUDI type instruments, particle number data can be available in near-real-time, a significant advantage which allows better measurement of the time variation of the size distribution through the sampling period, rather than an integrated measurement over a long period. (Keskinen et al., 1992). The instrument consists of a corona charger mounted ahead of a cascade impactor. Particles are charged to a known level by the unipolar corona charger and passed into the impactor, where they are separated according to aerodynamic diameter and then can either be detected in real time by electrometers in each stage or collected for later analysis on filter substrates, as in MOUDI-type impactors. For real time number measurements, it has been shown through calibration tests with monodisperse aerosol that the distributions produced by the ELPI are in close agreement with Scanning Mobility Particle Sizer data (Marjamaki et al., 2000). Keskinen et al. (1992) also reported good agreement with differential mobility analyser data although the resolution was low compared to Differential Mobility Analysis when analysing aerosol of narrow size ranges. The technique has been successfully applied to size-segregated ultrafine particle studies incorporating trace metal analysis by Pakkannen et al. (2001) and Hays et al. (2011) in both background and near-highway settings. In both of these cases the instrument was used as a conventional impactor to collect filter samples for later offline analysis (Hays et al., 2011; Pakkanen et al., 2001).

Important considerations in the employment of impactors are sampling artefacts such as particle bounce and blow-off, which lead to larger particles being carried over into later stages producing less accurate size distributions. Some studies use coatings on the impaction surfaces to reduce this, but if chemical or gravimetric analysis is to be performed on the samples this may present problems. A recent study of interstage nanoparticle losses in the MOUDI concluded that particles below 40 nm aerodynamic diameter were significantly affected by interstage loss between the inlet and the lower stages (7-10). The authors also suggest that in the 13-stage MOUDI and nanoMOUDI instruments, interstage losses of nanoparticles would be even more serious. It was also observed that the nozzles in the 7^{th}-10^{th} stages clogged easily during sampling and must be cleaned regularly, otherwise an increase in the pressure drops will result and cause a decrease in the cut-points of these stages. However, since the plates are fragile it is not possible to use ultrasonic cleaning to remove deposited particles (Liu et al., 2013).

One method which has been used to mitigate these problems was reported by Cass et al. (2000), who used a cyclone impactor upstream of the MOUDI to impose a cut of 1800 nm before the airstream entered the impactor. This reduced carryover of coarser material into the lower stages. Geller et al. (2002) achieved a similar effect by putting a 10 stage MOUDI with no afterfilter ahead of the nanoMOUDI, which prevented particles > 180 nm D_a from entering the instrument. While effective, these techniques can only be employed if the study does not intend to measure coarser material.

During a study in Gwangju reported in 2008, Park et al. (2008c) used a Differential Mobility Analyser to size segregate particles, which were then collected onto TEM grids in a nano-aerosol sampler for offline TEM analysis (Park et al., 2008c).

1.5.2 Filter substrates

An important consideration in the the employment of impactor-type instruments is the filter substrate on which the sample is deposited. There are numerous different types available which differ considerably in physical and chemical characteristics, including Al foils, quartz fibre filters, PTFE membrane filters and membrane filters made from cellulose nitrate or polycarbonate. Mechanical (to avoid biasing mass measurements) and chemical stability are paramount, especially given the small masses collected in ultrafine sampling. Similarly, low blank concentrations and low variability for the species of interest are crucial. Selection of filter type depends on the type of analytical procedure which will be applied and the subject under investigation. A number of publications are available which discuss this issue in depth (Chow, 1995; Wieprecht et al., 2004).

The studies referenced in Table 2 all utilised either PTFE or polycarbonate filters for collection of samples for metal analysis. Such substrates offer good particle retention and PTFE filters are non-reactive (Wieprecht et al., 2004). Although quartz filters are more resistant to artefact effects and moisture absorption (Wieprecht et al., 2004), they are also more brittle, which can lead to fibres being lost during handling introducing a negative mass bias (Chow, 1995). Ultrafine and nanoparticle sampling would be highly sensitive to such errors owing to the small sampled masses.

1.6 Off-line Studies Using Electron Microscopy

Bzdek et al. (2012) recently published a review of many of the most prominently used on-line and off-line techniques for the analysis of individual particles. They noted that it is crucially important that the sampled nanoparticles give an accurate representation of the particle classes and morphologies present in ambient air, but that off-line methods such as Transmission Electron Microscopy – X-ray – Energy Dispersive Spectroscopy (TEM-X-

EDS) offer better characterisation of physical structure and chemical composition than on-line single particle techniques are currently able to do (Bzdek et al., 2012b). Smith et al. (2012) observed that one weakness of TEM is a tendency to lose volatile material. This is not relevant to all metallic particles, but some elements do appear in volatile or semi-volatile material. Smith et al. (2012) also reported Na and K-bearing non-aggregated beam sensitive particles which they associated with inorganic salts. A further problem is that analysis by these techniques is laborious and time-consuming, so only relatively small numbers of particles from any given sample can be imaged and analysed, with a corresponding effect on the statistical validity of the results (Smith et al., 2012).

X-ray energy dispersive spectroscopy has been used to investigate the chemical composition at the individual particle level (Smith et al., 2012). Patel et al. (2012) did report, however, that zinc and calcium could only be detected by EDS in larger agglomerates, and not the primary particles ranging between 20-50 nm. They also established through comparison with results from selected area diffraction patterns that these elements were likely to be present as compounds rather than in their elemental forms, and probably as amorphous structures (Patel et al., 2012).

Smith et al. (2012) identified 8 characteristic particle morphologies in fine/ultrafine urban particles during the REPARTEE study in London. Carbonaceous particles dominated the size ranges between 0.2 μm and 1.2 μm; these particles were mainly aggregates of spherules composed either wholly of C or incorporating some O and sometimes Si. Amorphous aggregates similar to these were also observed containing metals. Ca, K and Fe were most common. Crystalline Fe oxide particles and Ca based particles, both amorphous and

crystalline, were reported; the Ca particles showed strong peaks in Ca, O and C, along with Na, Al and Si. This is typical of mineral and soil based sources (Smith et al., 2012).

Adachi and Buseck (2010) also used TEM with EDS, reporting a range of trace metals in nanoparticles and determining that Fe was the commonest constituent (often associated with Cr, Mn and/or Ti), followed by Pb and Zn, which were frequently found together, They also examined co-existence in multimetallic particles in detail. However, their results also gave prominence to elements which are not generally emphasised in bulk studies. For instance, Hg was also detected in over 10% of nanoparticles, both in aggregates and adhered to host particles, and was quite beam sensitive. Hg has several known sources, of which fossil fuel combustion is most important globally, but local industrial sources may dominate at individual sampling locations (Adachi and Buseck, 2010).

Utsonomiya et al (2004) examined trace metals in fine/ultrafine particulates from Detroit using TEM-X-EDS and gave particular prominence to Pb, found in the form of PbO included in carbonaceous soot, indicative of origin in fossil fuel combustion. Zn tended to occur in complex aggregates with other nanoparticles such as Fe, Si and Al oxides and phosphates. Some larger Fe-Zn particles (100-150 nm) were found to be Fe_3Zn_{10}, associated with metallurgical processes, and correlation analysis showed both metallurgical and fossil fuel sources (Utsunomiya et al., 2004).

Ultrafine material generated from the road-tyre interface has been reported to exhibit five major particle types, two of which are liquid (Dahl et al., 2006). The solid phase particles consist of single near-spherical particles and agglomerates of near-spherical particles, whose mobility diameters are between 10-100 nm. It is suggested that the spherical primary particles

originate from carbon black used as a reinforcing filler though it is possible that small inclusions of ZnO or ZnS are responsible for the spherical morphology. The fractal structure of the agglomerates implies that they were detached under tensile stress rather than excessive heating, which would cause the chains to contract (Dahl et al., 2006).

Vehicle exhaust particles are typically the dominant source of ultrafine particulate matter, especially in urban areas and their characterisation is vital for assessing the effects of exposure. According to Tumolva et al. (2010), such particles are typically highly agglomerated with a high surface area to mass ratio, consisting of large numbers of small spherical carbon based primary particles. Diesel soot, which forms a large part of the total ultrafine particulate matter burden, has been the subject of a number of attempts to characterise physical as well as chemical characteristics more closely. A recent study (Lu et al., 2012) using TEM established that freshly emitted medium duty diesel engine particulate matter is generally composed of spherical or near spherical particles averaging 23.8 nm-28.5 nm diameter; however, the characteristics of the emitted particles were found to vary depending on engine speed and load, with low engine speeds and high loads generating larger primary particles. The study also discovered that higher engine speeds produce more disordered structures. (Lu et al., 2012). Tumolva et al. (2010) reported a mean primary particle diameter of 24 nm (SD 3.5 nm) for diesel soot produced in the laboratory, with a mean maximum length of 262 nm (SD 222 nm). This study also reported a relatively low fractal dimension of 1.69 for diesel exhaust particles, indicating a high level of branching in diesel particle agglomerate structures.

Jung et al. (2005) determined that CeO_2 additives in diesel engines contribute ceria to the particulate phase in two main morphological types. Firstly, fractal agglomerates of

carbonaceous spherules of around 20-30 nm (the typical structure for diesel soot) with nanoparticulate cerium oxide (around 5-7 nm) adhered to the surface, and secondly, metallic aggregates formed from CeO_2 nanoparticles (5-7 nm) with some carbon. (Jung et al., 2005). The second particle class contains proportionally far more cerium than the first. They point out that the very high melting point of ceria (2200-2400°C) means that a nanoparticulate ceria additive should remain unchanged through diesel combustion.

Some similar morphological characteristics for diesel engine derived metallic particles are also observed with the Fe fuel additives, depending on the level of doping. In a trial of ferrocene doping, Miller et al. (2007a) discovered that at low Fe concentrations (20 ppm doping level), exhaust particles exhibit typical diesel soot morphology, but above an Fe/C ratio of 0.013 the morphology switches to homogeneously nucleated metallic particles which form agglomerates across a wider size range. Miller et al. (2007a) reported two principal agglomeration modes, the first where 5-10 nm Fe nanoparticles attach to carbon agglomerates, and the second where larger iron agglomerates coagulate with carbon agglomerates In this second case, the primary metallic particles can be so small they are not easily resolved by TEM, but can be observed through EDS spectra of large particles, implying it is present through vapour deposition onto carbon particles. Results suggest that particle size is dose-dependent, since iron primary particles are larger at higher doping levels (Miller et al., 2007a).

A more recent study of ferrocene fuel additives by Nash et al. (2013) assumes a formation process whereby Fe nucleates in the early phase of soot formation and then the Fe particles are incorporated in larger agglomerates in the exhaust. As well as the additive, substantial (> 1000 ppm) concentrations of Ca and Zn were present in the lubricating oil along with smaller

(< 100 ppm) levels of Cu, Cr, Fe, Mg and Mn. A doping level of 25 ppm Fe was found to change the normal particle distribution (volume mean 80-90 nm) by introducing a second smaller mode. This effect, resulting in a reduction in volume and number concentrations in the accumulation mode and an increase in number and volume of nanoparticles, becomes more pronounced as the doping level increases. TEM analysis revealed that at 18 nm mean diameter, spherical and irregular morphologies are both present, attributed to Fe nuclei agglomerating to form clusters prior to soot formation and to Fe particles which coalesced and agglomerated after soot formation and oxidation. By comparison at 100 nm mean aerodynamic diameter, carbon agglomerates dominate, with Fe occlusions and surface deposits. Aerosol Time-of-Flight-Mass Spectrometry (ATOFMS) data demonstrated that almost all Fe was in the elemental form, with trace amounts of FeO but no Fe_2O_3. XRF show that in undoped diesel exhaust Fe represents around 0.1% of the total particle mass, increasing to 1% at 25 ppm ferrocene. The distribution changes as iron content increases; at 25 ppm Fe, some 81% of the Fe content is in particles smaller than 56 nm, but at 200 ppm Fe, this falls to around 50% (Nash et al., 2012).

Buonanno et al. (2011) reported that ultrafine particles from an incinerator stack demonstrated a wide range of morphologies, including platelets and thin plates with indented and rounded edges. The stack emissions were found to contain high quantities of metal oxides and silicates, with Fe, Fe-Cr, Zn, W-Fe-Cr and Ti oxides being prevalent (Buonanno et al., 2011).

1.7 On-line Studies Using Aerosol Mass Spectrometry

Early ATOFMS systems required the particle to be > 200 nm (optical diameter) to scatter the visible laser beam (Jayne et al., 2000). For particles below this limit, detection efficiency is

strongly dependent on size and composition. Aerodynamic focusing lens systems have been developed to improve transmission efficiencies in the ultrafine, leading to the ultrafine-ATOFMS instrument, which has much improved particle sizing and detection efficiencies in this size range (Su et al., 2003). This technique has successfully been applied by Toner et al. (2006) to the source apportionment of ultrafine and accumulation mode particles arising from diesel and gasoline emissions. Zauscher et al. (2011) developed a water-based growth tube system which uses condensation to grow particles which would be too small for optical detection. This enables the detection and analysis of particles down to 38 nm (Zauscher et al., 2011).

The rapid single particle mass spectrometer (RSMS) has also been applied to single particle studies (Lake et al., 2003; Phares et al., 2003; Tolocka et al., 2004) with some success. Lake et al. (2003) were able to analyse ultrafine particles down to an aerodynamic diameter of 45 nm, determining that around 10% of sampled particles in an optimum range of 50-770 nm contained metals. Phares et al. (2003) reported detection of Al, Fe, K, Pb and V at the Houston supersite. A more detailed treatment of the technique was published by Reinard et al. (2007).

Park et al. (2009) reported the development of a Laser-Induced Breakdown Spectroscopy (LIBS) method which can be applied to investigate the chemical composition of particles down to around 60 nm, by employing an aerodynamic lens system to allow focusing of smaller particles. This method has been found to exhibit linear mass-peak area relationships for several metals, and to be able to detect internally mixed metal aerosols. Previously LIBS techniques had only been applied above lower limits of 200-400 nm and no reported results existed for particles below 100 nm (Park et al., 2009).

Comparitively little work exists which combines bulk and single-particle characterisation, owing partly to the need for very long sampling times in bulk collection and the differences in collection characteristics in instruments. This is a gap which this study aims to start addressing, by collecting bulk and single-particle samples from the same sites under similar conditions, using the same instrumentation.

1.8 Source Apportionment

A number of source apportionment techniques are widely used to examine airborne particulate matter data. The most widely used techniques fall under the category of receptor models such as Chemical Mass Balance (CMB), Principal Component Analysis (PCA) and Positive Matrix Factorisation (PMF), which use chemical and physical properties of PM to assign contributions to different sources. Applying these methods to mass concentration data of ultrafine and nanoparticles poses several challenges. Chemical mass balance can be a valuable method, providing that sources are already known and there is already detailed information concerning source profiles (Wang et al., 2012). This is a severe hindrance in applying this technique to ultrafine particle data where source profile information is sparse. If some sources are not known, or source profile information is limited, chemical mass balance is less useful; in such circumstances PCA and PMF are preferred (Srimuruganandam and Shiva Nagendra, 2012).

Principal Component Analysis has been successfully applied to $PM_{0.25}$ metal composition data by Saffari et al. (2013), who used this technique to resolve data from 10 sites in the Los Angeles area into five separate components. The first component showed high loadings for mineral elements (Ca and Mg) and transition metals such as Fe, Co, Ti and Mn. This factor was attributed to road dust enriched by traffic-related emissions. PC2 was characterised by high loadings (< 0.7) for brake wear elements such as Ba, Cu and Sb. When PCA was applied

separately to urban and receptor sites, Ba and Cu appeared in different factors. At urban sites, these elements were classed in the road dust factor, but formed a separate factor at urban locations. The authors attributed this change to the dominance of vehicle emissions in urban areas making it more difficult to separate emission sources. Road dust was found to account for more of the total variance at urban sites (62%) compared to receptor sites (35%) (Saffari et al., 2013). Lin et al. (2005) also applied PCA to MOUDI and nanoMOUDI sample results from Pingtung, Taiwan. This study found four factors in nano/ultrafine particulates which corresponded to elements associated with diesel, gasoline, fuel oil and industrial emissions. They reported strong correlations between Ba, Pb and Zn in this size range, which supported a traffic source for these elements. The relative abundance for these elements in $PM_{0.056\text{-}0.1}$ and $PM_{0.056}$ was more similar to diesel emissions than to gasoline (Lin et al., 2005).

PMF is increasingly widely used for source apportionment. Unlike CMB, there is not a requirement for source profiles to be input into the model. However, in order to interpret the factors reported by the model as pollution sources, some knowledge of source profiles is still required (Wang et al., 2012). PMF can provide a robust solution provided that the sample:variable ratio is above 3:1. PMF is particularly suitable for analysing long time series, and observations need not be continuous for the method to work effectively. Assigning factors to sources is complex and to some extent subjective, as there are problems with the inconsistent use of species as source tracers (Reff et al., 2007). PMF results therefore have to be carefully interpreted. As of yet now, of PMF for nanoparticle source apportionment (especially mass-based) has been limited, owing to the difficulty of collecting enough samples to ensure the results are valid. Because of the long sampling times necessary, short term variations which would make factorisation easier tend to be averaged out, suppressing the impact of individual sources (Kumar et al., 2012).

1.9 Summary of current state of research

While much progress has been made in understanding the sources contributing ultrafine particles to the atmosphere and characterising them in terms of particle number and size distributions, there is far less knowledge of the metal components of the ultrafine fraction. There is some knowledge of physical and chemical properties such as whether metals are free-floating or hosted on or within carbonaceous or mineral matrices, single particles or agglomerates. In some cases these properties have been associated with different source types. At this stage there are few studies reporting bulk ambient metal concentrations. Progress has been made in understanding how physical and chemical atmospheric processes affect ultrafine particles, and understanding how concentrations, composition and distribution vary in different environments. Progress has been made in establishing elements, compounds and particle types which are diagnostic of particular emission sources in larger size ranges, but their applicability to ultrafine particles is very limited.

The greatest weaknesses in characterising the metallic content of nanoparticles in the atmosphere derive directly from the very low concentrations present and the fact that these require very long sampling times for conventional analytical methods to give useful data. This is very much apparent from the results presented in this thesis. Attempts at higher time resolution have to date had limited success although single particle techniques, and especially those based on mass spectrometric methods, offer the possibility of characterising both size and metal content of particles. However, current instruments have difficulties sampling particles right into the nanoparticle size range and low resolution mass spectrometry suffers from isobaric interference with ions derived from non-metallic species. Given the current rapid expansion in the use of nanomaterials in everyday consumer products, many of them metal-based, there is a pressing need for real-time measurements of specific nanoparticles. If

nanoparticle measurement technology is to rise to the associated challenges, there is a need to develop instruments capable of the sensitivity and specificity needed to characterise nano-sized particles for a range of chemical constituents in real time.

1.10 Research Aims

This project aimed to address a number of key research areas. One aim was to characterise the mass distributions of particulate matter at roadside, background and rural sites and determine; first, how these differ from each other; second, to characterise which size ranges roadside increments occur in and how large they are. This aim was addressed by the plotting of size distributions from PM masses sampled on filters at six separate sites in Britain and Spain, including the collection of simultaneous roadside/background distributions.

A second aim was to characterise the size distributions of total metals in bulk particulate using ICP-MS, at roadside, background and rural sites allowing comparisons of individual metals in the same manner as for total PM. A further aim of total metal collection was to determine which metals correlated with each other and in which size ranges, which would allow some inferences to be made about which sources may be contributing these elements.

A further aim was to characterise the metallic content at the single-particle level using TEM-X-EDS. Both chemical composition and physical morphology (particle size and shape) were determined using this method. Evidence has been presented in the past showing that combinations of elements could be indicative of sources, so the characterising of the composition of mixed-metallic particles was an important goal in this part of the project.

To give context to the ambient measurements, it was decided to collect samples for analysis by the same methods from a static brake test rig and from a diesel engine. This allowed both morphology and composition of particles from these sources to be compared to ambient measurements.

REFERENCES

Adachi, K., Buseck, P.R., 2010. Hosted and Free-Floating Metal-Bearing Atmospheric Nanoparticles in Mexico City. Environmental Science & Technology 44, 2299-2304.

Adachi, K., Tainosho, Y., 2004. Characterization of heavy metal particles embedded in tire dust. Environment International 30, 1009-1017.

Attfield, M.D., Schleiff, P.L., Lubin, J.H., Blair, A., Stewart, P.A., Vermeulen, R., Coble, J.B., Silverman, D.T., 2012. The Diesel Exhaust in Miners Study: A Cohort Mortality Study With Emphasis on Lung Cancer. Journal of the National Cancer Institute.

Bérubé, K.A., Jones, T.P., Williamson, B.J., Winters, C., Morgan, A.J., Richards, R.J., 1999. Physicochemical characterisation of diesel exhaust particles: Factors for assessing biological activity. Atmospheric Environment 33, 1599-1614.

Block, M.L., Elder, A., Auten, R.L., Bilbo, S.D., Chen, H., Chen, J.-C., Cory-Slechta, D.A., Costa, D., Diaz-Sanchez, D., Dorman, D.C., 2012. The outdoor air pollution and brain health workshop. Neurotoxicology 33, 972-984.

Boogaard, H., Kos, G.P.A., Weijers, E.P., Janssen, N.A.H., Fischer, P.H., van der Zee, S.C., de Hartog, J.J., Hoek, G., 2011. Contrast in air pollution components between major streets and background locations: Particulate matter mass, black carbon, elemental composition, nitrogen oxide and ultrafine particle number. Atmospheric Environment 45, 650-658.

Bräuner, E.V., Forchhammer, L., Møller, P., Simonsen, J., Glasius, M., Wåhlin, P., Raaschou-Nielsen, O., Loft, S., 2007. Exposure to ultrafine particles from ambient air and oxidative stress–induced DNA damage. Environmental health perspectives 115, 1177.

Buonanno, G., Ficco, G., Stabile, L., 2009. Size distribution and number concentration of particles at the stack of a municipal waste incinerator. Waste Management 29, 749-755.

Buonanno, G., Stabile, L., Avino, P., Belluso, E., 2011. Chemical, dimensional and morphological ultrafine particle characterization from a waste-to-energy plant. Waste Management 31, 2253-2262.

Buzea, C., Pacheco, I.I., Robbie, K., 2007. Nanomaterials and nanoparticles: sources and toxicity. Biointerphases 2, MR17-MR71.

Bzdek, B.R., Pennington, M.R., Johnston, M.V., 2012a. Single particle chemical analysis of ambient ultrafine aerosol: A review. Journal of Aerosol Science 52, 109-120.

Bzdek, B.R., Ross Pennington, M., Johnston, M.V., 2012b. Single particle chemical analysis of ambient ultrafine aerosol: A review. Journal of Aerosol Science.

Cass, G.R., Hughes, L.A., Bhave, P., Kleeman, M.J., Allen, J.O., Salmon, L.G., 2000. The chemical composition of atmospheric ultrafine particles. Philosophical Transactions of the Royal Society of London. Series A: Mathematical, Physical and Engineering Sciences 358, 2581-2592.

Cassee, F.R., Campbell, A., Boere, A.J.F., McLean, S.G., Duffin, R., Krystek, P., Gosens, I., Miller, M.R., 2012. The biological effects of subacute inhalation of diesel exhaust following addition of cerium oxide nanoparticles in atherosclerosis-prone mice. Environmental research 115, 1-10.

Cassee, F.R., van Balen, E.C., Singh, C., Green, D., Muijser, H., Weinstein, J., Dreher, K., 2011. Exposure, Health and Ecological Effects Review of Engineered Nanoscale Cerium and Cerium Oxide Associated with its Use as a Fuel Additive. Critical Reviews in Toxicology 41, 213-229.

Cernuschi, S., Giugliano, M., Ozgen, S., Consonni, S., 2012. Number concentration and chemical composition of ultrafine and nanoparticles from WTE (waste to energy) plants. Science of the total environment 420, 319-326.

Chang, C., Demokritou, P., Shafer, M., Christiani, D., 2013. Physicochemical and toxicological characteristics of welding fume derived particles generated from real time welding processes. Environmental Science: Processes & Impacts 15, 214-224.

Chang, M., Sioutas, C., Cassee, F.R., Fokkens, P.H.B., 2001. Field evaluation of a mobile high-capacity particle size classifier (HCPSC) for separate collection of coarse, fine and ultrafine particles. Journal of Aerosol Science 32, 139-156.

Chang, M.C., Sioutas, C., Fokkens, P.H.B., Cassee, F.R., 2000. A mobile high-capacity particle size classifier (HCPSC) for separate collection of coarse, fine and ultrafine particles. Journal of Aerosol Science 31, Supplement 1, 120-121.

Chow, J.C., 1995. Measurement Methods to Determine Compliance with Ambient Air Quality Standards for Suspended Particles. Journal of the Air & Waste Management Association 45, 320-382.
Chuang, H.-C., Fan, C.-W., Chen, K.-Y., Chang-Chien, G.-P., Chan, C.-C., 2012. Vasoactive alteration and inflammation induced by polycyclic aromatic hydrocarbons and trace metals of vehicle exhaust particles. Toxicology Letters 214, 131-136.
Daher, N., Hasheminassab, S., Shafer, M.M., Schauer, J.J., Sioutas, C., 2013. Seasonal and spatial variability in chemical composition and mass closure of ambient ultrafine particles in the megacity of Los Angeles. Environmental Science: Processes & Impacts 15, 283-295.
Dahl, A., Gharibi, A., Swietlicki, E., Gudmundsson, A., Bohgard, M., Ljungman, A., Blomqvist, G., Gustafsson, M., 2006. Traffic-generated emissions of ultrafine particles from pavement–tire interface. Atmospheric Environment 40, 1314-1323.
Demokritou, P., Lee, S.J., Ferguson, S.T., Koutrakis, P., 2004. A compact multistage (cascade) impactor for the characterization of atmospheric aerosols. Journal of Aerosol Science 35, 281-299.
Dockery, D.W., Pope, C.A., Xu, X., Spengler, J.D., Ware, J.H., Fay, M.E., Ferris Jr, B.G., Speizer, F.E., 1993. An association between air pollution and mortality in six US cities. New England journal of medicine 329, 1753-1759.
Dodd, J.A., Ondov, J.M., Tuncel, G., Dzubay, T.G., Stevens, R.K., 1991. Multimodal size spectra of submicrometer particles bearing various elements in rural air. Environmental Science & Technology 25, 890-903.
Elsaesser, A., Howard, C.V., 2012. Toxicology of nanoparticles. Advanced drug delivery reviews 64, 129-137.
Garg, B.D., Cadle, S.H., Mulawa, P.A., Groblicki, P.J., Laroo, C., Parr, G.A., 2000. Brake Wear Particulate Matter Emissions. Environmental Science & Technology 34, 4463-4469.
Geller, M.D., Kim, S., Misra, C., Sioutas, C., Olson, B.A., Marple, V.A., 2002. A Methodology for Measuring Size-Dependent Chemical Composition of Ultrafine Particles. Aerosol Science and Technology 36, 748-762.
Gidney, J.T., Twigg, M.V., Kittelson, D.B., 2010. Effect of Organometallic Fuel Additives on Nanoparticle Emissions from a Gasoline Passenger Car. Environmental Science & Technology 44, 2562-2569.
Gietl, J.K., Lawrence, R., Thorpe, A.J., Harrison, R.M., 2010. Identification of brake wear particles and derivation of a quantitative tracer for brake dust at a major road. Atmospheric Environment 44, 141-146.
Grgić, I., Hudnik, V., Bizjak, M., Levec, J., 1993. Aqueous S(IV) oxidation—III. Catalytic effect of soot particles. Atmospheric Environment. Part A. General Topics 27, 1409-1416.
Guo, B., Zebda, R., Drake, S.J., Sayes, C.M., 2009. Synergistic effect of co-exposure to carbon black and Fe. Particle and fibre toxicology 6, 4.
Gustafsson, M., Blomqvist, G., Gudmundsson, A., Dahl, A., Swietlicki, E., Bohgard, M., Lindbom, J., Ljungman, A., 2008. Properties and toxicological effects of particles from the interaction between tyres, road pavement and winter traction material. Science of the total environment 393, 226-240.
Hays, M.D., Cho, S.-H., Baldauf, R., Schauer, J.J., Shafer, M., 2011. Particle size distributions of metal and non-metal elements in an urban near-highway environment. Atmospheric Environment 45, 925-934.
Hetland, R.B., Cassee, F.R., Refsnes, M., Schwarze, P.E., Låg, M., Boere, A.J.F., Dybing, E., 2004. Release of inflammatory cytokines, cell toxicity and apoptosis in epithelial lung cells after exposure to ambient air particles of different size fractions. Toxicology in Vitro 18, 203-212.
Hillamo, R.E., Kauppinen, E.I., 1991. On the performance of the Berner low pressure impactor. Aerosol Science and Technology 14, 33-47.
Hughes, L.S., Cass, G.R., Gone, J., Ames, M., Olmez, I., 1998. Physical and chemical characterization of atmospheric ultrafine particles in the Los Angeles area. Environmental Science & Technology 32, 1153-1161.
Jayne, J.T., Leard, D.C., Zhang, X., Davidovits, P., Smith, K.A., Kolb, C.E., Worsnop, D.R., 2000. Development of an aerosol mass spectrometer for size and composition analysis of submicron particles. Aerosol Science & Technology 33, 49-70.
Jung, H., Kittelson, D.B., Zachariah, M.R., 2005. The influence of a cerium additive on ultrafine diesel particle emissions and kinetics of oxidation. Combustion and Flame 142, 276-288.
Kelly, F.J., Fussell, J.C., 2012a. Size, source and chemical composition as determinants of toxicity attributable to ambient particulate matter. Atmospheric Environment 60, 504-526.

Kelly, F.J., Fussell, J.C., 2012b. Size, source and chemical composition as determinants of toxicity attributable to ambient particulate matter. Atmospheric Environment 60, 504-526.
Kenneth A, R., 1976. Silicon and aluminum in atmospheric aerosols: Crust-air fractionation? Atmospheric Environment (1967) 10, 597-601.
Kerminen, V.-M., Pirjola, L., Boy, M., Eskola, A., Teinilä, K., Laakso, L., Asmi, A., Hienola, J., Lauri, A., Vainio, V., Lehtinen, K., Kulmala, M., 2000. Interaction between SO2 and submicron atmospheric particles. Atmospheric Research 54, 41-57.
Keskinen, J., Pietarinen, K., Lehtimäki, M., 1992. Electrical low pressure impactor. Journal of Aerosol Science 23, 353-360.
Kim, S., Jaques, P.A., Chang, M., Froines, J.R., Sioutas, C., 2001. Versatile aerosol concentration enrichment system (VACES) for simultaneous in vivo and in vitro evaluation of toxic effects of ultrafine, fine and coarse ambient particles Part I: Development and laboratory characterization. Journal of Aerosol Science 32, 1281-1297.
Kittelson, D., Watts, W., Johnson, J., Schauer, J., Lawson, D., 2006. On-road and laboratory evaluation of combustion aerosols—Part 2:: Summary of spark ignition engine results. Journal of Aerosol Science 37, 931-949.
Kleeman, M.J., Schauer, J.J., Cass, G.R., 1999. Size and Composition Distribution of Fine Particulate Matter Emitted from Wood Burning, Meat Charbroiling, and Cigarettes. Environmental Science & Technology 33, 3516-3523.
Kukutschová, J., Moravec, P., Tomášek, V., Matějka, V., Smolík, J., Schwarz, J., Seidlerová, J., Šafářová, K., Filip, P., 2011. On airborne nano/micro-sized wear particles released from low-metallic automotive brakes. Environmental Pollution 159, 998-1006.
Kumar, P., Pirjola, L., Ketzel, M., Harrison, R.M., 2012. Nanoparticle emissions from 11 non–vehicle exhaust sources – A review. Atmospheric Environment.
Lahaye, J., Boehm, S., Chambrion, P., Ehrburger, P., 1996. Influence of cerium oxide on the formation and oxidation of soot. Combustion and Flame 104, 199-207.
Lake, D.A., Tolocka, M.P., Johnston, M.V., Wexler, A.S., 2003. Mass Spectrometry of Individual Particles between 50 and 750 nm in Diameter at the Baltimore Supersite. Environmental Science & Technology 37, 3268-3274.
Lee, D., Miller, A., Kittelson, D., Zachariah, M.R., 2006. Characterization of metal-bearing diesel nanoparticles using single-particle mass spectrometry. Journal of Aerosol Science 37, 88-110.
Lenin, M.A., Swaminathan, M.R., Kumaresan, G., 2013. Performance and emission characteristics of a DI diesel engine with a nanofuel additive. Fuel 109, 362-365.
Liati, A., Dimopoulos Eggenschwiler, P., Müller Gubler, E., Schreiber, D., Aguirre, M., 2012. Investigation of diesel ash particulate matter: A scanning electron microscope and transmission electron microscope study. Atmospheric Environment 49, 391-402.
Lin, C.-C., Chen, S.-J., Huang, K.-L., Hwang, W.-I., Chang-Chien, G.-P., Lin, W.-Y., 2005. Characteristics of Metals in Nano/Ultrafine/Fine/Coarse Particles Collected Beside a Heavily Trafficked Road. Environmental Science & Technology 39, 8113-8122.
Linak, W.P., Yoo, J.-I., Wasson, S.J., Zhu, W., Wendt, J.O.L., Huggins, F.E., Chen, Y., Shah, N., Huffman, G.P., Gilmour, M.I., 2007. Ultrafine ash aerosols from coal combustion: Characterization and health effects. Proceedings of the Combustion Institute 31, 1929-1937.
Liu, C.-N., Awasthi, A., Hung, Y.-H., Tsai, C.-J., 2013. Collection efficiency and interstage loss of nanoparticles in micro-orifice-based cascade impactors. Atmospheric Environment 69, 325-333.
Lough, G.C., Schauer, J.J., Park, J.-S., Shafer, M.M., DeMinter, J.T., Weinstein, J.P., 2004. Emissions of Metals Associated with Motor Vehicle Roadways. Environmental Science & Technology 39, 826-836.
Lu, S., Feng, M., Yao, Z., Jing, A., Yufang, Z., Wu, M., Sheng, G., Fu, J., Yonemochi, S., Zhang, J., 2011. Physicochemical characterization and cytotoxicity of ambient coarse, fine, and ultrafine particulate matters in Shanghai atmosphere. Atmospheric Environment 45, 736-744.
Lü, S., Zhang, R., Yao, Z., Yi, F., Ren, J., Wu, M., Feng, M., Wang, Q., 2012. Size distribution of chemical elements and their source apportionment in ambient coarse, fine, and ultrafine particles in Shanghai urban summer atmosphere. Journal of Environmental Sciences 24, 882-890.
Lu, T., Cheung, C.S., Huang, Z., 2012. Effects of engine operating conditions on the size and nanostructure of diesel particles. Journal of Aerosol Science 47, 27-38.

Lyyränen, J., Jokiniemi, J., Kauppinen, E.I., Joutsensaari, J., 1999. AEROSOL CHARACTERISATION IN MEDIUM-SPEED DIESEL ENGINES OPERATING WITH HEAVY FUEL OILS. Journal of Aerosol Science 30, 771-784.
Mahowald, N.M., Baker, A.R., Bergametti, G., Brooks, N., Duce, R.A., Jickells, T.D., Kubilay, N., Prospero, J.M., Tegen, I., 2005. Atmospheric global dust cycle and iron inputs to the ocean. Global Biogeochemical Cycles 19, GB4025.
Marjamaki, M., Keskinen, J., Chen, D.R., Pui, D.Y.H., 2000. Performance evaluation of the electrical low-pressure impactor (ELPI). Journal of Aerosol Science 31, 249-261.
Martin, L.R., Good, T.W., 1991. Catalyzed oxidation of sulfur dioxide in solution: The iron-manganese synergism. Atmospheric Environment. Part A. General Topics 25, 2395-2399.
McClellan, R.O., Hesterberg, T.W., Wall, J.C., 2012. Evaluation of carcinogenic hazard of diesel engine exhaust needs to consider revolutionary changes in diesel technology. Regulatory Toxicology and Pharmacology 63, 225-258.
Miller, A., Ahlstrand, G., Kittelson, D., Zachariah, M., 2007a. The fate of metal (Fe) during diesel combustion: Morphology, chemistry, and formation pathways of nanoparticles. Combustion and Flame 149, 129-143.
Miller, A.L., Stipe, C.B., Habjan, M.C., Ahlstrand, G.G., 2007b. Role of Lubrication Oil in Particulate Emissions from a Hydrogen-Powered Internal Combustion Engine. Environmental Science & Technology 41, 6828-6835.
Misra, C., Kim, S., Shen, S., Sioutas, C., 2002a. A high flow rate, very low pressure drop impactor for inertial separation of ultrafine from accumulation mode particles. Journal of Aerosol Science 33, 735-752.
Misra, C., Singh, M., Shen, S., Sioutas, C., Hall, P.M., 2002b. Development and evaluation of a personal cascade impactor sampler (PCIS). Journal of Aerosol Science 33, 1027-1047.
Moldanová, J., Fridell, E., Popovicheva, O., Demirdjian, B., Tishkova, V., Faccinetto, A., Focsa, C., 2009. Characterisation of particulate matter and gaseous emissions from a large ship diesel engine. Atmospheric Environment 43, 2632-2641.
Morawska, L., Ristovski, Z., Jayaratne, E., Keogh, D.U., Ling, X., 2008. Ambient nano and ultrafine particles from motor vehicle emissions: Characteristics, ambient processing and implications on human exposure. Atmospheric Environment 42, 8113-8138.
Morawska, L., Wang, H., Ristovski, Z., Jayaratne, E., Johnson, G., Cheung, H.C., Ling, X., He, C., 2009. JEM Spotlight: Environmental monitoring of airborne nanoparticles. J. Environ. Monit. 11, 1758-1773.
Nash, D.G., Swanson, N.B., Preston, W.T., Yelverton, T.L.B., Roberts, W.L., Wendt, J.O.L., Linak, W.P., 2012. Environmental implications of iron fuel borne catalysts and their effects on diesel particulate formation and composition. Journal of Aerosol Science.
Ntziachristos, L., Ning, Z., Geller, M.D., Sheesley, R.J., Schauer, J.J., Sioutas, C., 2007. Fine, ultrafine and nanoparticle trace element compositions near a major freeway with a high heavy-duty diesel fraction. Atmospheric Environment 41, 5684-5696.
Pakkanen, T.A., Kerminen, V.-M., Korhonen, C.H., Hillamo, R.E., Aarnio, P., Koskentalo, T., Maenhaut, W., 2001. Urban and rural ultrafine (PM0.1) particles in the Helsinki area. Atmospheric Environment 35, 4593-4607.
Park, B., Donaldson, K., Duffin, R., Tran, L., Kelly, F., Mudway, I., Morin, J.-P., Guest, R., Jenkinson, P., Samaras, Z., Giannouli, M., Kouridis, H., Martin, P., 2008a. Hazard and Risk Assessment of a Nanoparticulate Cerium Oxide-Based Diesel Fuel Additive—A Case Study. Inhalation Toxicology 20, 547-566.
Park, K., Cho, G., Kwak, J.-h., 2009. Development of an Aerosol Focusing-Laser Induced Breakdown Spectroscopy (Aerosol Focusing-LIBS) for Determination of Fine and Ultrafine Metal Aerosols. Aerosol Science and Technology 43, 375-386.
Park, K., Heo, Y., Putra, H., 2008b. Ultrafine metal concentration in atmospheric aerosols in urban Gwangju, Korea. Aerosol Air Qual. Res 8, 411-422.
Park, K., Park, J.Y., Kwak, J.-H., Cho, G.N., Kim, J.-S., 2008c. Seasonal and diurnal variations of ultrafine particle concentration in urban Gwangju, Korea: Observation of ultrafine particle events. Atmospheric Environment 42, 788-799.
Patel, M., Azanza Ricardo, C.L., Scardi, P., Aswath, P.B., 2012. Morphology, structure and chemistry of extracted diesel soot—Part I: Transmission electron microscopy, Raman spectroscopy, X-ray photoelectron spectroscopy and synchrotron X-ray diffraction study. Tribology International 52, 29-39.

Pennanen, A.S., Sillanpää, M., Hillamo, R., Quass, U., John, A.C., Branis, M., Hůnová, I., Meliefste, K., Janssen, N.A.H., Koskentalo, T., Castaño-Vinyals, G., Bouso, L., Chalbot, M.C., Kavouras, I.G., Salonen, R.O., 2007. Performance of a high-volume cascade impactor in six European urban environments: Mass measurement and chemical characterization of size-segregated particulate samples. Science of the total environment 374, 297-310.
Phares, D.J., Rhoads, K.P., Johnston, M.V., Wexler, A.S., 2003. Size-resolved ultrafine particle composition analysis 2. Houston. Journal of Geophysical Research: Atmospheres 108, 8420.
Querol, X., Viana, M., Alastuey, A., Amato, F., Moreno, T., Castillo, S., Pey, J., de la Rosa, J., Sánchez de la Campa, A., Artíñano, B., Salvador, P., García Dos Santos, S., Fernández-Patier, R., Moreno-Grau, S., Negral, L., Minguillón, M.C., Monfort, E., Gil, J.I., Inza, A., Ortega, L.A., Santamaría, J.M., Zabalza, J., 2007. Source origin of trace elements in PM from regional background, urban and industrial sites of Spain. Atmospheric Environment 41, 7219-7231.
Reff, A., Eberly, S.I., Bhave, P.V., 2007. Receptor modeling of ambient particulate matter data using positive matrix factorization: review of existing methods. Journal of the Air & Waste Management Association 57, 146-154.
Saffari, A., Daher, N., Shafer, M.M., Schauer, J.J., Sioutas, C., 2013. Seasonal and spatial variation of trace elements and metals in quasi-ultrafine (PM< sub> 0.25</sub>) particles in the Los Angeles metropolitan area and characterization of their sources. Environmental Pollution 181, 14-23.
Sillanpää, M., Hillamo, R., Mäkelä, T., Pennanen, A.S., Salonen, R.O., 2003. Field and laboratory tests of a high volume cascade impactor. Journal of Aerosol Science 34, 485-500.
Singh, M., Misra, C., Sioutas, C., 2003. Field evaluation of a personal cascade impactor sampler (PCIS). Atmospheric Environment 37, 4781-4793.
Smith, S., Ward, M., Lin, R., Brydson, R., Dall'Osto, M., Harrison, R.M., 2012. Comparative study of single particle characterisation by Transmission Electron Microscopy and time-of-flight aerosol mass spectrometry in the London atmosphere. Atmospheric Environment 62, 400-407.
Song, J., Wang, J., Boehman, A.L., 2006. The role of fuel-borne catalyst in diesel particulate oxidation behavior. Combustion and Flame 146, 73-84.
Srimuruganandam, B., Shiva Nagendra, S.M., 2012. Application of positive matrix factorization in characterization of PM10 and PM2.5 emission sources at urban roadside. Chemosphere 88, 120-130.
Steiner, S., Mueller, L., Popovicheva, O.B., Raemy, D.O., Czerwinski, J., Comte, P., Mayer, A., Gehr, P., Rothen-Rutishauser, B., Clift, M.J., 2012. Cerium dioxide nanoparticles can interfere with the associated cellular mechanistic response to diesel exhaust exposure. Toxicology letters 214, 218-225.
Su, Y., Sipin, M.F., Furutani, H., Prather, K.A., 2003. Development and Characterization of an Aerosol Time-of-Flight Mass Spectrometer with Increased Detection Efficiency. Analytical Chemistry 76, 712-719.
Thorpe, A., Harrison, R.M., 2008. Sources and properties of non-exhaust particulate matter from road traffic: A review. Science of the total environment 400, 270-282.
Tissari, J., Lyyränen, J., Hytönen, K., Sippula, O., Tapper, U., Frey, A., Saarnio, K., Pennanen, A.S., Hillamo, R., Salonen, R.O., Hirvonen, M.R., Jokiniemi, J., 2008. Fine particle and gaseous emissions from normal and smouldering wood combustion in a conventional masonry heater. Atmospheric Environment 42, 7862-7873.
Tolocka, M.P., Lake, D.A., Johnston, M.V., Wexler, A.S., 2004. Number concentrations of fine and ultrafine particles containing metals. Atmospheric Environment 38, 3263-3273.
Tolocka, M.P., Lake, D.A., Johnston, M.V., Wexler, A.S., 2005. Size-resolved fine and ultrafine particle composition in Baltimore, Maryland. Journal of Geophysical Research: Atmospheres 110, D07S04.
Utsunomiya, S., Jensen, K.A., Keeler, G.J., Ewing, R.C., 2004. Direct Identification of Trace Metals in Fine and Ultrafine Particles in the Detroit Urban Atmosphere. Environmental Science & Technology 38, 2289-2297.
Wang, H.-C., John, W., 1988. Characteristics of the Berner Impactor for Sampling Inorganic Ions. Aerosol Science and Technology 8, 157-172.
Wang, Y., Hopke, P.K., Xia, X., Chalupa, D.C., Utell, M.J., 2012. Source apportionment of airborne particulate matter using inorganic and organic species as tracers. Atmospheric Environment.
Wieprecht, W., Acker, K., Müller, K., Spindler, G., Brüggemann, E., Maenhaut, W., Chi, X., Hitzenberger, R., Bauer, H., Brink, H.t., 2004. INTERCOMP2000: ionic constitution and comparison of filter and impactor. Atmospheric Environment 38, 6477-6486.

Zauscher, M.D., Moore, M.J.K., Lewis, G.S., Hering, S.V., Prather, K.A., 2011. Approach for Measuring the Chemistry of Individual Particles in the Size Range Critical for Cloud Formation. Analytical Chemistry 83, 2271-2278.

CHAPTER 2: METHODOLOGY OF SAMPLE COLLECTION AND ANALYSIS

2.1 Site Descriptions

The metals the project sought to investigate are primarily associated with traffic sources and the choice of sampling locations was made accordingly with the aim of acquiring samples from a range of different traffic-impacted scenarios; traffic roadsides, urban background sites with some level of traffic impact, and rural background sites. It was assumed that urban and suburban sites would show comparable concentrations with the most important differences being between traffic-impacted and non-traffic impacted areas.

2.1.1 Bristol Road Observatory

This site served as the traffic roadside site for the project. Located at the South Entrance to the University of Birmingham campus, Edgbaston, adjacent to the A38 main road (approximately 4m distance). The most recent figures from the Department for Transport record an average annual daily flow (AADF) of 27,265 vehicles in 2011. HGVs account for 1.46% of this traffic and buses/coaches 2.4%. The site is slightly elevated relative to the road so the inlet was approximately 3 m above the road surface.

Mass concentration data for 26 samples collected between June 2011-November 2011, and March-April 2013 are presented for this site.

ICP-MS mass concentration data for 10 metals are presented for 8 sample sets selected from the 2011 samples.

Mass concentration data for Cl^-, NO_3^- and SO_4^{2-} ions are presented for 5 sample sets collected between March-May 2013.

2.1.2 Elms Road Observatory

This site was used as the urban background site, and is located on the university campus around 800m from the A38. Comparisons with AURN data for these two sites had to be made with the AURN stations at Tyburn and Tyburn roadside, which were the nearest comparable AURN site. According to the latest figures, the AADF at Tyburn was 26,457 vehicles per day. Of these, 3.91% were HGVs and 0.63% buses/coaches. Tyburn therefore has a slightly higher proportion of heavy duty diesel vehicles (4.54% compared to 3.86%) compared to BROS.

Total mass concentration data are presented for 10 samples collected from September-November 2011.

ICP-MS mass concentration data are presented for 9 metals (Ce excluded owing to insufficient data) for 5 sample sets collected between September-November 2011.

2.1.3 Harwell Campus

Samples were collected at the existing DEFRA rural air monitoring station. The site has been used extensively for rural air monitoring in since 1998 (Charron et al., 2008). It is located on the edge of the Harwell campus, with the surrounding area being largely flat and open, with farmland to the west. The closest road, on the east of the campus, is used for access only and the site is 800m from the nearest main road, the A4185, which has an average annual daily flow of 8,000 vehicles.

Total mass data and ICP-MS mass concentration data for 10 metals are presented for two 14-day samples collected in December 2011.

2.1.4 Newcastle Central AURN Station

The AURN station at Newcastle Civic Centre, Newcastle-upon-Tyne was used as a traffic roadside site to collect nanoMOUDI and MOUDI filter and TEM grid samples. The site was chosen because

Newcastle's public buses are run by Stagecoach, who used cerium oxide fuel additives in their fleet in this area during the period of sampling. The physical and chemical composition of these samples would therefore make a useful comparison the two sites in Birmingham, where cerium oxide additives are not used by the major local transport firms.

There is not a DfT count point on the road adjacent to the site to record traffic flows past the site.

Total mass concentration data are presented for 19 nanoMOUDI samples from January-June 2012 and 14 MOUDI samples from February-July 2012.

ICP-MS mass concentration data for 9 metals are presented for 7 nanoMOUDI sample sets selected from throughout this period.

2.1.5 Barcelona Sites

The roadside site at 445 Valencia Street, Barcelona. The site is a four-lane road with parking to one side, located in the city centre quite close to Sagrada Familia. There are high buildings to both sides of the road forming a street canyon. The MOUDI was sited in a steel electric cabinet mounted on top of the van which serves as the mobile site, putting the inlet around 3m above street level.

The other site was located on the campus of the Polytechnic University of Catalonia. This served as an urban background site but is heavily influenced by the nearby Avenue Diagonal, approximately 300 m from the site and carrying up to 100,000 vehicles per working day.

Data are presented for 7 sample sets from the roadside site and 8 from the background.

2.2 Sampling Equipment and Practices

2.2.1 nanoMOUDI

A nanoMOUDI-ii 125R cascade impactor (MSP Corporation) was used to collect size resolved particulate samples. The instrument has thirteen stages with nominal 50% cutpoints of 10000, 5600,

3200, 1800, 1000, 560, 320, 180, 100, 56, 32, 18 and 10 nm when operated at an inlet flow rate of 10.0 L/min. The impactor was paired with a Leybold SV 16 rotary vane oil pump from May 2011 to September 2012, and then with an SV 25 pump for the soluble ion sample collection in April – May 2013.

The instrument separates particles into a series of logarithmically equal size fractions based on atmospheric diameter, by accelerating particles through a fine jet under which a filter mounted on a rotating plate collects the heavier particles while the lighter ones remain in the gas streamline. Employing progressively higher velocities on successive stages allows collection of progressively smaller particles. Cascade impactor instruments such as the nanoMOUDI-ii can require long sampling times to collect sufficiently high masses of nanoparticulate material for accurate quantification of mass and chemical composition. The length of sampling periods had to be decided based on the limits of detection established for the analytical processes.

The experimental set-up at the sampling sites had the impactor and pump housed in a steel electrical cabinet, with an inlet at the top of the housing covered by a rain hood. Two fans were positioned next to the pump to keep it as cool as possible during operation, but nevertheless temperatures in the region of 40-45 Celsius during operation were still recorded, particularly during the summer months. This would have the effect of reducing the mass of volatile material collected by this method, but this is unlikely to affect the collection of metal samples.

Other considerations in the employment of impactors are sampling artefacts such as particle bounce and blow-off, which may produce less accurate size distributions. It is also possible that reduced sampling flow rates would change the cut points and require a correction to be made.

2.2.2 MOUDI

During the sampling campaign at the Newcastle Civic Centre site, the instrument used was an MSP M110 12 stage MOUDI, although the ultrafine stages were left out owing to pre-existing problems

with clogging, making the instrument effectively a 10-stage instrument. This means that all material passing the 180 nm cutpoint should be collected on the afterfilter. The same Whatman 47 mm PTFE membrane filters were used as in the nanoMOUDI. The nominal sampling flowrate was 30 l/min, although in practice values between 26-28 l/min were typical during use.

In Birmingham the 12-stage MOUDI (MSP model 110) was operated alongside the nanoMOUDI during the soluble ion sample collections at the Bristol Road sampling site. The MOUDI was operating at 30 l/min and ran for 7-day periods alongside the nanoMOUDI. Since quantifiable results for a number of metals have been obtained by researchers at the university of Birmingham using this instrument over much shorter sampling periods, it was unlikely that there would be many problems in getting useful data for a range of metals, especially more abundant species such as iron, copper and zinc.

2.2.3 Sampling strategy

When using the nanoMOUDI, it was initially proposed to sample twice weekly, collected a 3-day sample during the week and a 4-day sample incorporating the weekend (eg Monday-Thursday, Thursday-Monday). However, during summer 2011 it was decided that the limits of detection in the weighing process would make 7-day sampling a more viable strategy, so this is what was used since then (BROS concurrent measurements, BROS/EROS concurrent measurements, NCC samples, BROS soluble ions sampling).

TEM samples were collected by affixing the copper grids to aluminium filter substrates, then mounting the filter substrates in the nanoMOUDI as normal. Sampling was initially carried out at for three hours in Birmingham, but this time was extended to 6 hours at BROS and 8 hours in Newcastle to give suitable particle density on the smaller size fractions below 180 nm. The trade-off for getting useful particle numbers in the ultrafine/pseudo-ultrafine range was that particles in the fine and coarse range were somewhat too dense, with particles overlaying each other on the grid surface.

However, this was considered acceptable as collection and analysis of smaller particles was the priority.

2.3 Analytical methodology

2.3.1 Gravimetric analysis

Samples were collected in the nanoMOUDI and MOUDI instruments using PTFE filters (47mm diameter, 1 micron pore size, reference code 7590 004, Whatman). In both instruments the main stages were collected using 47 mm diameter filters. In the nanoMOUDI, two types of filters were used in the backup stage, both 47 mm PTFE types supplied by Pall Corporation, 1 type with a supporting O-ring and 1 without.

Filters were conditioned for 24hrs prior to weighing in a controlled environment (wrt temperature and relative humidity). An ionisation strip and radioactive deioniser were employed to minimise errors caused by electrostatic effects. Each filter is weighed in the positive and negative ie. the filter was weighed as normal, then the balance zeroed with the filter paper still in place, then the paper removed and the mass recorded. It was very rare that the negative mass deviates by more than 5 microgrammes from the positive.

Where difference between measurements exceeds this threshold, outlying measurements must necessarily be excluded. Once the two positive and two negative weighings have been carried out, measurements which lie within 5 microgrammes are accepted, and any outside that range are excluded. If this means that only two out of four readings were within 5 microgrammes a third weighing, both positive and negative, was carried out, and the closest measurements accepted.

Early in the project 6 unexposed filters were used to assess limits of detection through analysing variability between multiple weighings. Limit of detection was taken to be 3 times the standard

deviation of the 6 recorded changes in mass and limit of quantification taken to be 10 times the standard deviation. This produced a LOD of 4.58 micrograms and limit of quantification of 17.72 micrograms, equivalent to 0.51 μgm^{-3} and 1.97 μgm^{-3} respectively in a 90 m^3 nanoMOUDI air sample. In data from ambient samples the smallest total mass collected in a sampled filter is 6.25 micrograms – blank levels are lower than sampled levels. Visual inspection of the Harwell filters after 1 week showed that sampling would have to be extended to 14 day periods, of which two sets were collected over 4 weeks.

2.3.2 Acid digestion procedure

Filter samples were prepared for bulk chemical analysis by acid digestion in reverse aqua regia, based on the procedure described by Harper et al. (Harper et al., 1983). Filter samples were subjected to an acid leaching extraction procedure employing a reverse aqua regia solution prepared by mixing 66 cm^3 HCl with 189 cm^3 HNO_3 (ultrapure, supplied by Romil) and made up to 1000 cm^3 with 18.2 MΩ deionised water. The filters were placed in 4 cm^3 Nalgene vials and immersed in 2 cm^3 of the extract solution, then heated to 100°C in a water bath for 30 min, then sonicated at 50°C for 30 min. The heating and sonicating steps were repeated, before the extract was transferred to a clean 30 cm^3 vial and the extract vial washed with 4 cm^3 deionised water twice, which was also transferred to the 30 cm^3 vial to make up a total solution of 10 cm^3. Samples were stored at 5°C. This procedure is well established within the department.

To try to minimise contamination, a solution of 2% Aristar grade HNO_3 in 18.2 MΩ deionised water was used to soak all vials, pipette tips and glassware used in the procedure for 24 hours prior to the extraction taking place.

Blank filters (both lab blanks and field blanks) were analysed for all elemental analyses to correct for background levels of elements in the filters used; and to determine limits of detection for the analytes.

2.3.3 Chemical (Bulk)- ICP-MS

The extracts were analysed for several metals by Inductively Coupled Plasma Mass Spectrometry by Dr Stephen Baker. Analysis was carried out on an Agilent 7500ce ICP-MS with an Octopole reaction system (ORS) which is used to remove polyatomic interferences such as ClO at mass 51 (V) and ArO at mass 56 (Fe). Masses used for analysis are as follows: ^{27}Al, ^{137}Ba, ^{140}Ce, ^{63}Cu, ^{56}Fe, ^{60}Ni, ^{121}Sb, ^{88}Sr, ^{51}V and ^{56}Zn. The plasma runs with an RF power of 1500 W. A Miramist nebuliser is used for sample introduction. Detection limits are approximately 10 times lower than the reporting limits i.e. the detection limit for V is about 0.02 ppb giving a reporting limit of < 0.2 ppb. Reporting limits are quoted to give a greater confidence in the results being reported rather than giving values near to the detection limits.

Element	Reporting limit (Solution) / ng cm^{-3}	Reporting limit (Air) / ngm^{-3}
Al	0.5	0.056
Ba	0.1	0.011
Ce	0.1	0.011
Cu	0.1	0.011
Fe	0.5	0.056
Ni	0.1	0.011
Sb	0.1	0.011
Sr	0.1	0.011
V	0.2	0.022
Zn	0.2	0.022

Table 4. Reporting Limits for ICP-MS data assuming 9L/min flowrate.

A series of laboratory blanks analysed in 2012 showed limits of detection which were probably low enough to work for the likely airborne concentrations (*Table 5*).

Sample	**SD**	**LOD (ng cm^{-3})**	**LODair (ng m^{-3})**
Al	42.70	128.09	14.23
Ba	0.04	0.13	0.01
Ce	< 0.1	< 0.1	< 0.011
Cu	< 0.2	< 0.2	< 0.022
Fe	1.52	4.56	0.51
Ni	0.13	0.39	0.04
Sb	< 0.1	< 0.1	< 0.011

Sr	0.01	0.02	0.00
V	< 0.2	< 0.2	< 0.022
Zn	< 0.2	< 0.2	< 0.022

Table 5. Dectection Limits for ICP-MS lab blanks assuming 9L/min flowrate for equivalent LOD in air.

However, when the field blanks from the samples collected in the UK were analysed, high variability was seen especially with Al and Fe, which resulted in high detection limits and suggests that the Fe and Al data from the UK sites should be treated with some caution (*Table 6*). It is apparent that with these elements, contamination is introduced in some aspect of handling the filters, during loading and unloading from the instrument. The disparity between lab and field blanks shows that this problem is in the field, not the lab.

Sample	**SD**	**LOD (ng cm^{-3})**	**LODair (ng m^{-3})**
Al	23.42	70.25	7.81
Ba	0.09	0.28	0.03
Ce	< 0.1	< 0.1	< 0.011
Cu	1.97	5.92	0.66
Fe	1397.09	4191.26	465.70
Ni	3.65	10.94	1.22
Sb	< 0.1	< 0.1	< 0.011
Sr	0.14	0.43	0.05
V	1.51	4.52	0.50
Zn	1.85	5.54	0.62

Table 6. Dectection Limits for ICP-MS field blanks assuming 9L/min flowrate for equivalent LOD in air.

In retrospect, the use of X-ray fluorescence to corroborate data on these two elements would have been a useful addition. The method was not originally envisaged owing to lower sensitivity than ICP-MS. The Fe issue does not affect the TEM data, as it seems to be related to the handling of filters in either sampling or extraction, which will not affect particles deposited on the carbon films, as only the support ring and not the sampled surface is touched by equipment.

2.3.4 Physical characterisation by TEM

Transmission Electron Microscopy is a well-established technique for single-particle characterisation. Electrons emitted from a source are focused by electromagnetic lenses into a tight beam and directed down a column under vacuum, in which the sample is located on a thin film. As the electrons pass through the specimen, some are scattered and disappear from the beam, a process dependent on the density of the material. The unscattered transmitted electrons hit a fluorescent screen at the bottom of the microscope, forming a shadow image of the specimen in which the different parts are displayed in varied darkness according to density.

Samples were collected on TEM grids (holey carbon film on copper, Agar Scientific) mounted on aluminium foil substrates in the nanoMOUDI instrument. This type of approach has proven effective in previous studies (Smith et al., 2012). Sampling was carried out in the normal manner, but for much shorter times. The necessary sampling time in order to get sufficient particle density for easy imaging and analysis, but avoid too much particle build up, depended on the conditions around the sampling site, such as proximity of roads and traffic density. 3 hours proved sufficient for the Birmingham roadside site (Bristol Road), but not for the Newcastle site where a total of 8 hours over 3 sessions (owing to limited time on site per sampling day) was sampled.

Imaging of samples was carried out using a Tecnai F20 Transmission Electron Microscope working on high tension at 200kV, with an extraction voltage of 4450eV. Bright-field particle imaging in TEM mode was carried out using the GATAN digital micrograph attached to the instrument. For identifying likely particles and carrying out EDX analysis, the instruments STEM mode was used in conjunction with high angle annular dark field (HAADF) detection. This method allowed areas of high atomic number to be identified, which in air samples dominated by carbonaceous material was a good indicator of metallic content in the particles. Simultaneous collection of bright field and dark field images has proven difficult and finding particles again while switching between modes has not

proven straightforward; identifying the same particle is challenging owing to the different physico-chemical features emphasised in each mode.

2.3.5 Chemical (single particle) – EDS

Energy Dispersive Spectroscopy (EDS) is a form of chemical analysis carried out by bombarding a solid sample with a focused electron beam. X-ray lines can be assigned to particular elements, enabling identification; quantitative analysis requires measurement of relative intensities of X-ray lines at a given point. Scanning the electron beam across the sample in a raster enables a map of intensities to be constructed, showing the distribution of elements within the sample. Both point-analyses and raster-analyses were employed in this study. Particles were selected by working systematically around one grid square in each session similar to the system reported by Smith et al. (2012), likely particles being selected on brightness in HAADF indicating high atomic weight.

Single particle chemical analysis was carried out using x-ray energy dispersive spectroscopy (X-EDS or EDX). An Oxford Instruments detector is used for collection, with the sample α-tilt set at 15°. The system is controlled and the data managed by the INCA and AZTEC software systems also designed by Oxford Instruments.

2.3.6 EELS Analysis

Scanning TEM – Electron Energy Loss Spectroscopy was used to determine the speciation of Fe oxides in ambient samples. The technique measures the loss of energy in fast electrons backscattered from the sample, which can be used to determine what element caused the scattering and to determine the valence of the scattering element. Experiments were carried out using the Nion UltraSTEM^{TM}100 aberration-corrected dedicated STEM, equipped with a Gatan Enfina spectrometer. The microscope was operated at 100kV acceleration voltage with a convergence angle of 30mrad, corresponding to a probe size ~0.9Å probe (full width at half-maximum). The semi-angular ranges of high angle annular dark field and medium angle annular dark field detectors were

86-190 and 40-86mrad, respectively. The native energy spread of the electron probe was 0.3eV, as determined from the full width at half-maximum of the zero loss peak (ZLP). The collection semi-angle for the electron energy loss spectroscopy measurements was 36 mrad. Postsampling images were systematically acquired in order to assess specimen beam damage. Sample thicknesses were determined relative to the inelastic mean free path (t/λ) by the log-ratio method from low-loss EELS spectra (Egerton, 2011). For thicknesses exceeding 0.7 t/λ, core loss spectra were deconvoluted for plural scattering by the Fourier-ratio method using low loss spectra of the same specimen areas. Commercially available standards were used to obtain the L3/L2 intensity ratio values for each oxide to enable assignment of the particles in the samples. These compare well with values previously published in the literature.

2.4 Collection and analysis of soluble ion samples

2.4.1 Limits of detection imposed by ion chromatography

In any chromatographic method the limit of detection is normally considered to be a signal height of three times the baseline noise. In real terms, this imposed a limit of approximately 0.05 mg/L for the Dionex instrument.

The extraction procedure for PTFE filter papers used 0.5 ml of propan-2-ol to wet the filter, prior to immersion in 10 ml deionised water and 50 min on an automatic shaker.

If used on a sample collected for 3 days in a MOUDI (129.6 m^3 volume of air) this would equate to 0.004 μgm^{-3} limit of detection in air. A 7-day nanoMOUDI sample normally equated to around 90-95 m^3 of air. From equation 1 below, the limit of detection equated to (assuming 90 m^3) of 0.00583 μgm^{-3} in air. For a 3-day sample this equated to 0.0175 μgm^{-3} in air.

The necessary sampling time was dependent on factors such as temperature and sunlight intensity, which are extremely variable during the March-April sampling period.

Equation 1.

$$LODair = \frac{LODsoln \times extract\ vol.}{air\ sample\ volume}$$

2.4.2 Previous sulphate studies using impactors

A number of studies have previously reported the collection of sulphate samples in the ultrafine with MOUDI/nanoMOUDI instruments, which demonstrate that such work is possible.

Cass et al. measured sulphate concentrations at several source and receptor sites in Southern California, finding that sulphate formed on average 8.2% of particle mass between 56-100 nm aerodynamic diameter. This average includes sample collected from September through to February and includes sites with quite different source profiles. The range of sulphate varies from 1% - 18% total mass (Cass et al., 2000)

Similar mass composition was found by Sardar et al. also using the nanoMOUDI. At two urban source sites and two receptor sites in southern California, sulphate was found to account for between 0-24% of total particle mass below 180 nm. Sulphate was not detected for samples below 56 nm. The authors attributed this to the majority being formed on pre-existing particle surfaces, or liquid-phase sulphuric acid reactions. Summer concentrations were much higher at all sites, due to the photochemical formation processes of SO_4^{2-} particles (Sardar et al., 2004).

Sulphate concentrations were found to account for 21% of total $PM_{0.1}$ at an urban site in Helsinki and 25% at a rural background site, averaged over a year of sampling (Pakkanen et al., 2001).

Sardar et al. also reported that sulphate mass concentration as a proportion of the total mass concentration was very similar in the ultrafine and accumulation modes.

Applying the approximate sulphate contributions from these studies (assuming that proportion stays the same through the distribution) to some Birmingham nanoMOUDI figures (7-day samples, autumn 2011) gave a rough estimate of possible concentrations from which plausible sampling times were estimated using the instrumental limit of detection.

Stage	**LC/ nm**	**BROS**	**EROS**	**BROS**	**EROS**	**BROS**	**EROS**	**BROS**	**EROS**
$\%SO_4^{2-}$		Total	Total	1%	1%	20%	20%	5%	5%
		PM	PM	SO_4^{2-}	SO_4^{2-}	SO_4^{2--}	SO_4^{2-}	SO_4^{2-}	SO_4^{2-}
5	1000	9.716	5.408	0.097	0.054	1.943	1.082	0.486	0.270
6	560	3.976	3.417	0.040	0.034	0.795	0.683	0.199	0.171
7	320	3.154	3.002	0.032	0.030	0.631	0.600	0.158	0.150
8	180	1.957	1.763	0.020	0.018	0.391	0.353	0.098	0.088
9	100	2.750	1.920	0.027	0.019	0.550	0.384	0.137	0.096
10	56	0.835	0.557	0.008	0.006	0.167	0.111	0.042	0.028
11	32	0.586	0.533	0.006	0.005	0.117	0.107	0.029	0.027
12	18	0.460	0.404	0.005	0.004	0.092	0.081	0.023	0.020
13	10	0.722	0.383	0.007	0.004	0.144	0.077	0.036	0.019
Assuming sulfate contribution to total mass is within previously reported ranges and distributed consistently									

Table 7. Estimates of possible concentration ranges, reported in µgm^{-3}.

The figure of 1% $PM_{0.1}$ as sulphate is slightly lower than reported contributions for winter presented by Kudo et al. for Tokyo winter samples, where sulphate formed around 5% of $PM_{0.1}$ mass in total (Kudo et al., 2011). Their summer values of 20-25% agree well with other publications.

The similarity between sulphate contributions to total $PM_{0.1}$ at a number of very different sites gives some confidence in making such an estimate.

2.4.3 Sulfate Concentrations in Birmingham

Previous measurements made in Birmingham by UoB researchers suggested that these estimates are approximately valid. Such samples were collected for 3 days using a MOUDI.

MOUDI results - winter 2000 at EROS		
	µg m^{-3}	
Stage	Sulphate	Particle diameter (µm)
V0	0.0029	22.097
V1	0.0093	14.468
V2	0.0259	8.484
V3	0.0885	4.779
V4	0.1050	2.608
V5	0.1837	1.483
V6	0.3147	0.820
V7	0.6872	0.463
V8	0.4963	0.265
V9	0.2009	0.149
V10	0.0414	0.085
VE	0.0302	0.018

Table 8. Reported sulphate ion concentrations from the Elms Road site (J.Yin – private communication).

The estimates presented above demonstrated that it was possible to collect reliable results for sulphate concentrations in Birmingham using 3-4 day samples without serious problems with the limits of detection provided sulphate concentrations are around 5% total PM or higher.

Sampling was nevertheless carried out over 7-day periods to ensure good results and this approach was justified by the fairly low concentrations observed in the analysed samples, which are presented in Chapter 5.

2.4.4 Preliminary Test Results using Dionex Ion Chromatograph

The Anion Chromatograph used for analysing the blanks and samples was a Dionex ICS2100 fitted with an Ion Pac AS11HC analytical column and Ion Pac AG11HC guard column. The eluent used was water, fitted with a KOH eluent generator cartridge.

Two blank sample sets were extracted and analysed in 2013. The blank filter papers were wetted with 0.5 ml of propan-2-ol to open the pores of the Teflon filter membrane, then immersed in 9.5 ml of 18 MΩ deionised water and agitated for 30 minutes using a mechanical shaker. 6 Blanks in each batch were analysed in triplicate.

Standards for phosphate, nitrate, sulphate and chloride were prepared in deionised water at 1, 2, 5, 10, 50 and 100 ppm.

Sample Name	**Nitrate**	**Chloride**	**Sulphate**
	Concentrations / μgcm^{-3}		
Mean Blanks (1)	1.47	1.57	2.09
Stdev	0.09	0.02	0.06
LOD solution	0.26	0.07	0.18
LOD air (μgm^{-3})	0.03	0.01	0.02

Table 9. Sulphate Concentrations, first batch of blanks for IC (October 2013).

The limit of detection reported here would therefore be adequate for a sample in which the sulphate is around 5% total PM mass in each fraction. Further tests were undertaken with the intention of improving these results.

Sample Name	**Chloride**	**Sulphate**
Concentration / μgcm^{-3}		
Mean Blanks (2)	0.016	-0.10
Stdev	0.02	0.67
LOD solution	0.06	2.02
LOD air (μgm^{-3})	0.01	0.22

Table 10. Sulphate Concentrations, second batch of blanks for IC (October 2013).

The analytical procedure was altered slightly for the second batch of samples. As the calibration standards for 50 ppm and 100 ppm were far above the expected values for the samples, it was decided to prepare calibration standards at lower concentrations to get a better calibration in the lower range where the sample concentrations would likely appear. The new standards were prepared using a 1000 ppm stock solution diluted to 1, 2, 5, 10, 15 and 20 ppm, each standard being prepared by one dilution to minimise the risk of dilution errors and contamination resulting from repeated dilution.

These samples were run shortly after the instrument had been refitted with a new column and new suppressor. In the first run, the calibration from 5 ppm downwards was not particularly reliable. Nitrate and fluoride did not provide an effective calibration and in some samples, fluoride and chloride were hard to separate. Consequently, fluoride was not analysed when the nanoMOUDI samples were analysed in 2015.

2.5 Collection of samples from static brake rig

In order to help with the apportionment of particles observed in the environmental samples from Birmingham and Newcastle, arrangements were made with the Department of Mechanical Engineering to use the static brake test rig in that department to produce particles which could be collected in isolation. This would allow samples of particles generated from wear and heating of the surfaces of brake pads and brake discs to be compared with particles from the field, to examine whether there are typical compositions and morphologies which would help to identify particles from this source in ambient samples.

2.5.1 Methods

The rig was enclosed within a Perspex casing, through which a single outlet supplied the nanoMOUDI, and later also the ATOFMS and dust sampler. It was not possible to filter the incoming air owing to the rotating shaft connecting the rig to the motor, however, the number of particles generated at the interface was high above background and this was not a problem.

Air drawn from the rig housing was collected in the nanoMOUDI, using PTFE filters for bulk samples which were extracted for ICP-MS analysis and TEM-X-EDS to characterise particle shape, size and chemical composition of individual particles, with the main aim of comparing to results from ambient measurements.

In this project, the intention was to characterise brake wear particles collected under controlled conditions to enable a comparison with samples collected in the ambient environment to explore whether similar particle types were detected in both samples.

The braking pressures suggested by the rig operators were 1 bar, 2 bar and 4 bar. These are similar to the range (0.14 MPa – 0.68 MPa used by Wahlstrom et al. in a pin-on-disc study testing low-metallic pad material against a cast-iron rotor, which were specifically intended to represent normal driving conditions corresponding to a vehicle speed of 55 km/h (Wahlström et al., 2012). Deciding experiment lengths especially for TEM samples required an element of trial and error despite referring to previous studies to make estimates. From previous studies, Kukutschova used a braking cycle of 24 repetitions of 30 seconds braking from 73-67 km/h followed by 120 seconds idle for cooling, which produced acceptable bulk samples for a 25 l/min Berner Impactor (Kukutschová et al., 2011). Sanders et al. (collecting with MOUDI and ELPI) employed a 24 stop braking cycle from low speeds (<90 km/h) and low deceleration (0.6-1.6 ms^{-2}) to simulate suburban driving (Sanders et al., 2003). The same study used the AMS braking test – 10 stops from 100 km/h at 7.9 ms^{-2} – to collect under extremely harsh braking. We found that 12 repetitions were sufficient for the collection of bulk samples, and 4 cycles more than sufficient for TEM sample collection.

2.5.2 Possible sampling issues

One area of concern in collecting from the rig was the possibility of particle losses in the sampling lines (reinforced PVC hose, European Standard) affecting the results, especially in view of the possibility that charged particles may be produced. It has been previously established that particles below 20 nm are particularly affected by losses in sampling lines (Kumar et al., 2008). The line running to the nanoMOUDI was as short as possible (<1 m) to try to minimise the effect of particle loss on the results.

2.5.3 Concurrent Experiments with ATOFMS/SMPS/APS/SMPS

Four filter sets and two sets of TEM grids were collected concurrently with the Aerosol Time-of-flight Mass Spectrometer, Aerosol Particle Sizer and Condensation Particle Counter/Scanning Mobility Particle Sizer. The filter samples were collected at 30 (two samples), 45 and 60 psi, and TEM samples at 30 and 60. Application times were shortened with pressure so that the brakes were applied every 2.5 minutes, but for 30 seconds at 30 psi, 20 seconds at 45 psi and only 6 seconds at 60 psi (intended to represent a rapid stop from 60 mph). 12 cycles were used for all pressures for filter samples, with stages 5 and 6 having to be changed at 6 cycles for 45 and 60 psi runs to prevent overloading.

ICP-MS data from these tests is included in chapter 6 for 45 and 60 psi samples, and TEM-X-EDS data from a test at 60 psi.

2.5.4 Bulk and surface brake pad analysis: Volatilisation tests

To investigate the emission of particles by volatilisation-condensation pathways, a tube furnace was used to heat samples from the brake pads. The samples were heated under HEPA-filtered compressed air. Brake pad samples were chiselled from the backing plate, broken up into fragments (though not powdered) for heating and placed into the tube furnace at 200°C, 300°C and 600°C. These temperatures were selected on the basis of previously reported results in the literature – Kukutschova et al. reported a nanoparticle release when the average rotor (brake disc) temperature reached 300°C (Kukutschová et al., 2011), and Sanders et al. reported a change in wear mechanism producing a large submicron fraction under very heavy braking at 500-600°C, which did not exist in the standard braking test cycle (temperature around 200°C) (Sanders et al., 2003). A filter attached beyond the outlet of the furnace was used to hold a TEM grid (Agar, Gold with holey carbon) for single particle characterisation and quartz microfiber filter (Whatman QM-A 1851-025) for bulk characterisation to collect the volatilised material. Pre- and post-heating analysis of the bulk sample

by X-ray Fluorescence was carried out along with analysis of the quartz filters using the normal $HCl/HNO_3/H_2O$ extraction solution for digestion and ICP-MS analysis.

It is likely to be the case that volatilisation and abrasion processes have some overlap. It was hoped these comparisons would help infer whether this is true, and whether is it the case that particles from different formation processes agglomerate together.

Thermodynamic Data for Common Brake Pad and Disc Components		
Element/Compound	*MP/°C*	*BP/°C*
Al_2O	2072	2977
Ba	725	1140
Barite	1345	1600
Calcite	1339	Decomposes
Cu	1083	2567
Fe	1535	2750
Fe_2O_3	1566	Decomposes
Fe_3O_4	1538	Decomposes
Mn	1245	1962
Pb	327	1740
Sb	630	1750
Sb_2S_3	550	1150
Si	1410	2355
Zircon	2550	Decomposes

Table 11. Melting and boiling temperatures of common brake pad constituents.

As shown in *Table 11*, the melting and boiling temperatures of common metallic components in brakes are very high and release would generally be expected at high temperatures only, which was generally what was found in the tests.

2.6 Collecting TEM samples of diesel exhaust

TEM grids (Agar Scientific, holey carbon films on gold mesh) were loaded into the 10-stage MOUDI (Model 110, MSP Corporation) mounted on aluminium foil substrates in the established method and sampled from the FASTER project diesel engine, a EURO 5 compliant unit supplied by Jaguar Land Rover, at conditions of 2000 RPM and 200 Nm load for 10 minutes. Particle load was

not excessive but metallic particles could be observed on the grids collected on the submicron size fractions. This process was repeated after the first TEM analysis to accumulate more particles on the grids.

References

Cass, G.R., Hughes, L.A., Bhave, P., Kleeman, M.J., Allen, J.O., Salmon, L.G., 2000. The chemical composition of atmospheric ultrafine particles. Philosophical Transactions of the Royal Society of London. Series A: Mathematical, Physical and Engineering Sciences 358, 2581-2592.

Charron, A., Birmili, W., Harrison, R.M., 2008. Fingerprinting particle origins according to their size distribution at a UK rural site. J. Geophys. Res. 113, D07202.

Egerton, R., 2011. Electron energy-loss spectroscopy in the electron microscope. Springer Science & Business Media.

Harper, S.L., Walling, J.F., Holland, D.M., Pranger, L.J., 1983. Simplex optimization of multielement ultrasonic extraction of atmospheric particulates. Analytical Chemistry 55, 1553-1557.

Kudo, S., Sekiguchi, K., Kim, K.H., Sakamoto, K., 2011. Spatial distributions of ultrafine particles and their behavior and chemical composition in relation to roadside sources. Atmospheric Environment 45, 6403-6413.

Kukutschová, J., Moravec, P., Tomášek, V., Matějka, V., Smolík, J., Schwarz, J., Seidlerová, J., Šafářová, K., Filip, P., 2011. On airborne nano/micro-sized wear particles released from low-metallic automotive brakes. Environmental Pollution 159, 998-1006.

Kumar, P., Fennell, P., Symonds, J., Britter, R., 2008. Treatment of losses of ultrafine aerosol particles in long sampling tubes during ambient measurements. Atmospheric Environment 42, 8819-8826.

Pakkanen, T.A., Kerminen, V.-M., Korhonen, C.H., Hillamo, R.E., Aarnio, P., Koskentalo, T., Maenhaut, W., 2001. Urban and rural ultrafine (PM0.1) particles in the Helsinki area. Atmospheric Environment 35, 4593-4607.

Sanders, P.G., Xu, N., Dalka, T.M., Maricq, M.M., 2003. Airborne Brake Wear Debris: Size Distributions, Composition, and a Comparison of Dynamometer and Vehicle Tests. Environmental Science & Technology 37, 4060-4069.

Sardar, S.B., Fine, P.M., Mayo, P.R., Sioutas, C., 2004. Size-Fractionated Measurements of Ambient Ultrafine Particle Chemical Composition in Los Angeles Using the NanoMOUDI. Environmental Science & Technology 39, 932-944.

Smith, S., Ward, M., Lin, R., Brydson, R., Dall'Osto, M., Harrison, R.M., 2012. Comparative study of single particle characterisation by Transmission Electron Microscopy and time-of-flight aerosol mass spectrometry in the London atmosphere. Atmospheric Environment 62, 400-407.

Wahlström, J., Olander, L., Olofsson, U., 2012. A Pin-on-Disc Study Focusing on How Different Load Levels Affect the Concentration and Size Distribution of Airborne Wear Particles from the Disc Brake Materials. Tribol Lett 46, 195-204.

CHAPTER 3: INVESTIGATION OF SUBMICRON AND ULTRAFINE BRAKE INTERFACE EMISSIONS USING NANOMOUDI AND TRANSMISSION ELECTRON MICROSCOPY – ENERGY DISPERSIVE SPECTROSCOPY

3.1 Introduction

Brake wear is an important source of particulate matter emissions into the environment and is therefore highly relevant to public health. It is a known source of a number of metallic elements which pose a known risk to health, such as Fe. There has been considerable effort to characterise brake wear emissions physically and chemically and this has largely focused on wear in the coarse and fine fractions (Garg et al., 2000; Mosleh et al., 2004; Wahlström et al., 2010). Understanding of the fraction of brake wear emissions in the ultrafine/pseudo-ultrafine is more limited, but it has been reported that number distributions from brake wear peak in this size range (Kukutschová et al., 2011). This has important implications for health because smaller particles can penetrate further into the respiratory system and potentially cross into the circulatory system and translocate to internal organs.

Available literature concerning the relationship between bulk composition and emitted particles demonstrate that they can be quite different . Fewer data are available on the change in composition and/or morphology with size, although some evidence is available that both particle shape and composition are different at smaller sizes.

Some previous work suggests that nanoparticle number emissions can be very high (Kukutschová et al., 2011). Furthermore, the modal diameters identified by Wahlstrom et al. (2012) of 280 nm, 350 nm and 550 nm would seem to agree with the size ranges of the Pb-based and Fe-based particles which we have observed in the environment (see chapter 5). This 350 nm mode is consistent across more than one study and has been attributed to agglomeration of nanoscale primary particles (Sanders et al., 2003; Wahlström et al., 2012).

A previous study reported a significant emission of nanoparticles at an average rotor temperature of 300°C which was attributed to the initiation temperature of the organic material – nanoparticles of carbon black and metallic NPs were detected in that study (Kukutschová et al., 2011). It must be said that normal driving conditions are unlikely to result in such a high temperature, which results from repeated heavy braking (Wahlström et al., 2012).

3.2 Aims

Through analysis of TEM and bulk filter samples from roadside sites heavily impacted by traffic emissions and therefore by brake wear emissions, several particle classes were identified (see Chapter 7). Brake wear is a candidate for the emission of several relevant elements from pad and disc, including Fe, Mn, Cu, Ba, Pb, S, Sb and Si. In order to explore these questions samples of emitted wear particles were collected using the nanoMOUDI and screened using TEM-X-EDS to ascertain particle morphology and composition, and ascertain what similarities there may be with particles observed in the ambient environment.

3.3 Mass-Size Distributions

3.3.1 Mass-Size Distributions: Batches 1-3

To test the necessary sampling time to collect an extractable bulk sample on the nanoMOUDI and gain experience in operating the rig, three test runs were carried out, using pressures of 1, 2 and 4 bar. These runs were originally intended to emulate previous studies in employing a 24 brake cycle, 1 minute on and 2 minutes off to allow the pads and rotor to cool between applications. However, in the first test (20 psi braking pressure, 1 min on/2 min off), the visible dust released led us to inspect the filters after only three cycles. Much material had been deposited from 560 nm upwards (stage 6-stage 1), with less material on the inlet stage (10,000 – 18,000 nm) and on the fine/ultrafine stages. The filters were reloaded for another four cycles to try and increase the loading in the nano-fraction. This was successful although the deposits on the upper stages were now very heavy. Therefore it was decided that in future tests more application cycles would be used but with the upper stages replaced at the halfway point to avoid overloading.

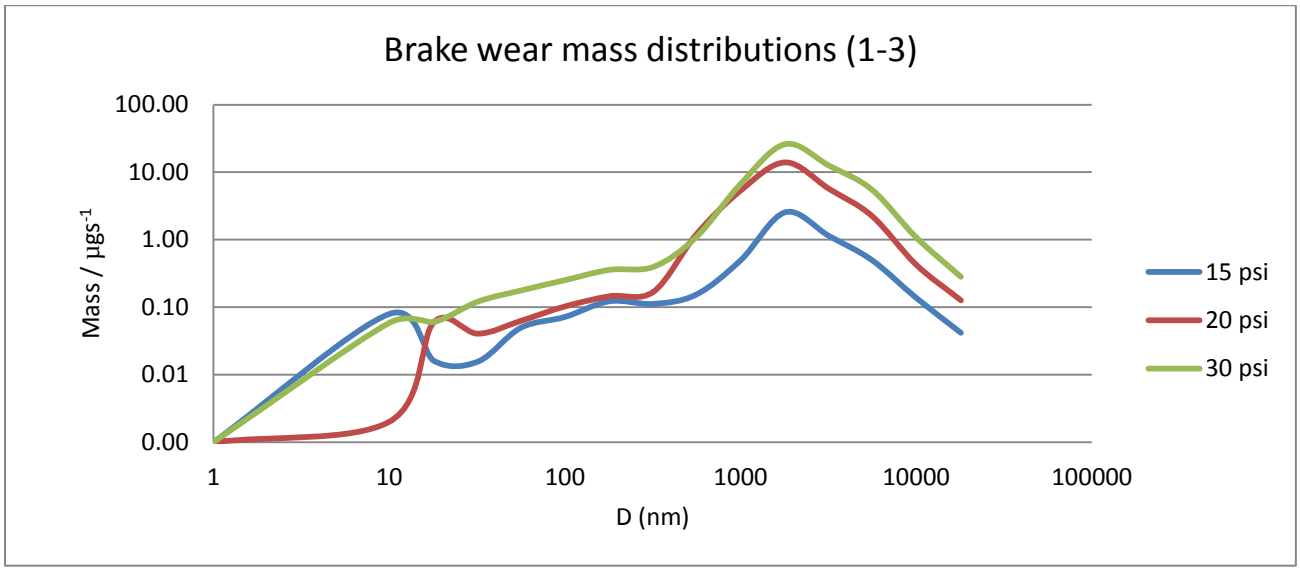

Figure 1. Mass distribution of Brake wear filters batches 1-3 (15, 20 and 30 psi application pressure).

The fraction below 320 nm D_a represented a very small proportion of total mass in the 20 psi distribution (*Figure 1*). The distribution was overwhelmingly dominated by a large mode from 560 – 3,200 nm, peaking at 1,000 – 1,800 nm.

In the second preliminary test (30 psi), the dust and odour from the rig was evident after around 30 seconds of brake application. Consequently, for the remainder of this test, a 30 second application was used. There were therefore a total of 8 cycles, 1 for 1 minute and the other 7 for 30 seconds. This generated a heavy loading of particles in a similar distribution to the previous run.

The application of a higher braking pressure (20 psi) shifted the mass distribution slightly towards the coarse end, although the peak remains in the same range. The fraction <320 nm remained a very small part of the proportion of total mass.

In the final preliminary, it was decided to test whether a lower pressure for a longer application might affect the particle distribution (15 psi at 1:30 on/1:30 off). This produced a lighter particle loading with a slightly different distribution.

The large mode peaking in the 1,000 – 1,800 size range was still evident, but the <320 nm fraction was slightly larger relative to the rest of the distribution than in the higher pressure samples (*Figure 3*). This may indicate a different balance in the formation pathways (abrasion vs volatilisation), but this would have to be confirmed by future tests.

3.3.2 Cumulative Mass Distributions Batches 1-3

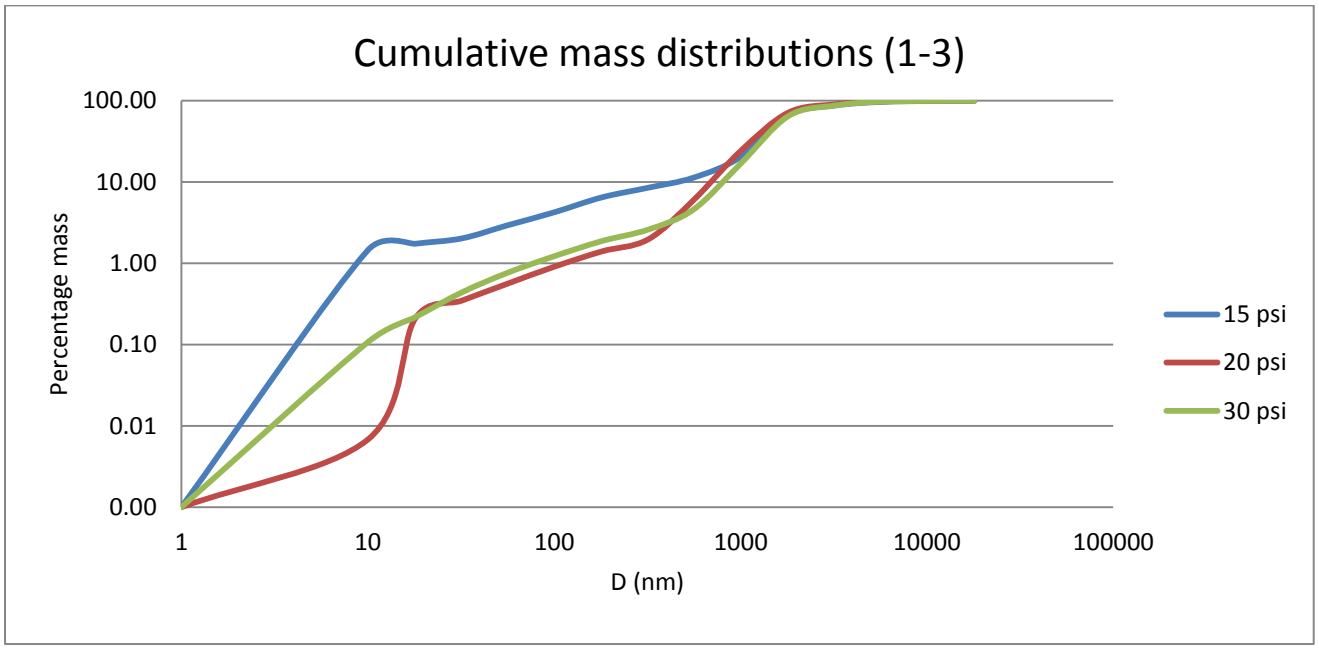

Figure 2. Cumulative mass distribution, Batches 1-3 (15, 20 and 30 psi).

The cumulative distributions were quite similar in the 20 psi and 30 psi curves but the 15 psi curve (*Figure 2*) was somewhat different demonstrating the greater proportion of total mass released in the smaller size fractions in this trial. This agreed with previous observations that ultrafine particle release from brakes is dependent on temperature rather than load and UFP release is very limited when the rotor is cold (Kukutschová et al., 2011). The longer application period, even at a lower pressure, in this trial may have favoured submicrometre particle generation.

3.3.3 Mass Size Distributions: Batches 4-6

For the subsequent tests it was decided to replace the heavily loaded coarse filters (Stages 2-6) halfway through, enabling a longer test to collect more ultrafine material. 12 cycles were now used swapping the coarse filters after the 6th cycle.

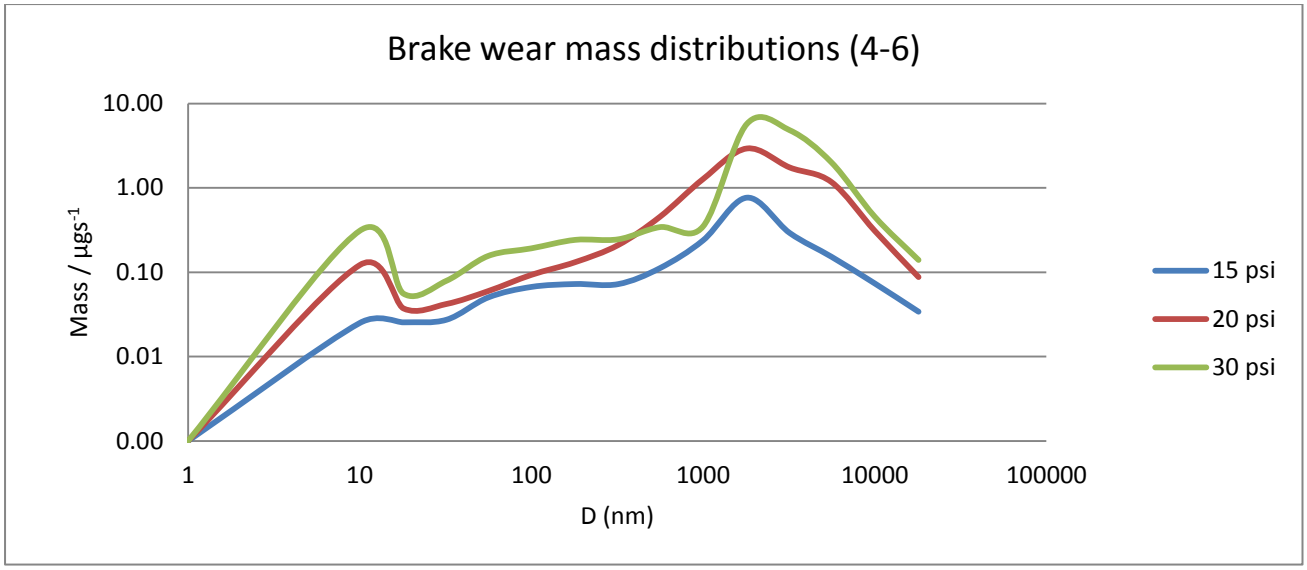

Figure 3. Mass distribution of Brake wear filters batch 4-6 (15, 20 and 30 psi).

This second group (*Figure 3*) showed that the mass distribution continued to peak in the same range (1000-1800 nm) and showed a clear trend towards an increase in coarse particle mass with increasing braking force. The cumulative distributions (*Figure 4*) make this trend more clear, but also show that the mass in the 30 psi distribution moved towards both the high and the low end compared to the 20 psi test. The increase in ultrafines may reflect higher temperatures generated by the higher braking pressure. The higher pressure may also increase the tendency for larger particles to be broken off by abrasive action at the friction interface.

3.3.4 Cumulative Mass Distributions: Batches 4-6.

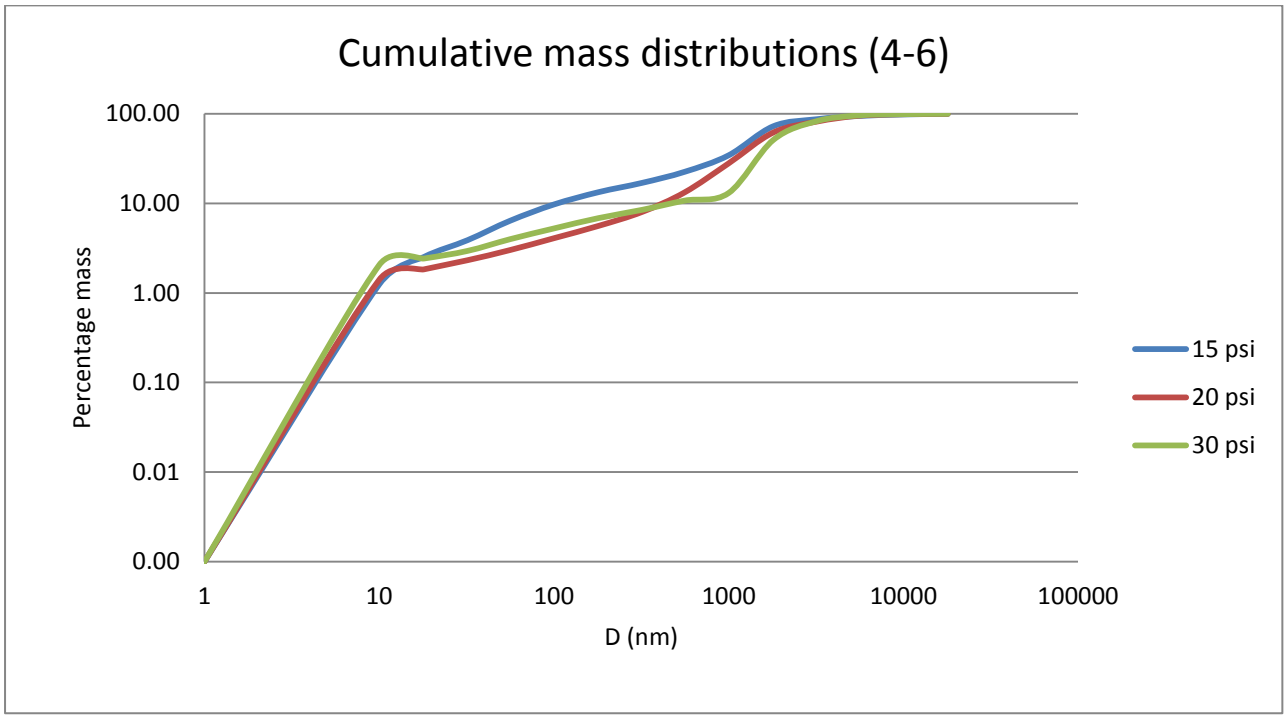

Figure 4. Cumulative mass distributions, Batches 4-6 (15, 20 and 30) psi.

3.3.5 Mass Size Distributions: Batches 7-9

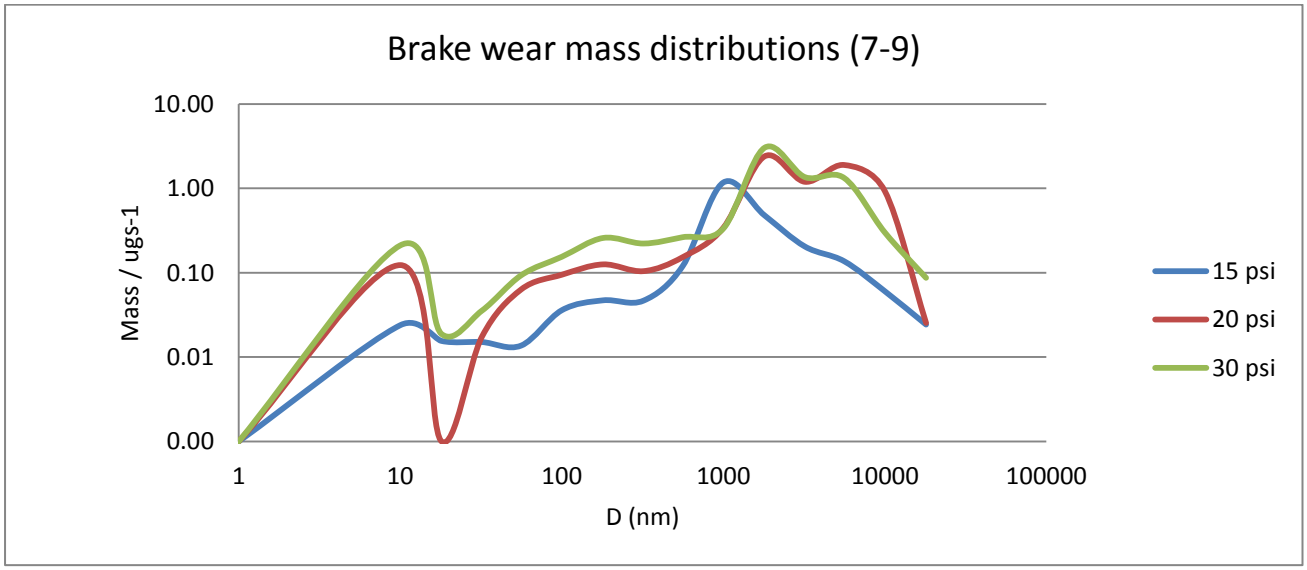

Figure 5. Mass distribution of Brake wear filters batch 7-9 (15, 20 and 30 psi application pressure).

By comparison with the earlier runs (see *Figures 1 & 3*) there were some unusual features in the distributions of batches 7-9 (*Figure 5*). Most unusual was the appearance of a bimodal distribution in batch 8 (20 psi) (see *Figure 5*), which was not observed in either of the previous tests. Also, in batch

7 (15 psi, see *Figure 5*) the mass peak was between560-1000 nm instead of 1000-1800 nm (the peak in all other samples) which leads to an unusual 'step' in the cumulative distribution (*Figure 6*).

3.3.6 Cumulative Mass Distributions: Batches 7-9.

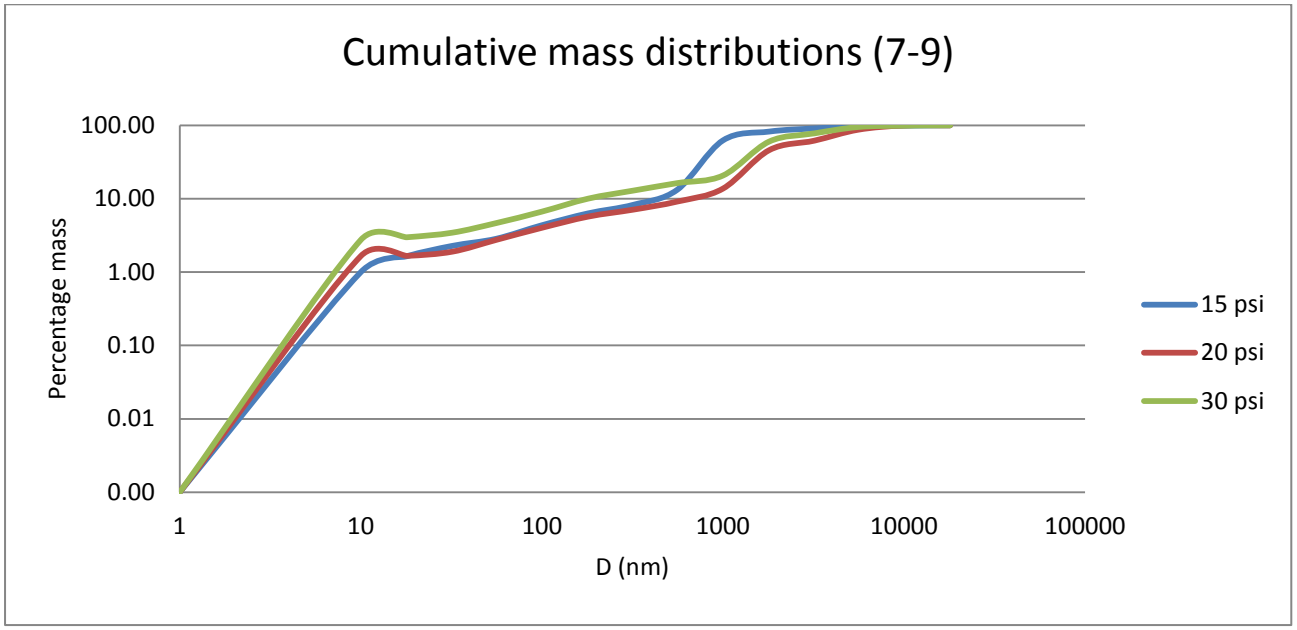

Figure 6. Cumulative distributions, batches 7-9 (15, 20 and 30 psi).

3.3.8 Summary of low-medium pressure tests

Therefore, the mass peak of suspended wear particles from the rig at braking pressures from 15-30 psi was at 1000-1800 nm, albeit with certain variations in the distributions depending on the applied force. In particular, the distribution of mass appeared to broaden at greater pressures as the tendency to shear larger particles off increased and the greater temperature promoted the release of more small particles. Both observations are consistent with previous studies. Garg et al. (2000) reported a mean mass peak of 1490 nm, but found that different linings produced a wide range of distributions peaking between 620-2490 nm (Garg et al., 2000). Adachi and Tainosho (2004) reported a peak at 1000 nm, Zhao et al. (2014) at 2000 nm and Iijima et al. (2007) observed a number peak at 1000-2000 nm, but the mass peak between 3000-6000 nm (Adachi and Tainosho, 2004; Iijima et al., 2007; Zhao et al., 2014). Mosleh et al. (2004) have reported a bimodal number distribution in which a number peak at 350 nm diameter remains unchanged regardless of the application pressure or sliding

speed, but the second mode occurs between 2,000 and 15,000 nm diameter depending on pressure and sliding speed, with higher pressure and/or speed increasing the diameter of this mode (Mosleh et al., 2004).

Differences in size distributions may reflect the differences in the wear characteristics of different pad formulations and braking forces, but differences in sampling instruments and methodologies introduce further complications which make direct comparisons difficult.

3.4 TEM-X-EDS Analysis

3.4.1 30 psi Braking pressure, Stage 7 (320-560 nm nominal cutpoints)

On 19/08/14 the Stage 7 sample from the 30 psi grid batch was examined by electron microscope. Stage 7 was chosen first for continuity with the ambient samples. The sample was heavily loaded, as shown by the overview in *figure 7* below.

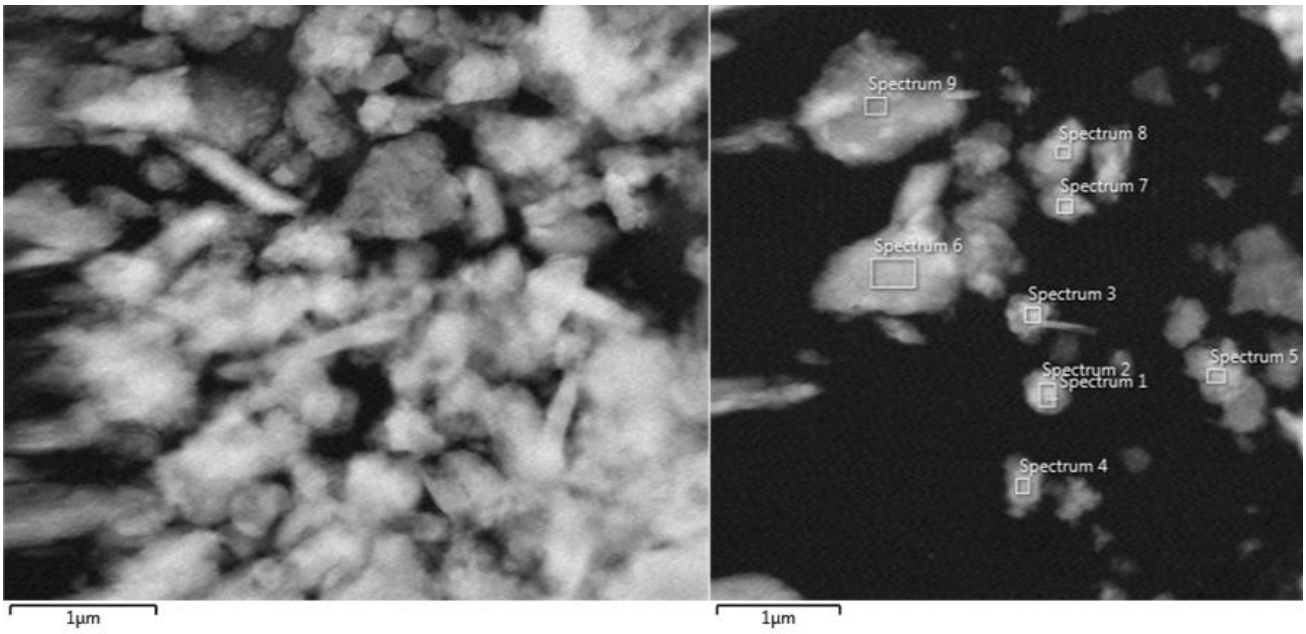

Figure 7. Overview of particles from stage 7, 30 psi test.

With C, O and Au removed from the weight data (owing to presence in grid and film materials) the dominant element was Fe, present in almost all particles. Cu, Zn, Mg, Mn and Sn were also present in many particles and all these elements have been associated with brake wear in the past. Ba was observed only once in 55 spectra from particles collected at 30 psi, though this may only be by chance. Morphology was highly irregular with a wide range of shapes and sizes present, including elongated angular particles and broad flake-like particles in excess of 1000 nm, as shown in *figure 18*. Although variable in size, many of the particles were generally larger than would be expected for the stage. These observations concerning particle size and shape agree with previous studies. In

particular, Zhao et al. (2014) reported heterogenous particles from 10-15 nm upwards including angular particles with flat surfaces and sharp edges which are indicative of being mechanically sheared off from the brake surface, along with some smaller particles formed of agglomerates of spherules indicative of a volatilisation → condensation → agglomeration pathway (Zhao et al., 2014).

Agglomerated spherules were not observed in these samples, although that does not necessarily mean that they were not produced, as the method of searching for particles by HAADF tends to produce a bias towards larger particles, which appear much brighter in the image than smaller particles.

3.4.2 30 psi Braking pressure, Stage 11 (32-56 nm nominal cutpoints)

The grid was much less heavily loaded than stage 7, but the actual particles displayed some similar characteristics. A wide range of sizes were observed with many particles exceeding the nominal 32-56 nm cut-point of this stage, showing that particle bounce from larger stages is a major problem in analysing these samples, especially as the high contrast of Fe particles in HAADF leads to the smaller particles being obscured by the larger. Elemental composition was similar to the samples collected from stage 7, with Fe the dominant element, Cu the most common minor constituent (present in most particles) and Si also appearing in some particles. Zn appeared in one particle from this session. There were generally fewer minor constituents in this sample than in stage 7. Particle shapes were highly variable, although there seem to be more aggregate-types than in stage 7.

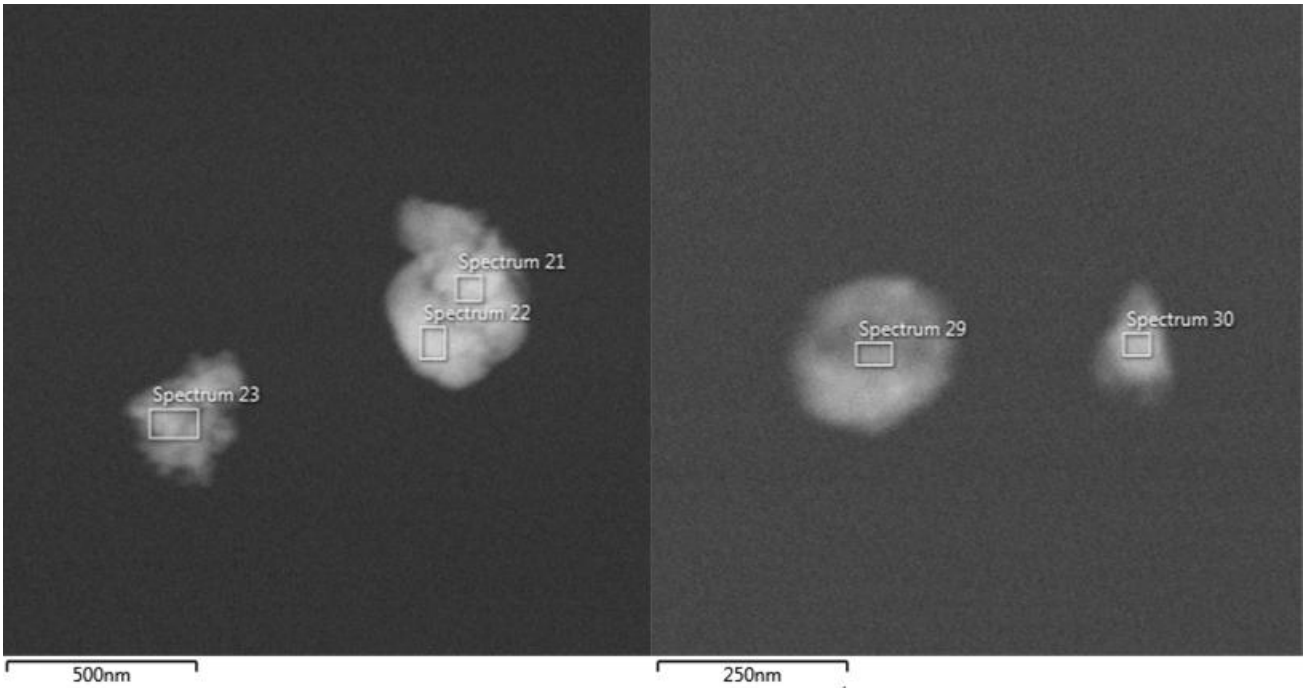

Figure 8. Particles in Stage 11, illustrating large size and irregular morphologies.

3.4.3 60 psi Braking pressure, Stage 7 (320-560 nm nominal cutpoints)

Despite the doubling of braking pressure, the particle compositions and morphologies were found to be very similar to the particles in the same stage generated at the lower pressure. Again many very large particles, above the nominal size ranges for the stage, were observed, mostly showing irregular morphologies. Fe was the most important element in all spectra usually at mass percentages in excess of 75%. The one exception is shown below in figure 20. Cu, Zn, Mn and Sn were consistently present, along with Si and S. Some particles contained Ba, Cr and Al in addition, but these made a much smaller contribution, generally <0.1% by weight.

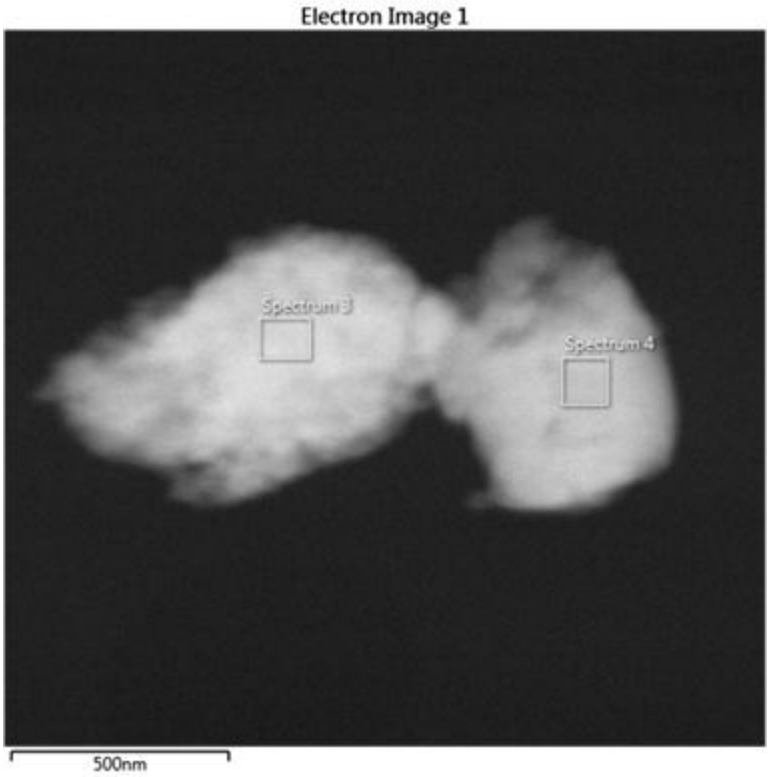

Figure 9. HAADF image of brake wear particle from Stage 7 (320-560 nm).

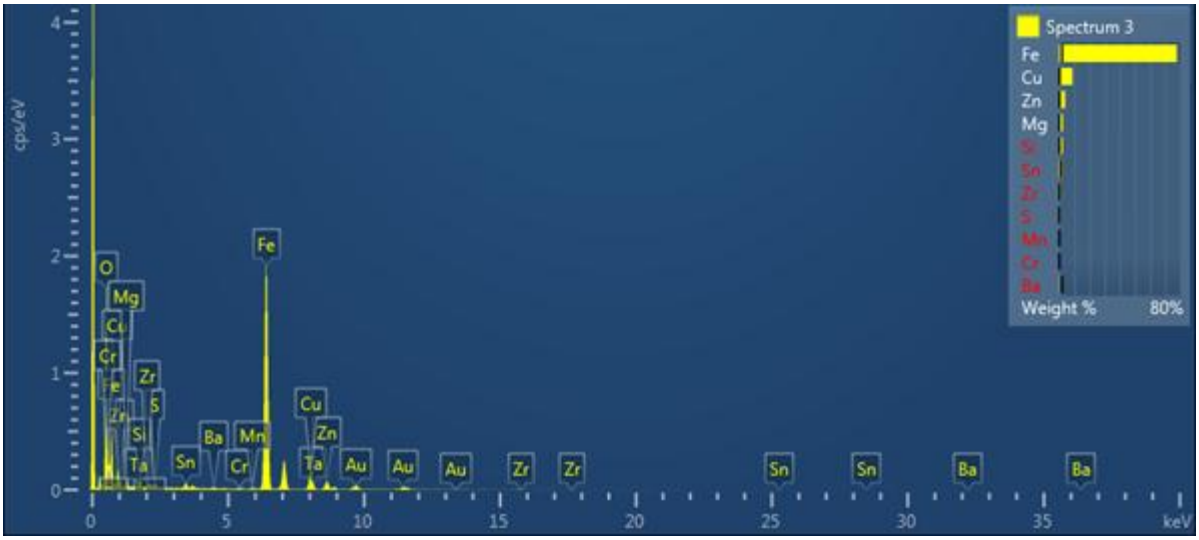

Figure 10. EDX Spectrum from area marked as Spectrum 3.

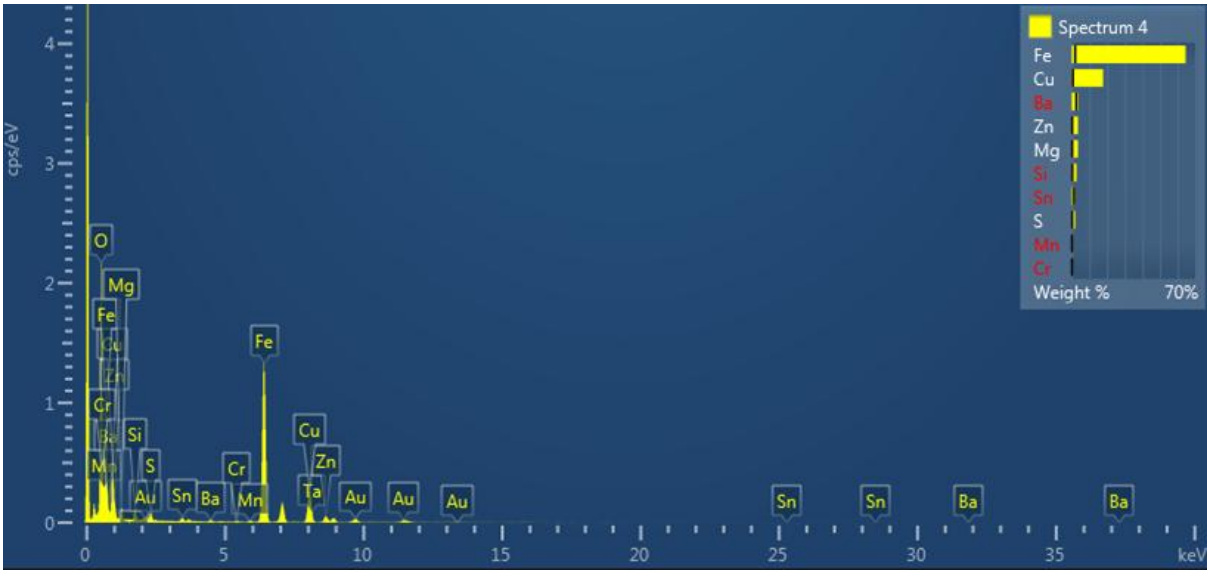

Figure 11. EDX Spectrum from area marked as Spectrum 4.

Figure 9 illustrates a large particle from stage 7 whose composition is iron-dominated with a number of typical brake pad elements as minor constituents, such as Zn, Cu and Ba. The particle in question is somewhat unusual in that one part (spectrum 3) has a significantly lower Fe content than the other (spectrum 4), in which the mass percentage of Cu and Ba is much higher.

Spectrum 3		**Spectrum 4**	
Element	**Wt%**	**Element**	**Wt%**
Mg	2.37	Mg	3.44
Si	2.24	Si	2.66
S	0.76	S	1.9
Cr	0.34	Cr	0.29
Mn	0.4	Mn	0.48
Fe	77.75	Fe	64.52
Cu	8.75	Cu	17.65
Zn	3.91	Zn	3.45
Zr	1.1		
Sn	2.12	Sn	2
Ba	0.26	Ba	3.61
Total:	*100*	*Total:*	*100*

Table 12. Elemental composition of particle in Figure 9.

3.4.4 60 psi Braking pressure, Stage 12 (18-32 nm nominal cutpoints)

Particle composition and morphology were remarkably similar through the stages. The similarity in appearance between particles generated at 30 psi and 60 psi application pressure was also striking. Examination of stage 12 (32-56 nm) from the 60 psi sample showed similar characteristics and large particle sizes. Very small particles were not common, with much material being far larger than the expected cutpoints. These features are clearly illustrated by *figure 23* below, showing two large Fe particles. It was not possible to identify droplet-type particles which may have come from condensation of volatilised material in samples collected using the nanoMOUDI even in the finest stages, perhaps due to the presence of large particles due to particle bounce.

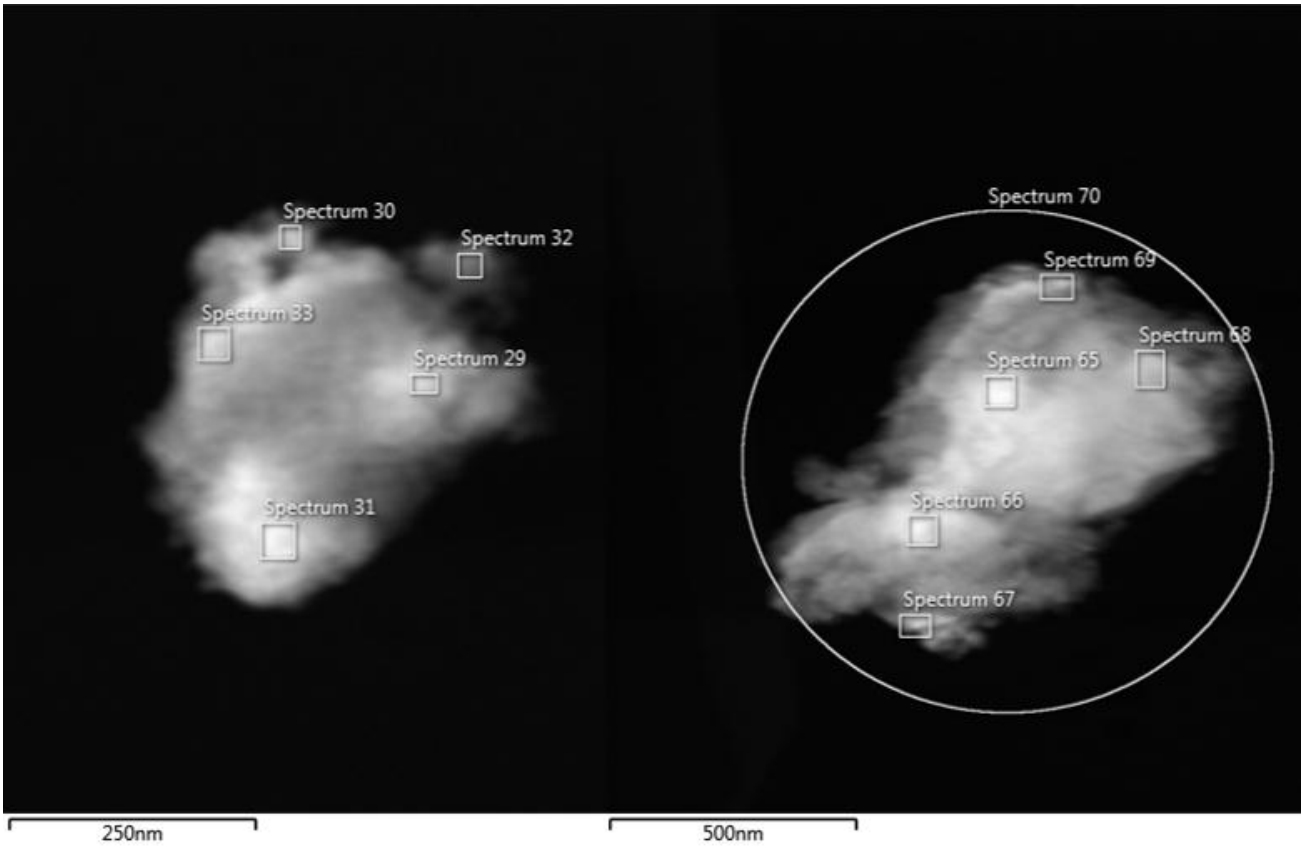

Figure 12. Outsized Fe particles collected in stage 12 (18-32 nm nominal) from 60 psi test.

Element	Total Contribution %	Stdev	N	Contribution % (30 psi)	Stdev	N	Contribution % (60 psi)	Stdev	N
Fe	79.208	10.771	82	85.479	8.745	82	68.081	10.229	82
Cu	10.735	11.164	76	7.941	6.532	76	15.693	15.070	76
Si	3.905	9.973	57	2.131	3.739	57	7.052	13.076	57
Sn	2.092	15.519	40	2.204	27.253	40	1.892	1.089	31
Zn	1.457	0.851	50	0.994	0.704	50	2.279	0.963	40
Mg	1.110	1.168	31	0.571	1.401	31	2.068	0.942	50
S	0.759	0.557	42	0.421	0.466	42	1.357	0.600	42
Mn	0.313	0.319	36	0.232	0.409	36	0.456	0.141	14
Ba	0.242	1.072	14	0.025		14	0.626	1.116	36
Cr	0.106	0.827	17	0.017	0.042	17	0.264	0.884	17
Zr	0.054	0.340	8				0.149	0.340	8
Al	0.022	1.146	2				0.060	1.146	2
Ca	0.004	0.021	4				0.010	0.021	4
K	0.001		1				0.002		1
Cl	0.001		1				0.002		1
Cu:Fe %	13.553			9.29			23.050		
Particle Size/nm	174.162	455.493		204.170	332.063		120.922	674.481	
Agglomerate Size/nm	323.095	370.660		351.408	289.893		251.381	432.362	
Spectra = 86				***Spectra = 55***			***Spectra = 31***		

Table 13. Elemental contributions, particles collected in stage 7 and below.

Regardless of braking pressure Fe was the dominant wear element. Cu also made an important contribution. Many of the minor elements have already been reported in brake wear, including Ba which is often regarded as a useful tracer in the environment. The Ba contribution in these samples was quite small. One frequently reported element which was not detected in this pad is Sb. Sb was also absent in measurements made by Zhao et al. (2014) who therefore argued that it may not be a good environmental tracer (Zhao et al., 2014). Although Sb_2S_3, which oxidises to Sb_2O_3, has been used as a solid lubricant in brake linings in the past this is being discontinued owing to its toxicity, so our results may also indicate that with more modern materials, Sb might be less useful as a tracer for brake dust. However, it does not follow that Sb is not useful as a tracer for the vehicle fleet as a whole, as many pads do still contain Sb. It may become less useful as the fleet composition changes over time.

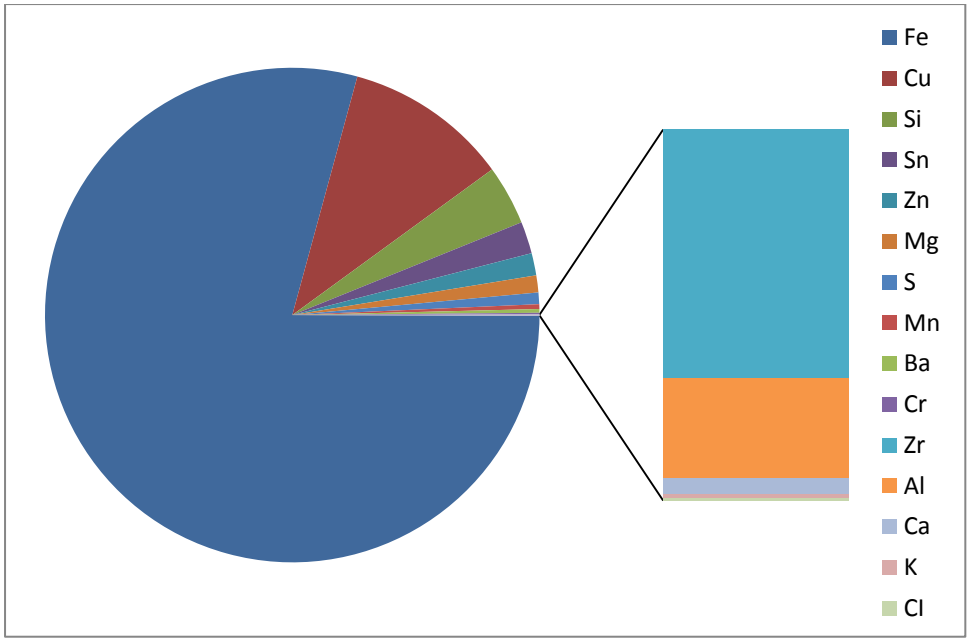

Figure 13. Pie chart of total elemental contributions (30 psi and 60 psi data together).

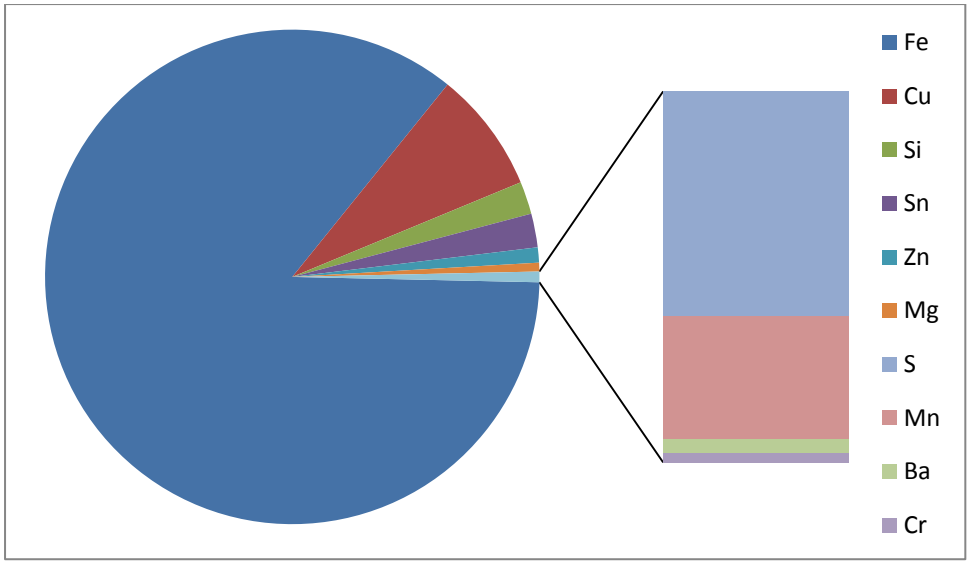

Figure 14. Pie chart of total elemental contributions (30 psi data).

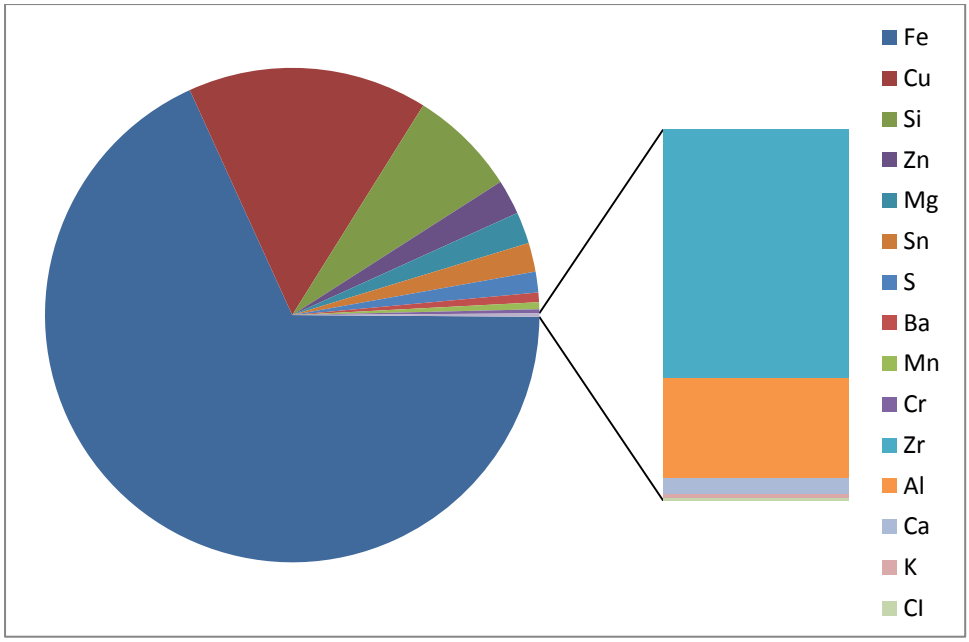

Figure 15. Pie chart of total elemental contributions (60 psi data).

From the charts illustrated in *Figures 13-15*, it can be seen that the Fe mass percentage was reduced at the higher braking pressure and the contribution of other elements, especially Cu and Si, much increased. There were also more minor constituents, including Al, Ca and K, which are not seen in the 30 psi set. However, plotting Fe and Cu contents and the Cu:Fe percentage ratio against particle size and agglomerate size yielded no clear trend. Fe was essentially constant with both particle and agglomerate sizes (*Figure 16*). Cu may exhibit a slight tendency to decrease with increasing particle and agglomerate size (*Figure 16*) but the correlation coefficients were so weak that no firm conclusion could be drawn from the available data.

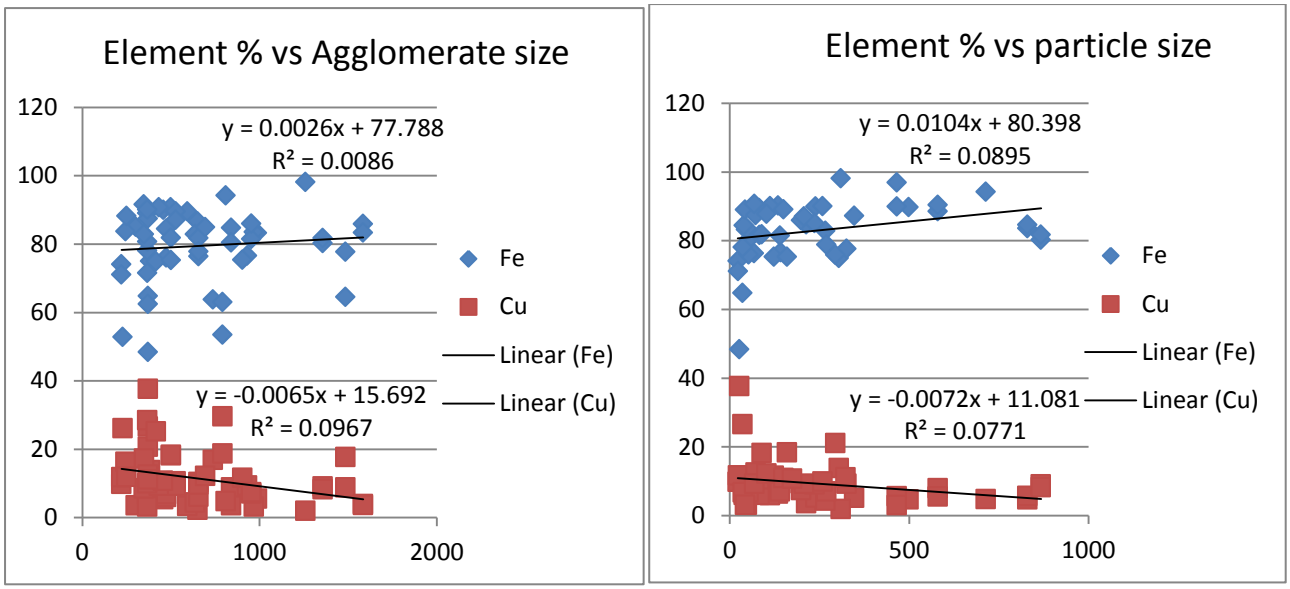

Figure 16. Fe and Cu mass percentages (all stages) vs agglomerate (left) and primary particle (right) sizes.

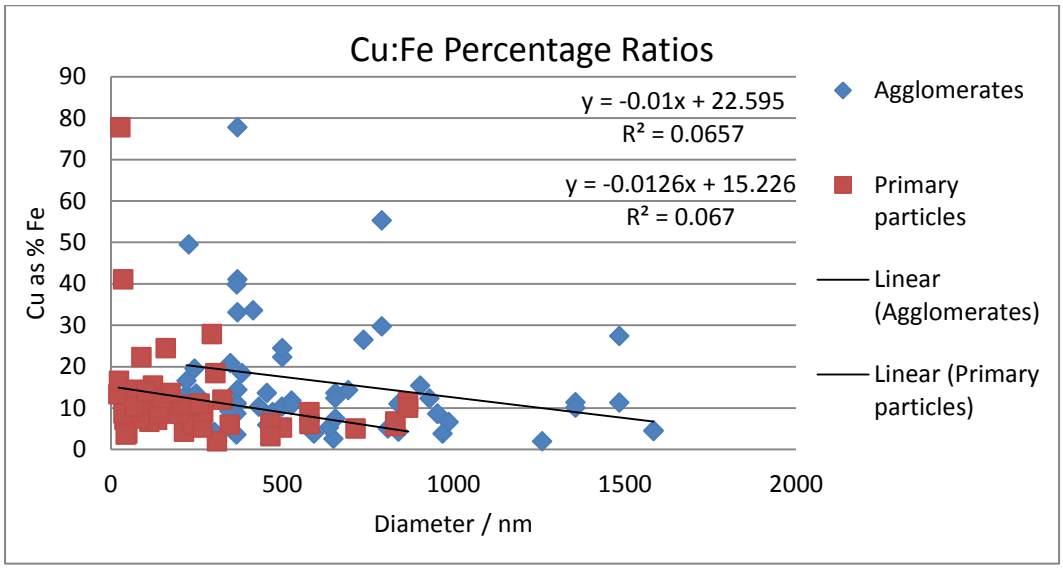

Figure 17. Cu:Fe % ratio vs particle and agglomerate size (all stages, both pressures combined).

With 30 psi and 60 psi datasets combined, the Cu:Fe percentage = 13.553, which is quite high for submicron particles. If the two sets are separated, the percentage ratio is 9.29 at 30 psi and 23.05 at 60 psi.

Plotting the ratio for each spectrum against the particle size and agglomerate size (*Figure 17*), the picture is not very clear. There are a number of outliers in which the ratio is very high – in primary particles these are both in very small particles. Since there are a small number of outliers in the

corresponding agglomerate plot with high Cu:Fe percentages, this may imply that Cu:Fe ratios can be high in small particles, but these then agglomerate with larger ones and the relative abundance of the two elements may not be the same in all primary particles in an agglomerate. More data would definitely be required to confirm such a hypothesis, but it might offer an explanation for the elevated occurrence of Cu relative to Fe which we have observed in the pseudo-ultrafine fraction of the roadside filter samples from Barcelona.

3.5 Thermal Degradation Experiments

Samples from a UK-sourced brake pad were chiselled from the backing and broken into fragments to allow analysis. Samples were heated for three hours to 200°C, 300°C and 600°C in a tube furnace. HEPA-filtered compressed air was used. The gas flow passed through the furnace with the pad fragments inside, and then over a TEM grid held in a metal filter holder, then finally through a Whatman QM/A 25 mm filter to collect a bulk sample. The pad material was subjected to X-ray fluorescence analysis before heating. Each of the heated samples was also analysed by the same method and these data are presented below.

3.5.1 X-Ray Fluorescence data

	Fe%	Ba%	Ca%	Si%	Al%	S%	Mg%	Sb%	K%	Mn%	Zn%	Sr%	Cl%	As % total
1	42.57	8.69	7.50	2.58	1.05	0.89	0.81	0.38	0.37	0.26	0.12	0.07		65.29
2	38.59	7.67	6.53	3.63	1.65	1.22	1.11	0.54	0.53	0.21	0.18	0.07	0.11	62.04
Mean	40.58	8.18	7.02	3.11	1.35	1.06	0.96	0.46	0.45	0.24	0.15	0.07	0.06	63.67

Table 14. XRF data, pre-heating.

	Fe%	Ba%	Mg%	Si%	Ca%	Sb%	Al%	S%	Mn%	K%	Cl%	Zn%	P%	Cu%	Sr%	As % total
1	50.66	4.72	2.07	1.58	1.33	1.06	0.67	0.64	0.22	0.19	0.18	0.10	0.06	0.04	0.03	63.55
2	39.19	4.05	0.90	0.63	1.13	0.73	0.27	0.50	0.18		0.14	0.10	0.04		0.02	47.88
Mean	44.93	4.39	1.49	1.11	1.2	0.90	0.47	0.57	0.20	0.10	0.16	0.10	0.05	0.02	0.03	55.72

Table 15. XRF data, 3hrs at 200°C

	Fe%	Ba%	Mg%	Si%	Ca%	Sb%	S%	Al%	Mn%	K%	Zn%	Cl%	Ti%	Cu%	Sr%	As % total
1	56.61	6.73	5.19	1.84	1.76	1.14	0.86	0.81	0.22	0.18	0.15	0.07	0.05	0.05	0.04	75.7
2	55.01	5.52	4.26	2.87	1.97	1.16	0.85	1	0.21	0.21	0.15	0.17	0.06	0.04	0.03	73.51
Mean	55.81	6.13	4.73	2.36	1.87	1.15	0.86	0.91	0.22	0.20	0.15	0.12	0.06	0.05	0.04	74.61

Table 16. XRF data, 3hrs at 300°C

	Fe%	Ba%	Mg%	Si%	Ca%	S%	Sb%	Al%	Na%	K%	Mn%	Zn%	Cl%	Cu%	Sr%	As%	Ti%	As % Total
1	57.47	6.26	4.63	2.70	2.06	1.32	1.09	1.00	0.52	0.36	0.23	0.19	0.09	0.06	0.04	0.02	0.00	78.04
2	47.04	9.21	1.99	3.53	8.19	1.65	0.82	1.57	0.00	0.40	0.25	0.28	0.10	0.00	0.07	0.00	0.13	75.23
Mean	52.26	7.74	3.31	3.12	5.13	1.49	0.96	1.29	0.26	0.38	0.24	0.24	0.10	0.03	0.06	0.01	0.07	76.64

Table 17. XRF data, 3hrs at 600°C

	Fe%	Ba%	Mg%	Si%	Ca%	Sb%	Al%	S%	Na%	K%	Mn%	Zn%	P%	Sr%	Sc%	Cr%	As % Total
1	62.66	2.91	2.87	1.85	1.19	1.00	0.71	0.61	0.46	0.32	0.27	0.12	0.07	0.02	0.01	0.00	75.07
2	61.40	4.61	4.29	2.20	1.46	1.27	0.88	1.42	0.78	0.44	0.27	0.30	0.05	0.03	0.00	0.03	79.43
Mean	62.03	3.76	3.58	2.03	1.33	1.14	0.80	1.02	0.62	0.38	0.27	0.21	0.06	0.03	0.01	0.02	77.25

Table 18. XRF data, fragment went through all 3 heating processes.

Elemental composition varied through the pad (particularly so in the minor constituents), especially in the heated samples where differences in fragment size may have had an influence (through differences in the exposed surface area). However, some trends can be discerned.

The percentage of pad material mass accounted for by elements from Na upwards increased sharply (from 55-60% up to around 75%) after 3 hrs heating at 300°C (*Table 16).* There was not such a pronounced difference between this run and the 600°C run (*Table 17*) as between 200°C (*Table 15*) and 300°C, although the total mass percentage is slightly higher. This would suggest that the components formed from lighter elements such as C, O and N were being lost from the pad at temperatures around 300°C and over, and that the bulk of this process occured before the temperature reaches 600°C. This concurred with Kukutschová's observation that there is a release of ultrafine particles at around 300°C (Kukutschová et al., 2011). Similarly, Sanders et al. (2003) reported that under the conditions of the AMS test number-weighted distributions are dominated by particles below 300 nm D_a, which they attributed to heat release of organic components followed by nucleation. This test employs quite harsh braking conditions (10 stops from 100 kmh^{-1}, deceleration 7.9 ms^{-2}) leading to surface T reaching 500°C-600°C. They also observed that this process was not apparent under the conditions of the UPS test (24 stop cycle from 90 kmh^{-1} at deceleration < 1.6 ms^{-2}), in which brake temperatures only reach 200°C (Sanders et al., 2003).

Analysis of the 200°C TEM grid revealed relatively few particles, some of which were very large, illustrating angular particle morphologies untypical of nucleation processes which therefore may not have come from the pad material (see *Figure 33*). Ca appeared in 11 spectra from 4 different particles. Apart from Si, no other element appeared in more than two spectra. The presence of Ca is interesting in the light of the XRF data, which showed a substantial drop in the Ca content of the pad between the pre-heating data (*Table 14*) and the 200°C sample. Fe appeared in two spectra from two particles.

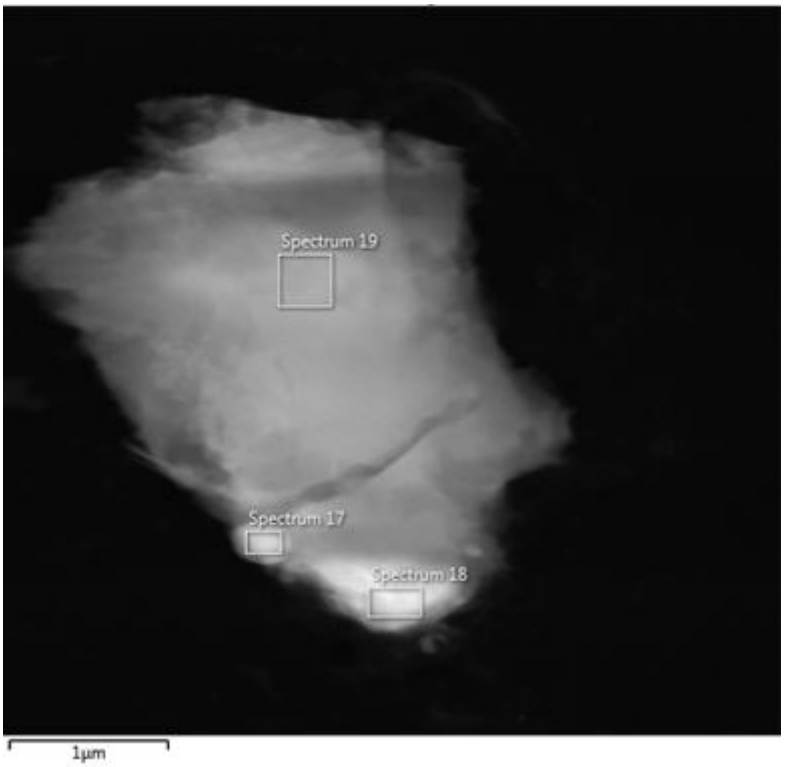

Figure 18. Large Ca particle from 200°C sample. All three sampled areas show 100% Ca by weight, discounting C, O and Au.

TEM analysis of the 300°C sample demonstrated that there was a major change in the types of particles detected. In this sample the grid had a large number of small (generally <200 nm) agglomerates of nanoparticles. These were similar to the combustion-derived soot agglomerates prevalent in the ambient samples and diesel exhaust although were not as large, and not formed into such complex structures, exhibiting less branching in the chains (see *figure 19*).

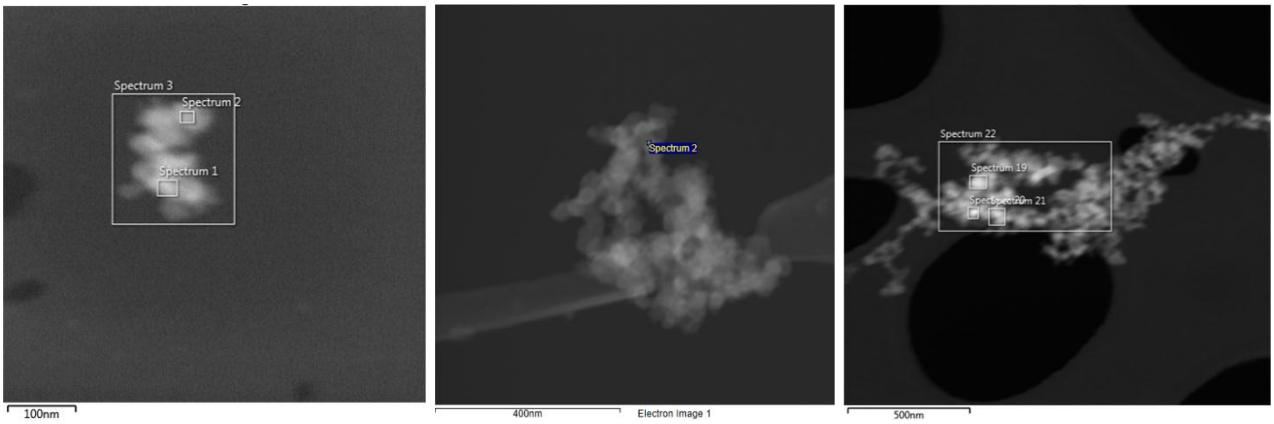

Figures 19. Volatilised brake particle, ambient carbonaceous soot, diesel soot from tailpipe.

In terms of elemental composition, Si was common, appearing in 14 spectra from 6 particles. In 12 of these spectra it was the only element except for grid elements detected (C, O and Au are removed from weight data as these are associated with the grid and film). Ca appeared in 5 spectra from 4 particles and Al in 2 from 1. An interesting development in this sample was the appearance of Hg in several spectra (see *Figure 20*). Since this element was below detection limit in the XRF analysis it is not clear whether this came from the pad – if so, this would be a relevant health concern if Hg was even a minor component of a large number of pads in the vehicle fleet.

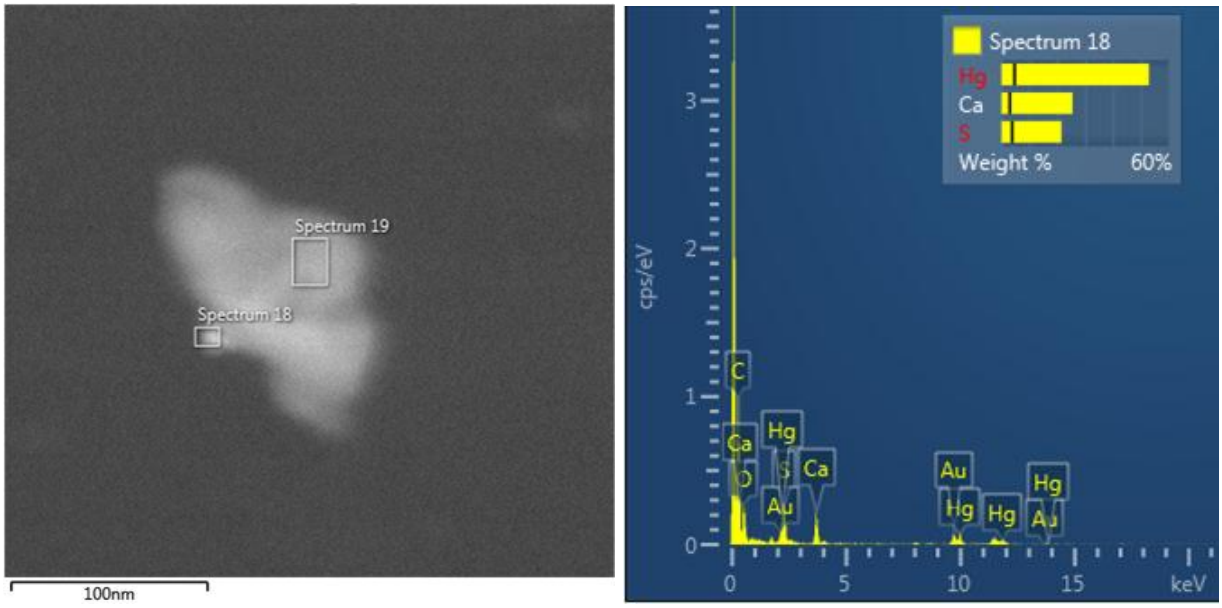

Figure 20. Hg particle and spectrum from 300°C brake pad thermal degradation test.

The mass collected over two three hour periods at each temperature is shown in the following table. The filter QMA1 was collected from a 3 hr blank run at 600°C, performed to ensure there was no volatile material in the tube furnace which would affect the results. This filter collected a lot of material, which suggested it was right to burn off any potential contaminants in the tube before starting the actual experimental runs. Very little material was collected at 200°C (within the variation in the unused filters (QMA4 &QMA5). The collected mass increases with heating temperature.

Sample	Gain (mg)
QMA1	0.530
QMA2 (200°C)	0.003
QMA3 (300°C)	0.021
QMA4 (600°C)	0.382
QMA5 (unused)	0.001
QMA6 (unused)	-0.011

Table 19. Mass gain in thermal analysis filter papers.

The chemical data from the filters offered very little useful information. The blank levels were very high, which could reflect the difficulty in preparing the filters for digestion which evidently introduced handling contamination. Al and Fe were worst affected which is typical of results throughout the ICP-MS analyses. No clear pattern of concentration vs temperature is discernible.

Sample	Al	V	Fe	Ni	Cu	Zn	Sr	Sb	Ba	Ce
QMA-1 (pretest)	14.89	< 0.2	159.1	6.06	5.70	2.23	0.31	7.43	1.40	< 0.1
QMA-2 (200C)	23.48	1.90	72.78	2.69	0.87	1.53	1.14	6.07	4.00	< 0.1
QMA-3 (300C)	19.74	< 0.2	93.82	4.31	1.09	0.98	0.43	5.59	6.49	< 0.1
QMA-4 (600C)	17.03	< 0.2	156.2	3.12	1.82	1.60	0.34	4.69	5.34	< 0.1
QMA-5 (blk)	24.14	0.49	785.5	2.31	1.20	1.35	0.34	< 0.1	6.56	< 0.1
QMA-6 (blk)	24.22	< 0.2	264.4	1.31	1.11	1.35	0.16	< 0.1	0.63	< 0.1

Table 20. Elemental Concentrations in thermal analysis filters ($ngcm^{-3}$).

3.6 Bulk Chemical Composition of Brake Wear Particles

Five batches of nanoMOUDI filter samples were digested in an $HCl/HNO_3/H_2O$ solution in the same way as the ambient samples in order to be analysed by ICP-MS to determine bulk chemical composition. These samples consisted of one batch each at 15 psi, 20 psi, 30 psi, 45 psi and 60 psi in order to examine whether composition changed with braking forces.

3.6.1 Elemental Mass Distributions

The general trend of the ICP-MS data was that the chemical distributions appeared to follow the total mass distributions closely. This was true of all the most common elements in the pad – Fe, Cu, Ba, Zn and Ni. Sb and Sr had lower concentrations but roughly similar mass distributions. Only Al, where there were large concentrations in the afterfilter, was slightly different. Iijima et al. (2007) also reported that the main pad elements in their tests (Fe, Ba, Ti, Cu, Zn and Sb) had very similar mass distributions to the total mass of the collected abrasion dusts (Iijima et al., 2007). This study also reported that Fe was found in large quantities in all size ranges, but associated this with the cast-iron disk rather than the pad.

There is a minor inconsistency in the data, in that the 20 psi sample did not give results that were fully consistent with the 15 psi and 30 psi samples; it might be expected that its characteristics in terms of chemical distributions and elemental ratios would lie between the others, but this was not the case. This may have been caused by the minor differences in experimental procedure between this sample and the others.

Fe was the most abundant element by at least an order of magnitude. Showing concentration per unit application time demonstrates that increasing pressure from 15 psi (barely exceeding atmospheric pressure) to 20 psi and then to 30 psi caused a large increase in concentration. Fe paralleled Cu and Ba very closely in these samples showing very similar distributions to those elements. The mass in

the size range 320-1000 nm was reduced at 60 psi compared to Fe at the lower pressures, although the 1-10 nm size range was largest in the 60 psi sample. The submicron contribution was slightly larger for Fe than Ba or Cu, including a very slight peak at 100-180 nm.

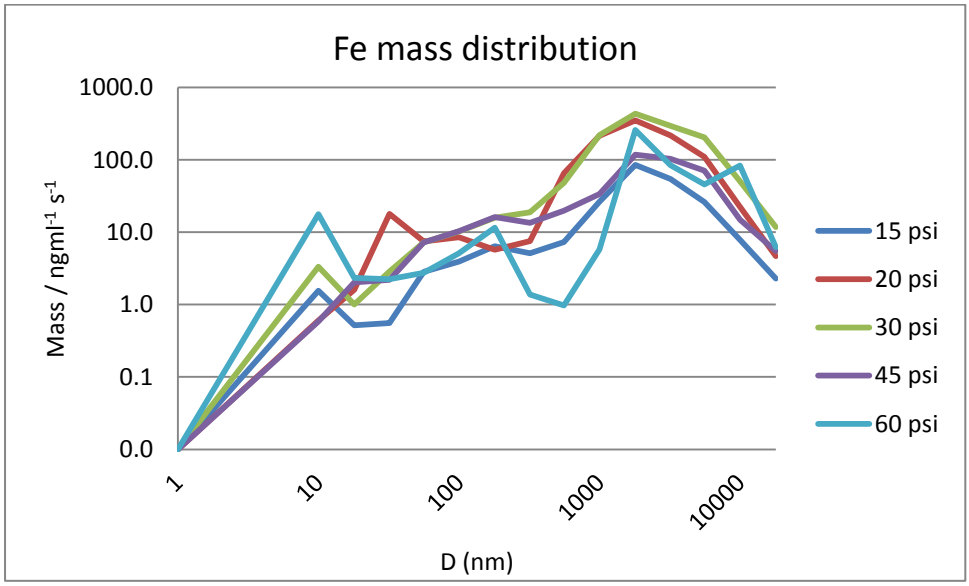

Figure 21. Fe mass-size distributions per unit application time.

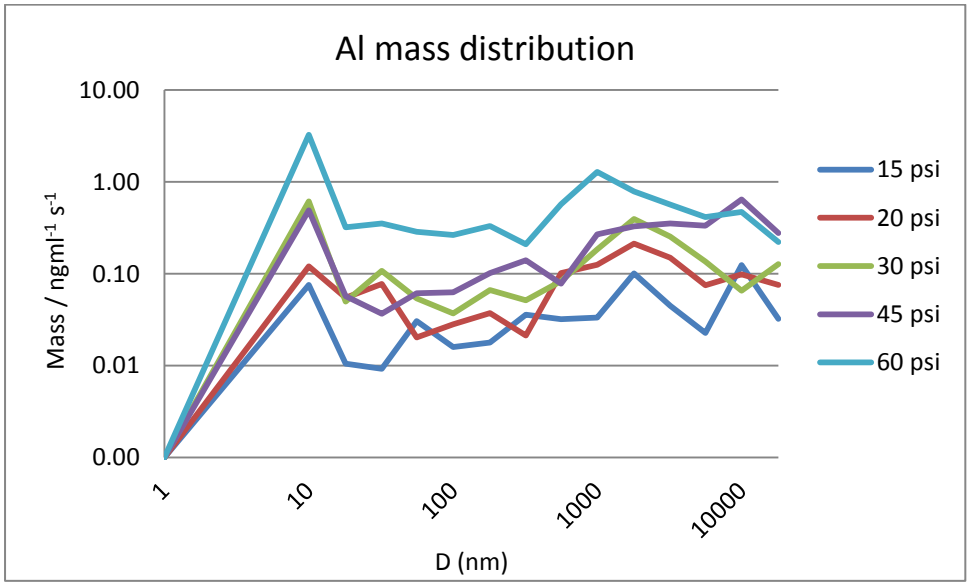

Figure 22. Al mass-size distributions per unit application time.

Concentrations of Al in bulk emitted ultrafine particles increased with braking pressure (*Figure 22*). The 60 psi sample suggested that the mass peak also shifted to a smaller size range at high pressure

compared to 15-30 psi, however, the 45 psi sample did not support this interpretation. The main feature of the distributions was the increased size of the peak in the finest particles (<10 nm) with increased braking pressure.

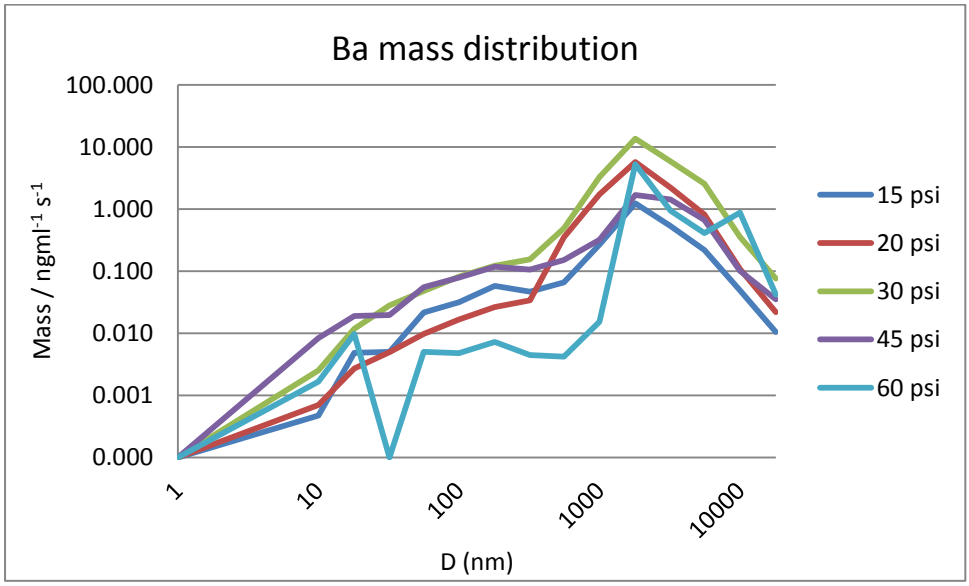

Figure 23. Ba mass-size distributions per unit application time.

For Ba (*Figure 23*), there was a shift towards larger particles (in the 1800-5600 nm range) at 45 psi compared to the lower pressures, however at 60 psi the main feature was the total dominance of the normal 1000-1800 nm mass peak, with submicron Ba almost absent and a very small peak above 10000 nm.

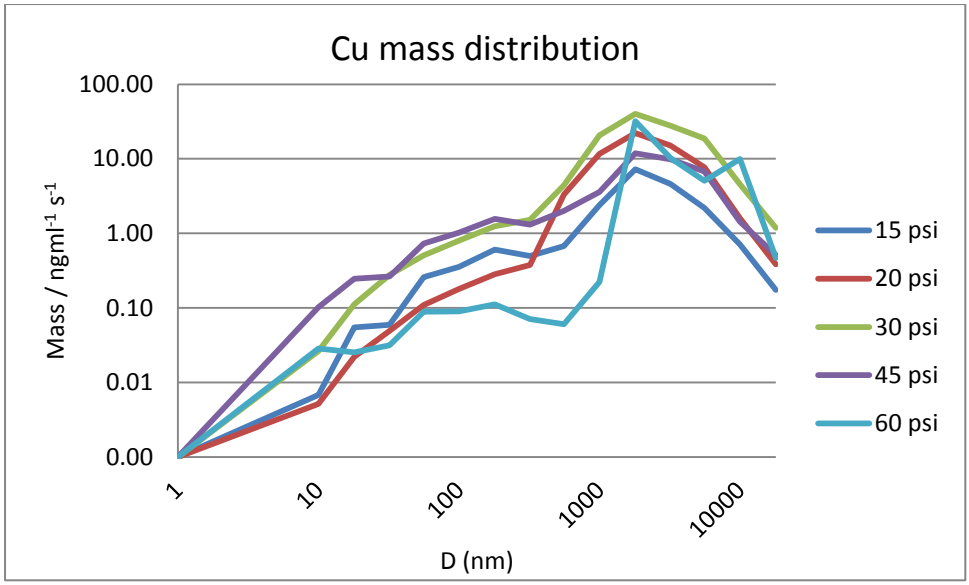

Figure 24. Cu mass-size distributions per unit application time.

Cu exhibited some similarity to Ba in these distributions (*Figure 24*). The 45 psi Cu distribution showed a slightly contribution below 560 nm than the lower pressures, but also proportionally more Cu in the 1800-5600 nm size range. At 60 psi the submicron fraction was extremely small, but a small peak was seen between 5600-10000 nm.

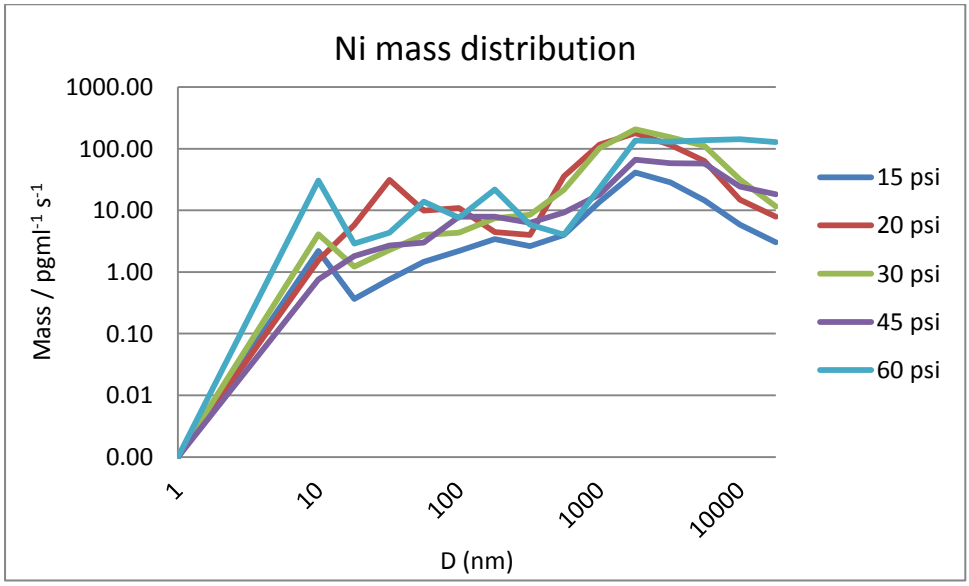

Figure 25. Ni mass-size distributions per unit application time.

Ni distributions were considerably different to Cu, Ba and Fe above 30 psi (*Figure 25*) and generally changed little with pressure. Masses were extremely low. At the lower pressures (15-30 psi), Ni exhibited similar characteristics to those elements, but in the high pressure samples a broadening of the main mass mode above 1000 nm was observed, resulting in a flat distribution from 1 µm to 18 µm in the 60 psi sample.

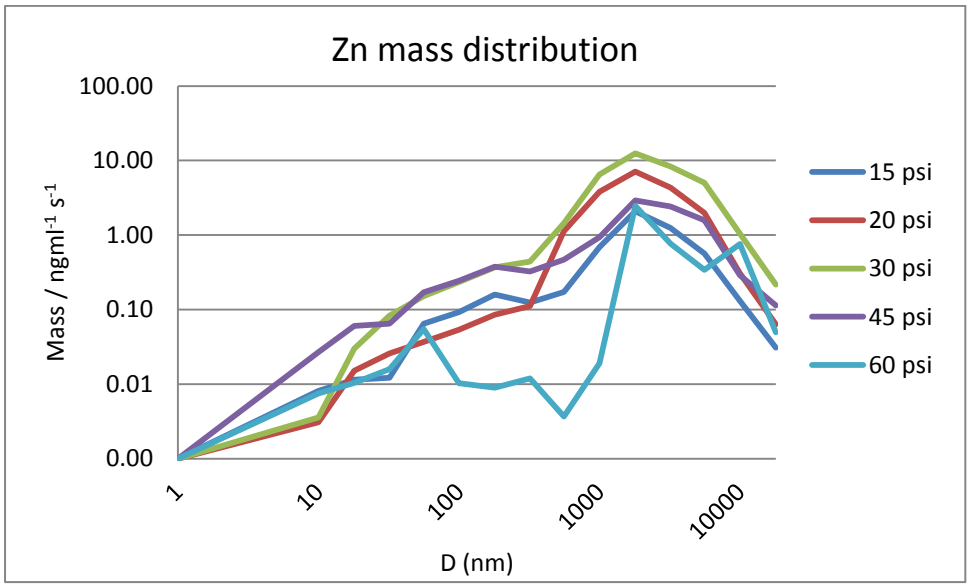

Figure 26. Zn mass-size distributions per unit application time.

The pattern of Zn distribution was very similar to Ba, Cu and especially to Fe. The 60 psi distribution above 320 nm closely follows Fe, however, the ultrafine peak is somewhat different.

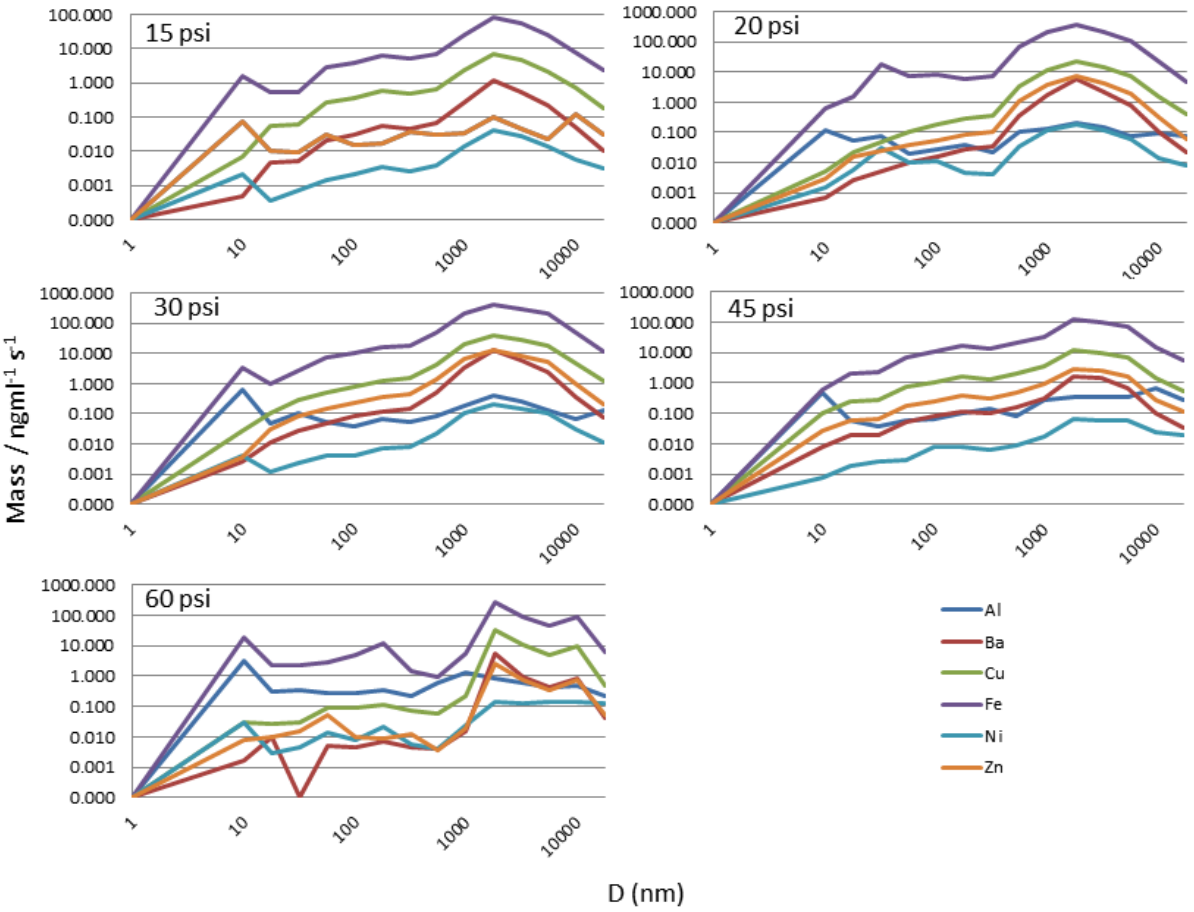

Figure 27. Elemental mass-size distributions per unit application time at five application pressures.All elements in ng ml^{-1} s^{-1} except Ni in pg ml^{-1} s^{-1}.

This could be interpreted to show that Ba, Cu, Fe and Zn were released into the suspended particulate by similar processes, with the caveat that the mass percentages showed some variations which are less significant than the total mass release. However, Al and Ni appeared to show important differences to the elements listed above especially at higher pressures, when Al had no coarse mode but a very large nanoparticle contribution.

3.6.2 Elements as percentages of total PM mass

The lack of reliable total mass concentration data owing to an unknown problem with the microbalance during the pre-sampling weighing (which only became evident in retrospect) was a considerable handicap in analysing the 45 psi and 60 psi sample sets in a manner comparable to the

low pressure tests. Consequently it was only possible for these samples to compare the mass-size distributions for each element to the low pressure samples.

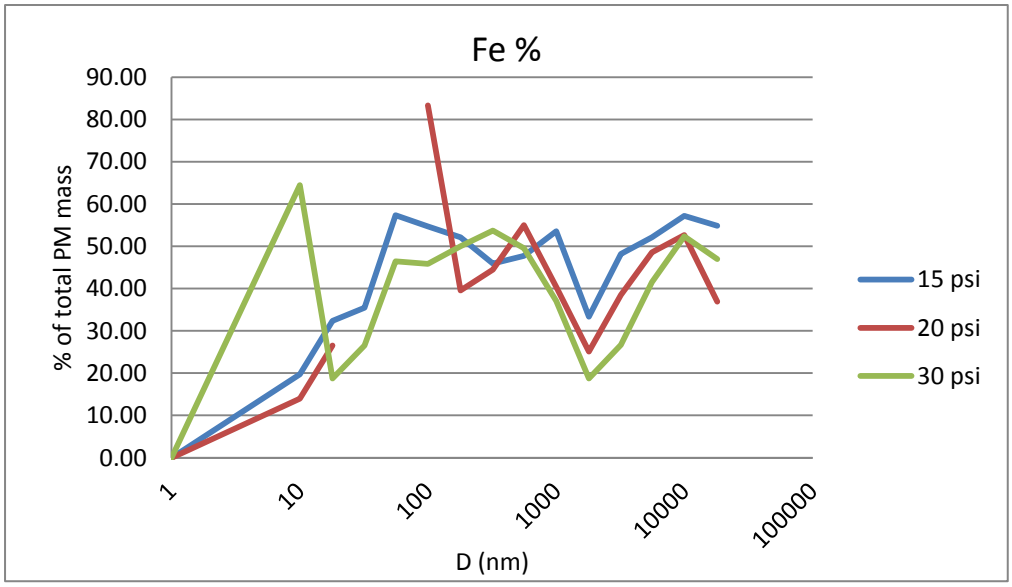

Figure 28. Fe as percentage of total PM mass at 15,20, and 30 psi application pressure.

Fe represented a smaller proportion of the total mass of released material in particles <50 nm except at 30 psi, in which sample there was a high proportion of Fe in the final stage (*Figure 28*). There was also a small drop in the Fe:PM percentage at 1000-1800 nm (the mass peak) where the Ba:PM_{total} and Ba:Fe percentages are highest.

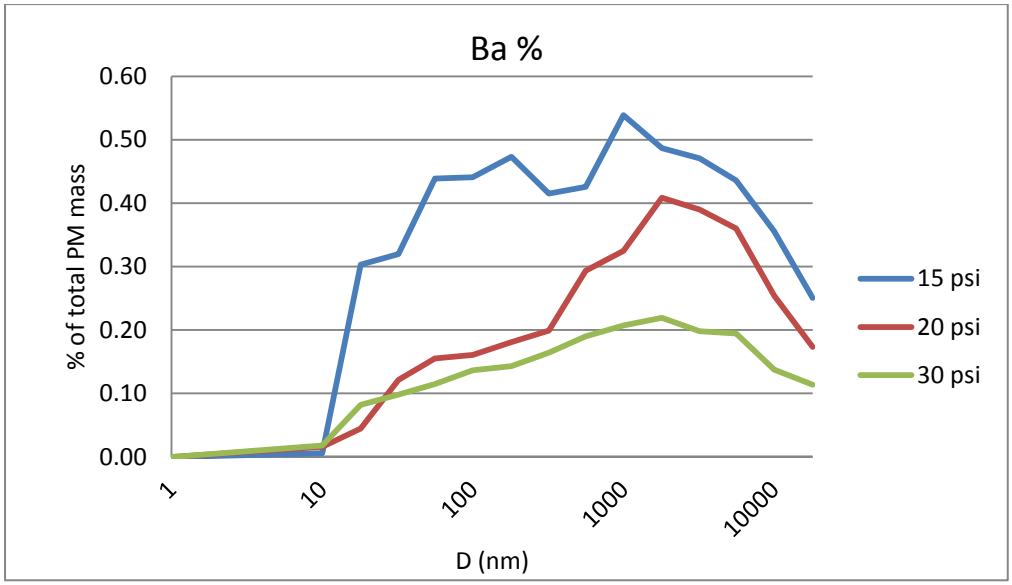

Figure 29. Ba as percentage of total PM mass at 15,20, and 30 psi application pressure.

In the case of Ba (*figure 29*), the percentage was highest at lower pressures and is also highest at the total mass peak (1000-1800 nm). This was not the case for some of the other elements although Sb did also have the highest percentage at the mass peak (lower cutpoint 1000 nm).

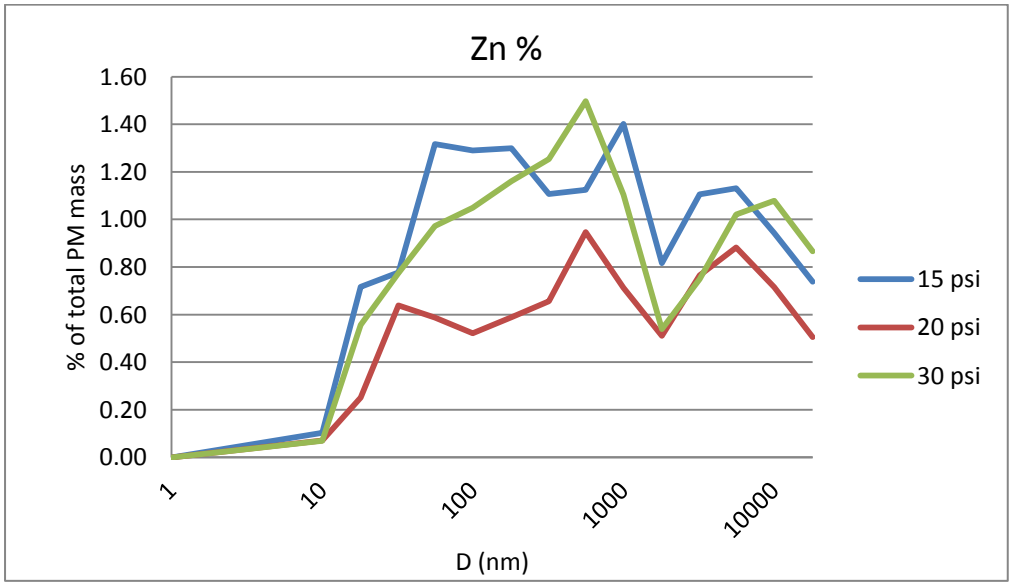

Figure 30. Zn as percentage of total PM mass at 15,20, and 30 psi application pressure.

As shown by *figure 30* the Zn:PMt percentage did not have a consistent relationship with braking pressure as 15 psi and 30 psi both showed higher percentages than 20 psi, and have quite similar

values. The lowest Zn percentages were found at the PM mass peak (1000-1800 nm) and at <10 nm. A peak in the Zn percentage was observed at 3200-5600 nm in all three samples. The Zn percentage below 1000 nm was more consistent at 15 psi than 20 or 30 psi, in which a trend towards increasing percentage with size to a peak at 320-560 nm was seen.

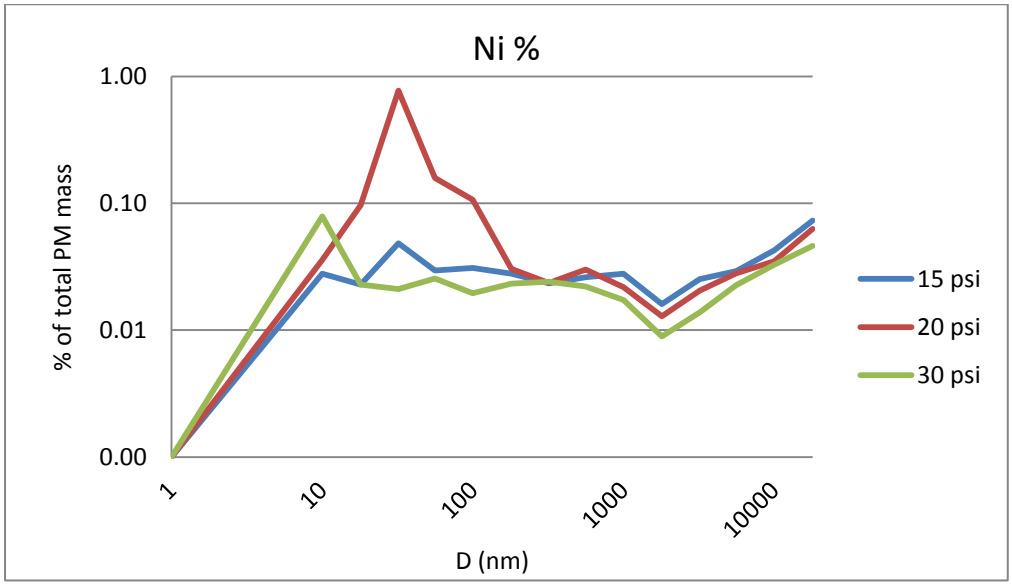

Figure 31. Ni as percentage of total PM mass at 15,20, and 30 psi application pressure.

Ni (*figure 31*) showed the same tendency as Fe in that the lowest Ni percentage, regardless of braking pressure, is at the peak of total PM mass (1000-1800 nm). All three samples showed similar percentages and distributions above this size range, though there was more variability below it, especially in the 20 psi sample. The sudden increase in the Ni percentage in the smallest stage at 30 psi was similar to Al, so could reflect an increase in metallic primary particles caused by the greater braking force.

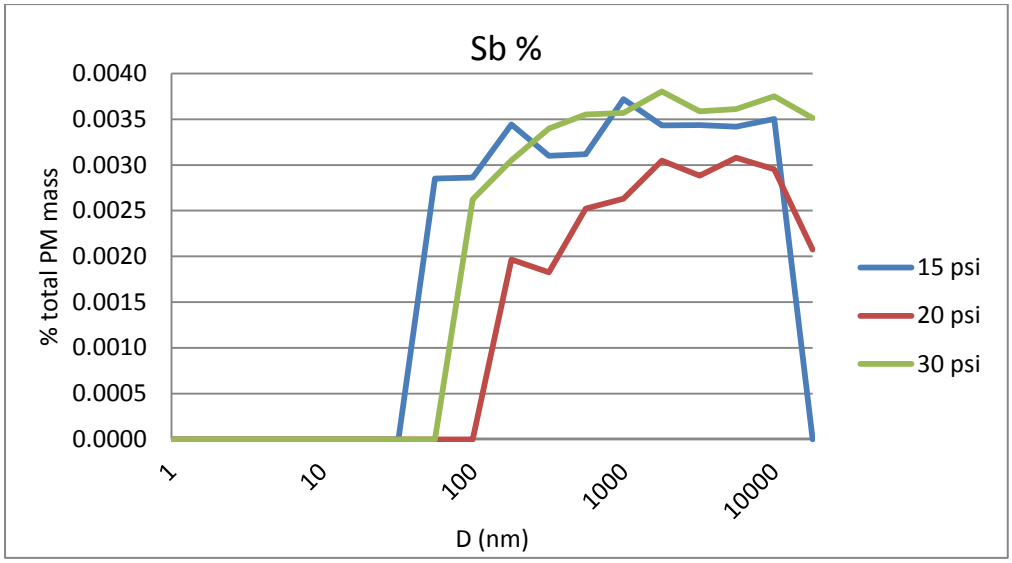

Figure 32. Sb as percentage of total PM mass at 15,20, and 30 psi application pressure.

Sb content in these samples was extremely small (*Figure 32*), which matches with this element not being seen by EDS during the TEM analyses. The plot of Sb as percentage of total PM mass versus size showed this element peaking around the total mass peak, similar to Ba, which might imply that the two elements are released most under similar conditions. The Sb percentage generally gets larger with increasing diameter, this being more pronounced in the samples collected at higher application pressures.

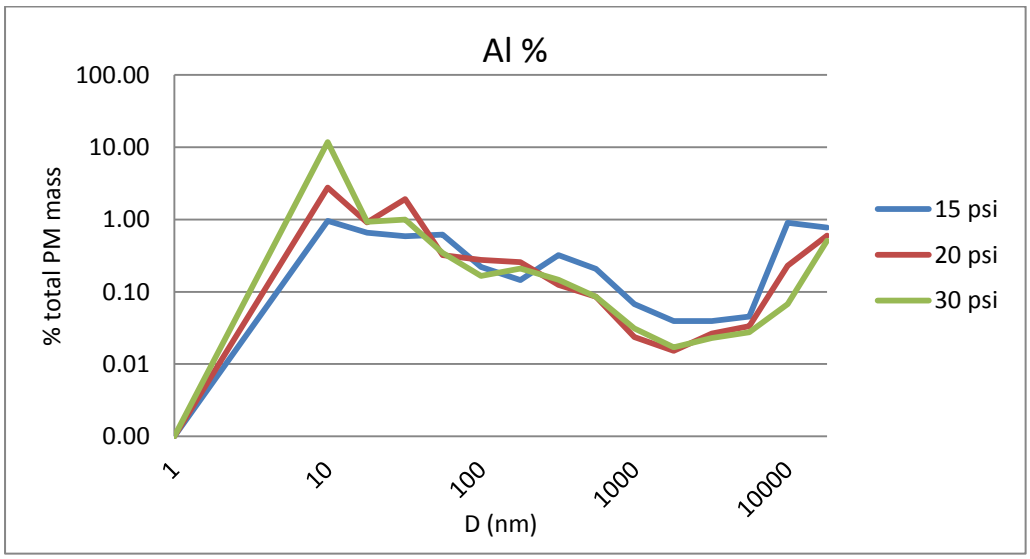

Figure 33. Al as percentage of total PM mass at 15,20, and 30 psi application pressure.

The largest Al percentage was in the afterfilter in all three samples. In the 30 psi sample the Al content in this fraction is 12% of the total, even though Al generally represented a very small proportion of the total PM. This was one of the clearest pressure-dependencies in the ICP-MS data.

This appears to be a useful way of establishing how metal emission varies with size in brake wear, as the variations are difficult to see when the mass concentration is plotted because this is generally too similar to the total mass distribution. Plotting mass percentages has enabled some differences in the distributions of metals such as Fe, Ba, Cu and Zn to be seen more clearly. Existing data on size distributions of elements in brake wear are comparatively limited and generally restricted to confirming the similarity with the total mass distribution. The difference between Fe and Ba is instructive as Fe is likely to be sourced mainly from the cast-iron disc and Ba from the pad.

Key features of the data from these samples include the close similarity of the distributions of Cu and Zn, the difference between Ba and other elements and the reduction of the Fe percentage in ultrafine particles and at the total mass peak.

The generally low percentages of metals in the ultrafine particles, especially at the lower application pressures, matches the expectation that these particles will be formed primarily from organic components released by heating and will contain less metals because the pad and disc surfaces do not reach sufficiently high temperatures at these pressures to generate particles by the volatilisation → condensation → agglomeration pathway. As such, the metals are found mostly in larger particles generated by abrasion.

Cu content expressed as a percentage of Fe content has been found to be a useful indicator of wear in earlier ambient studies and some interesting Cu:Fe % data emerged from the work in Barcelona in 2013, in which Cu;Fe was found to increase at smaller particle sizes. This is not consistent with the results of Sanders et al. (2003) who observed little difference in composition between finer airborne

and coarser hardware debris which implied that separation of elements during wear was negligible (Sanders et al., 2003).

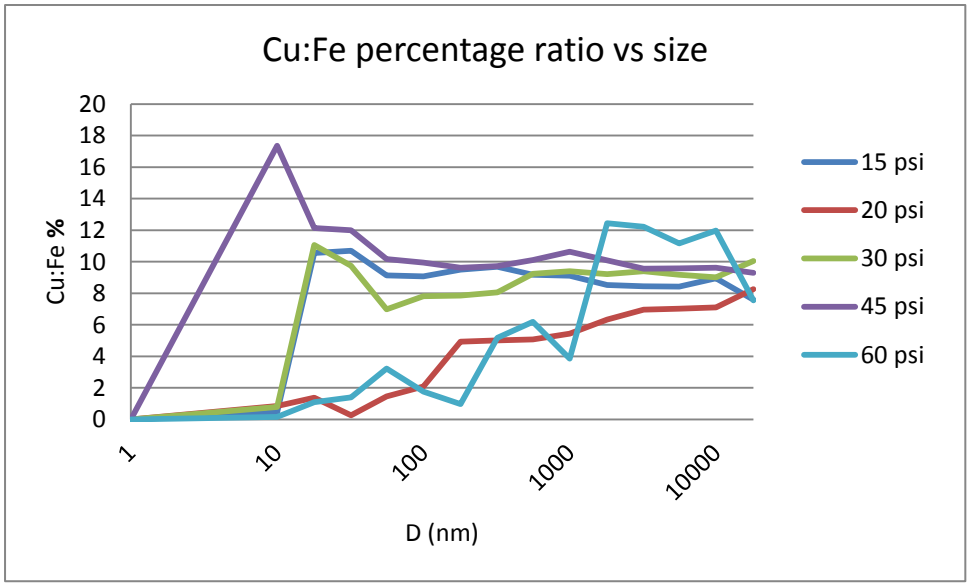

Figure 34. Cu:Fe percentage versus aerodynamic diameter of particles.

The 15 psi and 30 psi tests both gave Cu:Fe percentages similar to past ambient studies, and the 15 psi test furthermore showed the same pattern of increasing percentage at smaller sizes (*Figure 34*). The higher pressures did not show this pattern. While there did not seem to be a clear relationship in the 30 psi samples the 20 psi samples have higher percentages for larger particles, which does not agree with previous observations. The 45 psi sample was similar to the 15 and 30 psi samples from 18 nm upwards, with a very high afterfilter Cu percentage. Taken as a whole, it does not appear there was any consistent relationship between Cu:Fe ratio and either size or brake application pressure during these tests.

3.7 Conclusions and future research areas

The tests carried out so far demonstrate the reliability of the methods and the potential of the collection and analysis techniques and despite limited scope, have produced some important findings. Total released mass per unit time increased significantly with braking force and there is evidence that this was accompanied by changes in size distribution, with the release of more ultrafine particles. Although elemental distributions were found to be similar to the total mass distribution there is evidence presented to show that there were differences between some elements which could be related to the release process for them or to whether they are sourced mainly from the disc (Fe) or the pad (Ba). Morphology of particles was found to be mainly agglomerated irregular angular particles, which is largely consistent with existing literature.

Future research priorities following on from this work must be to assess a greater range of pads, including semimetallic and NAO pads. Bulk samples of the pad could be analysed to ascertain how the composition of the released material differs from the original pad. TEM analyses of milled pad material, as opposed to suspended dust, would also help to elucidate the distribution of elements within the material and by comparison to the wear dust would offer insight into the wear process, and how this changes with increasing braking force and friction surface temperatures. A wider range of braking conditions should also be tested in detail in order to develop a fuller picture of total mass distributions and elemental size distributions in brake abrasion particles. A valuable area to improve would be to employ EELS or XANES to analyse abrasion dusts for the exact chemical speciation. Another important direction of future research would be directed at assessing the biological impacts of exposure to brake wear particles, with simultaneous collection of particles for chemical analysis.

References

Adachi, K., Tainosho, Y., 2004. Characterization of heavy metal particles embedded in tire dust. Environment International 30, 1009-1017.
Garg, B.D., Cadle, S.H., Mulawa, P.A., Groblicki, P.J., Laroo, C., Parr, G.A., 2000. Brake Wear Particulate Matter Emissions. Environmental Science & Technology 34, 4463-4469.
Iijima, A., Sato, K., Yano, K., Tago, H., Kato, M., Kimura, H., Furuta, N., 2007. Particle size and composition distribution analysis of automotive brake abrasion dusts for the evaluation of antimony sources of airborne particulate matter. Atmospheric Environment 41, 4908-4919.
Kukutschová, J., Moravec, P., Tomášek, V., Matějka, V., Smolík, J., Schwarz, J., Seidlerová, J., Šafářová, K., Filip, P., 2011. On airborne nano/micro-sized wear particles released from low-metallic automotive brakes. Environmental Pollution 159, 998-1006.
Mosleh, M., Blau, P.J., Dumitrescu, D., 2004. Characteristics and morphology of wear particles from laboratory testing of disk brake materials. Wear 256, 1128-1134.
Sanders, P.G., Xu, N., Dalka, T.M., Maricq, M.M., 2003. Airborne Brake Wear Debris: Size Distributions, Composition, and a Comparison of Dynamometer and Vehicle Tests. Environmental Science & Technology 37, 4060-4069.
Wahlström, J., Olander, L., Olofsson, U., 2010. Size, Shape, and Elemental Composition of Airborne Wear Particles from Disc Brake Materials. Tribol Lett 38, 15-24.
Wahlström, J., Olander, L., Olofsson, U., 2012. A Pin-on-Disc Study Focusing on How Different Load Levels Affect the Concentration and Size Distribution of Airborne Wear Particles from the Disc Brake Materials. Tribol Lett 46, 195-204.
Zhao, J., Lewinski, N., Riediker, M., 2014. Physico-Chemical Characterization and Oxidative Reactivity Evaluation of Aged Brake Wear Particles. Aerosol Science and Technology 49, 65-74.

CHAPTER 4: INVESTIGATION OF METALLIC PARTICLES IN DIESEL EXHAUST BY TEM-X-EDS

4.1 Aims and Outcomes

Samples were collected from a Euro-5 compliant diesel engine using a 10-stage MOUDI for analysis by TEM-X-EDS in order to characterise elemental composition and physical morphology which would enable comparison to samples collected from the brake rig and from the ambient atmosphere, with a particular aim of exploring similarities and differences with the main Fe-based particle types detected by TEM analysis of roadside samples.

The results obtained appear to be explicable in terms of the engine components and the likely constituents of the fuel and lubricants. In terms of comparisons, composition of metallic particles is different from the two main classes of ambient Fe particles and different in most ways from the brake wear particles as well. The carbonaceous soot particles observed in the diesel exhaust are similar to those in the environment, however.

Diesel exhaust particulate has been extensively studied in the past and is known to be a source of a number of metals in the ambient atmosphere, including Al, Ca, Cu, Fe, Mg, Mn, V and Zn from trace components of fuel and lubricating oils emitted after combustion (Sanderson et al., 2014). It is clear that the composition and size distributions of the emitted particulate varies greatly from engine to engine, and on the conditions under which the sample is generated, for instance; whether the engine is started warm or cold; the composition of the fuel and lubricating oil; the engine speed and load. It would be unwise to expect that a test of quite limited scope like that described below produces universally applicable results. Rather, it shows the particulate emitted from this engine under specific conditions. However, it may show certain particle types which might be seen as indicative of engine-derived emissions.

4.2 Sample Collection

TEM grids were loaded into the MOUDI mounted on aluminium foil substrates in the established method and sampled from the FASTER project diesel engine, a EURO 5 compliant unit supplied by Jaguar Land Rover, at conditions of 2000 RPM and 200 Nm load for 10 minutes.

The engine combustion chamber (cylinders and pistons) are constructed from Al alloys, which is very clearly reflected in the composition of the emitted particulates. Some particles have been found to contain Bi, which can be attributed to the diesel oxidation catalyst coating. Cl is present in many particles and can be attributed to additives in the lubricating oil through use as a catalyst in synthesis of polyisobutylene hydrides as a detergent additive. Previous studies have shown that the metals in emitted diesel particulate correlate well with those contained in the fuel and also that the lubricating oil makes a contribution, especially in certain elements such as Ca and Zn (Sharma et al., 2005; Wang et al., 2003).

4.3 Characterisation of Chemistry and Structure by TEM-X-EDS

4.3.1 Stage 8 – 320-560 nm nominal cut-points

The initial conditions produced a fairly low particle load, but metallic particles were prominent in stage 8 (320-560 nm). This size range was analysed first for continuity with the ambient data where Fe nano-agglomerates were prominent in this range. The metallic particles observed featured Fe, Ni and Cr frequently and often in combination. Fe did not normally appear at the high weight percentages typical either of the ambient Fe particles or of the brake wear particles. There are many instances of Al and Ca particles. Ca is likely to have originated in the lubricating oil, but in this particular engine Al in the exhaust is likely to be attributable to wear to engine components. This would help to explain why Al is the dominant element in the larger stages (even in stage 8 the Al-

dominated particles appear to be present as a result of particle bounce) and is less common in the smaller particles.

Element	Av wt%	Stdev	N
Al	41.3	27.9	44
Si	23.7	39.5	51
Fe	10.6	13.1	50
Bi	5.1	21.9	19
Cu	4.5	8.6	36
Pb	3.3	17.3	17
S	3.2	13.8	33
Ca	1.8	5.9	26
Mn	1.5	8.4	28
Cr	1.5	11.6	22
Cl	0.8	3.4	19
Ni	0.7	5.4	23
Zn	0.6	0.8	22
K	0.5	1.4	21
As	0.3	0.4	2
Na	0.2	1.5	3
N	0.2		1
Co	0.1	0.5	6
F	0.04		1
Mg	0.03	0.2	2
Ti	0.02		1
I	0.01		1
Sb	0.01		1
Total Number of Spectra = 63			

Table 21. Elemental contributions to spectra taken from stage 8, diesel exhaust.

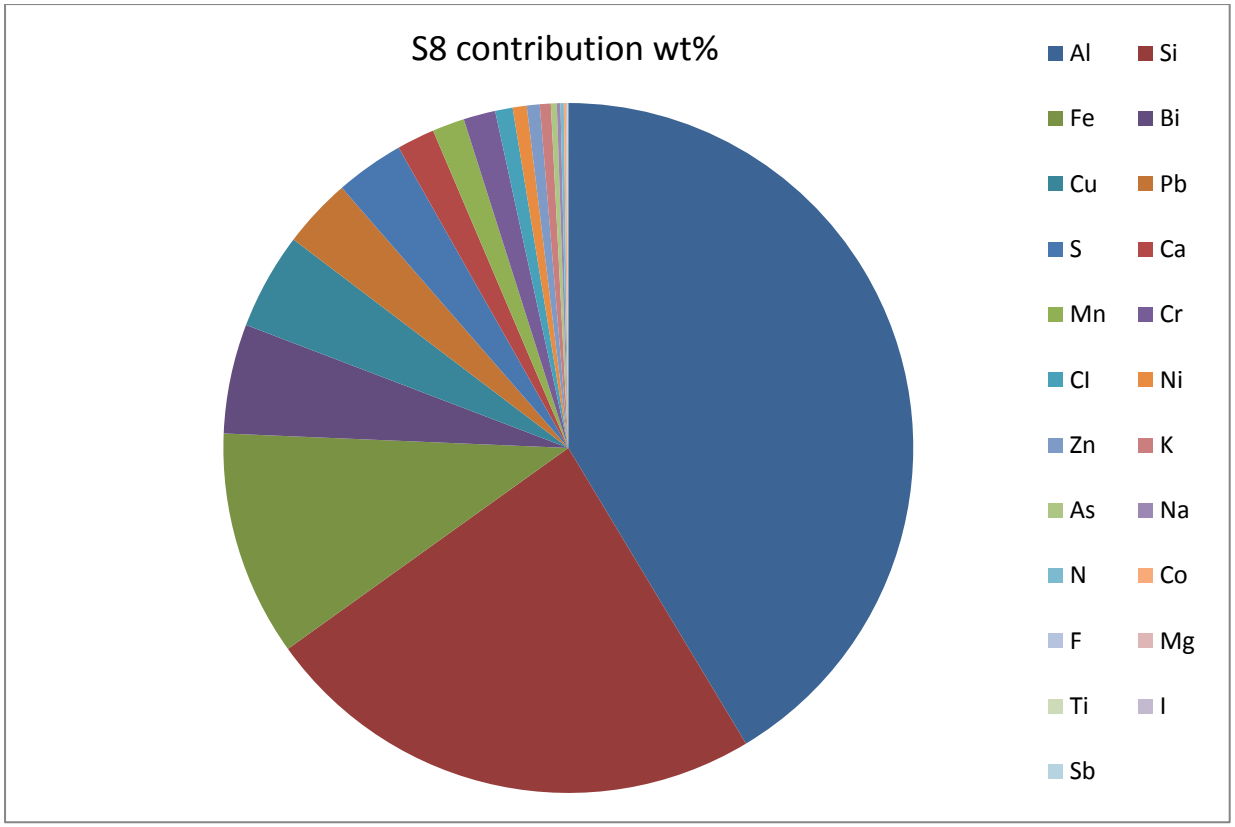

Figure 35. Pie chart of elemental contributions in stage 8 (N=63).

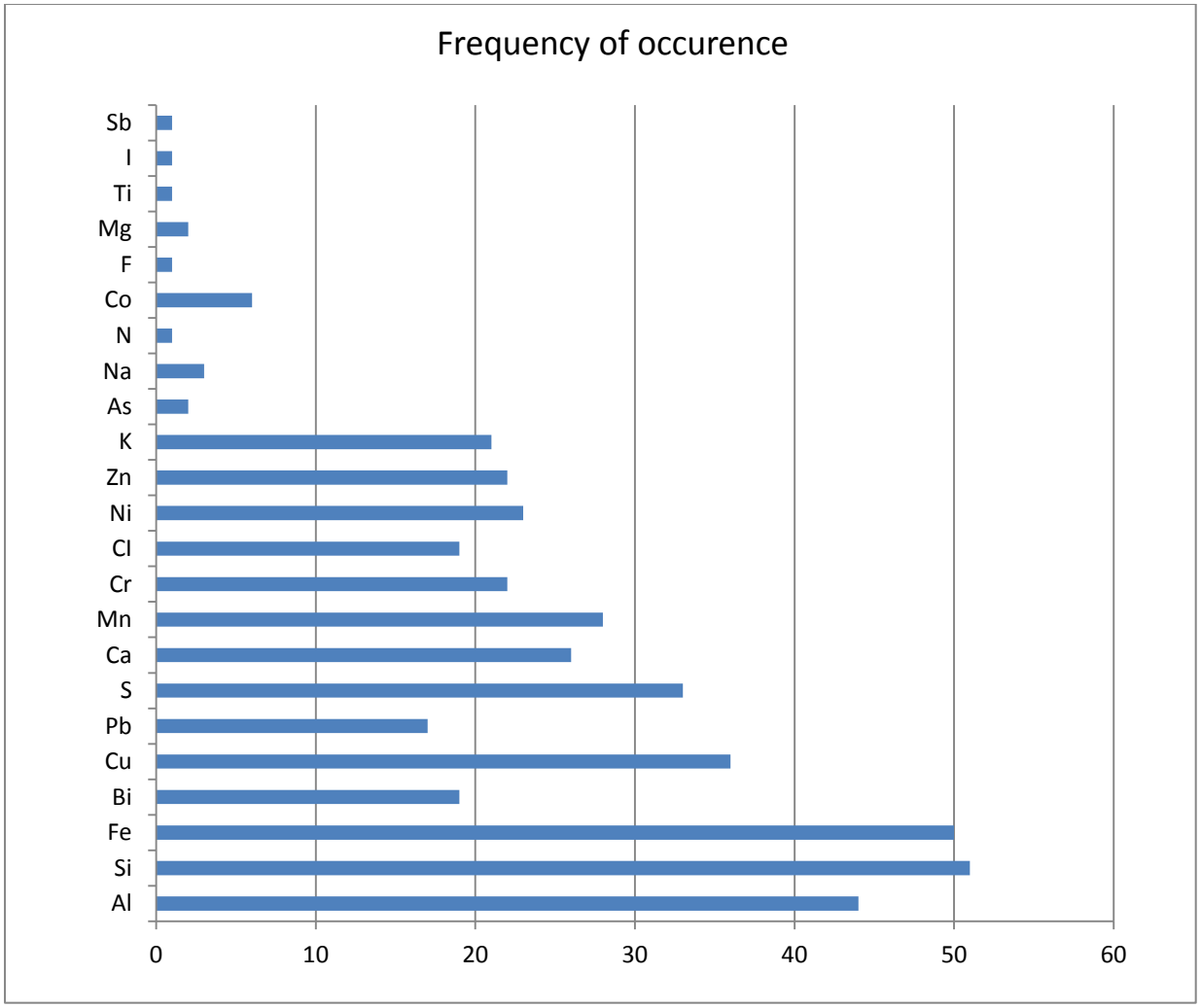

Figure 36. Number of occurrences for each element in the 63 spectra from Stage 8.

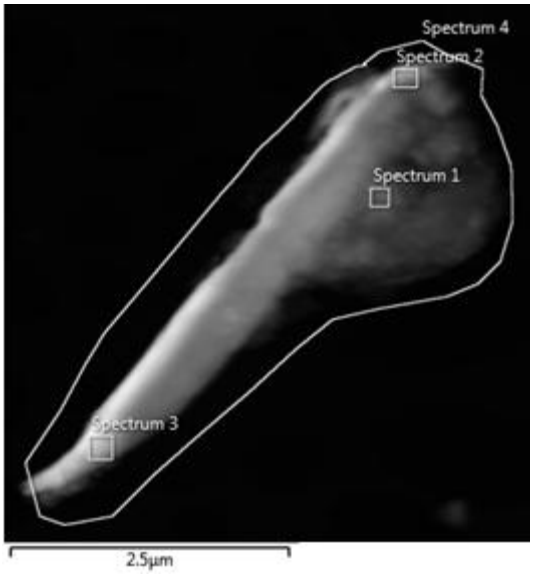

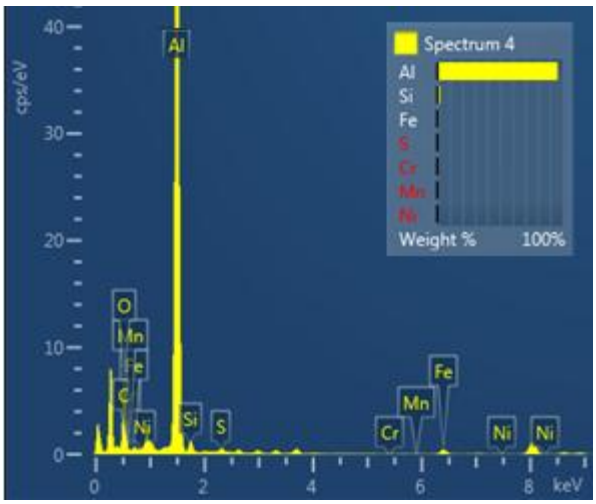

Figure 37 (left). Elongated diesel Al particle from S8 with Fe, Mn, Cr as minor constituents.

Figure 38 (right). EDX spectrum of whole diesel particle.

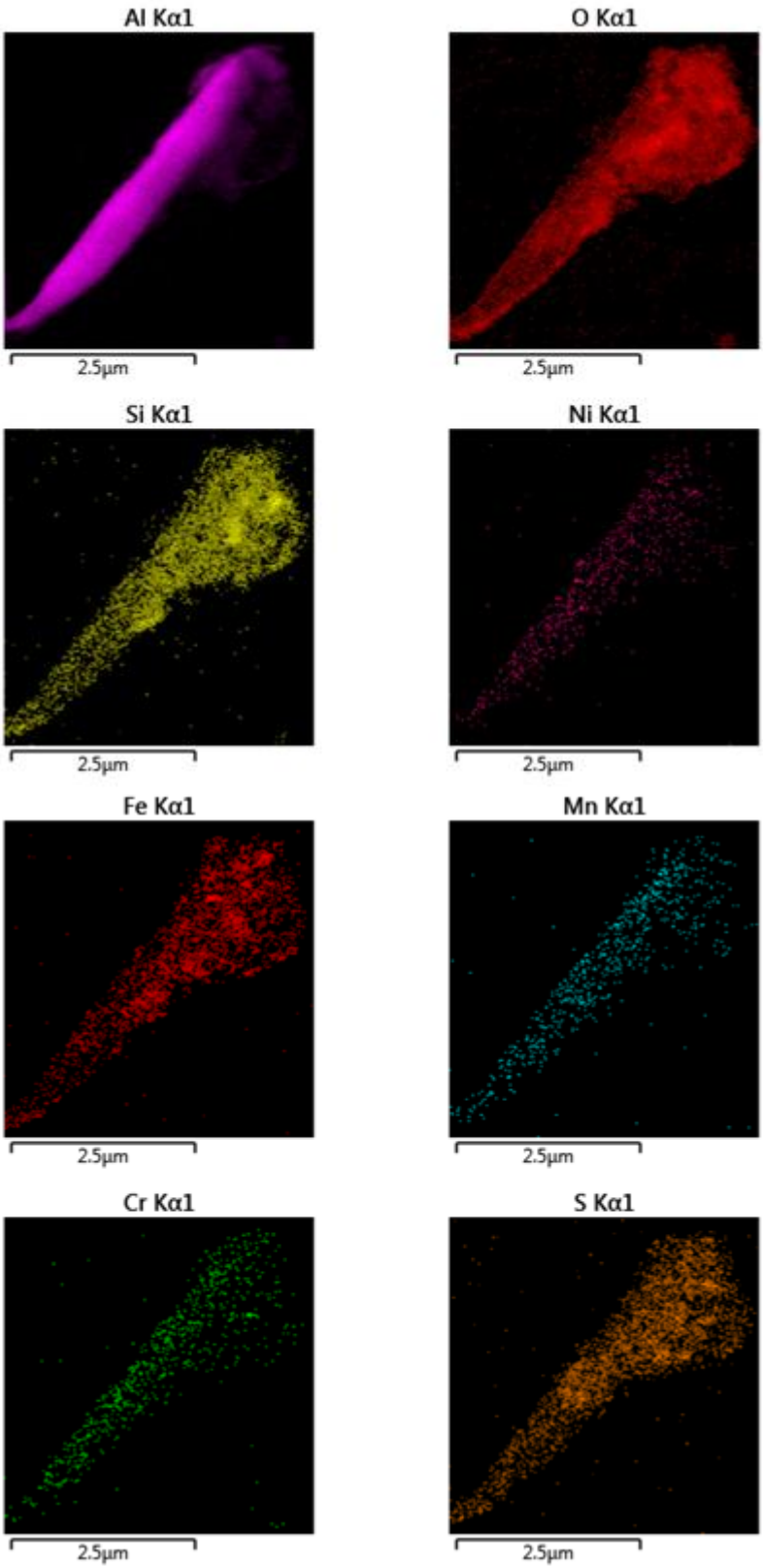

Figure 39. Elemental maps of diesel Al particle.

This large elongated particle (*Figure 37*) is highly complex in structure and is representative of the Al component of the exhaust particulate. The Al part appears to be a large wear fragment, but the other elements are distributed more evenly through the particle as a whole, in which a number of smaller non-Al-dominated primary particles have become attached to the Al particle (*Figure 9*). Figure 53 also shows a particle with similar characteristics.

An interesting aspect of the data amassed from this engine is that the Al found is in particles well above 100 nm in size – fine particles not nanoparticles. When describing the release of agglomerated Fe nanoparticles from wear to engine components, Liati et al. (2015) hypothesised that in engines where components likely to wear were manufactured from other metals (such as the Al-alloys of this unit) analogous nanoparticle agglomerates might form from those materials (Liati et al., 2015). If this is the case, we have not observed it in this instance.

The maps (*Figure 39*) demonstrate different spatial distributions within the particles from the aggregate. Ni, Mn and Cr are distributed in the same areas of the particle. Si and O also have similar distributions to each other.

4.3.2 Stage 10 – 100-180 nm nominal cut-points

Element	Av wt%	Stdev	N
Cu	20.9	23.6	9
Fe	17.8	31.5	16
Ca	14.0	19.6	17
Si	13.6	27.2	21
S	13.3	19.0	24
K	4.9	3.6	14
Na	4.6	11.9	6
Cr	4.3	8.2	16
Mg	3.8	2.0	3
Ni	2.1	3.7	16
Mn	0.5	0.7	15
Total number of spectra = 28			

Table 22. Elemental contributions to spectra taken from Stage 10, diesel exhaust.

The main differences in composition compared to stage 8 were; Al was not detected and Cu was very prominent. Ca was also an important element in this stage, appearing in several particles. Some of these were at low concentration in particles with other dominant elements, while Ca was the dominant element (>50% wt) in a number of particles. Fe was also an important element in this stage.

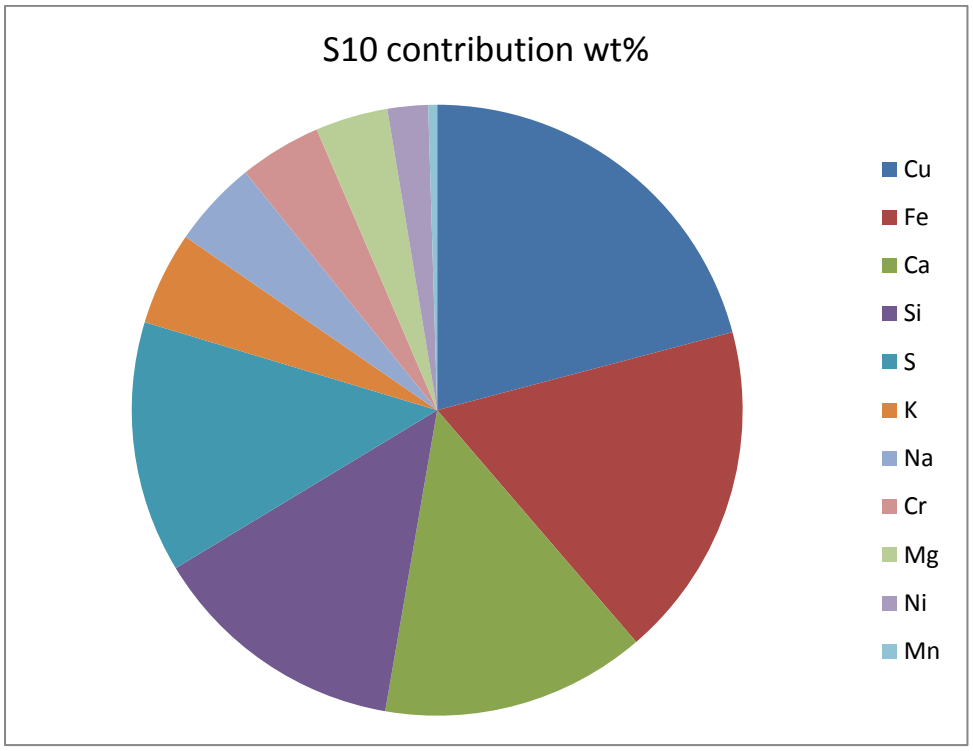

Figure 40. Average contribution, engine particles Stage 10 (N=28).

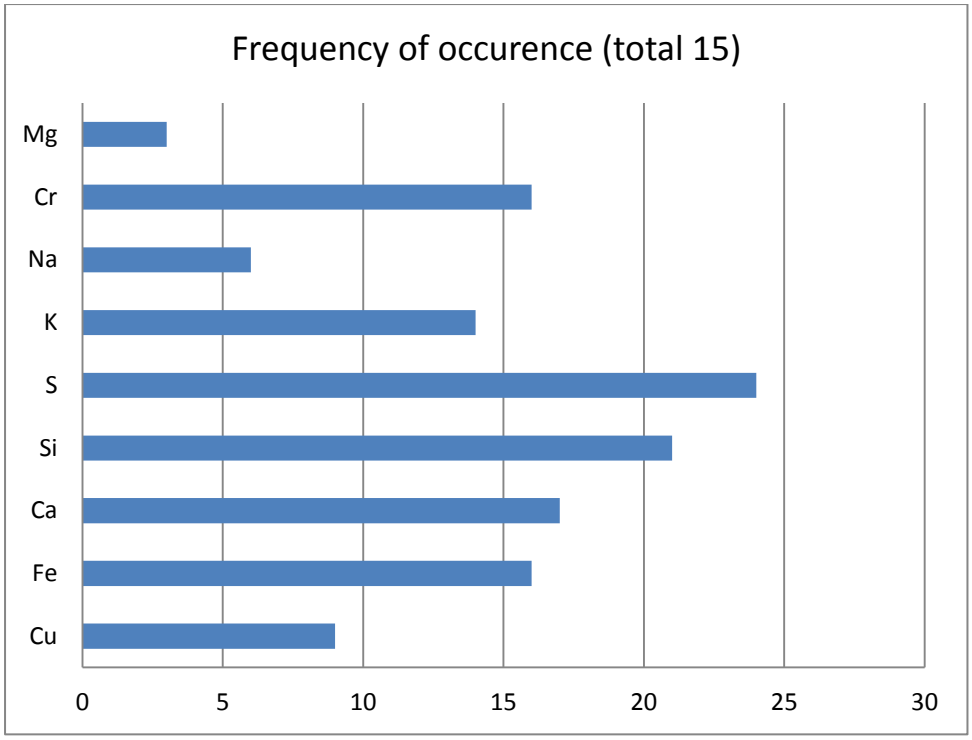

Figure 41. Number of occurences of each element in diesel spectra from Stage 10 (N=28).

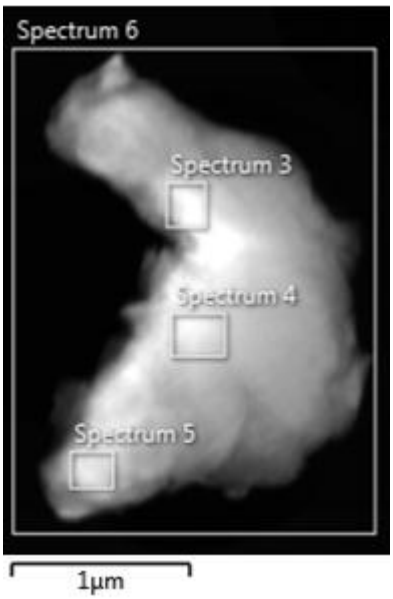

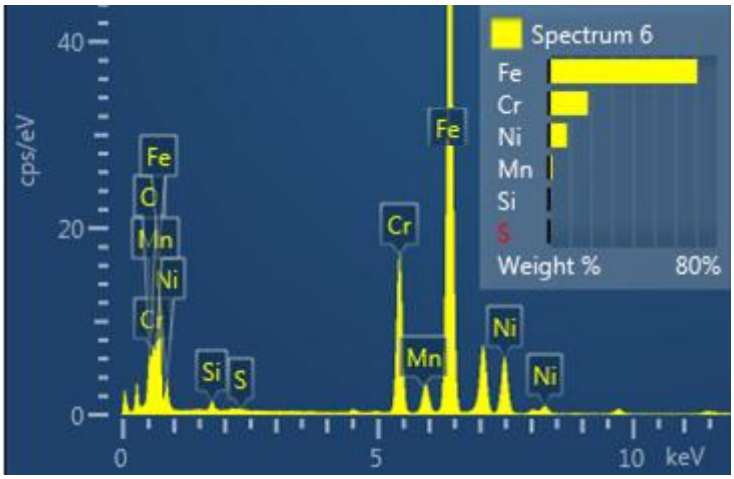

Figure 42 (left). Fe-Cr-Mn-Ni diesel particle from S10.

Figure 43 (right). EDX spectrum covering whole particle in Fe-Cr-Mn-Ni diesel particle.

With an Fe wt% of 70% this particle cluster was closer to the ambient type, but the high concentration of Cr (18%) and the morphology were rather different. Rather than the fractal chains of spherules observed in the environment, characteristic of high-temperature formation by a

condensation – nucleation – agglomeration process, this particle has an irregular morphology. Brake wear fragments of this size are typically angular (Chapter 3), presenting flat surfaces and sharp edges (Zhao et al., 2014). By comparison the physical features in this particle were softened. One possibility was that a mechanically produced fragment underwent some partial melting, softening or deformation at the exposed surfaces in the high-temperature environment of the engine (Liati et al., 2015).

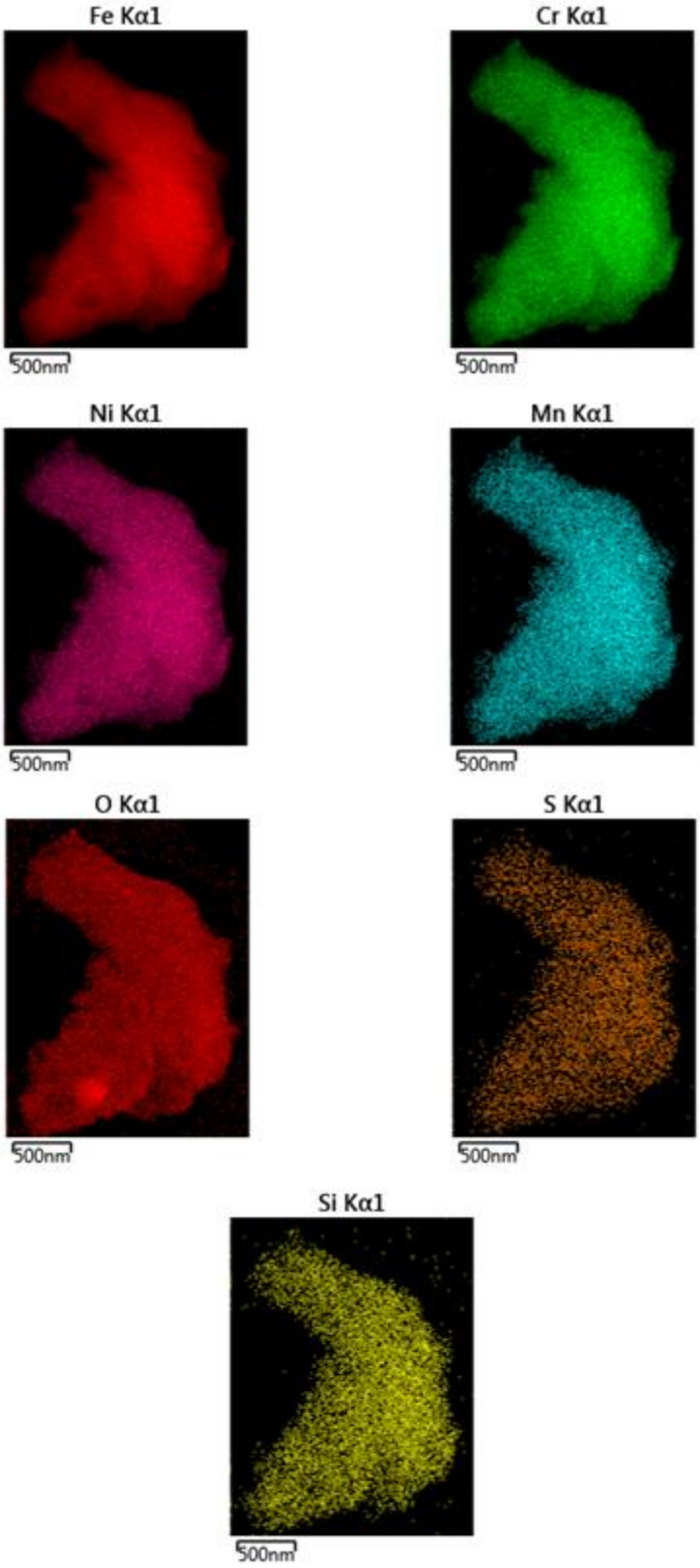

Figure 44. Elemental maps of Fe-Cr-Mn-Ni diesel particle.

The maps of this particle (*Figure 44*) demonstrated clearly very similar distributions for the metals, S and Si. O generally followed but there is one very O-rich area at the lower left, which is not paralleled by the other elements.

4.3.3 Stage 9 - 180-320 nm nominal cutpoints.

Reloading the grids at a higher engine load was intended to bring about higher particle loadings and generate more metallic particles due to higher temperatures, but the actual result observed in stage 9 (180-320 nm) was that a large amount of carbonaceous soot aggregates were produced, which are typical of diesel particulate emissions. These were closely comparable in size and shape to those observed in the environment. Figure 10 shows such particles in the bottom left corner and middle right.

This made it quite difficult to pick out the metals from the carbon, although they are still present, as demonstrated by the presence of the Ca-rich particle below. It could be that as higher loads generate more soot from incomplete combustion, the metals are unable to nucleate together and instead are dispersed in the carbon soot. Earlier studies have certainly indicated that the Fe:C ratio is the key factor in determining the form of the Fe particles observed in exhaust.

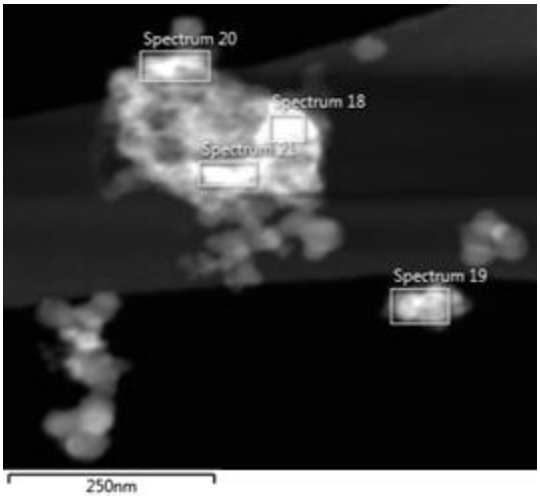

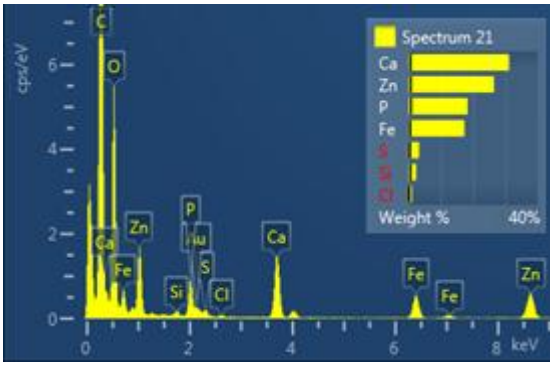

Figure 45 (left). HAADF image of diesel Ca agglomerate in stage 9.

Figure 46 (right). EDX Spectrum of Ca-Zn-P-Fe diesel particle from stage 9.

Element	Wt %
Ca	31.15
Zn	26.49
P	18.32
Fe	17.35
S	3.25
Si	2.34
Cl	1.1

Table 23. Composition table for diesel Ca-Zn-P-Fe particle.

The elemental composition of this particle is indicative of origin in lubricating oil. Miller et al. (2007) employed a hydrogen-fuelled engine to isolate the effects of lubricating oils and reported that Fe, Ca, P, Mg and Zn were all prominent in the emitted particulate, forming dense metallic spheres over a large size range (30-300 nm) (Miller et al., 2007). Patel et al. (2012) also stated that P, S, Ca and Zn became associated with diesel soot due to interactions with lubricating oil (Patel et al., 2012).

4.3.4 Stage 10 (high loading)

Examination of Stage 10 (afterfilter, <180 nm) after reloading found further examples of Ca particles, with S also much in evidence. Na and K were present in some particles generally at 10-15%/wt although one spectrum reported Na at 32%/wt. One agglomerate consisted of Mg-Si at an approximate ratio of 35:65 by weight. Mg has been previously reported as a component of lubricating oils (Miller et al., 2007; Patel et al., 2012).

Element	S8 Bham	S6 Bham	S7 Newc.	Diesel
Fe	63.18	15.71	78.26	70.55
Cr	16.05	12.52	15.89	18.48
Mn	14.47	3.47	2.1	1.54
Si	6.3	8.04	n/a	0.71
Ni	n/a	60.26	2.43	8.66
S	n/a	n/a	1.32	0.06

Table 24. Weight percentage table for example Fe-Cr particles.

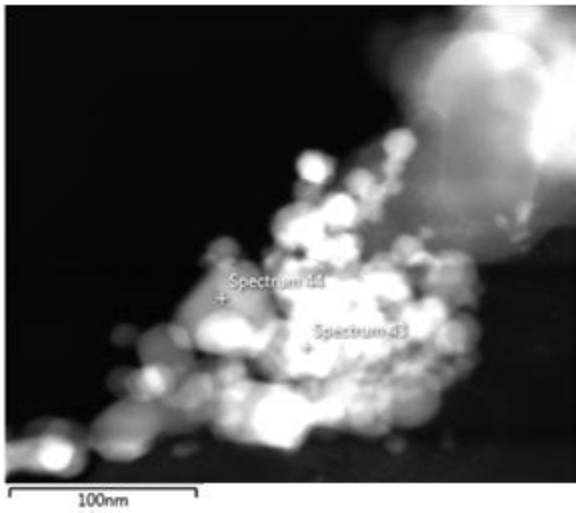

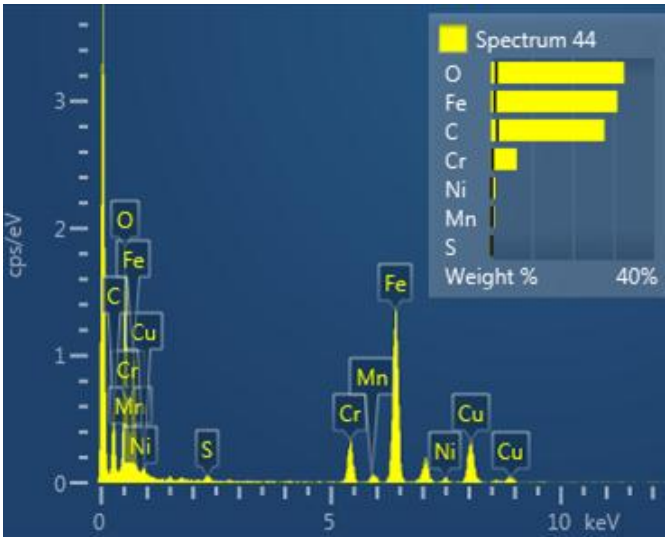

Figure 47 (left). Fe-Cr-Ni particle from Newcastle..

Figure 48 (right). EDX Spectrum for Fe-Cr-Ni particle from Newcastle.

Figure 47 shows an irregular agglomerate formed of nanoparticles of various sizes and shapes, mostly spherical or near spherical.

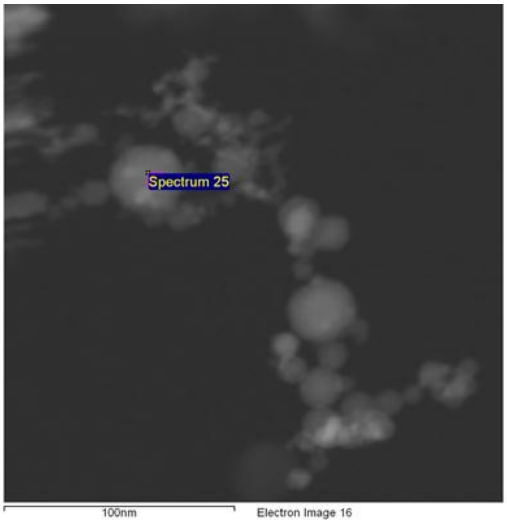

Figure 49. Image of Ni-Cr-Fe agglomerate from Birmingham.

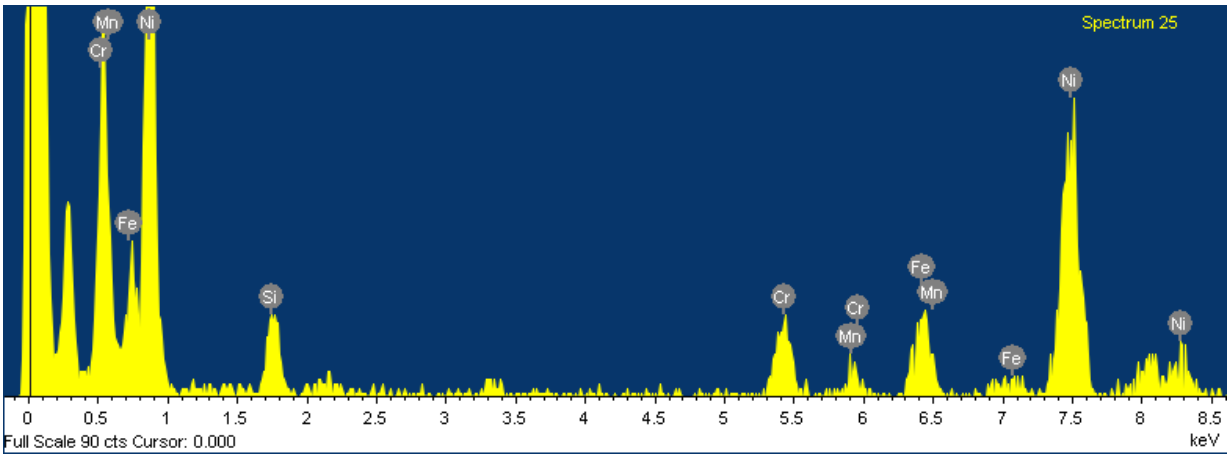

Figure 50. EDX spectrum for Ni-Cr-Fe agglomerate from Birmingham.

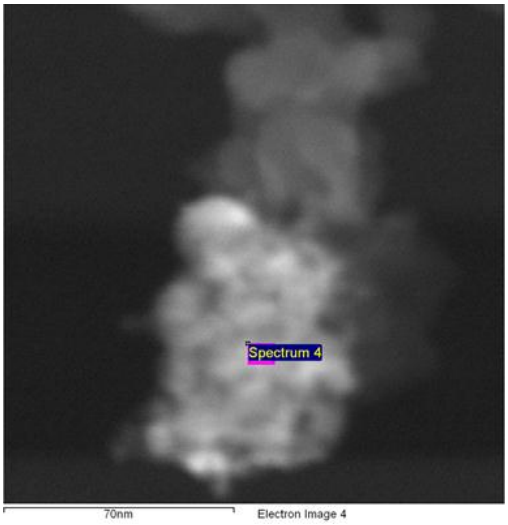

Figure 51. HAADF image of Fe-Cr particle collected in Birmingham.

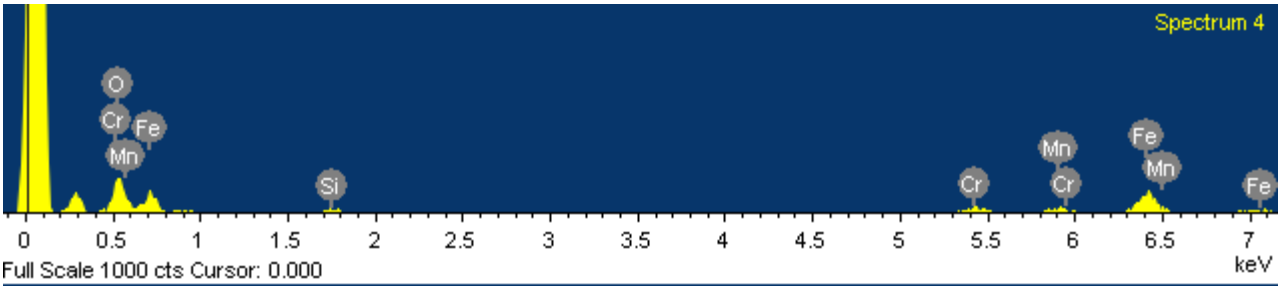

Figure 52. EDX spectrum of Fe-Cr particle collected in Birmingham.

4.3.5 Combined Data

Element	Av wt%	Stdev	N
Al	27.12	27.91	44
Si	21.58	37.71	72
Fe	12.35	20.20	66
Cu	9.06	26.86	19
Ca	7.40	22.24	45
S	6.15	16.44	17
Bi	3.36	21.89	57
Cr	2.25	10.36	43
Pb	2.15	17.30	43
K	1.78	4.84	38
Na	1.58	12.30	19
Mg	1.14	19.21	39
Mn	1.13	6.87	22
Ni	1.06	4.81	35
Zn	0.67	5.22	2
Cl	0.55	3.31	9
P	0.27	6.60	1
As	0.18	0.40	6
N	0.10		1
Co	0.07	0.49	5
F	0.03		1
Ti	0.01		1
I	0.01		1
Sb	0.00		1
Total number of spectra = 96			

Table 25. Elemental contributions, diesel exhaust, combined results from stages 8-10 (N=96).

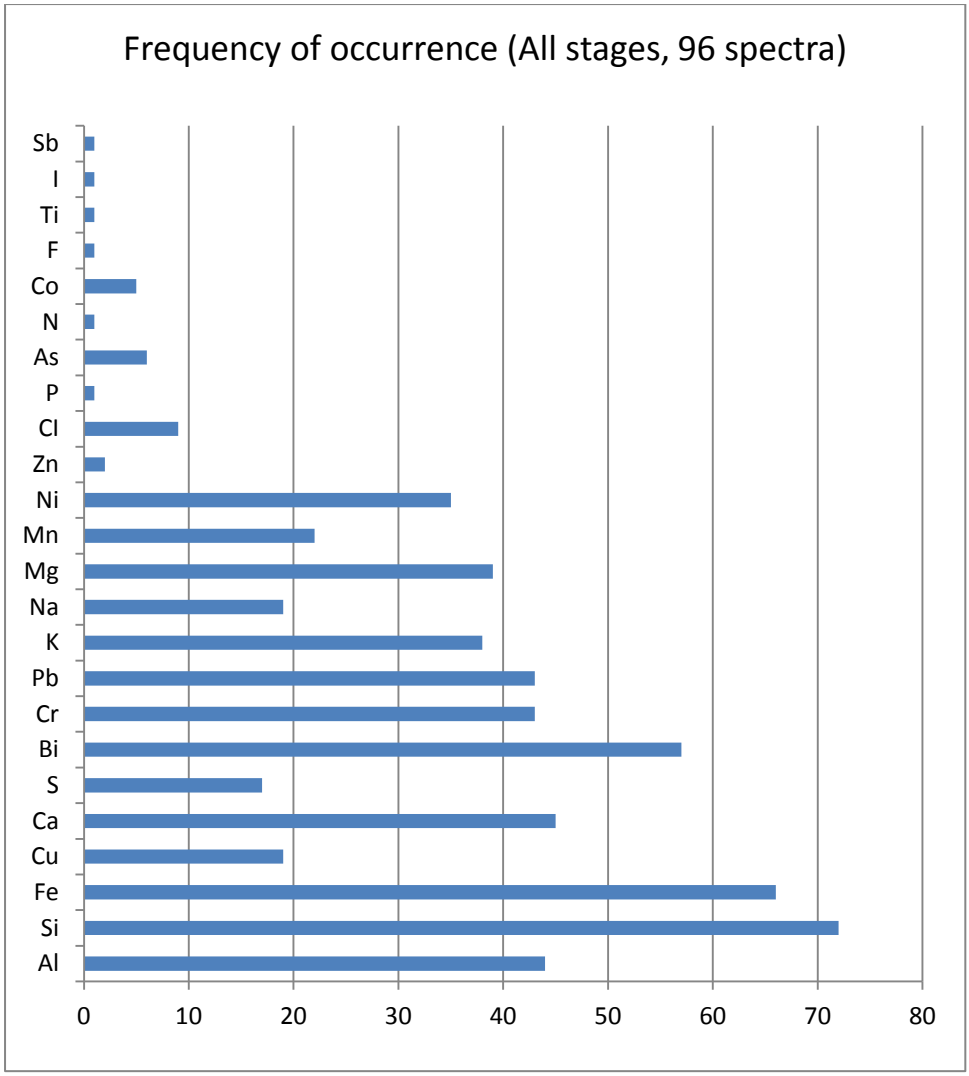

Figure 53. Number of occurrences in spectra, all data combined.

Bi was detected in a number of particles from the exhaust, at a range of weight percentages. Although Bi is sometimes used as a Pb substitute in some applications due to having similar properties while being less toxic, the most likely source of Bi in exhaust from this particular engine was the diesel oxidation catalyst, where it is present along with Pt and Pd. Neither of those elements was detected by EDX in this study.

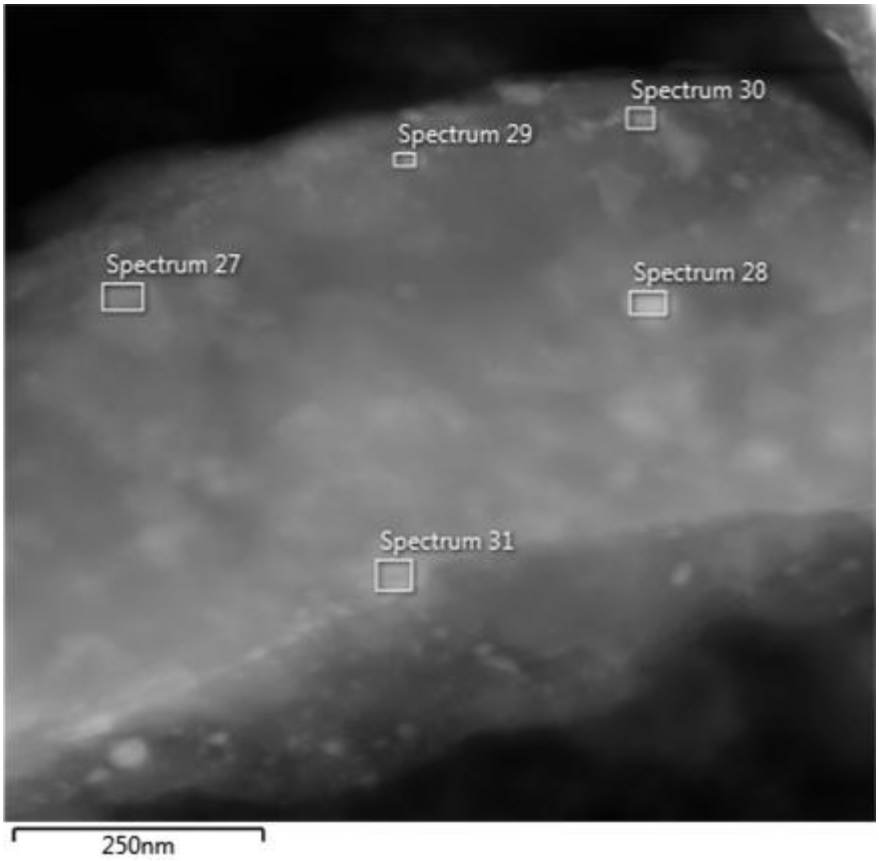

Figure 54. HAADF image of large particle with many small primary particles adhered and/or embedded.

Spectrum 28	
Element	**Wt%**
Al	23.8
Fe	1.13
Co	0.9
Cu	5.73
Bi	68.45
Total:	100.00

Table 26. Elemental composition of primary diesel particle in Spectrum 28.

Table 26 shows the elemental composition in spectrum 28 of single primary particle in agglomerate above (*Figure 54*). Bi is the main metallic element and Al the most important minor constituent. This contrasts with the spectra taken from a different area of this agglomerated structure, illustrated below in Figure 55 and Table 27.

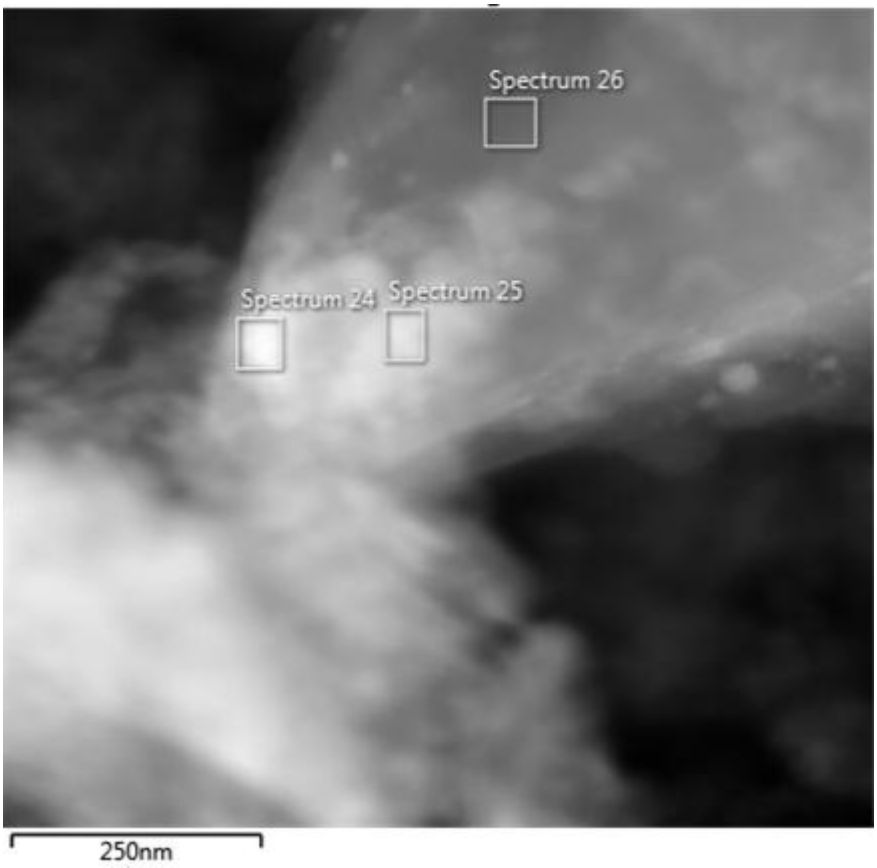

Figure 55. HAADF image of different area of the large agglomerate in Figure 54.

Element	Wt%
Al	59.09
Si	1.04
S	0.45
Cl	0.82
K	0.41
Ca	0.31
Mn	0.34
Fe	25.11
Ni	0.34
Cu	6.54
Zn	1.41
Pb	2.09
Bi	2.05
Total:	100

Table 27. Elemental composition of area of diesel particle shown as Spectrum 25.

The particle in spectrum 25 (centre of *Figure 55*) contrasts dramatically with 28. Al is the dominant element in this case, followed by Fe. The maps of the whole agglomerate shown below in *Figure 56*

also confirm the different distributions of the metals within it, and demonstrate that numerous primary particles, some of them nanoscale, are combining to form large complex structures. The distribution of O would imply that the Fe and Al in the agglomerate are in the form of oxides, but Pb and Bi do not show the same pattern.

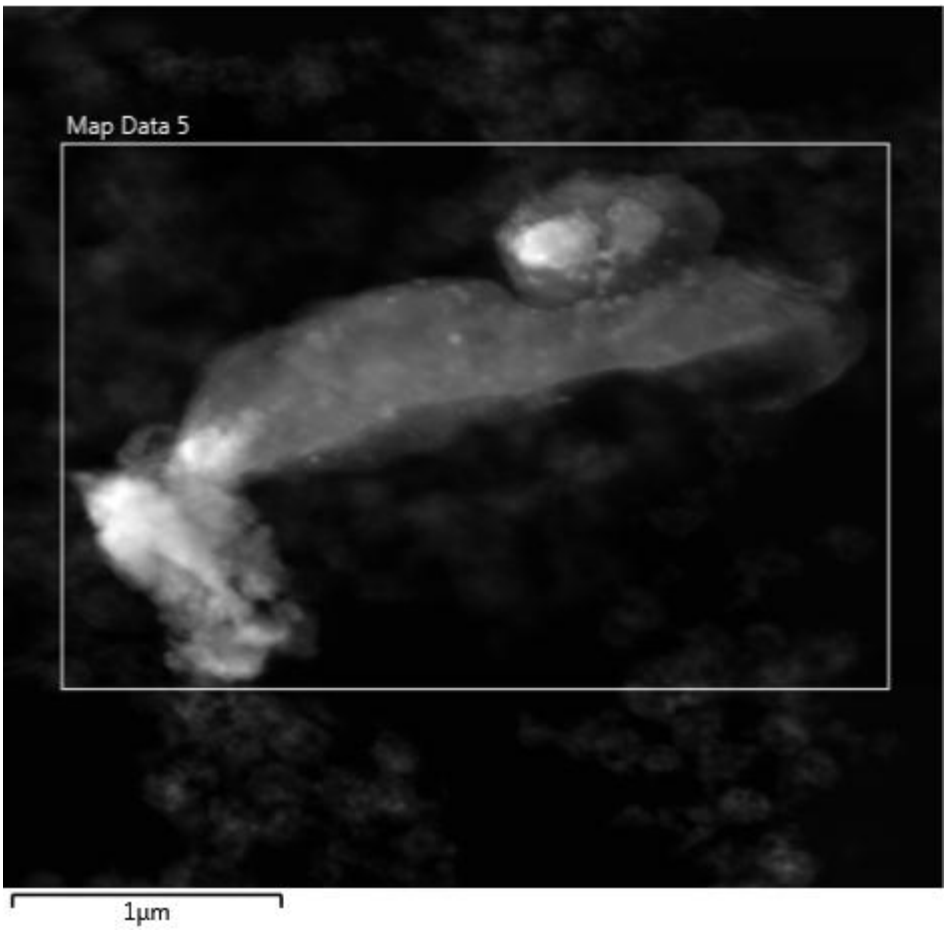

Figure 56. HAADF image of whole agglomerate structure, of which smaller areas are shown in Figures 54 and 55.

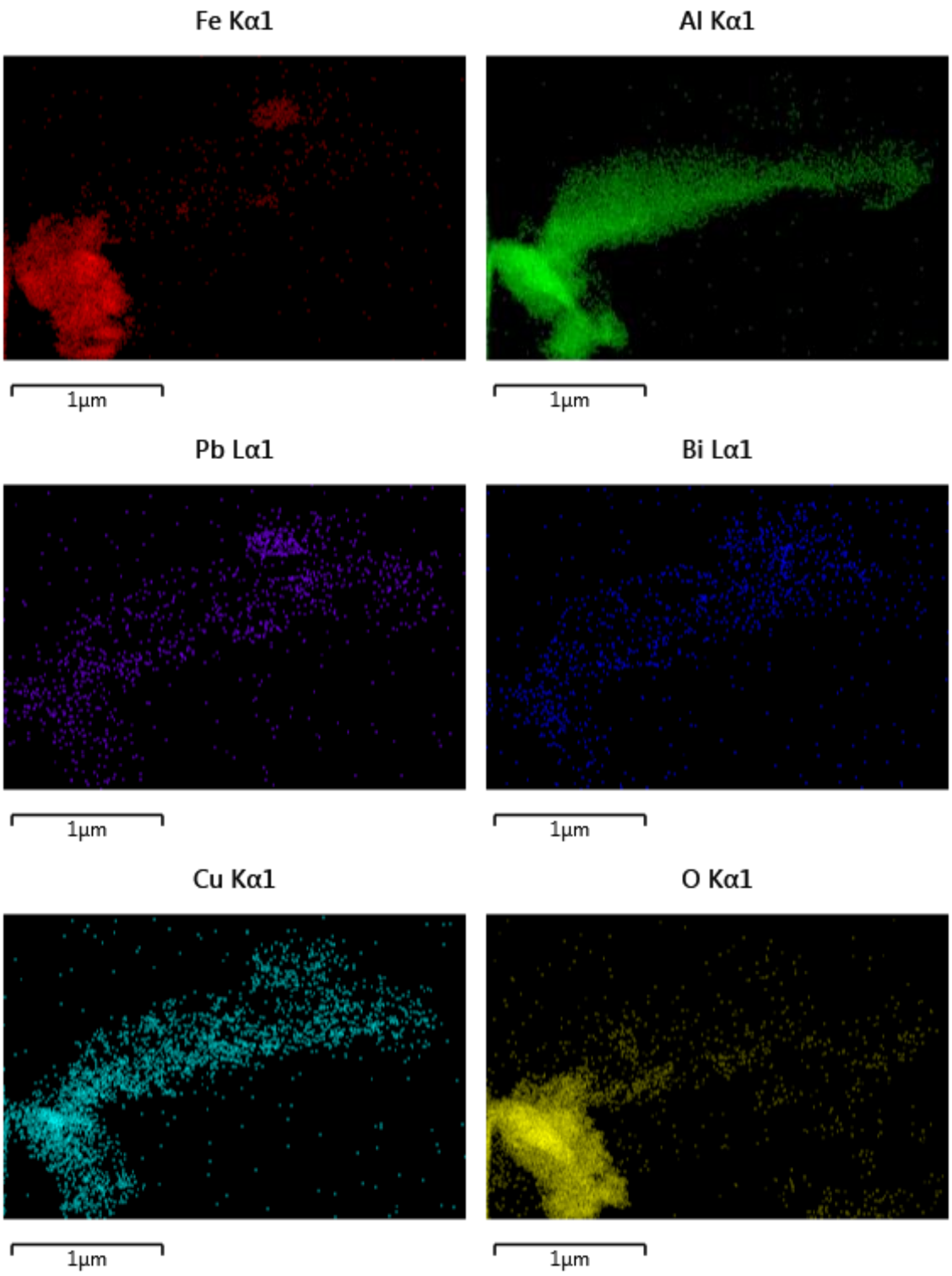

Figure 57. Elemental maps corresponding to Figure 56.

4.4 Conclusions

The data obtained in these tests confirmed the presence in diesel exhaust particulate of a number of metals and other inorganic components, among which S, Si and Cl were also common. These data demonstrated that the co-occurrence of Fe and Cr is likely to be an important indicator of engine-derived particles (see Figures 5 and 10, sections 7.3.1 & 7.3.2), particularly when associated with Ni. Other important features to emerge are that engines making significant use of Al alloys in construction, such as the unit used in this study, will contribute wear particles formed primarily of that material, thus providing another source of Al. It was found that – under these specific conditions – the Al was mostly found in fine ($PM_{0.1}$ – $PM_{2.5}$) particles rather than ultrafine. Furthermore, submicron particles are likely to include engine-derived Cu, which has certain implications for the use of Cu as a brake tracer. This may agree with the results obtained in Barcelona and presented in Chapter 6 where there were some anomalous results in Cu in $PM_{0.22}$ which did not correlate with Ba, the other favoured tracer of brake emissions.

The results presented above should not be considered representative of the vehicle fleet in the UK as a whole, only for this engine under the stated conditions. Further similar investigations covering a wider range of engine models and engine load cycles would be required to provide more comprehensive data. However, the data certainly show that valuable insights into the morphology and composition of engine-derived particles can be obtained through this method.

References

Liati, A., Pandurangi, S.S., Boulouchos, K., Schreiber, D., Arroyo Rojas Dasilva, Y., 2015. Metal nanoparticles in diesel exhaust derived by in-cylinder melting of detached engine fragments. Atmospheric Environment 101, 34-40.

Miller, A.L., Stipe, C.B., Habjan, M.C., Ahlstrand, G.G., 2007. Role of Lubrication Oil in Particulate Emissions from a Hydrogen-Powered Internal Combustion Engine. Environmental Science & Technology 41, 6828-6835.

Patel, M., Azanza Ricardo, C.L., Scardi, P., Aswath, P.B., 2012. Morphology, structure and chemistry of extracted diesel soot—Part I: Transmission electron microscopy, Raman spectroscopy, X-ray photoelectron spectroscopy and synchrotron X-ray diffraction study. Tribology International 52, 29-39.

Sanderson, P., Delgado-Saborit, J.M., Harrison, R.M., 2014. A review of chemical and physical characterisation of atmospheric metallic nanoparticles. Atmospheric Environment 94, 353-365.

Sharma, M., Agarwal, A.K., Bharathi, K.V.L., 2005. Characterization of exhaust particulates from diesel engine. Atmospheric Environment 39, 3023-3028.
Wang, Y.-F., Huang, K.-L., Li, C.-T., Mi, H.-H., Luo, J.-H., Tsai, P.-J., 2003. Emissions of fuel metals content from a diesel vehicle engine. Atmospheric Environment 37, 4637-4643.
Zhao, J., Lewinski, N., Riediker, M., 2014. Physico-Chemical Characterization and Oxidative Reactivity Evaluation of Aged Brake Wear Particles. Aerosol Science and Technology 49, 65-74.

CHAPTER 5: GRAVIMETRIC ANALYSIS OF FILTERS AT UK URBAN AND RURAL SITES AND AT ROADSIDE AND BACKGROUND SITES IN BARCELONA

5.1 Aims and Outcomes

The aim of these sample collections was the characterisation of the mass-size distribution of total particulate mass in urban roadside, urban background and rural background environments, to determine what differences exist in the absolute magnitude and shape of the distributions at sites with different source impacts.

These goals were accomplished by the use of nanoMOUDI and MOUDI instruments to collect suspended particulates onto PTFE filters, weighed under controlled conditions as described in Chapter 2, to enable determination of total mass in each of a number of size fractions so that size distributions could be plotted.

5.2 Mass-size Distributions of Particulate Matter

Size-segregated filter samples were collected at 6 sites using nanoMOUDI and MOUDI instruments. These were roadside sites in Birmingham, Newcastle and Barcelona, urban background sites in Birmingham and Barcelona and a rural background site at Harwell in central England. Particulate mass distributions were found to be quite variable not only between sites but also between different sample sets at the same site. This demonstrates how sensitive PM concentrations at a given location can be to a range of factors, such as meteorological conditions including precipitation, wind direction, temperatures and sunlight and to changing patterns of local emissions (Price et al., 2014; Wu et al., 2015). Due to our samples being time-averaged over relatively long periods, we do not have the time-resolution necessary to assess such short-term changes easily.

Comparison to the pollutant and meteorology data from the Automatic Urban and Rural Network has been used to help validate the data. Generally, it was found that the PM_{10} values

from the AURN correlated quite well with PM_{10} values obtained by summing collected masses of nanoMOUDI filters, although the AURN values are generally higher. A possible explanation for this is that the low pressures inside the instrument (especially in the finer stages) make nanoMOUDI and MOUDI instruments very prone to losing volatile material (such as nitrates) over longer sampling periods (Delgado-Saborit et al., 2014; Singh et al., 2003).

5.2.1 Birmingham Filters

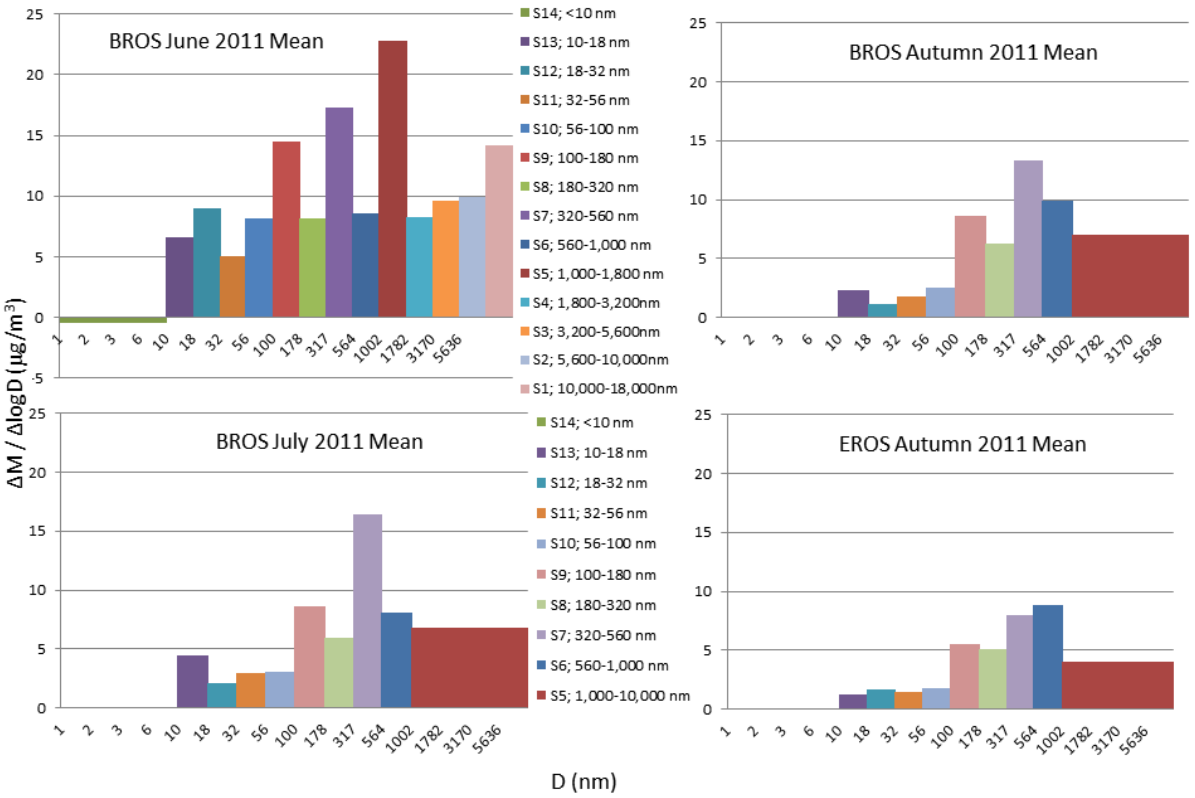

Figure 58. 2011 Birmingham nanoMOUDI mass distributions.

The first sets of samples collected in Birmingham were 3 and 4 day samples collected at the Bristol Road (*Figure 58*, upper left) in 6 batches from 7-6-11 to 30-6-11. The sampling pattern set 3-day samples in midweek (Monday-Thursday) and 4-day samples from Thursday-Monday over the weekend. The results of these early samples were unusual in the light of the later data, as the 7-day samples collected at the site generally show certain characteristics which are not clear in these samples. One anomalous mass value was excluded from the calculation of mean and standard deviation of mass concentration.

The mean distribution in June showed some odd features, in particular the peak at 1000-1800 nm. Generally in the later samples, a minimum was seen at this size range. However, the submicron distribution was more conventional showing two features that are largely

consistent at this site throughout all the sampling periods in Birmingham – peaks at 100-180 nm and 320-560 nm.

In subsequent samples all PM >1000 nm was collected on stage 5 to save on filters and preparation time, the upper stages being removed. The loss of size resolution in the data above 1000 nm was not considered a great loss as the priority was the analysis of ultrafine material.

The most significant feature in the second batch of samples (5 sets from 8-7-11 to 25-7-11) was the peak in the 320-560 nm size fraction (*Figure 58*, lower left). This was characteristic of the Birmingham samples from this sample onward, and from the BROS/EROS samples it would also appear there was a substantial roadside increment in this fraction. A mass peak at 500 nm was also reported in a previous study at the Elms Road site which establishes that our results are in line with existing data (Taiwo et al., 2014), although the exact size and position of the submicron fine mode were variable, being broader in some samples than others.

From the TEM studies on samples from this site (Chapter 7), it seemed that carbon-based soot aggregates characteristic of diesel soot grow considerable size and many such particles appeared in the 320-560 nm size range. Agglomerated iron oxide nanoparticles were also commonly observed in this size range.

5.2.2 Simultaneous Roadside/Background Samples, Birmingham

To make full use of the availability of two equivalent nanoMOUDI instruments, the loaned HPA instrument was located at the Elms Road site in September 2011 to carry out concurrent sampling at the roadside and urban background with the aim of establishing which size fractions were most traffic impacted. The two instruments were tested side-by-side at the roadside site to ensure comparability, yielding a correlation (R^2) between them of 0.93.

The distribution observed in the autumn samples at the roadside site (10 sets from 6-9-11 to 16-11-11) was essentially very similar to the July distribution in both distribution shape and absolute concentrations (*Figure 58*, upper right). The characteristic peak at the 320-560 nm is slightly less prominent in this case. There was also a small mode at 100-180 nm, the upper end of the pseudo-ultrafine fraction which has previously been associated with emissions from heavy-duty diesel engines (Ntziachristos et al., 2007).

The background site distribution (*Figure 58*, lower right) was similar in shape with slightly smaller absolute concentrations. The main difference was that the submicron fine mode is broader at the background site and the peak shifted slightly to a larger size, so that the concentration was reduced at 320-560 nm compared to the roadside but the concentration in the 560-1000 nm size range was larger. This could indicate continued particle growth as particles disperse away from the roadside. This was a slightly broader distribution of this mode than was indicated by Taiwo et al. (2014) at this site but generally agreed with previous results (Taiwo et al., 2014).

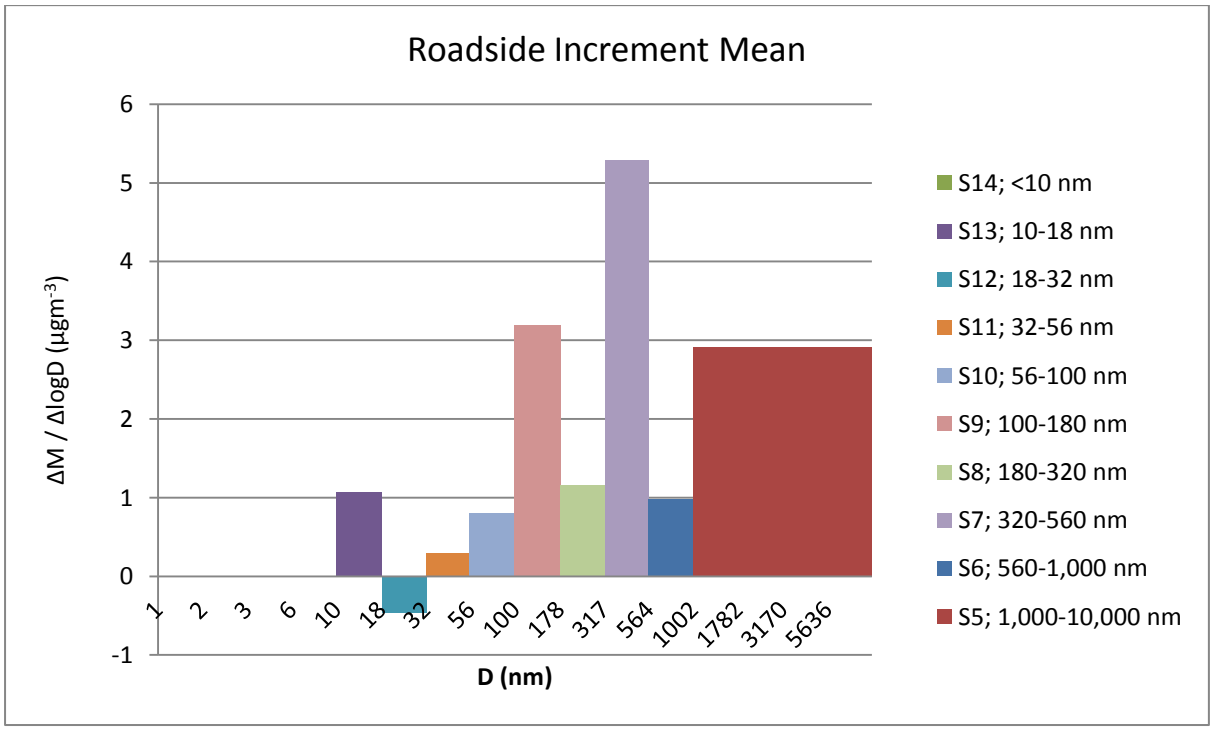

Figure 59. Mean roadside increment (BROS – EROS) September-November 2011.

Important roadside increments (Roadside minus Background for each stage in each sample) were found in three size ranges (*Figure 59*) – 10-18 nm, 100-180 nm, 320-560 nm and >1000 nm. The large coarse increment can probably be attributed to abrasive and resuspension processes such as brake wear, tyre wear and road dust resuspension, while the increment in the nucleation mode (10-18 nm) is more difficult to attribute. New particle formation by nucleation typically forms particles smaller than this, although these grow very rapidly. However nucleated material tends to be semivolatile and may be subject to evaporative losses in the impactor (Singh et al., 2003). The primary particle size was similar to the primary particles of metallic oxides discussed in Chapter 7, but it was generally found that those particles agglomerate readily. The two increments at 100-180 nm and 320-560 nm matched the submicron modes observed in the Birmingham Roadside samples. In one stage (S12, 18-32 nm) the increment was reversed so that the background site concentration is greater than the roadside. This may not be significant, but it was also possible that the effect is caused by continuing particle growth away from the roadside. The collected masses from which the increments were calculated were above limits of detection, although some of the increment values were smaller than these limits.

5.2.3 Simultaneous MOUDI/NanoMOUDI collection, Birmingham

Samples were collected for analysis of metals and soluble ions in spring 2013 at BROS. Mass data for 5 sets of nanoMOUDI samples is available and presented below. Only 4 MOUDI samples are available as the instrument was removed to prepare for transport to Barcelona.

The mean distribution (*Figure 60a*) from the nanoMOUDI samples illustrates the features we have previously found to be typical of samples collected in Birmingham, a trimodal distribution in which there is a large coarse peak, a submicron fine peak at 320-100 nm and a pseudo-ultrafine peak from 100-180 nm.

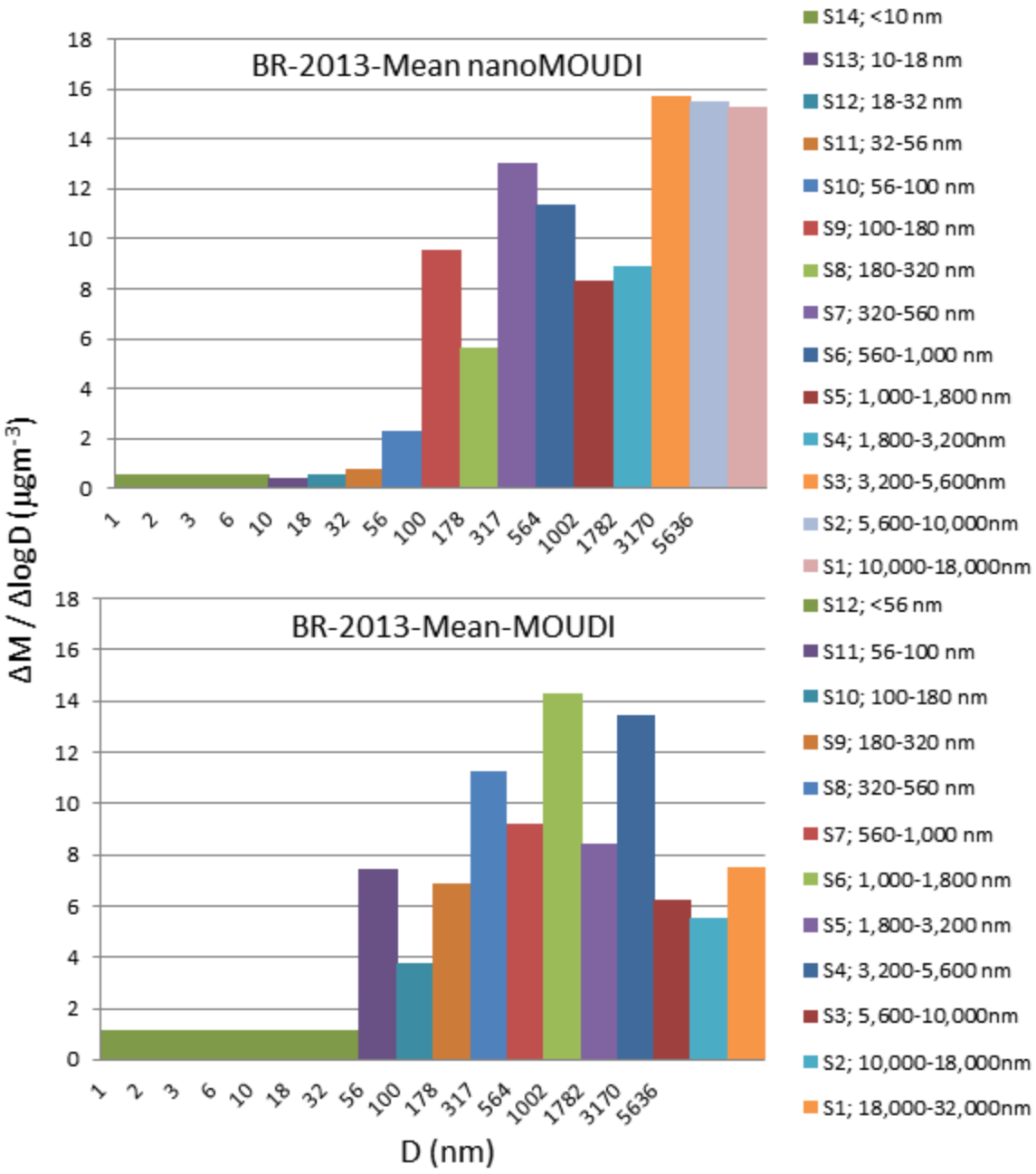

Figure 60a. Mass-size distributions from nanoMOUDI and MOUDI, Birmingham (Rs), 21-3-2013 to 23-5-2013, in µgm^{-3}.

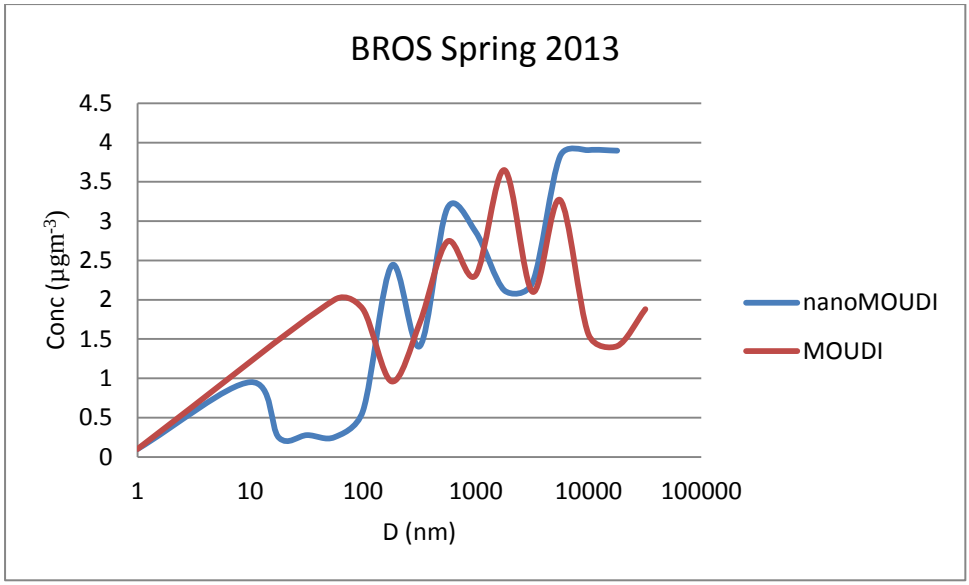

Figure 60b. Mass-size distributions from nanoMOUDI and MOUDI (same axis), Birmingham (Rs), 21-3-2013 to 23-5-2013, in µgm^{-3}.

Concentrations in the ultrafine were very low in these samples, while the coarse mode concentrations were slightly higher than in the 2011 examples. The coarse mode has been reported to correspond principally to emissions from brake wear, tyre wear and road dust resuspension at roadside urban sites in the UK (Harrison et al., 2012). The close proximity of the road, which is heavily trafficked and has a substantial proportion of heavy-duty vehicles, probably accounts for the pseudo-ultrafine load, which may be caused by large diesel engines.

There were some deviations from the mean distribution among these samples, in particular the sample starting 11-4-13 in which the usual submicron mode was absent, but a broad mode from 1000 -5600 nm was present. This also contrasted with the normal pattern of the coarse peak starting at around 3200 nm. The preceding sample, starting 4-4-13, was also somewhat unusual, exhibiting a very weak coarse mode and highly exaggerated submicron fine peak. This was more similar to the earlier samples collected at BROS in which the nanoMOUDI was operated collecting all the supermicron particulate on one filter. It was found that

collecting S1-5 on one filter did not have any meaningful effect on the shape of the submicron distribution.

The MOUDI distribution (*Figure 60b, lower*) did not agree very well with the nanoMOUDI distribution. Although the fine mode peak (320-560 nm) appeared similar, the ultrafine mode appeared in the true ultrafine at 56-100 nm instead of pseudo-ultrafine and the coarse distribution was different as well.

The correlations between PM_{10} showed some variation, although the small number of concurrent samples makes this difficult to assess. The $PM_{0.1}$ correlation was poor. One possibility is that the two instruments have different collection characteristics for ultrafine particles. Liu et al. (2013) reported significant interstage losses for nanoparticles in the upper stages of the MOUDI and hypothesised that this would be even worse when collecting particles below 56 nm in nanoMOUDI instruments (Liu et al., 2013).

5.2.4 Harwell Rural Background Samples

These samples had to be collected over 14-day periods owing to the low masses collected, confirmed by visual inspection on 14/12/11. The values correlate quite well with the AURN PM_{10} values, which gives some confidence in the mass data. The characteristics of the size distributions are distinctly different to the urban sites.

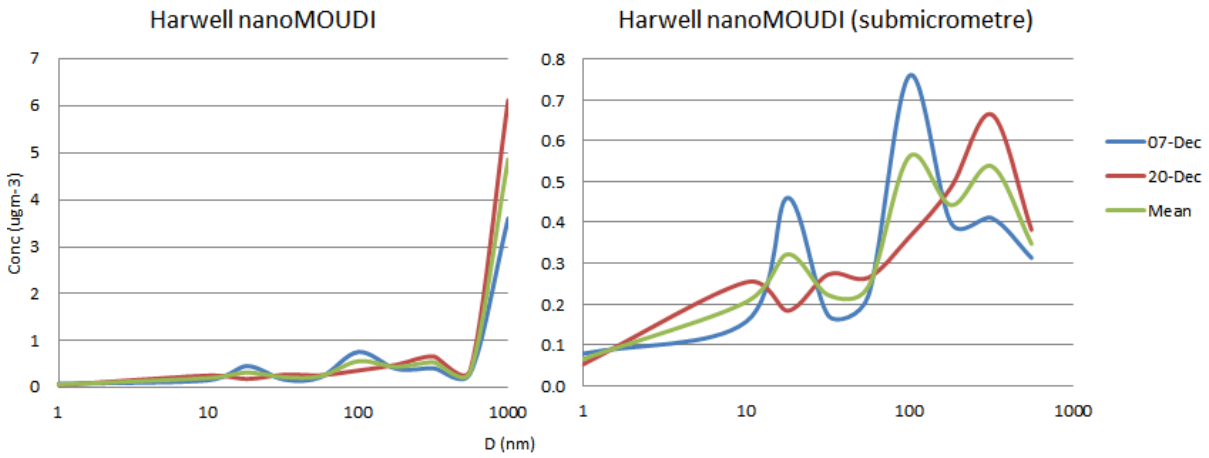

Figure 61. Mass distribution in Harwell samples, 7-12-11 to 4-1-12, in µgm^{-3}.

The plots above (*Figure 61*) illustrate that a very large coarse mode was the dominant feature of the Harwell data and a comparatively small proportion of the total mass appeared in particles below 1 µm in diameter. The submicrometre distributions were slightly different, despite both being time-averaged over two weeks. Unfortunately we do not have summer distributions for the site, which might show different characteristics. In most stages the absolute concentrations were slightly higher in the second sample (HW-20-12-11, see *Figure 61*). The only major differences in the distributions were the two peaks in the HW-7-12-11 (*Figure 61*) distribution at 180-320 nm and 32-56 nm. The larger of these two size fractions represents a fraction where large soot agglomerates from heavy-duty vehicles are often observed and in which a large roadside increment was observed in Birmingham, so it is most likely that there was more traffic input into the first sample. Although the > 1µm fraction was larger in the second sample, larger particles do not travel as far from the road, which may help to explain the change in distribution. There is likely to be little industrial contribution to the PM burden at the site and the power station at Didcot, though operational at the time of sampling, is quite distant and ran on natural gas at the time of sampling, so was unlikely to make a large contribution. Although the roads around the Harwell campus are not heavily

trafficked and the main road is quite a long way from the site, vehicles probably represented the main local particulate contribution.

5.2.5 Newcastle Samples

From January to July 2012, the nanoMOUDI and 12-stage MOUDI (operating as 10-stage) were collected at the AURN station at Newcastle Civic Centre. The initial rationale for the location was to try to detect Ce in the ambient particulate matter originating from the use of Envirox by the local bus company Stagecoach. Envirox is a nanoparticulate CeO_2 additive used in diesel fuel as an oxidising catalyst to improve fuel combustion and reduce total particulate emissions. Evidence suggests that the size distribution as well as total mass is changed when oxycatalysts are used (Jung et al., 2005; Park et al., 2008). However, having an urban site to compare to the Birmingham locations was also a benefit.

Stage	**Lower Cut/nm**	**Mean/µgm^{-3}**	**Median/µgm^{-3}**	**Stdev**
5	1000	4.206	3.813	1.973
6	560	1.215	0.773	2.029
7	320	1.454	1.190	0.892
8	180	1.190	0.899	0.766
9	100	0.819	0.650	0.517
10	56	0.448	0.370	0.224
11	32	0.382	0.352	0.181
12	18	0.364	0.326	0.242
13	10	0.422	0.315	0.311
14	1	0.263	0.206	0.206
PM_{10}		10.763	9.985	4.356
$PM_{0.1}$		1.879	1.911	0.683
Avg Ambient Temp /°C		6.892	7.269	3.113

Table 28. Mean and Median mass distributions, Newcastle.

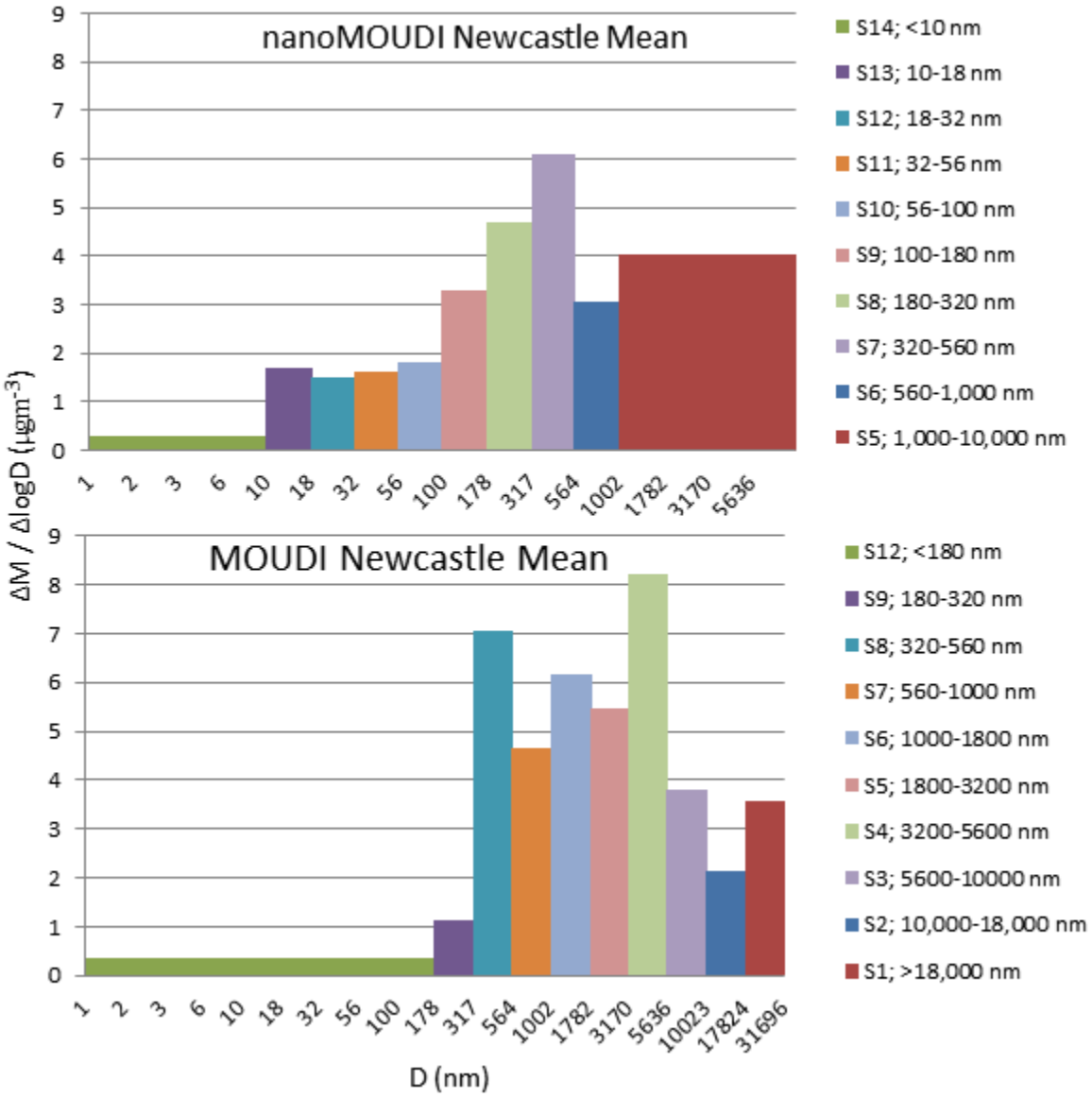

Figure 62. Mean mass size distributions, Newcastle nanoMOUDI and MOUDI.

Newcastle's mean mass distribution (*Figure 62*) showed a broad mode peaking in the 320-560 nm size range with quite a large coarse fraction. The minimum was at 560-1000 nm which is quite typical of urban PM samples. The distributions were quite variable within the set (see Appendix A for tabulated data) even if the sample for 25-4-12, which had unusually high values in stages 6 and 8, was excluded. A pattern of bimodal distribution with coarse and submicron peaks was generally followed. In some samples, such as 12-4-12 and to a lesser extent 9-2-12 the submicron peak was found in to the 180-320 nm size range. The first

sample (12-1-12) had a large peak extending from 100-560 nm. Compared to Birmingham, the Newcastle samples showed a similar mode at 320-560 nm, but generally the mode found at BROS in the 100-180 nm size fraction was absent. Instead there was a smooth drop in concentrations from the 320-560 nm peak to the low concentrations observed in the ultrafine. It is not clear why, as the dominant sources at both sites were quite similar and because of the bus routes passing the Newcastle site there was still a large amount of heavy duty traffic. There were fewer heavy goods vehicles passing the Newcastle site, which may have some influence.

Because most of the size bins in the MOUDI instrument are above 1 μm, the distribution (*Figure 62*) visually appears quite different to the nanoMOUDI distribution but it does preserve the same key features. These were; firstly that the peak at 320-560 nm which is seen in the nanoMOUDI data was also present, and secondly that the minimum in the stage above (560-1000 nm) was also observed. Compared to the MOUDI distributions from Barcelona, this plot showed a similar minimum at 10000-18000 nm and a peak at 3200-5600, which in the Barcelona data corresponds to the brake wear elements. However, the submicron distribution was slightly different as the peak was lower.

Previously reported results from a number of studies and locations certainly indicate that this is typical. Keywood et al. (1999) stated that there was no correlation between ultrafine particle mass concentration and either PM_{10} or $PM_{2.5}$ (Keywood et al., 1999).

Although the dependence was not strong, there was a trend towards lower PM_{10} concentrations when the average temperature across the sampling period is higher. A possible explanation for this phenomenon is nitrate evaporation at higher temperatures. *Figure 63* confirms that the submicron fine peak is much smaller in the higher-temperature group. Predicting new particle formation events would be extremely complex, as several factors

must be considered. While enhanced photochemistry on sunny days would cause an increase in new formation, greater atmospheric turbulence would cause more dispersion (Ma and Birmili, 2015). Furthermore, vapour condensation is favoured by lower temperatures. Given that nucleation events tend to be short-term, long-term time averaged mass data are unlikely to offer much insight, as the short-term variations are averaged out.

Dividing the samples into those with an average temperature above or below 7°C shows that the distributions are broadly very similar but that one fraction in particular – 10-18 nm (Stage 13) – did increase in at higher temperatures, which would support the idea of greater new particle formation, as this has been found to take place at particle sizes below 20 nm (Viana et al., 2015).

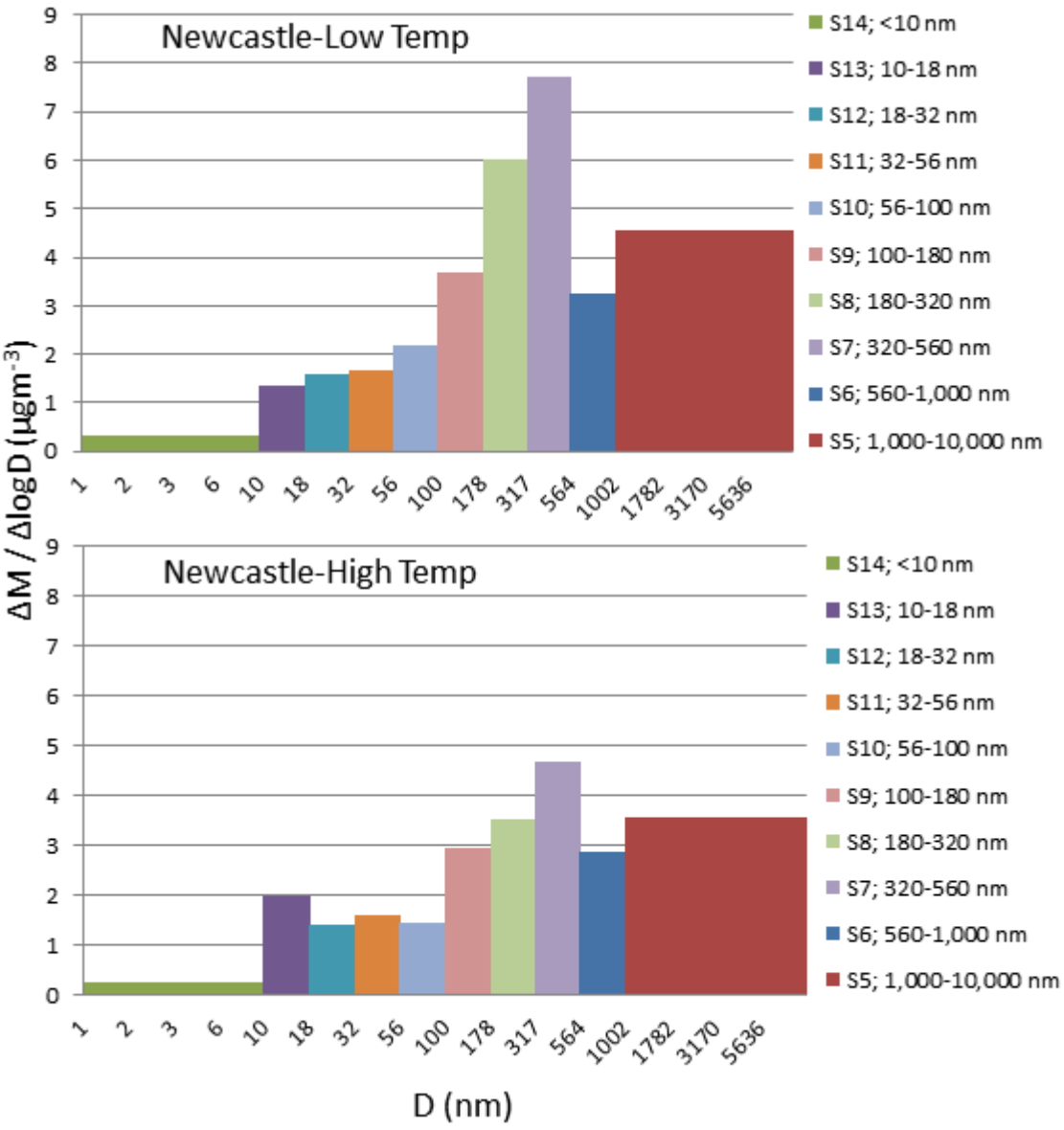

Figure 63. Mass size distributions above (top) and below (bottom) mean temperature during sampling of 7°C.

A similar pattern of temperature dependence was observed for the MOUDI data as for the nanoMOUDI data – PM_{10} was observed to decrease at higher temperatures while $PM_{0.18}$ (pseudo-ultrafine) was observed to increase with increasing temperature.

This appears to be the first extended impactor-based sampling campaign at the site, so it is not possible to make any detailed comparison of our data to prior results.

In 2004, Cabada et al. reported that mass concentrations in all size fractions below $PM_{2.5}$ were found to increase during periods of higher temperature, which is consistent with our results (Cabada et al., 2004).

5.3 Comparisons to AURN data

Data on a range of pollutants is available from the Automatic Urban and Rural Network (AURN) monitoring station and some comparisons with our data are discussed below. Full correlation matrices are presented in Appendix C.

The Newcastle Central AURN station was also the location for the MOUDI and nanoMOUDI for that sampling campaign. The nearest equivalent AURN stations to the BROS and EROS sites are the Birmingham Tyburn Roadside and Birmingham Tyburn sites, respectively. Site descriptions can be found in Chapter 2.

PM_{10} from the AURN stations, averaged over the same sampling periods, correlated quite well with the PM_{10} concentrations calculated from the nanoMOUDI data (R^2 = 0.7-0.8, except at BROS, see Appendix C). The nanoMOUDI concentration was often lower than the AURN concentration, which may be attributed to the loss of volatile material over the 7-day sampling period. The strong correlation at Newcastle is expected due to the co-location of samplers, with corresponding similarity of source inputs and local conditions. As noted in the Methodology (see Chapter 2 for details), the nearest equivalent central monitoring point to the BROS site is on the A38 at Tyburn roadside, north of the centre of Birmingham. Consequently the correlations between pollution parameters at this site and the nanoMOUDI data were not as good as at the Newcastle site where the AURN station and the nanoMOUDI were co-located. However, while this is true at BROS, the correlation at EROS was higher than at Newcastle. It can be inferred that background concentrations are more consistent

across an urban area when averaged over long times, compared to kerbside readings which will change significantly with changing local conditions.

Cabada et al. (2004) reported that concentrations of PM_{10} recorded by an integrated sampler correlated well with summed PM_{10} from a MOUDI, although the MOUDI consistently reported at approximately 20% lower (Cabada et al., 2004). In the data reported in this chapter, the nanoMOUDI reports an average of 6.51% lower at BROS, 45.97% lower at EROS and 39.8% lower at Newcastle. The difference between BROS and the other sites could be explained by the unavailability of some AURN data from July 2011, the warmest period of the year when the difference between the two methods would be expected to be largest.

5.3.1 Temperature dependences

At the Birmingham sites no consistent relationship in either direction was found between temperature and either PM_{10} or $PM_{0.1}$ – R^2 values were below 0.05. At the Newcastle site PM_{10} correlated better (R^2 = 0.37), but $PM_{0.1}$ was similar to the Birmingham sites (see Appendix C).

5.3.2 NO_x correlations

Using the NO_x concentration from the AURN station as a proxy for exhaust emissions should correlate well with the ultrafine particle concentrations from the nanoMOUDI, but this was not the case at any of the three sites. Correlations between $PM_{0.1}$ and AURN NO_x data were found to be quite poor in this data, correlation coefficients below 0.12. PM_{10} correlated very poorly at the Birmingham sites, but the PM_{10}/NO_x correlation was 0.7 in Newcastle. This was consistent with expectation based on the spatial distance between the Tyburn sampling sites

and the campus sites (BROS and EROS) and the consequent differing local conditions impacting NO_x and PM levels at the two sites.

While it might be expected that the two stages containing the submicron modes would correlate with PM_{10}, as these are primarily traffic influenced this was not found to be the case.

It seems that when comparing NO_x to PM, co-location of samplers is important, because in the Newcastle data plotting NO_x correlations for individual stages showed that the nanoMOUDI data correlated best in the range 180-320 nm (Stage 8). Stages 7 (320-560 nm) and 9 (100-180 nm) also exhibited quite strong correlations. That of the fractions below 100 nm was weaker – Stage 10 (56-100 nm) had an R^2 value of only 0.19 and the lower stages had even weaker correlations than this. It is not clear whether this was because of the proportionally greater uncertainties in the small mass concentrations in these stages however.

NO_x concentrations have previously been found to correlate well with ultrafine particle number concentration (Eeftens et al., 2015). Attempting to correlate with UFP mass, especially at spatially separated sampling locations, is found to be very difficult owing partly to the long sampling times necessary to collect UFP for analysis.

5.3.3 Correlations between MOUDI and AURN data

Broadly similar conclusions can be drawn from the Newcastle MOUDI data. PM_{10} calculated from the MOUDI filter concentrations correlated quite well with the AURN data while plotting the AURN NO_x concentrations against pseudo-ultrafine mass concentrations produced poor correlations (Table 5, Appendix C).

Interestingly it was found that the MOUDI data also correlated best with the AURN NO_x data in the same size fraction (320-560 nm) as shown above while the coarse mode peak did not

correlate as well which implies more diverse sources of coarse particles. From these plots we can infer that the submicrometre mass peak in the Newcastle data was primarily caused by traffic.

Assuming that NO_x represents a proxy for traffic contribution, the Newcastle samples would suggest that the major traffic contribution at that site came in a range approximately between 100 nm D_a and 560 nm D_a. From TEM analysis of the samples collected in Birmingham and Newcastle, it seems that this broad size range was dominated by carbonaceous soot agglomerates probably originating in diesel combustion. This size range also included Fe and Pb particles of several distinct physico-chemical types which may originate in vehicle engines (see Chapter 7 for a full analysis).

5.4 Cumulative Mass Distributions

The cumulative mass distributions for the four British sites varied considerably.

Stage	D/nm	B'ham Rs	B'ham Bg	Harwell	Newcastle
5	10000	100	100	100	100
6	1000	45	66	39	61
7	560	37	47	34	50
8	320	26	31	28	36
9	180	21	20	22	25
10	100	14	15	14	17
11	56	11	11	11	13
12	32	9	8	8	10
13	18	4	5	4	6
14	10	1	2	1	2

Table 29. Cumulative percentage total mean mass in nanoMOUDI data from UK sampling sites.

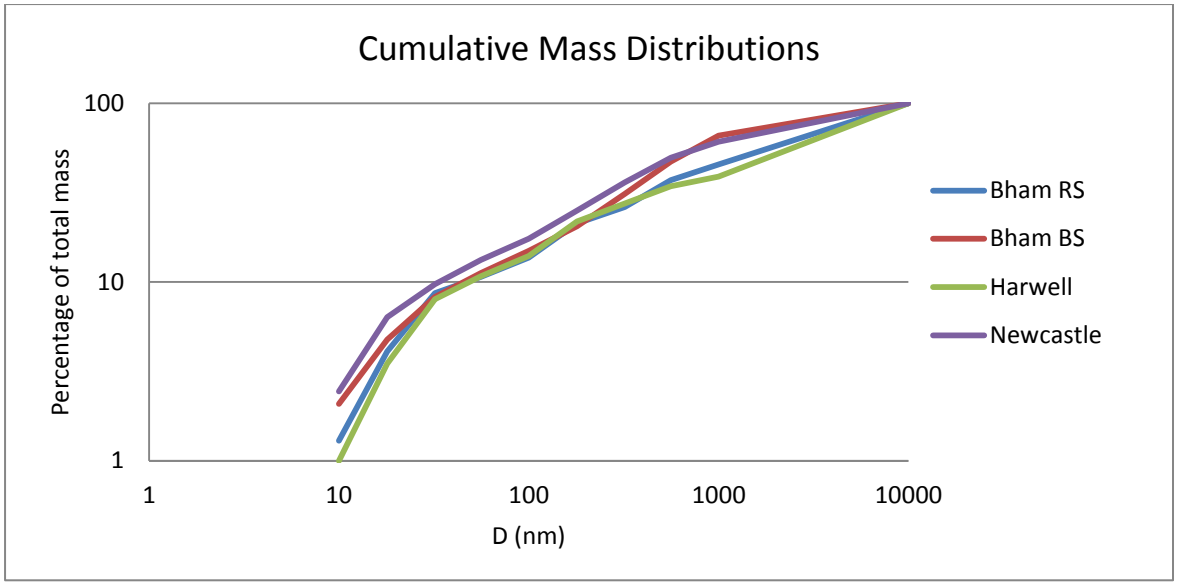

Figure 64. Cumulative nanoMOUDI mass distribution graph, UK sites.

At Harwell, the contribution of the submicrometre particles was quite small, especially in the second sample in which the >1000 nm mass accounts for over 67% of the total. Plotting the cumulative mass distribution makes it clear how high the proportion of the total PM accounted for by material exceeding 1µm actually is.

This would indicate that PM at the Harwell site is dominated by resuspension processes, such as windblown dust and soil. As *Figure 64* shows, the cumulative distribution from the BROS site was more similar to Harwell than to either of the other sites, thanks to its higher coarse mass percentage. This site has a greater contribution from abrasion and resuspension sources than the other urban sites due to the close proximity of the road and a junction at which vehicles are braking and restarting, so it could be suggested that different sources are contributing a large percentage of mass to the same fraction.

The cumulative distribution from Elms Rd (*Figure 64*) confirms the importance of the broad fine mode peak in the mass data from this site. This is much more similar to the distribution from Newcastle than to Harwell or BROS.

The cumulative mass distribution (*Figure 64*) indicates that around 60% of the total mass collected is below 1µm in diameter. This is a much higher percentage than at Harwell or BROS, where submicron particulates accounted for less than 50% of total collected mass, but quite similar to EROS.

It should be noted that none of the distributions bear a close resemblance to the cumulative mass distributions for brake wear presented in Chapter 3. However, our brake wear data are limited in scope and not likely to be representative of the vehicle fleet as a whole. Furthermore, the characteristics of the total suspended brake wear component at each site are likely to be different owing to differences in driving conditions and fleet composition.

5.5 Internal correlations in nanoMOUDI data

At BROS, EROS and Newcastle it is observed that correlations between $PM_{0.1}$ and PM_{10} obtained from the nanoMOUDI are generally weak. Too few samples were collected at Harwell to permit a similar analysis. Similarly poor correlations between different particulate size ranges have previously been reported for six Australian cities by Keywood et al., who stated that there was not a consistent relationship between ultrafine particles and fine and coarse mode particles (Keywood et al., 1999).

5.5.1 PM_{10} vs $PM_{0.1}$ Correlations: Bristol Rd, Elms Rd and Newcastle

It is found that the fine mode peak (S7, 320-560 nm) tends to correlate better than the UFP concentrations with PM_{10} at all three sites (*Tables 2-4, Appendix C*). In 2004 Cabada et al. reported that correlations with PM_{10} and $PM_{2.5}$ became weaker as smaller size fractions were plotted, and this trend is evident in the data presented in *Appendix C* (Cabada et al., 2004).

Comparing the fine peak to the ultrafine and pseudo-ultrafine might help to establish which sources are contributing most to the submicron fine mode. Plotting individual stages against

each other to establish correlations shows clearly that the peaks in the nucleation mode (S13, 10-18 nm) correlate poorly with the submicron fine peak. The correlation at BROS was slightly better than the other sites which could suggest that the nucleation mode correlates better with the fine if a road is in the immediate vicinity (kerbside sampling).

5.5.2 Modally defined correlation plots

A general rule would be that the fine mode peak correlated quite well with a soot mode (defined by summing S9-11, 32-180 nm) at the roadside sites but very poorly with a nucleation mode (summed stages 12-14, particles <32 nm). This relationship appeared to break down at the background site.

5.5.3 Correlations between soot mode and nucleation mode

At both Birmingham sites some correlation was found between the soot mode and nucleation mode albeit with some variability, the R^2 values being 0.39 at BROS and 0.44 at EROS. The Newcastle coefficient was affected by two outliers which made the R^2 value very small (<0.0001). The two outliers did not represent unusual conditions from the NO_x data, PM_{10} or average temperature, so it is difficult to explain them with reference to the supporting data. It has been suggested by earlier studies of particulates in urban areas that the nucleation mode is primarily formed of condensed sulphate material and organic precursors, while the soot (accumulation) mode is formed of carbonaceous particles and other solid-phase material (González and Rodríguez, 2013). This difference in sources appears to be reflected by the correlation coefficients which were below 0.5 for all three sites.

Since the size range 32-180 nm is associated with soot exhaust emissions especially from heavy-duty diesel engines (Ntziachristos et al., 2007), it can be said that vehicle emissions are a significant contributor to the submicron fine mode at our sites. Correlating this with the

nucleation mode is difficult because of the nature of our data, which is time-averaged over long sampling periods. The nucleation mode is formed mostly from condensation of organics and sulphates and is a transient phenomenon heavily influenced by local meteorology and chemistry on a short-term basis (Viana et al., 2014). Consequently these inherent variations overwhelm any correlations in long-term datasets. Real-time monitoring would be necessary to establish the relationship between nucleation mode and fine particles more effectively.

5.6 Barcelona

Tabulated concentration data are presented in full in Appendix A. Filters were weighed (pre- and post-sampling) by the author in Birmingham. The instruments were operated by the author for the first sample (starting 3/5/13) to demonstrate use, while the remainder were collected by Dr Amato and Dr Karanasiou (*see acknowledgements*).

5.6.1 Mass distributions at the Roadside site

The roadside component of the Barcelona MOUDI dataset for AIRUSE consisted of 6 sets of 12 filter samples, collected using the 12-stage MOUDI 110R at the roadside at 445 Valencia Street, Barcelona between 3rd May and 6th June 2013.

In stage 9 (filter 10) of the MOUDI a problem (unknown cause) with the nozzle plate caused material to pass through to the next stage, so filters 10 and 11 (56-180 nm) were combined in these plots. This produced a bimodal distribution in these data which is much more in line with expectation. Most samples exhibited minima at the 560-1000 nm and 10000-18000 nm stages (filters 6 and 2).

The PM_{10} concentrations collated by summing up from filters 2-12 were unusually low given the heavy traffic impact on the site, city centre location and confined location. However, concentrations recorded in street canyon environments can vary considerably depending on

variations in local meteorological conditions as wind speed and direction exert a strong influence on the dispersion of particulates in such an environment (Vardoulakis et al., 2003). Consequently, concentrations ranging from background levels to highly elevated may be observed.

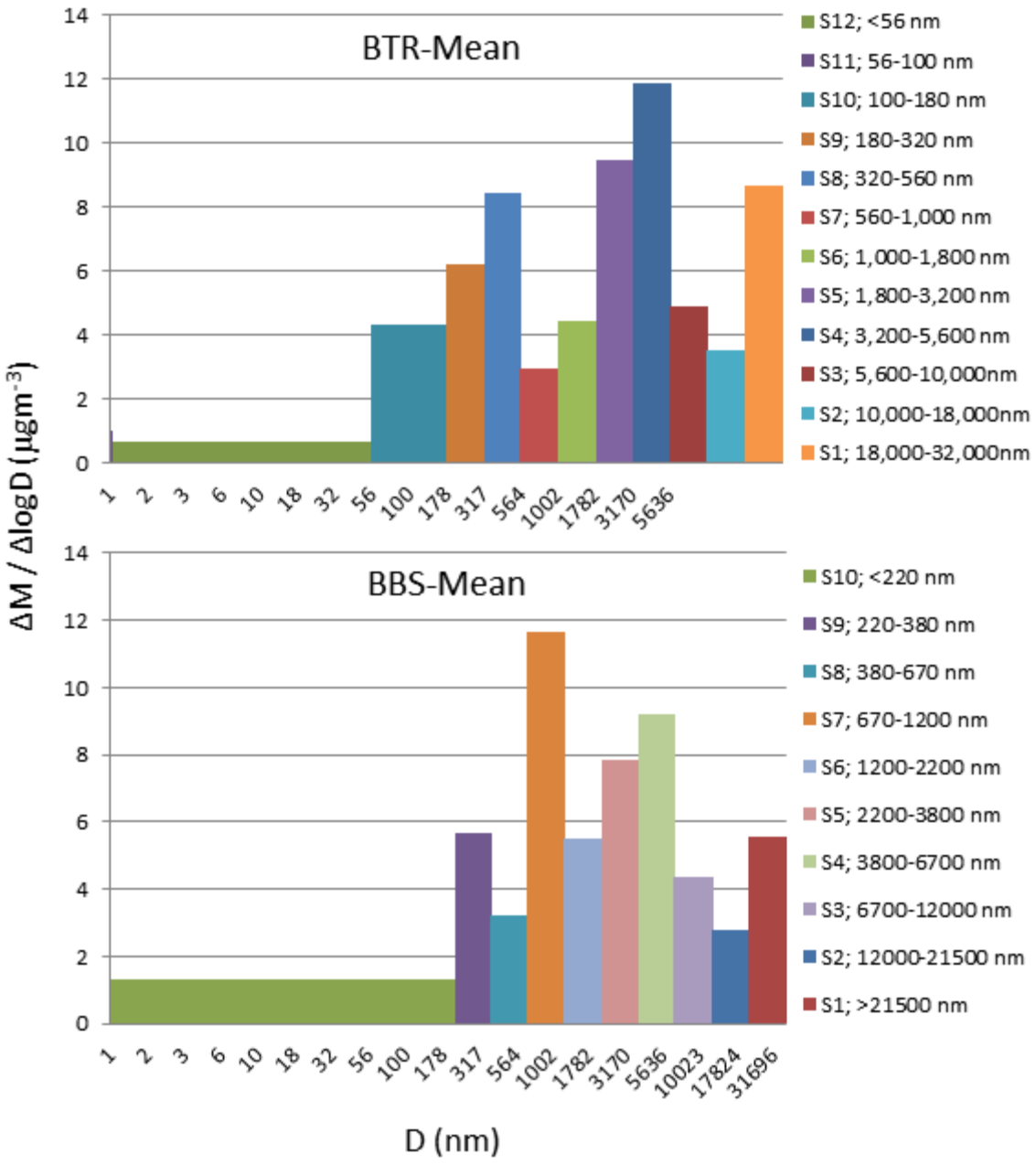

Figure 65. Barcelona Roadside and Background mass-size distributions.

As *Figure 65* shows the mean roadside distribution was bimodal for PM_{10} with a coarse mode and submicron fine mode. These features were generally consistent through the individual

samples but some subtle variations were found. The BTR-9-5-13 sample illustrated the bimodal distribution typical of urban PM samples, with minima around 1 µm to 10 µm. The unusual feature compared to the later samples was the very high mass concentration in the 1.8 µm – 5.6 µm range. In the BTR-13-5-13 sample the usual bimodal distribution was present, and a very high concentration in the 18 µm range. Since this filter is directly below the inlet, the concentrations recorded on it were quite variable. The sample from BTR-16-5-13 demonstrated a pronounced bimodal distribution with minima at 1 µm and 10 µm. BTR-21-5-13 exhibited pronounced minima at 1 µm and 10 µm. BTR-5-6-13 shows lower coarse mode concentrations.

Overall the kerbside distributions in Barcelona formed a useful comparison to the Birmingham samples. The presence throughout of a strong peak between 320-560 nm diameter was a common feature at both roadside sites and is therefore likely to be an indicator for high traffic contributions.

5.6.2 Mass distributions at the Urban Background site

There are 7 available datasets collected from 9th May to 11th June 2013 using a 10-stage MOUDI (Model 100). The sampled flowrates were consistent at 21-22 l/min, which is below the designed level of 30 l/min, and the cutpoints were recalculated accordingly.

Averaging the distributions preserves certain features which were common across the samples, such as the large coarse mode and the minimum in the 380-670 nm size ranges, but emphasises the peak at 670-1200 nm which was not present in all samples. The mass distributions from this instrument showed considerable variability from sample to sample. For example, BBS-9-5-13 exhibited an unusually pronounced minimum at 1200 nm. BBS-13-5-13 was the only sample in the batch where the 670-1200 nm peak extended into the

1200-2200 nm fraction, with the normal coarse mode relatively reduced. The BBS-16-5-13 sample showed a high proportion of mass in the pseudo-ultrafine size range.

BBS-27-5-13 was the most similar to the roadside distributions. The minima were found at 1200-2200 nm and 12000-21500 nm with high concentrations in the coarse mode and low levels of accumulation mode particles. Coarse mode distribution in the BBS-5-6-13 sample was consistent with the other samples but the sample also contained a very large peak below 1200 nm. The striking feature of the BBS-11-6-13 distribution was the high concentrations in the submicron range; while the normal coarse mode peak was still present it was overshadowed by the high fine concentrations.

5.6.3 Correlations within MOUDI data

At the background site, there was not a clear correlation between PM_{12} (coarse) and $PM_{0.22}$ (pseudo-ultrafine) particulate mass concentrations (*Table 7, Appendix C*). This was consistent both with the data presented for the Birmingham and Newcastle sampling sites and with previous studies (Keywood et al., 1999) showing similar characteristics. At the roadside site there was one outlier (BTR-9-5-13) which had a very large coarse mode, but if this is removed a fairly strong correlation was observed between PM_{10} and $PM_{0.18}$.

The 5 concurrent samples were not really sufficient to be totally confident in the correlations. Furthermore the cutpoints were not quite equivalent between the roadside and background instruments. With the coarse correlation, the fine and coarse peaks will both be included in PM_{10} and PM_{12} so the difference should not be too significant, but for the pseudo-ultrafine, more of the broad fine mode peak will be included in $PM_{0.22}$ at the background than in $PM_{0.18}$ at the roadside, which might have been a problem.

		Background	
		PM_{12}	**$PM_{0.22}$**
Roadside	**PM_{10}**	0.56	0.17
	$PM_{0.18}$	0.09	0.65

Table 30. Correlation coefficients in coarse and pseudo-ultrafine particles between the two Barcelona sites.

Concentrations in similar size ranges were found to correlate to some extent (see *Table 30*), but correlations between coarse and pseudo-ultrafine correlations were very poor, similar to results from other sites. Viana et al. (2015) reported that particle size distributions at heavily traffic impacted schools in Barcelona were more reflective of fresh emissions, while those at low-traffic schools were indicative of aged emissions characteristic of the urban background (Viana et al., 2015). Therefore, there is evidence that a different distribution dominated by the accumulation mode would be expected for the background site. Since the background site in this case may also be heavily traffic impacted depending on the local conditions, the picture is likely to be complex and a much longer dataset would be required for a fuller analysis of the relationship between kerbside ultrafine particles and the urban background.

A value was obtained for PM_{10} at the roadside of 15.36 (SD 6.47) μgm^{-3}, with $PM_{0.18}$ at 3.38 μgm^{-3}, which was approximately comparable with Birmingham. Viana et al (2014) reported averages for $PM_{0.25}$ almost an order of magnitude greater than this, averaged across 39 school sites in Barcelona using PCIS instruments over 32 hr sampling periods (Viana et al., 2014).

5.7 Conclusions

Mass-size distributions were found to be variable at all the sites examined. In roadside environments, large coarse contributions were observed, as well as submicron fine modes. A

persistent feature of the data from the Birmingham roadside site was a peak in the upper pseudo-ultrafine (100-180 nm), but this was not seen at the other sites. In the Barcelona data this specific fraction could not be separated from the rest of the ultrafine owing to the cutpoints of the instruments, but it was not present at Newcastle. Urban background data from the background site in Birmingham a fairly similar distribution to concurrent roadside data but significant roadside increments were observed in three size ranges (100-180 nm, 320-560 nm and >1000 nm). Rural data from Harwell emphasised the importance of the coarse contribution while finer particles associated with combustion sources were far less important.

PM_{10} and $PM_{0.1}$ and/or $PM_{0.18}$ and $PM_{0.22}$ were not found to correlate. This was consistent with earlier studies and demonstrative of the difference in sources between large and small particles. Poor correlations were found between particulate mass data and NO_x data, but reasonably good correlations between PM_{10} calculated from nanoMOUDI data and central monitoring stations. Co-location of sampling equipment was found to be important for comparing monitoring data to impactor data. MOUDI and nanoMOUDI instruments were found not to produce identical distributions, indicating that there may be some differences in collection characteristics.

Future work probably needs to emphasise the simultaneous collection of multiple data. Comparison of concurrent roadside and background data has been valuable, but the addition of particle number data and measurements of gaseous pollutants simultaneously could help to develop understanding of the relationships between different pollutants and between mass, number and volume data.

References

Cabada, J.C., Rees, S., Takahama, S., Khlystov, A., Pandis, S.N., Davidson, C.I., Robinson, A.L., 2004. Mass size distributions and size resolved chemical composition of fine particulate matter at the Pittsburgh supersite. Atmospheric Environment 38, 3127-3141.

Delgado-Saborit, J.M., Stark, C., Harrison, R.M., 2014. Use of a Versatile High Efficiency Multiparallel Denuder for the Sampling of PAHs in Ambient Air: Gas and Particle Phase Concentrations, Particle Size Distribution and Artifact Formation. Environmental Science & Technology 48, 499-507.

Eeftens, M., Phuleria, H.C., Meier, R., Aguilera, I., Corradi, E., Davey, M., Ducret-Stich, R., Fierz, M., Gehrig, R., Ineichen, A., Keidel, D., Probst-Hensch, N., Ragettli, M.S., Schindler, C., Künzli, N., Tsai, M.-Y., 2015. Spatial and temporal variability of ultrafine particles, NO2, PM2.5, PM2.5 absorbance, PM10 and PMcoarse in Swiss study areas. Atmospheric Environment 111, 60-70.

González, Y., Rodríguez, S., 2013. A comparative study on the ultrafine particle episodes induced by vehicle exhaust: A crude oil refinery and ship emissions. Atmospheric Research 120–121, 43-54.

Harrison, R.M., Jones, A.M., Gietl, J., Yin, J., Green, D.C., 2012. Estimation of the Contributions of Brake Dust, Tire Wear, and Resuspension to Nonexhaust Traffic Particles Derived from Atmospheric Measurements. Environmental Science & Technology 46, 6523-6529.

Jung, H., Kittelson, D.B., Zachariah, M.R., 2005. The influence of a cerium additive on ultrafine diesel particle emissions and kinetics of oxidation. Combustion and Flame 142, 276-288.

Keywood, M.D., Ayers, G.P., Gras, J.L., Gillett, R.W., Cohen, D.D., 1999. Relationships between size segregated mass concentration data and ultrafine particle number concentrations in urban areas. Atmospheric Environment 33, 2907-2913.

Liu, C.-N., Awasthi, A., Hung, Y.-H., Tsai, C.-J., 2013. Collection efficiency and interstage loss of nanoparticles in micro-orifice-based cascade impactors. Atmospheric Environment 69, 325-333.

Ma, N., Birmili, W., 2015. Estimating the contribution of photochemical particle formation to ultrafine particle number averages in an urban atmosphere. Science of The Total Environment 512–513, 154-166.

Ntziachristos, L., Ning, Z., Geller, M.D., Sheesley, R.J., Schauer, J.J., Sioutas, C., 2007. Fine, ultrafine and nanoparticle trace element compositions near a major freeway with a high heavy-duty diesel fraction. Atmospheric Environment 41, 5684-5696.

Park, B., Donaldson, K., Duffin, R., Tran, L., Kelly, F., Mudway, I., Morin, J.-P., Guest, R., Jenkinson, P., Samaras, Z., Giannouli, M., Kouridis, H., Martin, P., 2008. Hazard and Risk Assessment of a Nanoparticulate Cerium Oxide-Based Diesel Fuel Additive—A Case Study. Inhalation Toxicology 20, 547-566.

Price, H.D., Arthur, R., BéruBé, K.A., Jones, T.P., 2014. Linking particle number concentration (PNC), meteorology and traffic variables in a UK street canyon. Atmospheric Research 147–148, 133-144.

Singh, M., Misra, C., Sioutas, C., 2003. Field evaluation of a personal cascade impactor sampler (PCIS). Atmospheric Environment 37, 4781-4793.

Taiwo, A.M., Beddows, D.C.S., Shi, Z., Harrison, R.M., 2014. Mass and number size distributions of particulate matter components: Comparison of an industrial site and an urban background site. Science of The Total Environment 475, 29-38.

Vardoulakis, S., Fisher, B.E.A., Pericleous, K., Gonzalez-Flesca, N., 2003. Modelling air quality in street canyons: a review. Atmospheric Environment 37, 155-182.

Viana, M., Rivas, I., Querol, X., Alastuey, A., Álvarez-Pedrerol, M., Bouso, L., Sioutas, C., Sunyer, J., 2015. Partitioning of trace elements and metals between quasi-ultrafine, accumulation and coarse aerosols in indoor and outdoor air in schools. Atmospheric Environment 106, 392-401.

Viana, M., Rivas, I., Querol, X., Alastuey, A., Sunyer, J., Álvarez-Pedrerol, M., Bouso, L., Sioutas, C., 2014. Indoor/outdoor relationships and mass closure of quasi-ultrafine, accumulation and coarse particles in Barcelona schools. Atmos. Chem. Phys. 14, 4459-4472.

Wu, H., Reis, S., Lin, C., Beverland, I.J., Heal, M.R., 2015. Identifying drivers for the intra-urban spatial variability of airborne particulate matter components and their interrelationships. Atmospheric Environment 112, 306-316.

CHAPTER 6: BULK CHEMICAL ANALYSIS OF FILTERS USING INDUCTIVELY COUPLED PLASMA MASS SPECTROMETRY AND ANION CHROMATOGRAPHY

6.1 Aims

Concentrations of a number of metals were analysed in data from 6 UK and European sites, with the aims of assessing mass-size distributions and correlations between different elements, which might shed light on elemental sources and differences in sources in different size ranges. Further aims were to compare concentrations and distributions at sites with differing levels of traffic impact. Samples were analysed for three water-soluble ions with the aim of exploring how each contributed to the total mass distributions examined in the previous chapter.

Limited analytical time and difficulties with the extraction procedure mean that the ICP-MS dataset consists only of a subset of the samples presented in Chapter 5, for each site. These were selected to ensure a representative sample. Eight sample sets were chosen from BROS, collected from July – November 2011. Five sets were extracted from EROS (September-November 2011), all of which were concurrent with an equivalent sample set from BROS. Seven sample sets were extracted from Newcastle. Samples were spread evenly through the sampling campaigns to eliminate any seasonal bias which might arise from choosing samples adjacent in time.

6.2 Metal Data from UK sampling sites

6.2.1 Mass-size distributions

Examining the mass-size distributions of the analysed elements in these samples confirmed that there was considerable variability. Al and Fe in particular appeared at high concentrations in these samples – considerably in excess of values previously reported for the Elms Road site (Taiwo et al., 2014). Since the variability was unpredictable within these two elements (see Chapter 2.3 and Appendix B), this could be due to contamination issues in the extraction procedure.

Aluminium

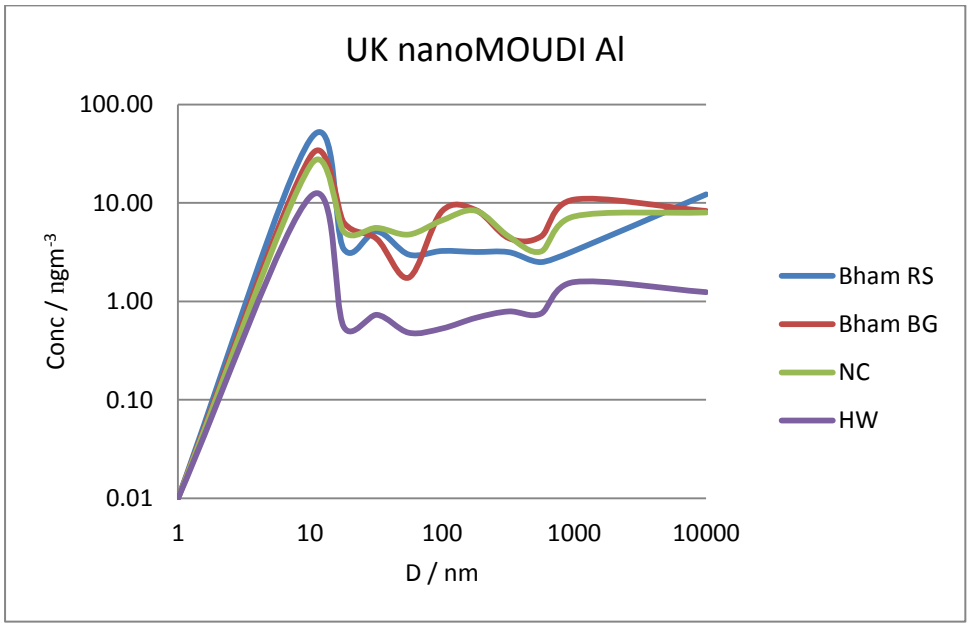

Figure 66. Mean mass-size distributions for Al.

Al (*figure 66*) was characterised by high ultrafine concentrations at both Birmingham sites. This was also found at Newcastle and Harwell and therefore may be an artefact of the sampling process, or of high Al content in the material of the afterfilters. Contamination from the filter holder is also possible; Niu et al. (2014) used a drain disk to avoid this but our

samples precede that study (Niu et al, 2014). The Newcastle Al distribution was more similar to the background distribution (B'ham) than the roadside, with an accumulation mode peak and a fine mode peak in evidence. The >1000 nm mass concentration was not very large. While there was not a clear peak below 100 nm, the mass concentrations were quite high, which was fairly consistent with the other sites. At Harwell, there were also high ultrafine concentrations in the afterfilter.

However, there are reasons to think that Al concentrations would be high in the ultrafine, as Al may be emitted from motor vehicle engines from wear to engine components and/or presence in lubricants and fuels. High-temperature processes would likely produce small primary particles. The high concentrations found in the afterfilter could then result from Al particles in the nano-stages of the nanoMOUDI bouncing or remaining in the gas-stream. Being less dense than the other metals reported in this study, Al could be more subject to this sampling issue. Since the digestion procedure employed on these samples does not extract aluminosilicates (Harper et al., 1983), there is also the possibility of lower extraction efficiency in the mineral-derived coarse Al compared to combustion-derived Al which will likely have different morphology.

Concentrations above 1000 nm were lower than expected relative to the UFP, however, given that it would be expected for the resuspended dust component in the larger sizes to have rather higher mass concentrations than the ultrafine component. Al has been reported by several studies in UFP and pseudo-UFP (Hays et al., 2011; Ntziachristos et al., 2007), although large ultrafine modes are less widely reported. Viana et al. (2015) reported a large ultrafine mode in Al in Barcelona (Viana et al., 2015). Dodd et al. reported a narrow mode at 100 nm for Al in rural Maryland, but there was no comparable mode in these data (Dodd et al., 1991).

Barium

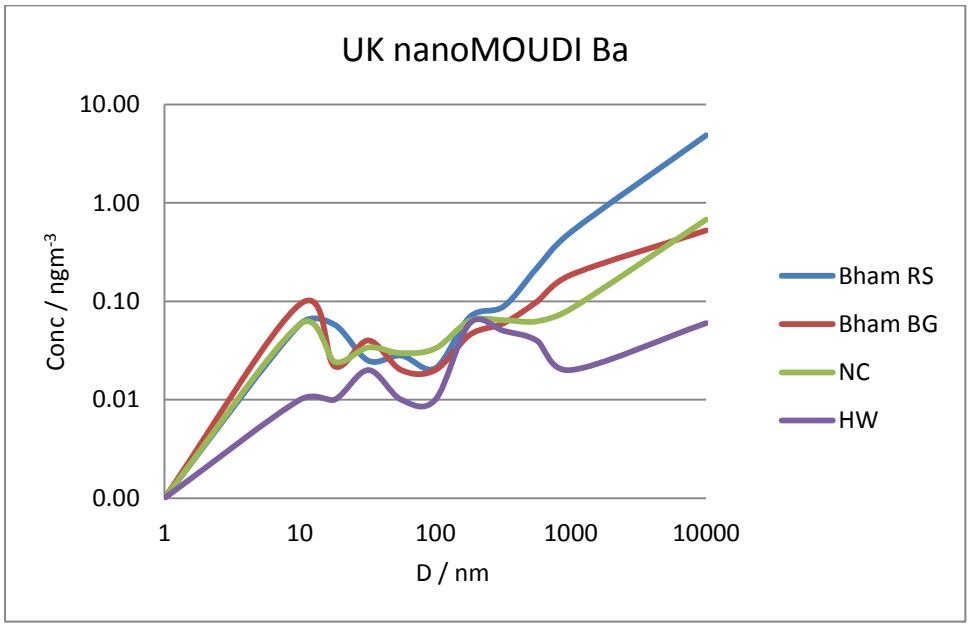

Figure 67. Mean mass-size distributions for Ba.

The mean distributions for Ba (*Figure 67*) showed a clear dominance of larger particles especially at the roadside site, which reflected the expected main source of Ba in abrasive brake wear. There was also a slight ultrafine mode in the background distribution (B'ham). The Newcastle plot showed a greater contribution from submicrometre particulate than BROS, but particles above 1000 nm were still the main contributor.

At Harwell Ba concentrations were extremely low in the 7-12-11 sample in a trimodal distribution – peaks at 18-32 nm, 100-180 nm and 320-1000 nm. Below 180 nm Ba peaked at the same points as Cu and Sr, but the peak at 320-560 nm corresponded with Ni and Zn. In the 21-12-11 sample Ba concentrations were slightly higher in a trimodal distribution with peaks in the same size ranges. Above 100 nm this was quite similar to Sr, but Sr had no ultrafine mode. The submicron fine mode was similar to Cu and Zn, but Cu had very low coarse concentrations in this sample. The ultrafine mode was broader and less pronounced

than Ni, in which concentrations at 18-32 nm were very high, but low in the stages either side.

Cerium

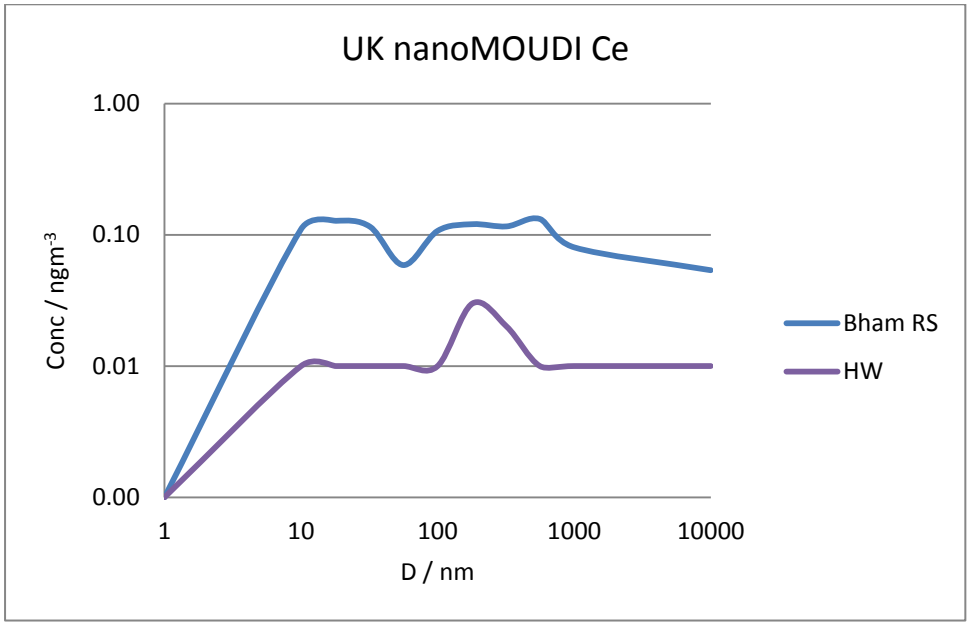

Figure 68. Mean mass-size distributions for Ce.

No distribution could be plotted from the Elms Road or Newcastle datasets, as most filters were below reporting limits for the ICP-MS analysis. From the available roadside data, Ce was mostly seen in size ranges where combustion-derived material would be expected (*Figure 68*). There was a nucleation mode corresponding to freshly emitted particles and a broad range from 56-560 nm, where agglomerated combustion products were observed. This was a wider size range than observed by TEM-EDX in Newcastle by Gantt et al, but the evidence is still showing that Ce is found in ranges corresponding to diesel emissions (Gantt et al., 2014). At Harwell, Ce concentrations were very low except for a mode from 100-560 nm which peaked at 180 nm, which also corresponds to Ce particles in larger soot agglomerates.

Copper

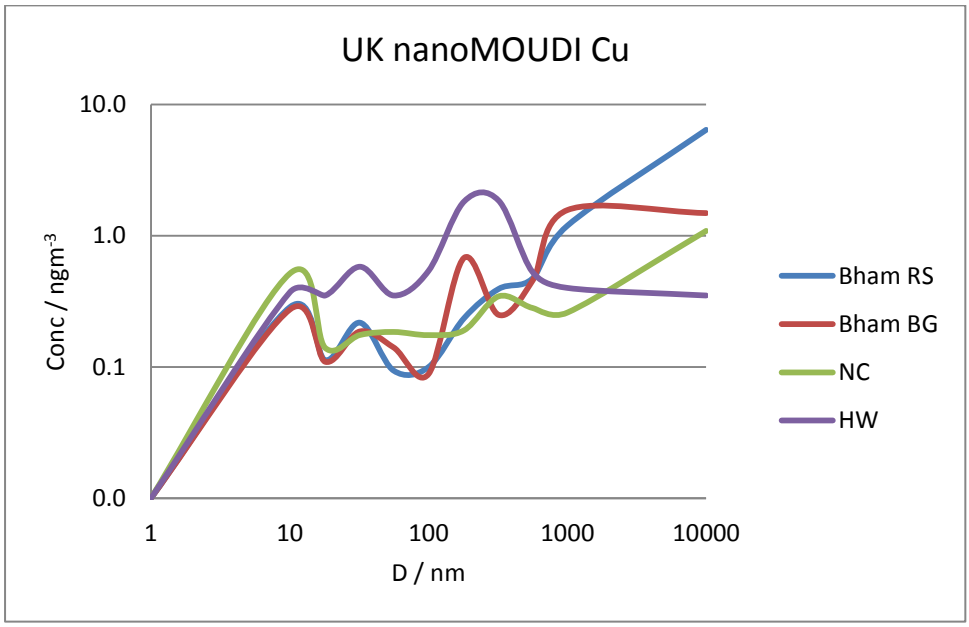

Figure 69. Mean mass-size distributions for Cu.

Cu at both Birmingham sites exhibited a small mode in the ultrafine which may correspond to high-temperature combustion and/or volatilisation sources (*Figure 69*). There was a minimum at both sites from 56-100 nm. At both sites mass concentrations rose steadily with increasing size, although the Birmingham background distribution peaked below 1000 nm. The roadside distribution peaked above 1000 nm, which better fits the expected sources (principally brake wear). Ultrafine concentrations at Newcastle formed a flat distribution without a peak, but consistent values from 32-180 nm – this is somewhat similar to some earlier publications (Ntziachristos et al., 2007). Concentrations peaked at 180-320 nm but were lower, both in absolute terms and relative to the <320 nm distribution, compared with both sites in Birmingham. The Cu distributions at Harwell is less complex in the 21-12-11 sample than the 7-12-11 sample. In the 21-12-11 sample a single large mode spanning two nanoMOUDI stages was observed, 100-320 nm. This was present but reduced in importance

in the 7-12-11 sample to a smaller peak mostly in the 100-180 nm size range. Two small peaks were also present, one at 18-32 nm (corresponding with Ni) and one at 560-1000 nm.

An ultrafine mode in Cu has been reported by Lough et al. (2004), thought to correspond to non-mechanically sourced emissions such as combustion of lubricating oil components in vehicle engines (Lough et al., 2004).

Iron

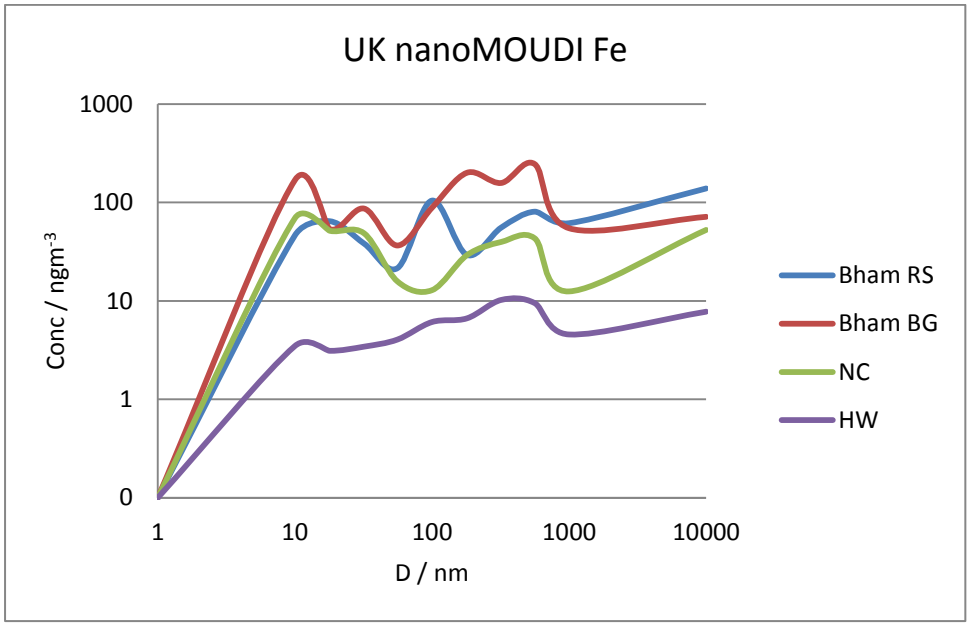

Figure 70. Mean mass-size distributions for Fe.

Fe concentrations were very high in some samples (see tabulated data in Appendix B), and the field blank levels were also high though reagent blanks were not, which implied an issue with introduced contamination from handling filters. Therefore, the Fe data must be treated with some caution. The high concentrations in the Birmingham background samples are another indicator of preparation problems as these are not only higher than the roadside samples but also much higher than previous data from the site (Taiwo et al., 2014).

There was evidence for ultrafine Fe mode at both Birmingham sites perhaps associated with combustion sources – engine particles are probably most likely (*Figure 70*). The nucleation mode corresponds to new formation/fresh release of such particles (Viana et al., 2015). The results in Chapter 7 suggest these tended to be prone to agglomeration. The prominent submicron fine mode was found in larger particles at the roadside than the background, which concurred with the TEM findings in which Fe particles of agglomerated NPs were found in stages 6-9 (Chapter 7). The most significant features of the mean Fe distribution were the presence of an ultrafine mode and a large mode at 320-560 nm. The ultrafine mode in the background was quite similar to that at the roadside, while the submicron fine mode was consistent with the TEM-X-EDS data from the site which showed agglomerates of Fe nanoparticles collected from this size range. The smaller mode was of a similar size to the primary particles which comprised the agglomerates (see chapter 7 for a full analysis of this subject).

The two Fe distributions at Harwell were surprisingly different. The 7-12-11 sample was unimodal, with a peak at 180-560 nm which tailed gradually either side, reaching minima at >1000 nm and <56 nm. The low concentrations above 1000 nm are unexpected given that Fe is normally associated with coarse modes from abrasion and dust sources (Daher et al., 2013). By contrast the 21-12-11 distribution was essentially bimodal, with a moderately sized mode >1000 nm and an ultrafine/pseudo-ultrafine mode running from 32-180 nm. Dodd et al.(1991) reported a narrow mode at 100 nm similar to Al, which is not similar to the samples collected at Harwell (Dodd et al., 1991).

Previous reports on Fe have emphasised unimodal distributions peaking in the coarse mode (Ntziachristos et al., 2007; Rogula-Kozłowska et al., 2015). However, Lough et al. did report a submicron mode considered to be indicative of combustion emissions (Lough et al., 2004). However, recent measurements at the Birmingham background site showed that the coarse

mode, associated with abrasive and resuspended sources, was dominant for Fe, which contradicts the results presented above (Taiwo et al., 2014).

Nickel

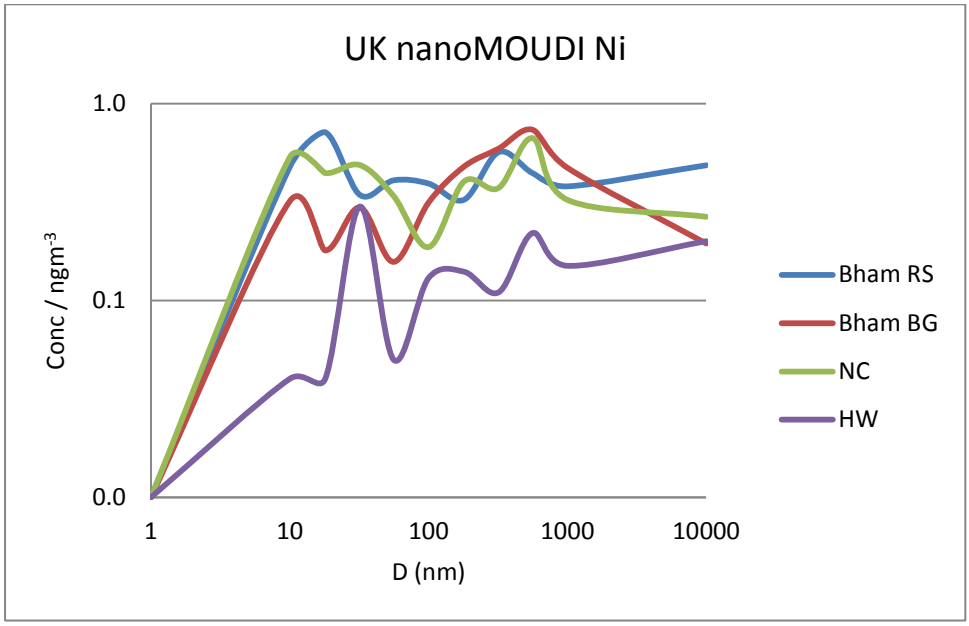

Figure 71. Mean mass-size distributions for Ni.

There was some evidence of an ultrafine Ni mode at both Birmingham sites, though this was not very clear (*Figure 71*). It was more apparent in the distribution obtained in Newcastle. A broad submicron fine mode was observable at both sites in Birmingham and was the main feature of the Newcastle plot, though in this case the peak was narrower – a single stage peak at 320-560 nm while the concentrations from 100-1000 nm were consistent except in this stage. This distribution was more similar to the Newcastle Fe distribution than to the Ni distributions at the other sites. Penannen et al (2007) reported Ni having a pseudo-ultrafine mode ($PM_{0.2}$), but only in areas heavily impacted by shipping emissions (Barcelona and Helsinki) (Pennanen et al., 2007).That finding is supported by Viana et al. (2015) who also reported high pseudo-ultrafine Ni concentrations (Viana et al., 2015) Studies outside

shipping-impacted areas have emphasised submicrometre fine modes for Ni (Ntziachristos et al., 2007; Rogula-Kozłowska et al., 2015).

At Harwell Ni was found to have a complex multimodal distribution, the constant feature being a prominent mode at 18-32 nm in both samples. Both samples had a submicron mode, which is found at 320-560 nm in the 7-12-11 sample and 560-1000 nm in the 21-12-11 sample. The second sample had a tendency for all the modes above the nucleation mode to be shifted to higher particle sizes. Daher et al. (2013) found that Ni, in common with other elements relating to specific industrial sources, was present in much reduced concentrations at remote rural sites compared to urban ones (Daher et al., 2013).

Antimony

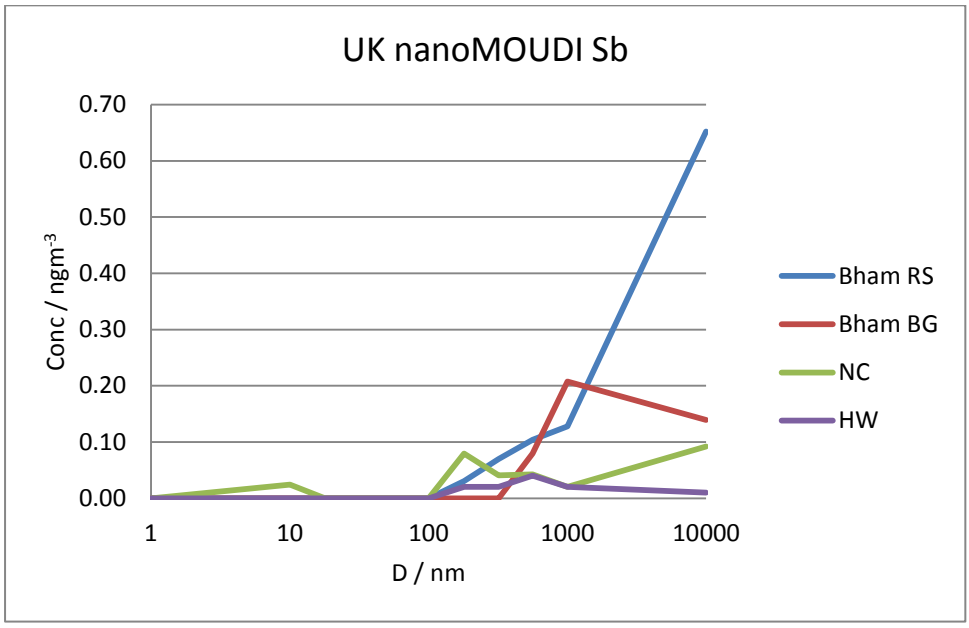

Figure 72. Mean mass-size distributions for Sb.

It was difficult to form conclusions from the very limited data available for Sb. Concentrations in lower size ranges were below reporting limits in most cases. There was limited evidence for a mode in particles above 1000 nm at the roadside which would fit with the expected origin of Sb in abrasive brake wear at the Birmingham sites (see *Figure 72*).

The magnitude and position of the fine mode peak at the background site in Birmingham was roughly consistent with the data for the same site presented in 2004 by Taiwo et al. However, that study also reported a coarse mode which was not clear in our data (Taiwo et al., 2014). The Newcastle site resembled neither of the Birmingham sites, exhibiting a fine mode peaking in the pseudo-ultrafine at 100-180 nm. Other urban studies have generally found Sb mostly in coarse particles, similar to Ba (Lough et al., 2004).

Strontium

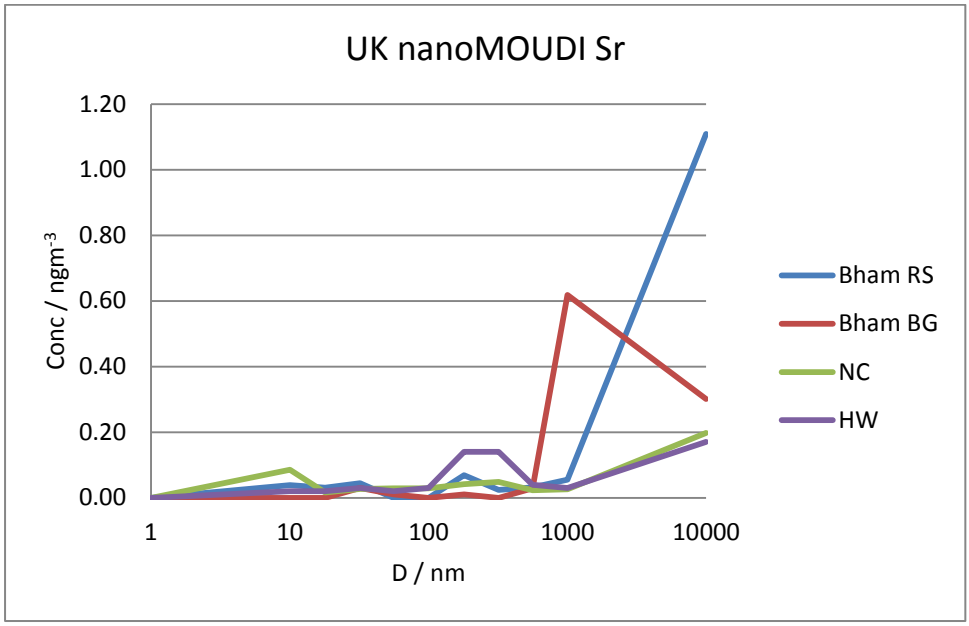

Figure 73. Mean mass size distributions of Sr.

Sr concentrations were generally very low and many filters were below reporting limits in the Birmingham samples, which led to means being skewed by outliers, similar to Sb. In the Newcastle samples, two peaks were observed above a fairly consistent base, at 100-320 nm and above 1000 nm. Few previous studies place much emphasis on distributions of Sr, but Lu et al. classed it as anthropogenic, ie. possessing a submicrometre fine mode (Lu et al., 2011). In both Harwell samples the distribution of Sr was quite similar to Cu, implying a common source for the two elements. Compared to Cu, the 21-12-11 sample for Sr had a slightly

greater contribution from particles > 1000 nm, but the submicron distribution was very similar.

Vanadium

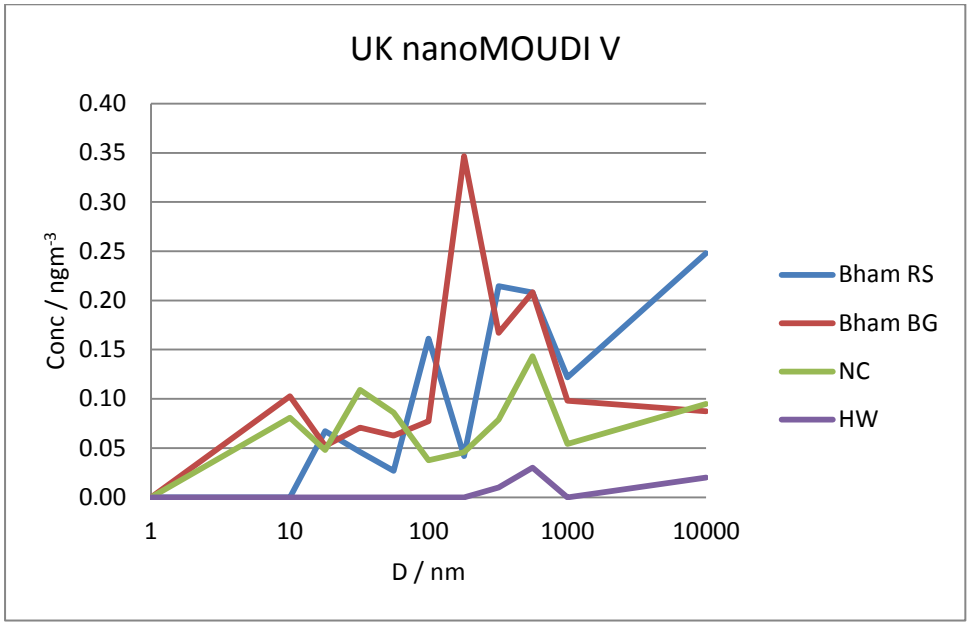

Figure 74. Mean mass size distributions of V.

V concentrations were quite low (*Figure 74*), but the two Birmingham distributions were somewhat different. A bimodal distribution (nucleation mode and 180-560 nm) was observed in the roadside data, while a unimodal distribution peaking at 100-180 nm was found in the background data. The contribution of >1000 nm particles was small at both sites, but more important at the roadside.

In the Newcastle data a more pronounced bimodal distribution was apparent, with a fine mode and an ultrafine mode, peaking at 320-560 nm and 18-32 nm respectively. Studies in urban areas likely to be impacted by emissions from shipping, such as by Pennanen et al. (2007) in Barcelona and Helsinki and Lu et al. (2012) in Shanghai, reported ultrafine modes for V (Lü et al., 2012; Pennanen et al., 2007). However, Ntziachristos et al. (2007) found a monotonic distribution for V in roadside samples in California similar to Fe (Ntziachristos et

al., 2007). Previous data for Birmingham presented by Taiwo et al. showed that V was dominated by the fine mode at the EROS site (Taiwo et al., 2014).

Zinc

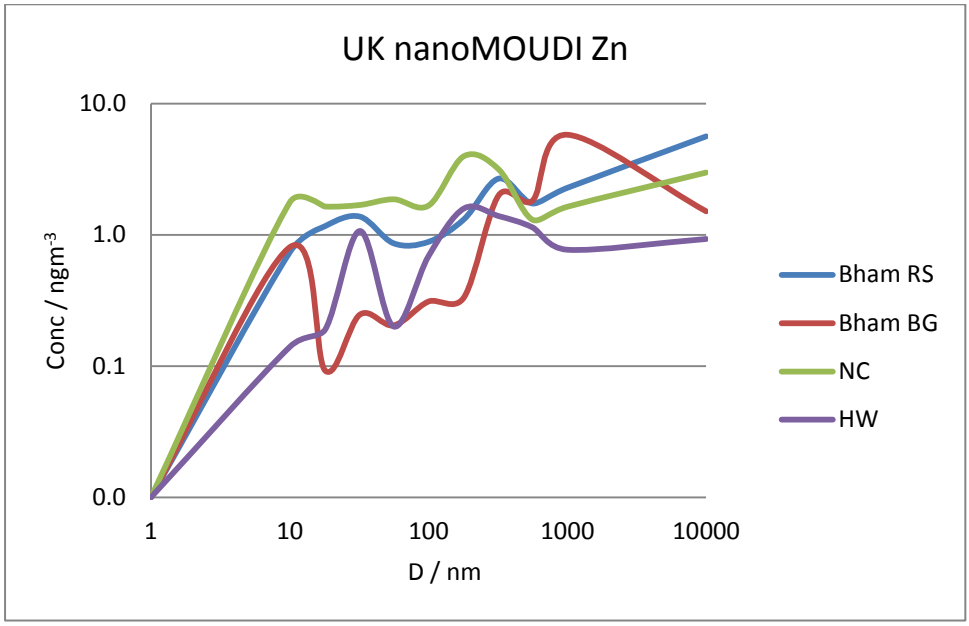

Figure 75. Mean mass size distributions of Zn.

In the roadside data, Zn was one of the elements which did have an ultrafine mode (*Figure 75*). This was similar to V, Ni, Cu, Fe and Ce, so it seems most likely that this mode corresponds to combustion sources such as exhaust emissions deriving from engine wear fragments or lubricating oil/fuel contaminants. The presence of Zn throughout the fine and coarse modes, but without particularly clear peaks, suggests that source inputs are quite complex. The background distribution showed the bulk of the Zn mass in the fine mode below 1000 nm, peaking at 560-1000 nm. At the background site there was a very large submicrometre fine peak at 560-1000 nm, but concentrations in the pseudo-ultrafine were very low and no mode evident. Both were quite different to the Newcastle distribution in which a single broad mode from 100-320 nm peaking in the 180-320 nm size fraction was observed.

In earlier urban particulate studies reported Zn distributions are variable. Ntziachristos et al. did find an ultrafine mode for Zn especially between 18-32 nm in roadside samples (Ntziachristos et al., 2007). However, Lough et al. found that Zn exhibited a similar profile to Sb and Ba, peaking in the coarse mode (Lough et al., 2004). Earlier data for the background site in Birmingham showed a bimodal Zn distribution with a coarse peak and a submicrometre fine peak (Taiwo et al., 2014).

In the 7-12-11 sample from Harwell Zn had a very similar mass distribution to Ni, trimodal with peaks at 18-32 nm, 56-180 nm and 320-560 nm. This contrasted with the 21-12-11 sample, where the distribution was much more similar to Cu – a large mode from 100-320 nm, although this sample also had a much smaller peak at 560-1000 nm. Pakannen et al. (2001) stated that Zn was important in rural UFP (Pakkanen et al., 2001). Dodd et al. reported complex multimodal distributions of rural Zn, a conclusion which is consistent with the findings of the Harwell tests (Dodd et al., 1991).

6.3 Elemental correlations at UK sites

6.3.1 Brake Wear Elements – Ba, Cu and Fe

In the Barcelona data (see section 6.4) good correlations were generally seen between these elements in PM_{10}, though normally the correlations were stronger at the roadside.

	Ba	**Cu**	**Fe**
Ba	1.00	0.74	0.08
Cu	0.74	1.00	0.21
Fe	0.08	0.21	1.00

Table 31. Correlation matrix, brake wear elements in PM_{10}, Birmingham Roadside.

The correlation between Cu and Ba (*Table 31*) was certainly indicative of a common source accounting for much of the input of these elements at the site, however, the weak correlations with Fe were indicative of the high variability of Fe in the ICP-MS data from the UK sites.

	Ba	Cu	Fe
Ba	1.00	0.06	0.21
Cu	0.06	1.00	0.18
Fe	0.21	0.18	1.00

Table 32. Correlation matrix, brake wear elements in $PM_{0.1}$, Birmingham Roadside.

Table 32 shows that the Ba/Cu correlation was much weakened in $PM_{0.1}$. While Cu has previously been reported to have submicron modes indicative of high-temperature emission processes (Lough et al., 2004), Ba has not been reported in ultrafine emissions from brakes, so there is evidence for a divergence of sources in ultrafine particles which would cause a weaker correlation (Kukutschová et al., 2011).

Fe did not show any meaningful correlation with either element in $PM_{0.1}$. In the Barcelona roadside data (chapter 6.4) pseudo-ultrafine Fe also correlates quite poorly with Cu and Ba which could suggest different sources in small particles.

The dataset for the Birmingham background site was not very large which made it more difficult to draw conclusions from the data. In PM_{10}, correlations with Fe were non-existent, and the Ba/Cu correlation in PM_{10} very weak, which was similar to the Barcelona data in that the correlation between these elements in the urban background was much weaker than at the roadside site.

	Ba	Cu	Fe
Ba	1.00	0.18	0.00
Cu	0.18	1.00	0.00
Fe	0.00	0.00	1.00

Table 33. Correlation matrix, brake wear elements in PM_{10}, Birmingham Background.

	Ba	Cu	Fe
Ba	1.00	0.03	0.08
Cu	0.03	1.00	0.98
Fe	0.08	0.98	1.00

Table 34. Correlation matrix, brake wear elements in $PM_{0.1}$, Birmingham Background.

However in ultrafine particles (*Table 34*), Cu and Fe were seen to correlate very well, but both elements correlated poorly with Ba.

	Ba	**Cu**	**Fe**
Ba	1.00	0.29	0.10
Cu	0.29	1.00	0.01
Fe	0.10	0.01	1.00

Table 35. Correlation matrix, brake wear elements in PM_{10}, Birmingham Background.

Table 35 shows poor correlations between the three elements at the Newcastle site in PM_{10}, even though traffic was likely to be the main source at the site. Like Birmingham, Cu and Ba correlated slightly better than Fe. In $PM_{0.1}$ (*Table 36*) it was found that Ba and Cu correlated somewhat, but that Fe did not correlate well with either Cu or Ba.

	Ba	**Cu**	**Fe**
Ba	1.00	0.38	0.23
Cu	0.38	1.00	0.03
Fe	0.23	0.03	1.00

Table 36. Correlation matrix, brake wear elements in $PM_{0.1}$, Newcastle.

Although it would have been ideal to examine the correlations of Sb with these elements as well, Sb was below reporting limits in too many samples to make this viable.

6.3.2 Correlations with other elements – Al, Ni, V and Zn

At the Birmingham roadside site, Cu showed some correlation (R^2 = 0.33) with Al in PM_{10}, although this was not very pronounced. In $PM_{0.1}$, there was no discernible correlation between the two elements. At the Birmingham background site and the Newcastle site this pattern was reversed – no correlation in PM_{10} but R^2 values of 0.45-0.5 in ultrafine particles.

Zn was found to correlate quite well with Cu (R^2 = 0.63) and Ba (R^2 = 0.88) at the Birmingham roadside site in PM_{10} (although not with Fe), but there was no correlation in $PM_{0.1}$ with either element. The Cu/Zn correlation at the background site was poor in both

PM_{10} and ultrafine particles. Zn/Ba correlations in both PM_{10} and $PM_{0.1}$ at the background site in Birmingham and the Newcastle site were found to be poor. In the Newcastle data, it was found that Cu correlated moderately well with Zn in PM_{10} ($R^2 = 0.62$) and slightly better in $PM_{0.1}$ ($R^2 = 0.77$). However, weak correlations were observed between Cu and Ni in both fractions.

At the roadside site in Birmingham Ni correlated poorly with Cu and Ba both in PM_{10} ($R^2 = 0.22$ and 0.15 respectively) and $PM_{0.1}$ ($R^2 = 0.13$ and 0.24 respectively). Ni correlated badly in PM_{10} at the background site but well in $PM_{0.1}$ ($R^2 = 0.9$). Very weak correlations were observed at Newcastle.

Ni was found to exhibit slightly better correlations with V ($R^2 = 0.34$) and Zn ($R^2 = 0.26$) in PM_{10}. In $PM_{0.1}$ the correlation between Ni and V was much higher ($R^2 = 0.84$) but the Ni/Zn correlation was even lower than in PM_{10}. Too few samples were above the reporting limits for V to allow a valid comparison between ultrafine V and Zn. Ni and V also correlated well ($R^2 = 0.87$) in PM_{10} at the background site in Birmingham and at this site a good correlation ($R^2 = 0.61$) was also observed in $PM_{0.1}$. Similarly, Ni/V correlations in both PM_{10} and $PM_{0.1}$ were good at the Newcastle site ($R^2 = 0.96$ and 0.79 respectively).

Full correlation matrices are shown in Appendix D.

6.4 Chemical Data from Barcelona

After weighing in Birmingham, the filters were sent back to Spain for chemical analysis by ICP-MS and ICP-OES at CSIC, for equivalence with other samples collected for the AIRUSE project.

6.4.1 Concentration data for elements associated with brake wear emissions

Background Site

The tabulated data (see Appendix B) demonstrate that the variation in concentrations between samples was quite large for all the elements, especially Sb. The ultrafine Cu concentration was high in all samples, in particular the sample from 16-05-13. It was generally the case (except in Sb) that the 3800-6700 nm size fraction contains the mass peak, and the percentage Standard Deviation is generally the highest in this fraction.

The Sb concentration was high in the 670-1200 nm size fraction. This feature was present, but nowhere near as pronounced with the other elements and furthermore was not shared with Sb at the other site. Unusual as this feature was, it does recur in several of the Sb samples, in particular 5-6-13 and 11-6-13.

Roadside Site

The Ba mass peak was in the 3200-5600 nm size fraction and this was consistent over the six samples, with a fairly small percentage standard deviation. The standard deviations are similarly small across the other stages with the exceptions of the 1800-3200 nm and 10000-18000 nm fractions.

It is striking that a similar pattern was in evidence in the Cu data. In both the Ba and Cu data, the high standard deviation in the 1800-3200 nm fraction was caused by an unusual low concentration in the dataset from 3-6-13. This feature was common to all elements in the dataset, so did not reflect on the brake wear elements only.

Being unaffected by the 3/6/13 dataset the Sb standard deviations were more consistent than the other elements. The percentage deviations were high in the smallest particles, which might reflect the very low mass concentrations in these fractions. The mass peak appeared in

the same fraction as the other elements and this was consistent through all five available samples.

6.4.2 Size distributions - Background Site

The mean size distributions of the four elements selected followed each other quite well but there were some variations. In particular, Ba and Fe exhibited closely similar distributions. Sb has an unusual minimum in the 268-469 nm fraction and its maximum in the 469-837 fraction is far more prominent than the small peaks shown in that range by the other elements. As shown in 2b, it is not as important at the other site either.

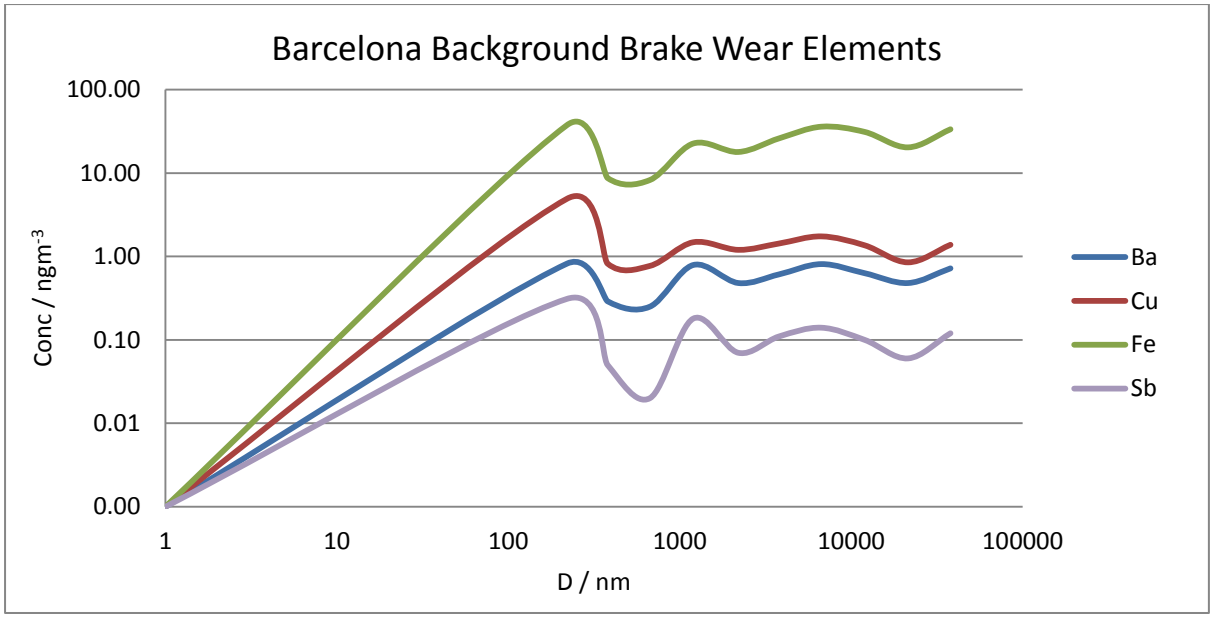

Figure 76. Mean brake wear element distributions at the background site.

For Fe, four distributions (13/5/13, 16/5/13, 5/6/13 and 11/6/13) were very similar to the mean. The others stood out as being unusual. The sample for 9/5/13 was a variant of the mean distribution, but with the concentrations from 1200-2200 nm being much lower – the maxima and minima were exaggerated. The 21/5 sample was radically different, however. In 21/5 the submicron distribution was similar to the common type, but the usual mass peak at

3800-6700 nm was absent along with the usual coarse peak. The absolute concentration values were lower than normal above 1 µm but similar to the others below this.

The Sb distribution for the unusual 21-5 dataset did not help to explain this, as the concentrations are so low that no Sb is reported between 220 and 6700 nm. The Ba and Cu distributions were flatter than the Fe distribution, but they also showed the change to the distribution around the normal mass peak for these elements.

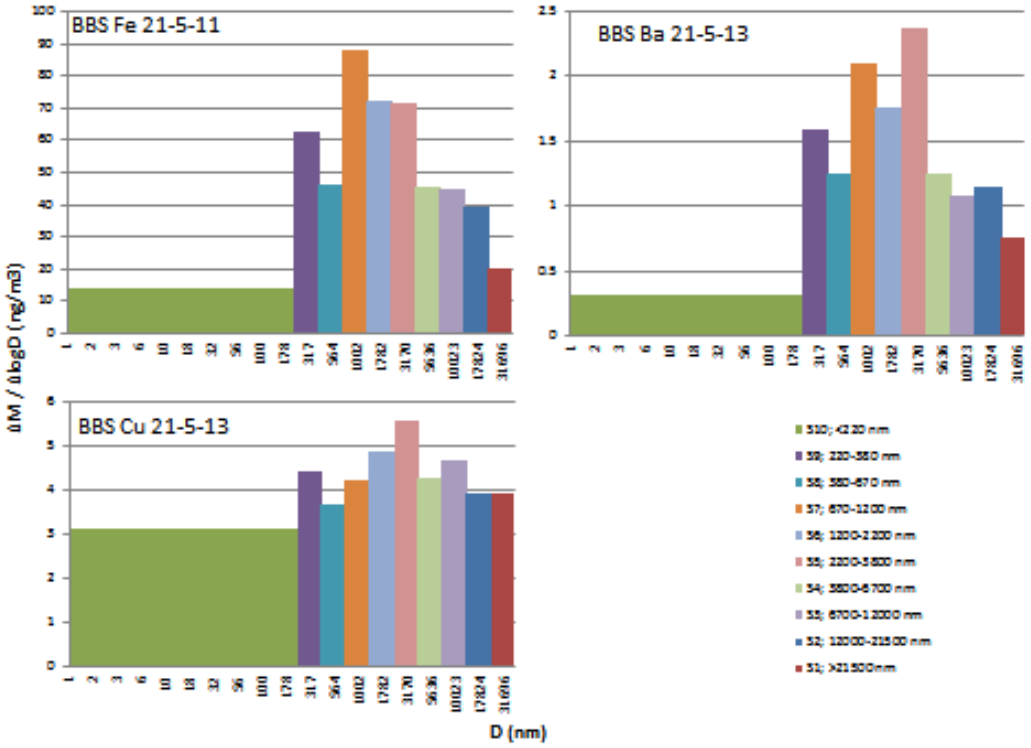

Figure 77 Fe, Ba and Cu distributions for the 21-5-13 dataset, Campus site.

6.4.3 Size Distributions - Roadside Site

By comparison with the background site the distributions obtained from the street canyon site were much more consistent. The distributions and absolute values were quite similar throughout and the mean was representative for all four elements across the six samples. The one exception to this appeared to be the stage 4 values (1800-3200 nm) in the 3-6-13 dataset.

These were low in all elements for both ICP-AES and ICP-MS techniques though, so it is difficult to assess what this may mean. The 21-5-13 dataset at this site did not show similar low concentrations in filters > 1 µm, unlike the corresponding set for the background site.

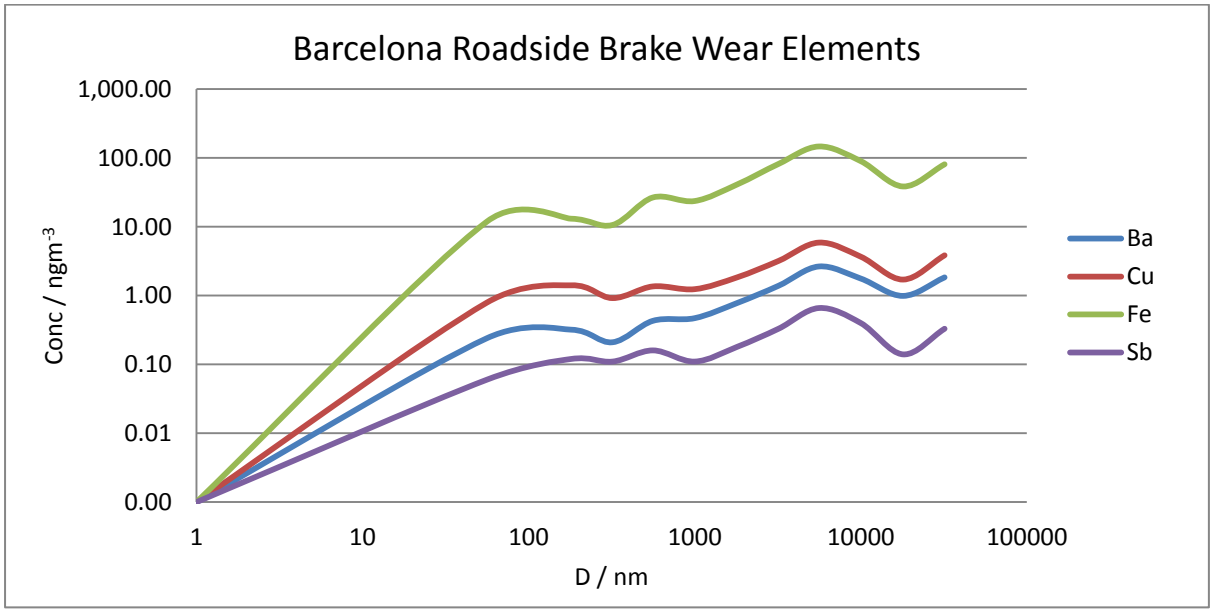

Figure 78. Mean distributions for brake wear elements, roadside site.

6.4.4 Correlation plots - Background Site

On the whole the correlations between the four elements at this site were not as good as at the roadside site. The Ba-Fe correlation was good, but the other elements correlated much more poorly (*Table 37*).

Background	Ba	Cu	Fe	Sb
Ba	1.00	0.36	0.83	0.66
Cu	0.36	1.00	0.40	0.86
Fe	0.83	0.40	1.00	0.53
Sb	0.66	0.86	0.53	1.00

Table 37. Background site correlation plots for brake-associated elements from mean concentrations.

The problem in plotting the correlations at this site was the comparatively high concentrations of Cu in the size fraction <220 nm. These were fairly consistent through the 7

samples and do not represent a rogue measurement skewing the mean, but they may suggest there was another, non-brake, source of this element affecting the site. Because the correlations between Cu, Ba and Fe were more consistent at the roadside, it would not seem that <220 nm brake wear particles include proportionally more Cu. Cu appeared in a number of particles coming from the diesel engine (Chapter 4), so it is possible that this source supplements the brake wear source in small particles, but in that case it might be expected that this would also affect the roadside site, which was not observed. The correlations between the other elements would suggest that the same source was predominant for all of them.

Table 38 below shows R^2 values without the <220 nm filter. The Cu/Ba and Cu/Fe correlations were much better. With Sb on the other hand, the correlation was worse when UFP was excluded. In this case, it was the 670-1200 nm range, where several of the Sb samples had a pronounced maximum which caused a worse correlation.

	Ba	**Fe**	**Sb**
Cu	0.87	0.74	0.78

Table 38. Correlation coefficents with Cu excluding final stage (<220 nm) from mean concentrations.

Data from 21-5-13

Examining the correlation coefficients from this date, instead of the means, suggested that there was a divergence of sources between Fe and Ba in one group and Cu in the other taking effect.

Background 21-5-13	**Ba**	**Cu**	**Fe**
Ba	1.00	0.51	0.92
Cu	0.51	1.00	0.64
Fe	0.92	0.64	1.00

Table 39. Correlation coefficients for 21-5-13 dataset at the background site.

Stage	Lower Cut / nm	Fe BG	Sb BG	Ba BG	Cu BG
Inlet	**21500**	4.98	0.05	0.19	0.98
1	**12000**	9.89	0.06	0.29	0.99
2	**6700**	11.36	0.04	0.27	1.18
3	**3800**	11.26	0.00	0.31	1.04
4	**2200**	17.01	0.00	0.56	1.32
5	**1200**	18.92	0.00	0.46	1.28
6	**670**	22.24	0.00	0.53	1.06
7	**380**	11.38	0.00	0.31	0.91
8	**220**	14.88	0.00	0.38	1.04
Backup	**1**	32.93	0.22	0.72	7.27

Table 40. Background site concentrations, 21/5/13.

The Cu distribution in this sample was highly unusual with low concentrations in all stages, then a very high concentration in the backup filter. While it was true that the Fe and Ba concentrations in this set were also lower than the norm in the coarse fractions especially, they did not parallel the Cu distribution very well in this dataset. Removing the <220 nm filter from the data improved the correlation in the mean concentrations in table a but made correlations worse in this dataset as the plots in Table c below illustrate.

Background 21-5-13 no UFP	**Ba**	**Cu**	**Fe**
Ba	1.00	0.39	0.86
Cu	0.39	1.00	0.28
Fe	0.86	0.28	1.00

Table 41. Correlation coefficients for the Barcelona background site, 21-5-13 with final filter not included.

6.4.5 Correlations - Roadside Site

Roadside	**Ba**	**Cu**	**Fe**	**Sb**
Ba	1.00	0.97	0.97	0.92
Cu	0.97	1.00	0.98	0.97
Fe	0.97	0.98	1.00	0.97
Sb	0.92	0.97	0.97	1.00

Table 42. Correlation coefficients for Ba, Cu, Fe and Sb at the Barcelona roadside site.

These correlation coefficients for the mean values (*Table 42*) in each stage supported the similarity in the shapes of the mass-size distributions for these elements, in showing a common source at the street canyon site. The Ba correlations demonstrated that this source was probably brake wear, as Ba concentrations are not thought to depend on another source as well.

6.4.6 Correlations with other elements

While these four elements are generally associated with brake wear, it was also useful to examine the distributions and correlations to see whether there are other elements which may be attributed to the same source. Sn, Zn, Mo and Pb are all possibly associated with this source. Pb concentrations in this dataset were very low, with the element not appearing in all filters, so its distributions may not be fully representative. Of the other elements in this class, Mo and Sn showed similar distributions to the brake wear elements at the roadside site. Zn at that site had an unusual distribution, quite flat except for a pronounced mass peak at 1000-1800 nm. This was a persistent feature of this element, rather than a mean distribution affected by one rogue measurement. Standard deviations for Sn were reasonably low except for the low measurement in stage 4 in the 3/6/13 set, which was common to all elements. Standard deviations in Mo were found to be more variable than in the 320-560 nm and 10000-18000 nm fractions, although these high deviations were largely the result of one measurement in each size range which lies far outside the norm.

The Zn mass concentration values at the mass peak (1000-1800 nm) were persistently higher than the other stages and the standard deviations for the stage were not unusually high, so the mean can be said to be quite representative in this case. The correlation was poor with the brake wear elements at the roadside ($R^2 = 0.024$).

By comparison the correlation between Ba and Sn (R^2 = 0.076) would imply a commonality of source, although it was not so good as between Ba and Cu or Fe.

6.4.7 Correlations plotted by stage

As opposed to plotting the correlation curve by showing a point for each stage (Ba stage 10 against Cu stage 10, for instance), it may also be instructive to plot the all the stage 10 figures for (eg) Ba against the corresponding (eg) Cu figures.

6.4.8 Roadside Correlations in $PM_{0.18}$ and PM_{10}

Somewhat contrary to expectation the R^2 value for the pseudo-ultrafine Ba-Cu correlation was higher than for the corresponding Ba-Fe curve (*Table 43*). This was particularly interesting because the Cu-Fe value for this size range shows a poorer correlation than either (*Table 43*). It may be that this indicated a divergence of sources between these elements in the lowest size fractions.

BTR $PM_{0.18}$	**Ba**	**Cu**	**Fe**
Ba	1.00	0.76	0.65
Cu	0.76	1.00	0.28
Fe	0.65	0.28	1.00

Table 43. Correlation coefficients for Ba, Cu, and Fe in $PM_{0.18}$ at the Barcelona roadside site.

These values can be contrasted with those obtained for PM_{10} by summing all stages below 10,000 nm.

BTR PM_{10}	**Ba**	**Cu**	**Fe**
Ba	1.00	0.96	0.31
Cu	0.96	1.00	0.25
Fe	0.31	0.25	1.00

Table 44. Correlation coefficients for Ba, Cu, and Fe in PM_{10} at the roadside site.

In total PM_{10}, the Ba-Fe and Cu-Fe correlations were poorer than in $PM_{0.18}$ while the Ba-Cu correlation was extremely good.

6.4.9 Background Correlations in $PM_{0.18}$ and PM_{10}

Owing to the difference in cut-points it was not easy to make a direct comparison between the two sites, as the size bins are not the same. The smallest fraction in this dataset is <220 nm or $PM_{0.22}$.

BBS $PM_{0.22}$	**Ba**	**Cu**	**Fe**
Ba	1.00	0.31	0.75
Cu	0.31	1.00	0.27
Fe	0.75	0.27	1.00

Table 45. Correlation coefficients for Ba, Cu, and Fe in $PM_{0.22}$ at the background site.

By comparison to the roadside site, the correlations in pseudo-ultrafine particles at the background site showed a different pattern (see *Table 45*). The Cu correlations were much worse, while the Ba-Fe correlation was the strongest of the three. Unfortunately, it was not possible to say for certain whether this was caused by different source inputs, which seems unlikely since road traffic was the most significant source in both cases, or to the slight difference in the size fractions.

BBS PM_{12}	**Ba**	**Cu**	**Fe**
Ba	1.00	0.03	0.05
Cu	0.03	1.00	0.02
Fe	0.05	0.02	1.00

Table 46. Correlation coefficients for Ba, Cu, and Fe in PM_{12} at the background site.

All three correlations in this set (PM_{12}) were extremely poor (*Table 46*). It is not clear why this should be the case, but it may be that the plots of PM_{10} and PM_{12}, which require many stages to be summed together, were highly susceptible to the variability in the datasets.

The brake wear elements all tended to exhibit their mass peak in the same stage; S4, which corresponds to 3200-5600 nm at the roadside site and 3800-6700 nm at the background owing to the lower flowrate of that instrument. At the roadside site coefficients for the Fe/Cu (R^2 = 0.058) and Fe/Ba (R^2 = 0.064) correlations were poor in this stage as well, which was surprising. The Ba-Cu correlation was very strong (R^2 = 0.97), which demonstrated commonality of source in this size fraction throughout the six samples.

BBS Stage 4	Ba	Cu	Fe
Ba	1.00	0.82	0.98
Cu	0.82	1.00	0.86
Fe	0.98	0.86	1.00

Table 47. Correlation coefficients for Ba, Cu, and Fe in MOUDI Stage 4 at the background site.

It was slightly surprising to find that the correlations between these elements in Stage 4 are better at the background site than they were at the roadside site.

Some useful data concerning elemental ratios likely to be indicative of brake wear have been published and the data collected in Barcelona made an interesting comparison to previous publications. A number of studies have consistently reported that the ratio of Cu:Fe of brake wear is approximately 4%, with quite a low coefficient of variation (~7%) (Hulskotte et al., 2014). The data from the roadside site were roughly in agreement with this figure in the larger stages – the mean of 6 sample sets in PM_{10} (obtained by summing masses) was 4.70% - but the corresponding figure in summed $PM_{0.18}$ was much higher. The table below shows clearly that these observations were consistent and not the result of outliers skewing the means.

It is not clear whether this was caused by the wear mechanisms which form smaller particles releasing proportionally more Cu or whether there is a confounding source of ultrafine Cu, such as exhaust emissions originating from lubricating oils.

Previous studies show some interesting similarities and differences. Two studies of $PM_{0.1}$ in Asia (Taipei and Shanghai) have Cu:Fe percentages far higher than these at 76.3% and 51.04% respectively (Chuang et al., 2012; Lü et al., 2012). This could reflect differences in the brake pad compositions typical of the vehicle fleet. Studies from Europe and the USA report numbers in $PM_{0.1}$, $PM_{0.18}$ and $PM_{0.25}$ which are much more similar to our observations. Percentage ratios of 2.8-5.7 were reported beside a California freeway by Ntziachristos et al. (2007), and ratios between 2.1 and 11.0 by Saffari et al. (2013) at four sites in California. (Ntziachristos et al., 2007; Saffari et al., 2013). Saffari's results would suggest that Cu as a percentage of Fe increases with the level of traffic impact at the site as the data from Los Angeles has a much higher percentage of Cu than the data from Lancaster. Pakkanen et al. (2001) found an urban Cu:Fe percentage of 7.70 in Helsinki and a percentage of 23.29 at a rural background site (Pakkanen et al., 2001).

Lower cutpoint (nm)	**09/05/ 2013**	**13/05/ 2013**	**16/05/ 2013**	**21/05/ 2013**	**27/05/ 2013**	**03/06/ 2013**	**Mean**	**St dev**	**%St dev**
18000	4.23	6.10	4.13	4.88	5.04	4.04	4.74	0.78	16.50
10000	4.20	4.76	3.65	4.66	5.22	4.39	4.48	0.53	11.92
5600	3.63	4.02	3.17	4.74	4.40	4.81	4.13	0.65	15.66
3200	3.35	3.55	3.12	4.84	4.90	4.73	4.08	0.82	20.20
1800	3.00	3.63	2.92	5.14	5.33	24.14	7.36	8.28	112.57
1000	3.52	3.85	3.43	5.44	6.63	5.33	4.70	1.30	27.61
560	4.11	4.36	4.55	5.84	8.05	5.75	5.44	1.47	27.01
320	4.77	3.20	4.36	6.90	6.94	7.09	5.54	1.65	29.83
180	6.64	7.96	8.41	8.62	14.33	8.14	9.02	2.69	29.88
56	10.13	7.40	11.13	12.48	13.78	12.37	11.21	2.25	20.05
Back-up	5.88	5.26	4.72	5.23	10.04	12.00	7.19	3.05	42.49
PM_{10}	3.78	3.99	3.56	5.41	5.83	5.64	4.70	1.03	21.94
$PM_{0.18}$	7.74	6.43	7.99	9.09	12.14	12.21	9.27	2.41	25.99

Table 48. Cu:Fe percentage ratio, Barcelona roadside site.

Cu:Fe % ratios at the background site were found to be similar to the roadside site in some samples but exhibited far more variability than at the roadside. On average, the ratios in both PM_{12} and $PM_{0.22}$ showed higher Cu content relative to Fe than at the roadside.

Lower Cut (nm)	**09/05/ 2013**	**13/05/ 2013**	**16/05/ 2013**	**21/05/ 2013**	**27/05/ 2013**	**05/06/ 2013**	**11/06/ 2013**	**18/06/ 2013**	**Mean**	**St dev**	**%St dev**
21500	4.02	4.20	6.11	19.59	4.09	3.26	3.06	3.07	5.93	5.61	94.64
12000	4.72	4.47	6.07	10.03	2.81	4.59	3.87	2.85	4.93	2.32	47.08
6700	4.11	5.72	5.81	10.39	3.90	3.22	3.59	3.00	4.97	2.43	48.96
3800	5.10	5.22	6.03	9.27	27.66	4.26	3.80	3.88	8.15	8.08	99.05
2200	6.19	5.44	6.44	7.75	5.89	4.74	4.68	4.67	5.72	1.08	18.78
1200	11.59	6.65	8.68	6.78	7.79	6.64	4.85	5.38	7.29	2.12	29.03
670	4.81	5.56	7.89	4.77	9.32	6.24	5.69	12.69	7.12	2.74	38.47
380	6.85	10.54	12.53	7.97	12.12	9.08	7.75	8.59	9.43	2.09	22.15
220	7.60	11.89	7.76	7.01	15.27	10.04	9.32	12.80	10.21	2.90	28.43
1	6.87	11.12	24.26	22.08	10.94	8.76	7.22	11.59	12.85	6.63	51.57
PM_{12}	5.92	7.11	11.35	10.79	7.99	5.49	4.96	6.32	7.49	2.40	32.06
$PM_{0.22}$	6.87	11.12	24.26	22.08	10.94	8.76	7.22	11.59	12.85	6.63	51.57

Table 49. Cu:Fe percentage ratio, background site.

The general trend of the Cu:Fe percentage being higher in the pseudo-ultrafine category was similar to the roadside site, so it is likely that the sources were broadly similar but with greater variability in measurements caused by the greater distance from the roads and more open nature of the site.

At the roadside site, the Cu/Sb ratio was quite consistent in PM_{10} but highly variable in $PM_{0.18}$. Unlike the Cu:Fe ratio there was not a consistent trend in ratio vs particle size. The ratios in this data agreed with earlier studies of European roadside environments, although they are towards the high end of reported ranges (Gietl et al., 2010; Hueglin et al., 2005; Hulskotte et al., 2014; Johansson et al., 2009). Calculating the corresponding ratios in UFP/pseudo-UFP from previous studies showed that these can be extremely variable although ratios between 6 and 10 were typical of ultrafine/pseudo-ultrafine data from urban environments in the USA and Europe. The ratio reported for rural $PM_{0.1}$ in 2001 by Pakannen et al. is 28.3 which must reflect the dominance of anthropogenic Sb sources (Pakkanen et al., 2001).

The Cu/Sb ratio exhibited rather high coefficients of variation especially in the fine and ultrafine stages, which reflected the very low abundance of Sb in the dataset.

Lower Cut (nm)	09/05/ 2013	13/05/ 2013	16/05/ 2013	21/05/ 2013	27/05/ 2013	03/06/ 2013	Mean	St dev	%St dev
18000	10.73	14.10	12.12	11.62	10.41	9.50	11.41	1.60	14.06
10000	10.70	13.84	12.17	12.85	12.79	11.31	12.27	1.14	9.27
5600	8.88	9.68	8.58	9.46	8.77	9.37	9.12	0.44	4.80
3200	8.29	9.34	8.85	9.49	8.74	8.78	8.92	0.44	4.92
1800	8.27	10.52	9.13	10.25	9.76	0.00	7.99	4.00	50.03
1000	9.11	10.45	9.99	9.71	12.78	8.72	10.13	1.44	14.20
560	10.40	11.73	12.35	11.64	14.21	8.34	11.45	1.97	17.18
320	9.21	8.34	9.02	12.36	9.96	5.32	9.04	2.29	25.38
180	9.27	7.65	13.88	10.82	18.14	3.61	10.56	5.04	47.73
56	0.00	8.18	20.78	12.50	26.78	3.98	12.04	10.18	84.61
Back-up	0.00	15.72	11.27	8.56	16.67	7.41	9.94	6.12	61.63
PM_{10}	9.82	9.69	9.76	10.10	10.57	7.30	9.54	1.14	12.00
$PM_{0.18}$	0.00	9.95	16.70	11.12	21.97	4.97	10.79	7.89	73.12

Table 50. Cu/Sb ratio, Barcelona roadside site.

Lower Cut (nm)	09/05/ 2013	13/05/ 2013	16/05/ 2013	21/05/ 2013	27/05/ 2013	05/06/ 2013	11/06/ 2013	18/06/ 2013	Mean	St dev	%St dev
21500	15.25	10.57	24.65	20.22	13.06	9.50	6.55	10.23	13.75	6.04	43.95
12000	19.23	11.66	0.00	17.03	13.33	11.70	8.32	15.42	13.81	3.69	26.74
6700	13.53	24.88	19.87	27.79	12.19	9.39	6.96	11.81	15.80	7.52	47.60
3800	11.97	14.09	13.76	0.00	0.00	8.87	9.36	11.54	11.60	4.56	39.29
2200	14.62	16.60	20.13	0.00	14.81	10.22	5.96	12.75	13.59	4.22	31.06
1200	0.00	19.88	26.02	0.00	15.26	11.21	6.09	14.65	15.52	6.89	44.42
670	6.55	15.28	15.07	0.00	15.63	4.30	3.03	14.62	10.64	5.30	49.82
380	0.00	0.00	0.00	0.00	20.38	22.67	5.33	20.18	17.14	7.96	46.42
220	13.25	0.00	12.22	0.00	26.67	11.20	4.17	20.82	15.02	8.80	58.57
1	10.91	23.71	28.42	33.27	16.71	9.35	3.49	19.35	18.15	10.10	55.62
PM_{12}	12.38	21.32	22.89	57.88	16.33	8.69	4.89	15.05	19.93	16.46	82.61
$PM_{0.22}$	10.91	23.71	28.42	33.27	16.71	9.35	3.49	19.35	18.15	10.10	55.62

Table 51. Cu/Sb ratio, Barcelona background site.

The corresponding data from the background site was more difficult to interpret because Sb was not always detectable in all the filters, but the averages showed ratios higher (18-20) than most published data in both size ranges. Coefficients of variation were also very high in this dataset.

It can be seen that if we wish to track elemental ratios to use as indicators for brake wear, this needs to be done at a roadside site where the influence of other sources and of weather

conditions (especially wind direction) on the results will be minimised. The roadside site at Carrer Valencia is ideal owing to its street canyon location.

6.4.10 Elements associated with shipping emissions

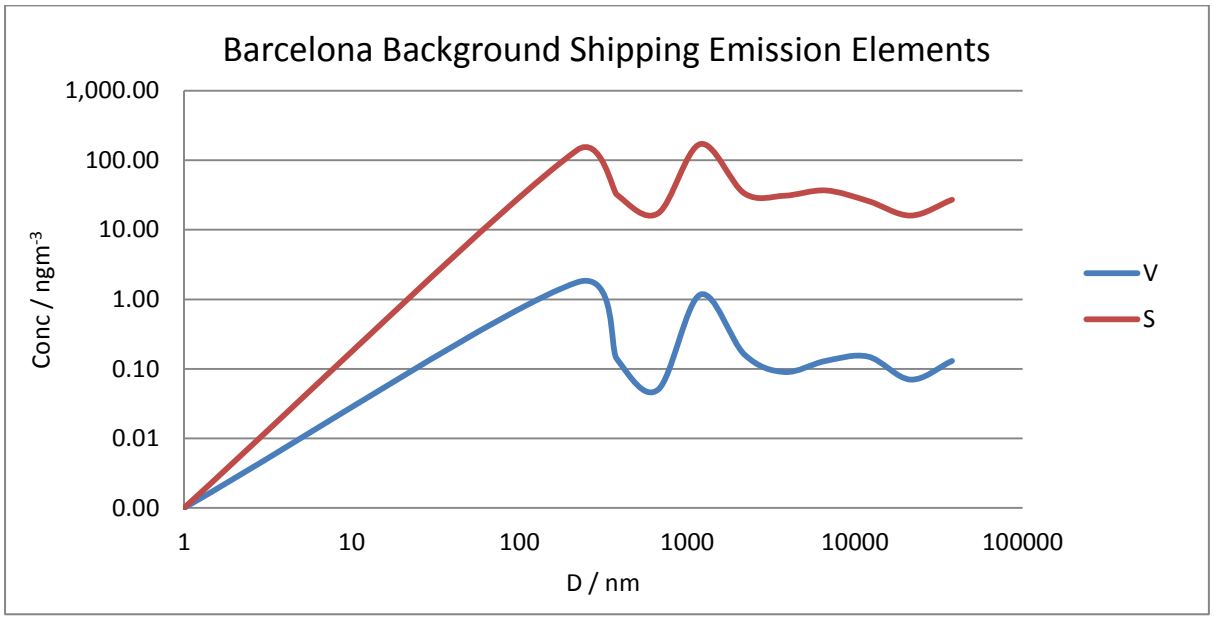

Figure 79. Mass-size distribution of V and S, background site.

At the background site the two elements had similar shaped size distributions, which had some differences with the brake wear elements. The distributions were bimodal, ultrafine (<220 nm) and fine (560-1000 nm) (*Figure 79*). The R^2 value for the two mean distributions was 0.86.

6.4.11 Indicators of Sea Salt Aerosol

Sea salt aerosol was considered likely to be an important contributor to total PM mass at both sites owing to their proximity to the coast. Na and Mg have previously been identified as likely tracers of sea salt, although neither is exclusively sourced from sea salt. The mass-size distributions were quite similar to each other at both sites (*Figure 80*).

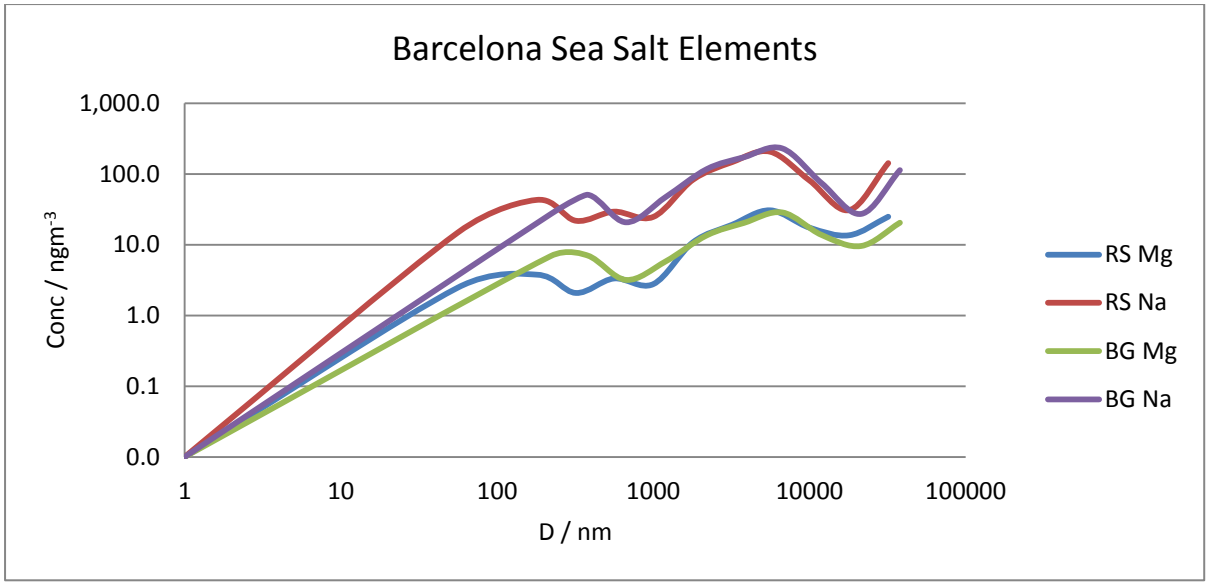

Figure 80. Mass-size distribution of Mg and Na, both sites.

The distributions of both elements were somewhat similar to the brake wear elements despite the expected difference in sources. The correlation coefficients of these elements were interesting. In PM_{10}, there was a clear correlation between Na and Mg from sample to sample, while in $PM_{0.18}$ the correlation was nowhere near as good. Na showed proportionally more mass in the submicron size fractions. These were very different to the distributions of V and S.

BTR PM_{10}	**Mg**	**Na**
Mg	1.00	0.81
Na	0.81	1.00

BTR $PM_{0.1}$	**Mg**	**Na**
Mg	1.00	0.28
Na	0.28	1.00

Table 52. Roadside elemental correlations between Na and Mg in PM_{10} and $PM_{0.18}$.

6.4.12 Concentrations of possible exhaust-associated elements

Roadside site

Analysis of TEM grids containing exhaust captured from a EURO-5 compliant diesel engine has shown the presence of Al, Ca, Cr and Ni (see Chapter 4). These elements are all known to have multiple sources in urban PM. Al and Ca are often associated with crustal resuspension and while that is likely to be the dominant source in large particles, exhaust sources such as lubricants and wear to engine components may be more important in ultrafine/pseudo-ultrafine particles. At the Barcelona roadside site Al and Ca were found to correlate well in both PM_{10} and $PM_{0.18}$ as shown in *Table 54*.

Stage		09/05/ 2013	13/05/ 2013	16/05/ 2013	21/05/ 2013	27/05/ 2013	03/06/ 2013	Mean	Stdev	%Stdev
PM_{10}	**Al**	232.03	576.23	96.02	292.92	267.97	120.52	264.28	172.14	65.14
$PM_{0.18}$		71.18	107.74	21.84	61.84	88.90	22.61	62.36	34.83	55.85
PM_{10}	**Ca**	448.48	793.94	301.86	593.91	698.82	338.40	529.24	198.82	37.57
$PM_{0.18}$		97.87	182.94	52.84	132.38	177.48	47.88	115.23	59.13	51.32

Table 53 Roadside Al and Ca concentrations in PM_{10} and $PM_{0.18}$, in ngm^{-3}.

BTR PM_{10}	**Al**	**Ca**	**BTR $PM_{0.18}$**	**Al**	**Ca**
Al	1.00	0.80	**Al**	1.00	0.90
Ca	0.80	1.00	**Ca**	0.90	1.00

Table 54. Al/Ca correlations in PM_{10} and $PM_{0.18}$, Roadside site.

However, when these elements are compared to Fe it was found that the Fe/Ca correlation was poor in PM_{10} (R^2 = 0.29) and better in $PM_{0.18}$ (R^2 = 0.55). This could suggest that while the two elements have different source inputs in the coarse and fine modes, smaller particles may be derived from exhaust sources. There was some evidence for this in our engine tests, so it was interesting to see that ambient particles may show similar characteristics.

The same effect was observed in the Fe/Al correlation coefficients. In this case the correlations in both PM_{10} (R^2 = 0.51) and $PM_{0.18}$ (R^2 = 0.72) were better than for Ca, and the

$PM_{0.18}$ correlation is much higher than PM_{10}. This may be high enough to show that the two elements share a source in this size range.

Cu exhibited strong correlations with Ca in both PM_{10} (R^2 = 0.89) and $PM_{0.18}$ (R^2 = 0.76) while the correlations with Al showed quite similar values to the Fe/Al correlation in both PM fractions. Neither Fe nor Cu correlated well with Ni, either in PM_{10} or $PM_{0.18}$.

Background site

At the urban background site on the CSIC campus the correlations of Fe with Ca and Al were far weaker in PM_{12} and $PM_{0.22}$ than the correlations in similar sizes at the roadside site (*Tables 55 & 56*).

BBS PM_{12}	**Fe**	**Al**	**BBS $PM_{0.22}$**	**Fe**	**Al**
Fe	1.00	0.12	**Fe**	1.00	0.19
Al	0.12	1.00	**Al**	0.19	1.00

Table 55. Fe/Al correlations in PM_{12} and $PM_{0.22}$, Background site.

BBS PM_{12}	**Fe**	**Ca**	**BBS $PM_{0.22}$**	**Fe**	**Ca**
Fe	1.00	0.15	**Fe**	1.00	0.14
Ca	0.15	1.00	**Ca**	0.14	1.00

Table 56. Fe/Ca correlations in PM_{12} and $PM_{0.22}$, Background site.

Stronger correlations were observed between Fe and Ni (*Table 57*) in PM_{12}, a result which contradicted the data from the roadside site in which the correlation between Fe and Ni was very weak. However, the $PM_{0.22}$ correlation was still weak.

BBS PM_{12}	**Fe**	**Ni**	**BBS $PM_{0.22}$**	**Fe**	**Ni**
Fe	1.00	0.49	**Fe**	1.00	0.14
Ni	0.49	1.00	**Ni**	0.14	1.00

Table 57. Fe/Ca correlations in PM_{12} and $PM_{0.22}$, Background site.

Correlations between Cu and Al, Ca and Ni were very weak at the background site in both size fractions with no clear trends in evidence.

6.5 Analysis of Soluble Ion Samples

The IC samples from spring 2013 were analysed for Chloride, Nitrate and Sulphate by anion chromatography and the data plotted as mass-size distributions. The aim of carrying out such experiments was that measuring these ions, especially sulphate and nitrate, would help explain some features of the total PM mass distributions obtained for the Birmingham sites. Of the six batches, gave what look like good results for these three ions but one (BR-11-4-13) looked unreliable from the available data. The mean distributions suggest that sulphate may be important in contributing to both the nucleation mode and to the submicrometer fine mode characteristic of the Birmingham roadside site.

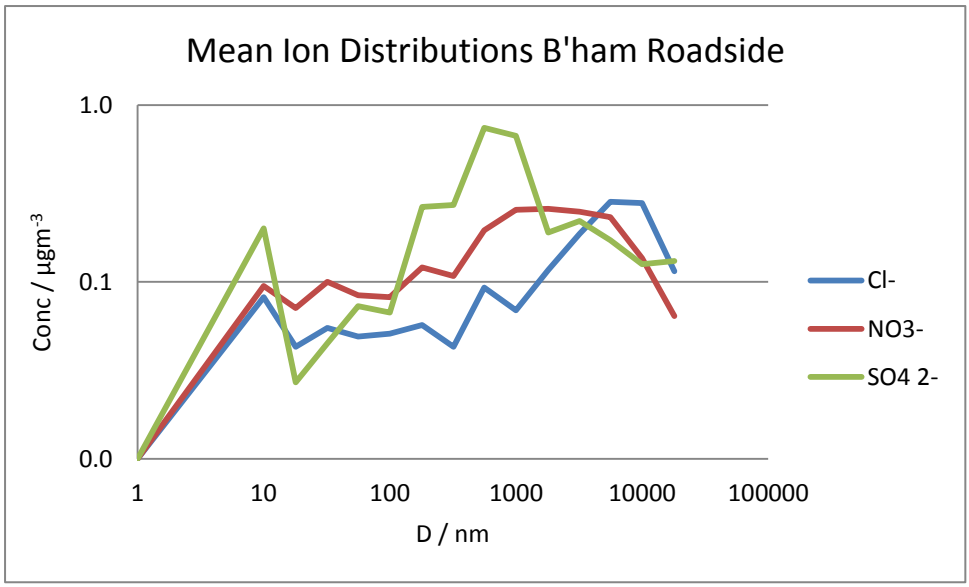

Figure 81. Mean Cl^-, NO_3^- and SO_4^{2-} mass-size distributions at the Birmingham Roadside site.

Chloride

Chloride (*Figure 82*) generally appeared in the coarse mode although the position and broadness of the peak varied slightly.

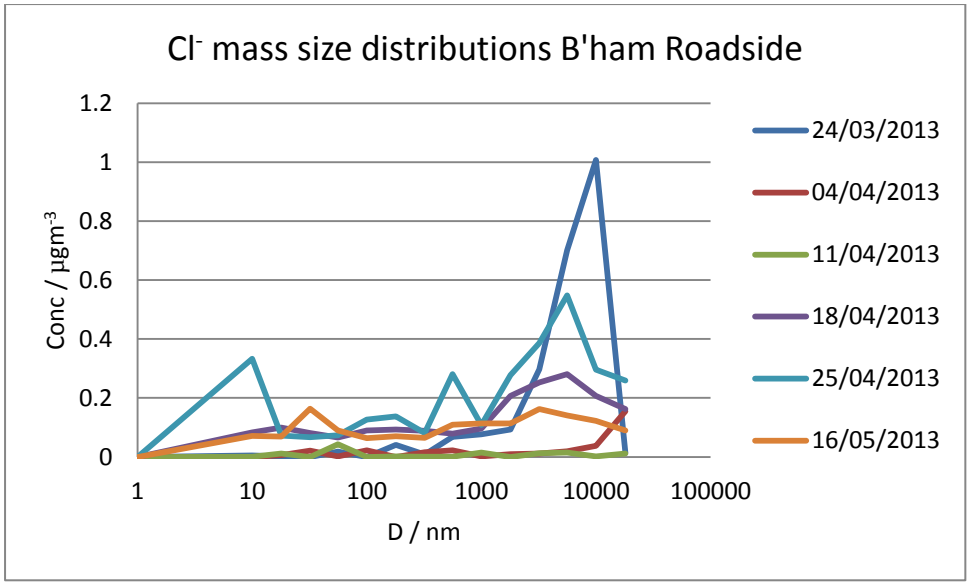

Figure 82. Chloride ion size distributions.

The Cl^- distribution in the 24-3-13 sample was largely in the coarse mode peaking at 5600-10000 nm. Mass concentrations below 1800 nm were small. S14 and S12 are below blank level and thus reported as zero concentration. Chloride was almost all in the largest size range in the BR-4-4-13 sample with less than half the total Cl^- mass concentration below PM_{10}. The chloride distribution in the BR-11-4-13 sample set appeared to be unreliable, with extremely low levels. The peaks in stages 11 and 13 were not reproduced in the BR-4-4-13 samples despite the ultrafine total mass distribution being roughly comparable in both samples. These appear to be contamination. The fine and coarse parts of the Cl^- distribution would probably follow the total mass distribution in the sample, but for the extremely low concentrations in stages 2 and 5. Low concentrations in those samples were a feature of that dataset for Cl^- and SO_4^{2-} but it was not clear why. The Cl^- distribution in the BR-18-4-13 sample was slightly different to the distribution in the 24-3 and 4-4 samples as it peaked at a lower size and had a broader mode, extending further into the fine particle range. As before, the submicron concentrations were low, but were slightly higher than in the 4-4 and 11-4 samples. The BR-25-4-13 distribution was very similar to the sample from 18-4 in having a broad fine/coarse

mode, but also had a submicron peak at 320-560 nm. The strong peak at 10 nm in this sample was not common to any of the other samples either. The most notable feature of the BR-16-5-13 sample compared to the previous ones was the reduction of the concentrations in the coarse mode leading to a much weaker mode in the 1800-5600 nm ranges. A peak also appeared in the ultrafine at 18-32 nm.

Earlier data from the Elms Road site in Birmingham demonstrate that Cl^- is found in a broad coarse mode, which is approximately consistent with the data presented above (Taiwo et al., 2014).

Nitrate distributions

The distribution of Nitrate (Figure 62) was quite variable (reflected in the poorly defined mean distribution), sometimes demonstrating an ultrafine mode in addition to a broad coarse mode peak, which sometimes stretched into the 1800-3200 nm size range.

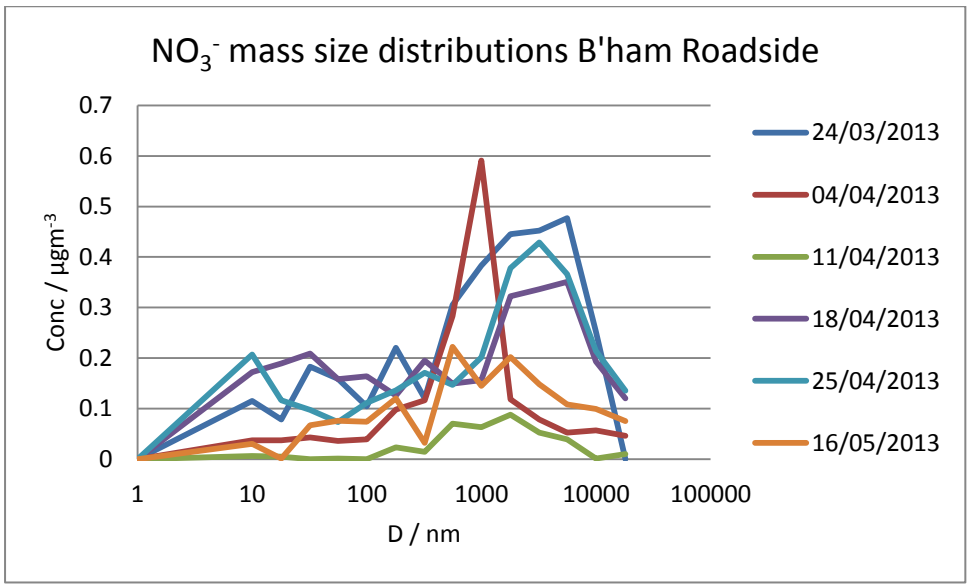

Figure 83. Nitrate ion size distributions.

The nitrate distribution in the BR-24-3-13 sample had a very broad mode stretching from 320-5600 nm as well as a smaller ultrafine mode. Nitrate had a narrow unimodal distribution

in BR-4-4-13 which peaked at 560-1000 nm and dropped off sharply either side of those values. That distribution was not exhibited by any of the other nitrate samples from this campaign. The NO_3^- distribution in the BR-11-4-13 sample essentially matched the total mass distribution of the sample. The mode at 100-180 nm appeared in PM_{total} and SO_4^{2-} as well. A very broad mode was observed starting at 320-560 nm and extended into the coarse mode at 3200-5600 nm. This was much wider than the droplet mode for NO_3^- which has been reported in previous urban studies (560-1000 nm). Low submicron concentrations were observed in the BR-18-4-13 sample with a single main mode from 1000-5600 nm. Although this sample was not very similar to the preceding samples the subsequent sample was much more similar to this. Both the absolute mass concentration values and the shape of the distribution in the BR-25-4-13 sample were similar to BR-18-4-13 with a single large mode in the upper fine and lower coarse mode. Contrasting BR-16-5-13 with the previous two samples showed the mass distribution flatter and broader with peaks below 1000 nm which did not occur in previous samples.

The results presented above are partially consistent with those of Taiwo et al. for the Birmingham background site, in which NO_3^- varied somewhat over several sampling periods, but averaged to a broad mode which peaked between 1000 – 2000 nm (Taiwo et al., 2014). However, the data from this project show the nitrate mode extending further into the fine fraction, down to 320 nm.

Sulphate distributions

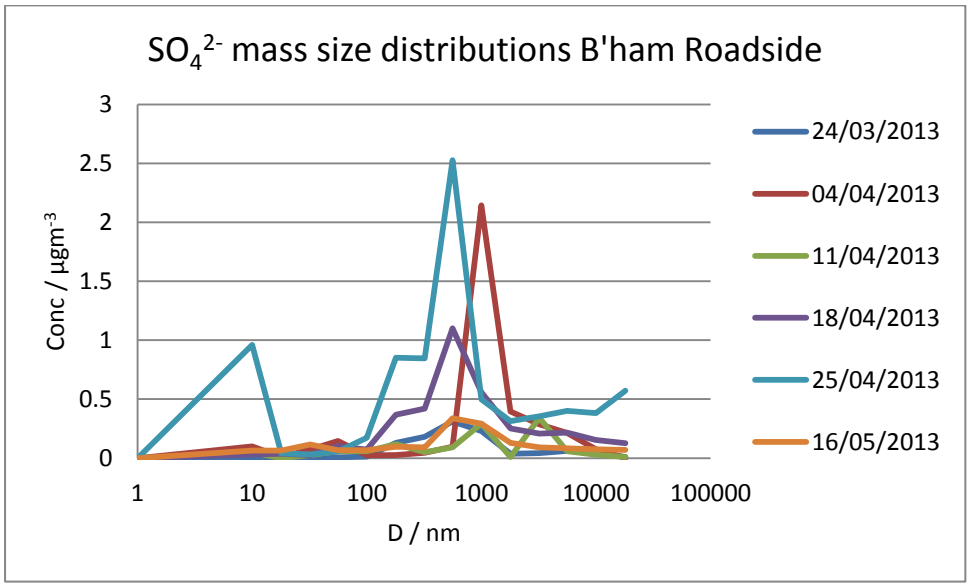

Figure 84. Sulphate ion size distribution.

The mean sulphate distribution in from the BROS site showed a submicron fine mode with low concentrations in the coarse and ultrafine size fractions.

In percentage terms sulphate formed high proportions (20-30%) of the total PM mass at two ranges, these being 560-1000 nm and 18-56 nm. The sulphate percentage in total $PM_{0.1}$ equalled 12%, which compared well with measures reported by previous studies which have indicated percentages from 0 up to ~25%, with higher values normally recorded in summer. The SO_4^{2-} distribution in the BR-4-4-13 set showed a bimodal distribution in which a small ultrafine mode (18-56) nm was observed along with a very pronounced submicron fine mode which tails off into the upper fine and coarse modes. It should be emphasised that this particular sample showed a very high total mass in this size fraction, so the SO_4^{2-} fine mode in this sample may be untypically pronounced. Sulphate concentrations above PM_{10} were very low. In the BR-11-4-13 sample the mode at 100-180 nm echoed the total mass distribution. Low coarse concentrations were similar to the result from BR-4-4-13, although

the peak in that sample at 56-1000 nm was much less pronounced in this set of samples and this set also contained a peak at 1800-3200 nm which was not found in the BR-4-4-13 samples. The sulphate distribution in the BR-18-4-13 set was far more typical than BR-11-4-13 and showed a broad submicron distribution peaking at 320-560 nm, similar to BR-24-3-13. The BR-25-4-13 sample again showed the majority of the sulphate between 100-1000 nm, but in this case the peak at 320-560 nm was much more dominant than in earlier samples. Furthermore, the 560-1000 nm size range showed reduced concentrations compared to the lower fractions. Compared to the previous sample, absolute concentrations were lower in the BR-25-4-13 sample. In terms of distribution, the peak was at 320-1000 nm and the 100-320 range was reduced in importance.

Comparison to previous work in Birmingham validates the sulphate data above. Both the absolute magnitude and pattern of distribution were very similar to the results from EROS presented by Taiwo et al. (2014), whose data showed a submicrometre fine peak and low concentrations in coarse particulate (Taiwo et al., 2014).

6.6 Conclusions

Data for Fe and Al in the UK samples showed high variability and distributions which were not wholly consistent with previous results. Other elements, such as V, Zn and Ni, appeared sounder and more confidence can be placed in them. V and Ni were generally found in the submicron fine mode, but pronounced ultrafine modes were seen at the Newcastle site. Zn was also mostly found in the submicron fine mode at the three urban sites. Ba was found mostly in particles above 560 nm at all locations. Sb distributions were incomplete, owing to low concentrations, but Cu was found distributed more evenly than Ba with a greater contribution from smaller particles indicative of some contribution by combustion/high temperature processes.

Data from Barcelona showed there were pronounced correlations between certain elements known to have common sources. Ba, Cu, Fe and Sb were generally found to correlate well, as indicators of brake wear. Mg and Na were found to exhibit similar mass-size distributions indicating a common source in sea salt. Likewise V and S, commonly associated with emissions from shipping, also had similar distributions to each other. Cu:Fe percentage ratios were consistent with earlier studies and showed a change with particle size, at the roadside site. Cu/Sb ratios were approximately consistent with previous studies although Sb was present at very low levels, so relatively large variations are seen.

The soluble ion data was consistent with previous studies, finding that although there was some variability in all three ions, Cl^- was primarily found in the coarse mode, NO_3^- between 560-3200 nm and SO_4^{2-} mainly in the submicrometre fine mode. It was also found that SO_4^{2-} is likely to be an important influence on the size and position of the submicrometre fine peak which was highly important in the Birmingham data.

Useful mass concentration data for metals in a number of environments are now available in the literature, but a useful direction of future research would be to further explore the correlations and ratios of different elements in atmospheric particulate matter, in different environments and size ranges. Some evidence in the data for Barcelona suggests that elemental ratios change in different size ranges and this may be indicative of sources. Such a proposition may be tested by comparison of ambient data to data obtained from known sources such as brakes, tyres and engines under controlled conditions.

References

Chuang, H.-C., Fan, C.-W., Chen, K.-Y., Chang-Chien, G.-P., Chan, C.-C., 2012. Vasoactive alteration and inflammation induced by polycyclic aromatic hydrocarbons and trace metals of vehicle exhaust particles. Toxicology Letters 214, 131-136.

Daher, N., Hasheminassab, S., Shafer, M.M., Schauer, J.J., Sioutas, C., 2013. Seasonal and spatial variability in chemical composition and mass closure of ambient ultrafine particles in the megacity of Los Angeles. Environmental Science: Processes & Impacts 15, 283-295.

Dodd, J.A., Ondov, J.M., Tuncel, G., Dzubay, T.G., Stevens, R.K., 1991. Multimodal size spectra of submicrometer particles bearing various elements in rural air. Environmental Science & Technology 25, 890-903.
Gantt, B., Hoque, S., Willis, R.D., Fahey, K.M., Delgado-Saborit, J.M., Harrison, R.M., Erdakos, G.B., Bhave, P.V., Zhang, K.M., Kovalcik, K., Pye, H.O.T., 2014. Near-Road Modeling and Measurement of Cerium-Containing Particles Generated by Nanoparticle Diesel Fuel Additive Use. Environmental Science & Technology 48, 10607-10613.
Gietl, J.K., Lawrence, R., Thorpe, A.J., Harrison, R.M., 2010. Identification of brake wear particles and derivation of a quantitative tracer for brake dust at a major road. Atmospheric Environment 44, 141-146.
Harper, S.L., Walling, J.F., Holland, D.M., Pranger, L.J., 1983. Simplex optimization of multielement ultrasonic extraction of atmospheric particulates. Analytical Chemistry 55, 1553-1557.
Hays, M.D., Cho, S.-H., Baldauf, R., Schauer, J.J., Shafer, M., 2011. Particle size distributions of metal and non-metal elements in an urban near-highway environment. Atmospheric Environment 45, 925-934.
Hueglin, C., Gehrig, R., Baltensperger, U., Gysel, M., Monn, C., Vonmont, H., 2005. Chemical characterisation of PM2.5, PM10 and coarse particles at urban, near-city and rural sites in Switzerland. Atmospheric Environment 39, 637-651.
Hulskotte, J.H.J., Roskam, G.D., Denier van der Gon, H.A.C., 2014. Elemental composition of current automotive braking materials and derived air emission factors. Atmospheric Environment 99, 436-445.
Johansson, C., Norman, M., Burman, L., 2009. Road traffic emission factors for heavy metals. Atmospheric Environment 43, 4681-4688.
Kukutschová, J., Moravec, P., Tomášek, V., Matějka, V., Smolík, J., Schwarz, J., Seidlerová, J., Šafářová, K., Filip, P., 2011. On airborne nano/micro-sized wear particles released from low-metallic automotive brakes. Environmental Pollution 159, 998-1006.
Lough, G.C., Schauer, J.J., Park, J.-S., Shafer, M.M., DeMinter, J.T., Weinstein, J.P., 2004. Emissions of Metals Associated with Motor Vehicle Roadways. Environmental Science & Technology 39, 826-836.
Lu, S., Feng, M., Yao, Z., Jing, A., Yufang, Z., Wu, M., Sheng, G., Fu, J., Yonemochi, S., Zhang, J., 2011. Physicochemical characterization and cytotoxicity of ambient coarse, fine, and ultrafine particulate matters in Shanghai atmosphere. Atmospheric Environment 45, 736-744.
Lü, S., Zhang, R., Yao, Z., Yi, F., Ren, J., Wu, M., Feng, M., Wang, Q., 2012. Size distribution of chemical elements and their source apportionment in ambient coarse, fine, and ultrafine particles in Shanghai urban summer atmosphere. Journal of Environmental Sciences 24, 882-890.
Niu et al., 2014. Evaluation of airborne particulate matter and metals data in personal, indoor and outdoor environments using ED-XRF and ICP-MS and co-located duplicate samples. Atmospheric Environment 44(2):235-245.
Ntziachristos, L., Ning, Z., Geller, M.D., Sheesley, R.J., Schauer, J.J., Sioutas, C., 2007. Fine, ultrafine and nanoparticle trace element compositions near a major freeway with a high heavy-duty diesel fraction. Atmospheric Environment 41, 5684-5696.
Pakkanen, T.A., Kerminen, V.-M., Korhonen, C.H., Hillamo, R.E., Aarnio, P., Koskentalo, T., Maenhaut, W., 2001. Urban and rural ultrafine (PM0.1) particles in the Helsinki area. Atmospheric Environment 35, 4593-4607.
Pennanen, A.S., Sillanpää, M., Hillamo, R., Quass, U., John, A.C., Branis, M., Hůnová, I., Meliefste, K., Janssen, N.A.H., Koskentalo, T., Castaño-Vinyals, G., Bouso, L., Chalbot, M.C., Kavouras, I.G., Salonen, R.O., 2007. Performance of a high-volume cascade impactor in six European urban environments: Mass measurement and chemical characterization of size-segregated particulate samples. Science of the total environment 374, 297-310.
Rogula-Kozłowska, W., Majewski, G., Czechowski, P., 2015. The size distribution and origin of elements bound to ambient particles: a case study of a Polish urban area. Environ Monit Assess 187, 1-16.

Saffari, A., Daher, N., Shafer, M.M., Schauer, J.J., Sioutas, C., 2013. Seasonal and spatial variation of trace elements and metals in quasi-ultrafine (PM< sub> 0.25</sub>) particles in the Los Angeles metropolitan area and characterization of their sources. Environmental Pollution 181, 14-23.
Taiwo, A.M., Beddows, D.C.S., Shi, Z., Harrison, R.M., 2014. Mass and number size distributions of particulate matter components: Comparison of an industrial site and an urban background site. Science of The Total Environment 475, 29-38.
Viana, M., Rivas, I., Querol, X., Alastuey, A., Álvarez-Pedrerol, M., Bouso, L., Sioutas, C., Sunyer, J., 2015. Partitioning of trace elements and metals between quasi-ultrafine, accumulation and coarse aerosols in indoor and outdoor air in schools. Atmospheric Environment 106, 392-401.

CHAPTER 7: SINGLE-PARTICLE CHARACTERISATION BY TRANSMISSION ELECTRON MICROSCOPY-ENERGY DISPERSIVE X-RAY SPECTROSCOPY AND ELECTRON ENERGY LOSS SPECTROSCOPY

7.1 Aims

The aim of the collection of samples for analysis by electron microscopy was the characterisation of the physical morphology and elemental composition of metallic particles at the single-particle level. This would enable us to determine whether particles are multimetallic, which elements occur together in particles and whether there are physical characteristics linked to the presence of particular elements or combinations of elements.

7.2 Introduction

3mm holey carbon films (Agar Scientific) were fixed to aluminium filter substrates and mounted in the nanoMOUDI as described in Chapter 2 to allow collection of size-segregated ambient particulate samples from the roadside sites in Newcastle and Birmingham for TEM, EDS and EELS analysis. Data is presented from 13 sessions in Birmingham and 3 at SuperSTEM from 2011-2014. It was found that the bulk of the metallic material detected by TEM was found in stages 7-9 of the nanoMOUDI. Even the metallic particles which were found in the lower stages generally exhibited similar characteristics and, when sized by measurement from the images, to be larger than the stated cutpoints which led to the conclusion that particle bounce from the larger stages was responsible. Free-floating ultrafine metallic particles were quite rare and not easy to locate, as the finer stages were dominated by amorphous carbonaceous material. We found that metallic particles were highly prone to agglomeration and to becoming adhered or embedded in larger particles, so that nanoscale primary particles actually appeared in a size range from approximately 100-560 nm aerodynamic diameter.

The focus of the study changed somewhat because in early TEM-X-EDS analyses Ce, V and Ni were not often observed. A handful of examples of Ce-bearing particles were identified which are discussed in section b (iii). Ni appeared in a small number of particles, usually as a minor

constituent in particles where Fe was the dominant element. Mn and Cr were often associated with Ni and Fe, suggesting that the co-occurrence of Fe-Ni-Cr may be indicative of a particular source. As Chapter 4 showed, this is likely to be engine exhaust emissions. The most abundant metallic elements proved to be Fe and Pb, and so attention turned to developing a more detailed characterisation of the physical and chemical composition of particles containing these elements.

Both elements proved ideal for detection using High-angle annular dark field imaging, as their high atomic weight makes them stand out strongly from surrounding non-metallic material on the grids. In the case of Fe in particular, finding particles in bright-field mode requires great care and skill to identify them from the carbon soot aggregates which dominate the grids. HAADF mode is also required to use the Energy Dispersive Spectroscope detector, so most of our images were collected in this mode. Imaging the same particle in both modes would have been ideal but in practice proved extremely difficult, as switching modes inevitably required some realignment of the microscope, making it very difficult to re-locate a given particle. Consequently, there are fewer bright-field images. However, HAADF images generally show the metallic particles more clearly so it may be better for the purposes of this study.

7.3 Elemental Composition from Energy Dispersive Spectroscopy

7.3.1 Classification by Factor Analysis

Stage 7 (320-560 nm) was selected for more detailed analysis to best characterise the Fe particulate and the following chapter is based on these analyses. Hierarchical cluster analysis was performed on the combined Newcastle and Birmingham roadside datasets to classify the collected particles by the weight percentage of each detected element once elements associated with the grid (Cu, Au, C, O) had been subtracted. The full dendrogram is too large to show in the main text but is contained in an insert with the Pb- and Fe- dominated regions of the diagram labelled for clarity. This work was undertaken in collaboration with researchers from Workpackages 2 and 3 of the FABLE

project, Dr Shei Su, who helped to analyse the samples collected by the author and Dr Ralf Weber, who prepared the cluster dendrogram from weight percentage data supplied by the author.

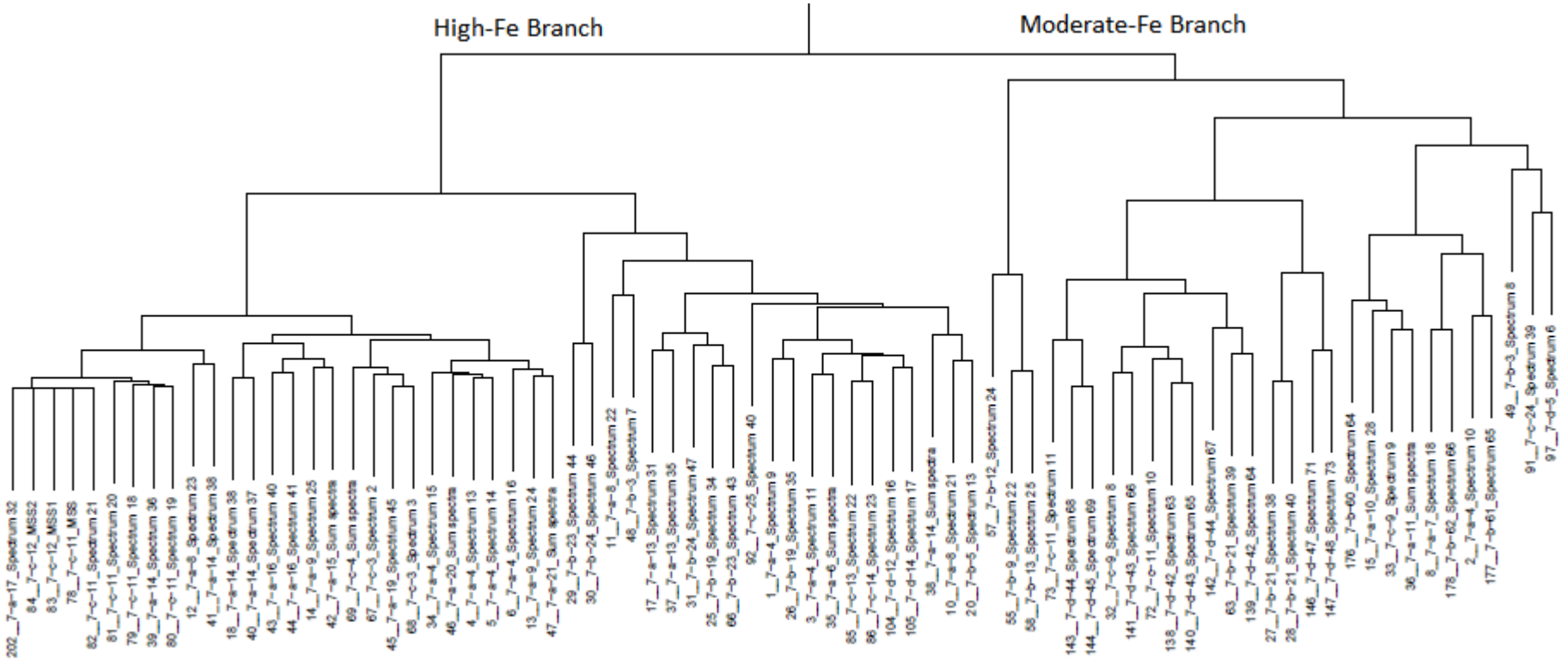

Figure 85. Fe-dominated particle groups, showing the two main branches.

This process revealed two major classes of iron-dominated particles (see *Figure 85*), not including particles where another metallic element such as Pb was dominant: a high-Fe type (Fe ca. 90%/wt) (*Figure 86*) and a moderate -Fe type (Fe ca. 75%/wt) which contained a much higher proportion of Mn and Si (*Figure 88*). The mean composition of these classes varied slightly between the two sites, but the pattern was generally similar and so this may not be highly significant.

The other major division in the cluster dendrogram was represented by the Pb-dominated spectra (*Figure 86*). The EDX spectra from the Stage 7 TEM grids collected in Newcastle and Birmingham revealed a surprising number of submicrometre Pb-rich particles. These have been found at both sites although far more were found at the Birmingham site than Newcastle. The Pb – rich particles detected from the TEM grids collected in Birmingham and Newcastle were clustered according to their elemental composition by weight, in the same way as the Fe-dominated particles. The results of this process implied that there are a range of sources contributing to submicrometre Pb particles in urban atmospheres.

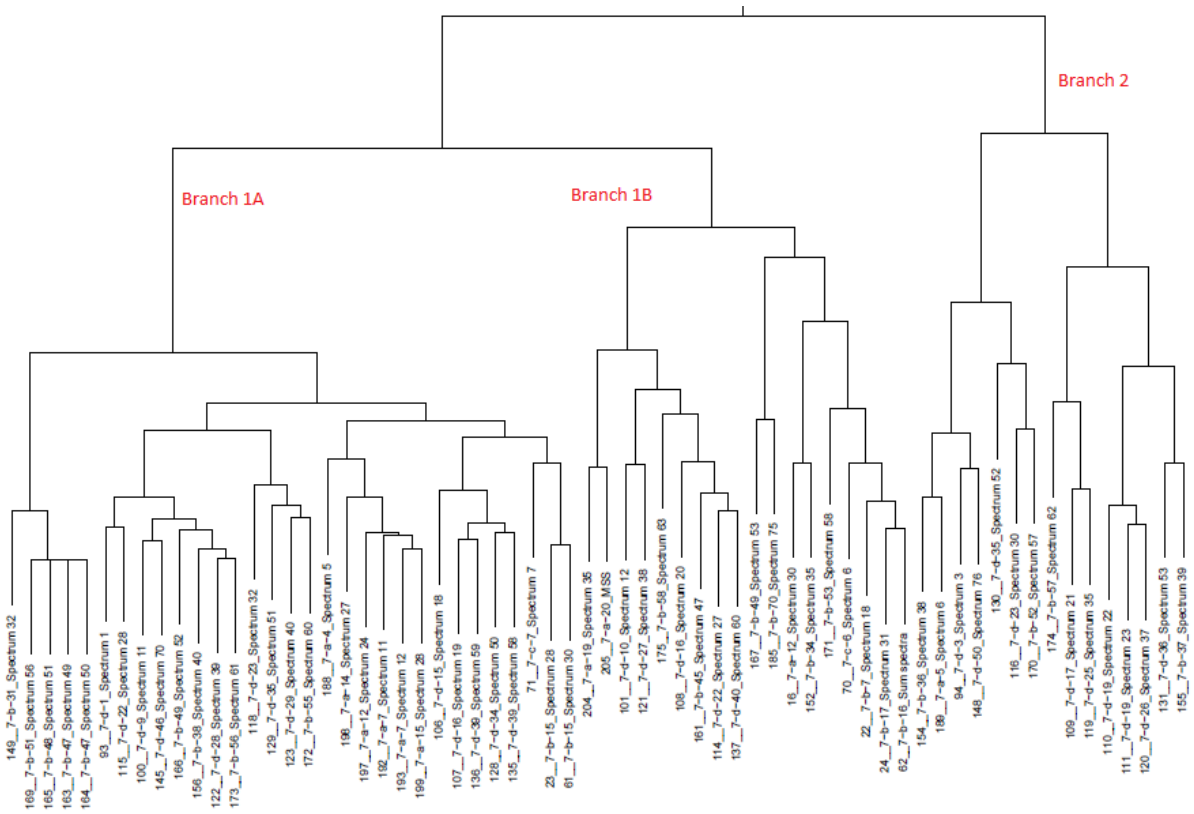

Figure 86. Pb-rich particle region of cluster dendrogram.

These form three main groups as labelled 1A, 1B and 2 in Figure 2.

7.3.2 Characteristic Particle Types: Iron

Iron in atmospheric particulate matter originates from a number of crustal and anthropogenic sources and the complexity of the iron source profile is reflected in the variable composition of our particles, albeit with traffic-derived particles appearing likely to be most important (Sanderson et al., 2014).

Moreover, each of these sources contributes iron with differing physical and chemical properties resulting from the effect of their different formation processes. Previously reported examples include nanoparticulate γ-Fe_2O_3 from fly ash (Linak et al., 2007), nanoparticulate Fe_3O_4 from in-cylinder melting of engine wear fragments (Liati et al., 2015), various oxides, silicates and W and Cr alloys from waste-to-energy plants (Buonanno et al., 2011) and agglomerates of nanoparticles of Fe_2O_3 and Fe_3O_4 from brake discs and pads (Kukutschová et al., 2011).

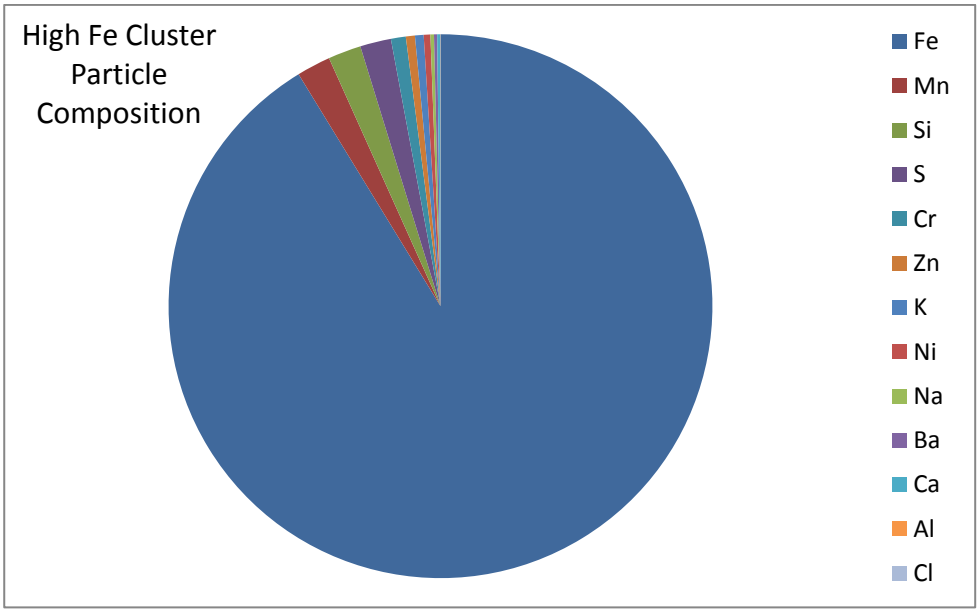

Figure 87. Pie chart average of High-Fe particle composition from EDX weight percentage data, both roadside sites combined (n = 48).

Element	Wt%
Fe	89.36
Mn	1.97
Si	1.92
S	1.80
Cr	0.87
Zn	0.53
K	0.50
Ni	0.39
Na	0.21
Ba	0.18
Ca	0.17
Al	0.01
Cl	0.01

Table 58. Tabulated average EDX data for high -Fe group particles.

The particles clustered into the high-Fe group (*Figure 87*) consisted of on average 91.4% Fe by weight, with a variable composition of minor and trace constituents together totalling slightly less than 10% by weight. Mn, Si and S were the most important of these constituents. Most of these elements are either associated with crustal origin or with abrasive emissions (road dust and tyre wear components), but some elements did appear for which exhaust emissions are likely sources in this size range. Ni and Zn in this size fraction were likely to be related to traffic exhaust. A variety of sources are probably represented by these elements.

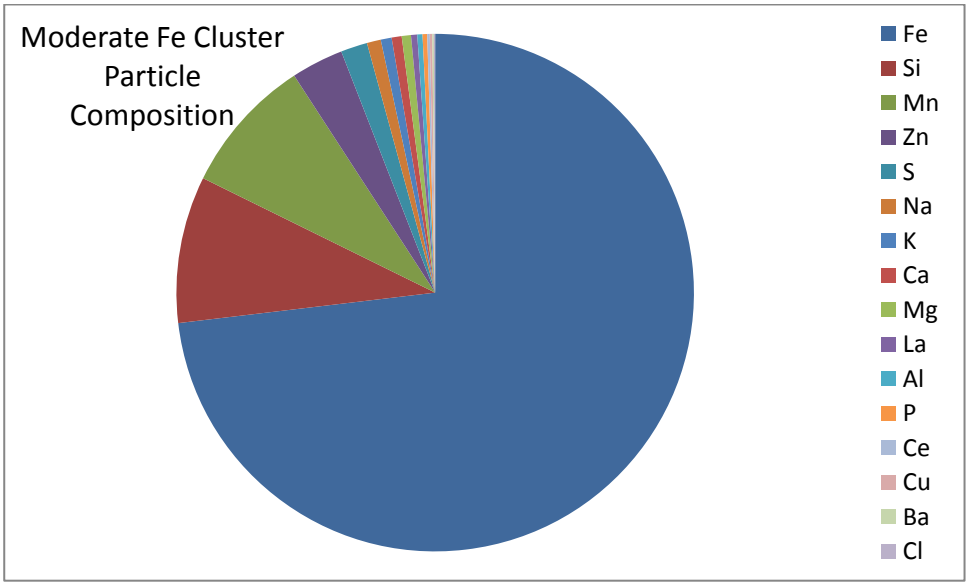

Figure 88. Pie chart of average composition of moderate -Fe particle group from EDX weight percentage data, both roadside sites combined (n = 28).

Element	Wt%
Fe	73.11
Si	9.17
Mn	8.54
Zn	3.26
S	1.66
Na	0.87
K	0.68
Ca	0.63
Mg	0.58
La	0.38
Al	0.33
P	0.29
Ce	0.16
Cu	0.16
Ba	0.09
Cl	0.09

Table 59. Tabulated average chemical EDX data for moderate -Fe group.

The average composition of the moderate-Fe cluster (*Figure 88*) showed a much lower weight percentage of Fe, with Mn and Si being the most important minor constituents, followed by Zn. Many of the same elements were classified among the trace constituents found in this cluster (not all present in every particle). Two rare earth elements (La and Ce) appeared in this cluster. Cu and Ba appeared as trace constituents. Some crustal/resuspension elements (Al, Ca, La) appeared too. Zn is more prominent than in the high-Fe group.

There were some differences between the two sites. At Newcastle the high-Fe type represented 70% of the sampled Fe-rich particles. At the Birmingham Roadside site, this figure is 48%. Fe content in this cluster was slightly higher in Birmingham than in the corresponding class for Newcastle – 96.0% compared to 89.9%. Many of the trace elements were the same but Ba, Al and Ca were not detected in the Newcastle high-Fe cluster.

A wider range of trace constituents were found at both sites in the moderate-Fe-Mn cluster compared to the high-Fe cluster, but Mn and Si were still the principal alloy elements. Fe content was again slightly higher in Birmingham than in the corresponding Newcastle cluster – 74%

compared to 70%. This cluster incorporated both combustion (Ce) and brake wear (Cu, Ba) associated elements.

The high-Fe cluster in the Newcastle samples contained fewer detectable trace components than that of the Birmingham samples. Unlike the latter, it contained Cr, but the most important minor constituents were still Mn/Si/S. The moderate-Fe group at Newcastle also contained fewer minor elements than the Birmingham group. Si and Mn were present in similar proportions to the Birmingham particles, but Zn was more prominent at Newcastle.

Both particle groups at both sites contained an interesting mix of elements. The common local source at both sites was traffic and most of the elements in these clusters are known to be associated with vehicle emissions. Fe, the dominant element in these samples, is associated mainly with wear from brake components, both pads and rotors although recent results published by Liati et al. (2015) confirm that wear to engine components is also an important source, and the particles produced in that process are similar in many ways to those reported here (Liati et al., 2015). Brake wear is also the main source of Cu, Sb and especially Ba in roadside environments (Thorpe and Harrison, 2008). Zn is associated with multiple sources, including tyres, brakes and exhaust emissions from trace levels in lubricating oils (Thorpe and Harrison, 2008). Al and Ca are associated with crustal origins, but in particles in this size range it is likely that lubricating oils in engines are responsible, at least for Ca (Harrison et al., 2004).

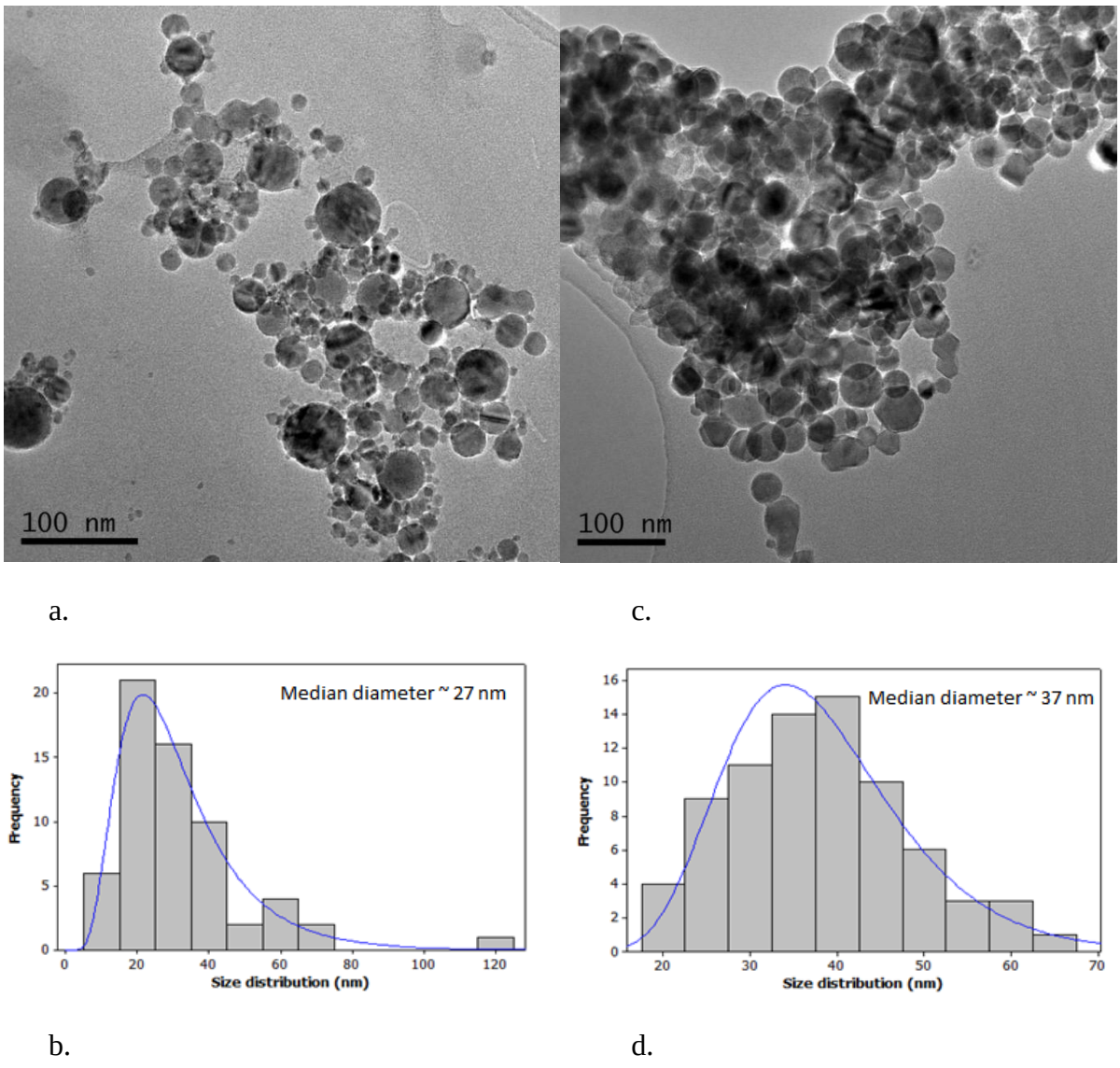

Figure 89. Bright-field TEM images of (a) high-Fe and (c) moderate-Fe agglomerates with size distribution plots for primary particles of (b) high-Fe and (d) moderate-Fe below. (Samples collected at Bristol Rd site, Birmingham, 7/1/14).

There was considerable variability of size and shape of both primary particles and agglomerates in the dataset. For the most part, the iron particles observed appeared to be oxides, taking the form of spheres or multifaceted regular polyhedra, as can be seen in *Figure 89 (a)* and *89 (c)*. The primary particles were mainly in the range of 20-40 nm although some much larger particles up to around 100 nm can also be observed, along with some very small particles of 10 nm or even less. As *Figure 89* shows, the primary particles in the high-Fe group had a smaller median diameter, along with a bimodal distribution in which the main peak occured at 20 nm and a much smaller second

peak at 60 nm. This feature was not shared by the moderate-Fe group, in which the distribution curve is broader peaking at a higher diameter. They also agglomerated readily, forming irregular agglomerates of many primary particles.

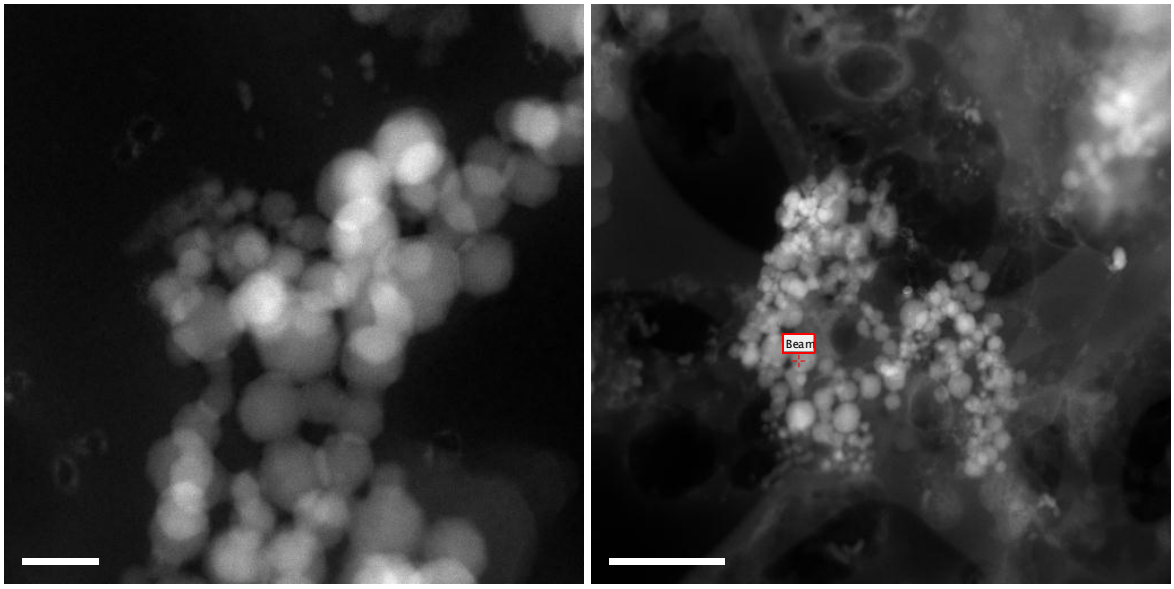

a **b**

Figure 90. SuperSTEM HAADF images of agglomerated nanoparticles (a = high-Fe group, b = moderate-Fe group).

Typical particles of both types are shown in *Figure 90*, which shows how similar the physical appearance of the two types was. In both cases a large number of spherical and near-spherical primary nanoparticles form irregular agglomerates in excess of 200 nm diameter. Primary nanoparticle size was somewhat variable in both cases, but generally 20-40 nm. The particle shape was indicative of a high-temperature formation process.

Kukutschova et al. (2011) reported that Fe was the dominant metallic element in ultrafine and submicron brake wear, primarily as agglomerates formed from nanoparticles of 20 nm upwards (Kukutschová et al., 2011). Such agglomerates would be similar to the observed environmental particles, but smaller particles can also be observed in some agglomerates. From this source, nanoparticle generation was reported to be negligible when the friction interface was cold, but

became highly significant at rotor temperatures above 300°C. Mosleh et al. (2004) reported that a population of particles rich in Fe, C and O was generated with an approximate average diameter of 350 nm, this composition showing the particles were generated from the cast-iron disc (Mosleh et al., 2004). This class was not dependent on sliding speed or load, which suggests that the formation process is temperature-dependent rather than load dependent. The approximate agglomerate size and composition would fit with the particles observed in the environment.

Liati et al. (2015) reported that Fe_3O_4 nanoparticles generated by melting and recooling of engine wear fragments were mostly 40-60 nm in diameter for spheres, but smaller particles showing cubic structures were also in evidence. These often appeared rounded at the edges but not spherical, possibly caused by heating (Liati et al., 2015). Rounded-edged cuboidal particles can be seen along with spherical particles in *Figure 89 (c),* which may represent a similar type to the particles reported by that study. The various agglomerate Fe nanoparticles reported by Liati et al. (2015) bear many morphological similarities to those we report although the size distributions are not identical.

Iron has also been detected in ultrafine particle emissions from a waste-to-energy plant as amorphous alloys with W and Cr, and in oxides (rounded, aggregated and suspended on phyllosilicates) which sometimes included one or both of these elements (Buonanno et al., 2011). Iron silicates with Al and Cr were also detected at the stack. In our observations Al and Cr are present in both particle classes but are not prominent, being only trace constituents. Furthermore we frequently find that Cr is accompanied by Ni. W was not observed in any of the particles we analysed.

Iron bearing particles from diesel engines using fuel additives have been reported to consist of nanoscale primary particles (5-10 nm) incorporated within complex carbon soot agglomerates. Particles of Fe included in carbonaceous soot in this fashion have not been observed in our ambient

measurements, most Fe particles appearing in the form of agglomerates with similar particles, although some agglomerates are attached to larger particles. It has been reported that at higher doping levels, primary particles become larger and iron nanoparticle clusters begin to form (Miller et al., 2007). Nash et al. (2012) reported that iron represents around 0.1% of the total mass of diesel soot from undoped fuel. Introducing iron into the fuel changes the size distribution by increasing the nanoparticle component. In small particles (18 nm mean) spherical nanoparticles and irregular clusters were reported. At 100 nm mean diameter, iron is mostly present as inclusions and surface deposits on carbon soot particles (Nash et al., 2012). By contrast the majority of Fe oxide particles we have observed in the environment were agglomerates of Fe particles, not inclusions or surface deposits. This suggested that they formed in an iron-rich environment, rather than having coagulated in the atmosphere where particle composition is very diverse.

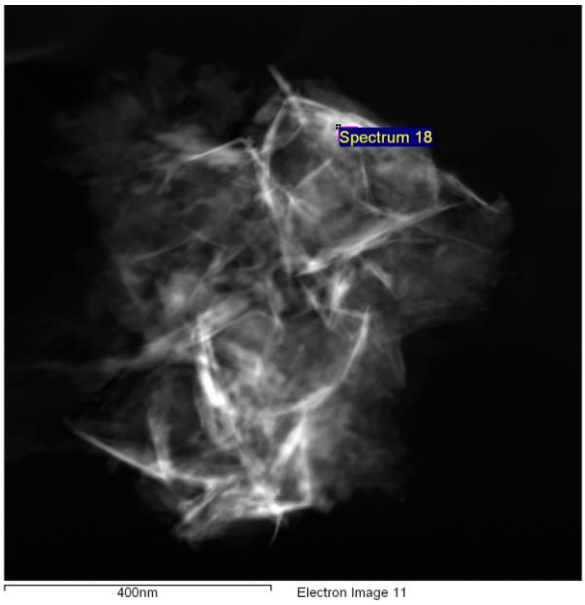

Figure 91. Irregular rod agglomerate formed of high-Fe primary particles.

Although much less common than the spherical type of primary particle, one unusual case of an agglomerate formed of elongated rod-shaped primary nanoparticles was observed (see *Figure 91*). This was a high-Fe particle with trace amounts of Mn and Cl and the primary particles formed an irregular agglomerate of around 725 nm length. Unlike the majority of particles in the study these appear to be the result of an abrasive formation process, perhaps at the friction interface between

brake disc and pad. Formation of elongated grains through plastic deformation of the rotor surface has been reported by Österle et al. in a previous study of brake wear (Österle et al., 2010).

7.3.3 Characteristic Particle Types: Lead

The mean composition by weight in each cluster is shown below in *Figures 92-94*. Pb was the dominant component, with Zn and Cl also being prominent. Fe was present in a number of particles though generally at quite low concentrations. Sb was prominent in cluster 2 being present at high weight percentages, but was only a minor constituent in the other clusters. Particle morphology was highly variable although some distinctive features can be identified. In all three clusters particles of Pb were generally irregular in shape and often took the form of multiple irregular inclusions in non-metallic host particles. These were easily identifiable when examining samples, as they were very different to the spherical or faceted particles typical of Fe, which was the other main metallic element in the ambient samples. Particles were commonly found to be adhered to carbon soot aggregates although it was not possible to tell at what stage this agglomeration took place, whether early in the formation process or post-formation in the atmosphere. The soot particles in question were of the type common at the top end of the accumulation mode in our ambient samples; long complex fractal agglomerates formed of many spherical and near-spherical carbon particles. There was some similarity to be seen in the images of particles from each group, but there were also some interesting morphological differences to be seen.

Cluster 1A

Element	Mean %	Stdev	N
	1A		
Pb	84.76	7.72	31
Cl	5.21	3.06	16
Zn	2.50	2.84	16
Co	1.82	3.27	8
Fe	1.74	3.57	9
Sb	1.56	3.06	8
K	0.86	1.28	11
Si	0.51	1.10	3
S	0.49	2.26	2
P	0.43	1.99	2
Cu	0.10	0.10	2
Particle size/nm	23.03	21.08	
Agglomerate size /nm	93.86	128.33	
Total number of spectra = 31			

Table 60. Particle composition, Pb cluster 1A.

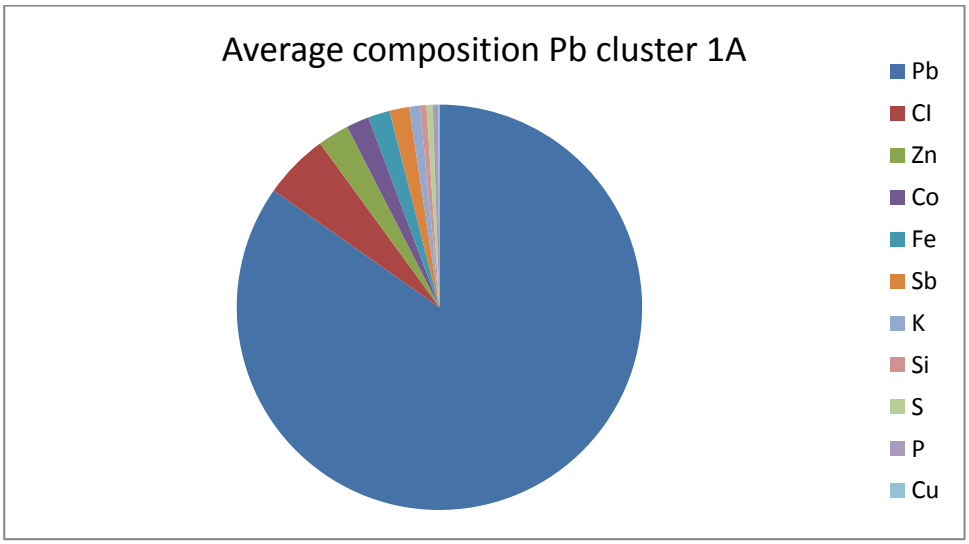

Figure 92. Composition chart, cluster 1A.

Cluster 1A consisted of the most Pb-rich group of particles with Pb content over 84%. Zn and Cl were the most important minor constituents both in terms of average wt% and the number of particles in the cluster they were detected in. Sb and K appeared in around one quarter of the spectra but at very low weight percentages. The Pb dominated composition would probably imply an

industrial origin of these particles. Only 3 of the 31 spectra in this cluster came from Newcastle, the remainder from Birmingham.

Cluster 1B

Element	Mean %	Stdev	N
	1B		
Pb	63.24	8.78	18
Zn	11.12	7.06	11
S	7.11	7.95	8
CI	5.59	9.08	8
K	5.53	4.99	12
Sb	1.58	4.54	5
Na	1.53	1.21	6
Co	1.51	3.41	7
Fe	1.50	3.91	6
Si	0.78	3.58	3
Ca	0.32	N/A	1
Mg	0.11	N/A	1
Cu	0.09	0.64	2
Particle size/nm	27.02	30.98	
Agglomerate size /nm	88.03	114.58	
Total number of spectra = 18			

Table 61. Particle composition, Pb cluster 1B.

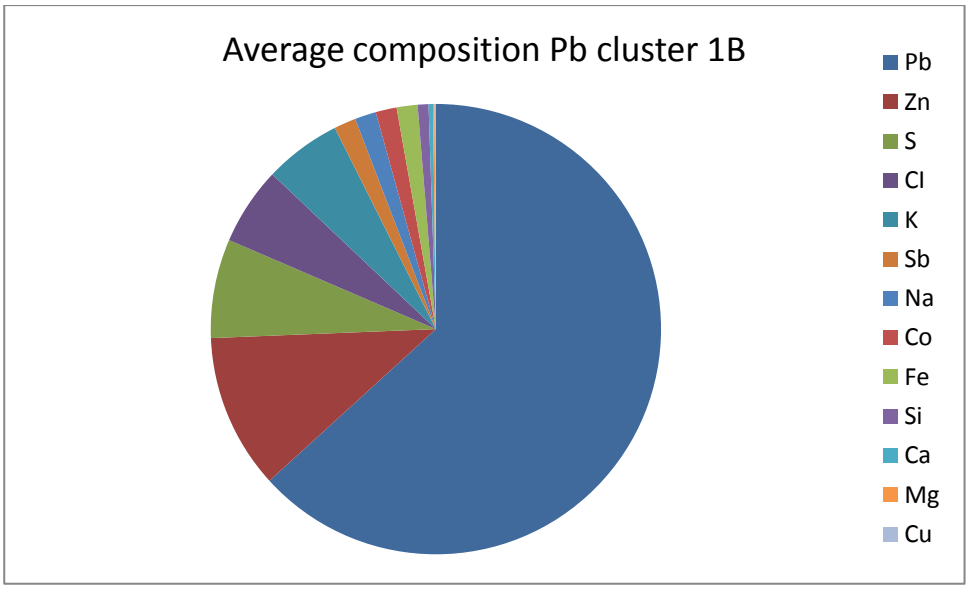

Figure 93. Composition chart, cluster 1b.

Cluster 1B showed a considerable reduction in Pb content by weight compared with cluster 1A down to 63%, with Zn, S and Cl the most prominent minor constituents. However, the average particle sizes and agglomerate sizes were quite close to those of cluster 1A. Spectra in this cluster came from both sites, 5 from Newcastle and 13 from Birmingham.

Cluster 2

Element	**Mean %**	**Stdev**	**N**
	2		
Pb	48.73	12.08	15
Zn	24.18	16.12	15
Sb	14.23	12.67	9
Cl	6.31	4.64	13
Na	2.29	1.74	4
K	1.89	7.45	6
Si	1.09	3.87	4
Fe	0.46	2.12	4
Co	0.37	3.38	2
S	0.32	N/A	1
Mn	0.12	N/A	1
Total	**99.99**	**N/A**	**15**
Particle size/nm	21.91	21.78	
Agglomerate size /nm	59.82	50.95	
Total number of spectra = 15			

Table 62. Particle composition, Pb cluster 2.

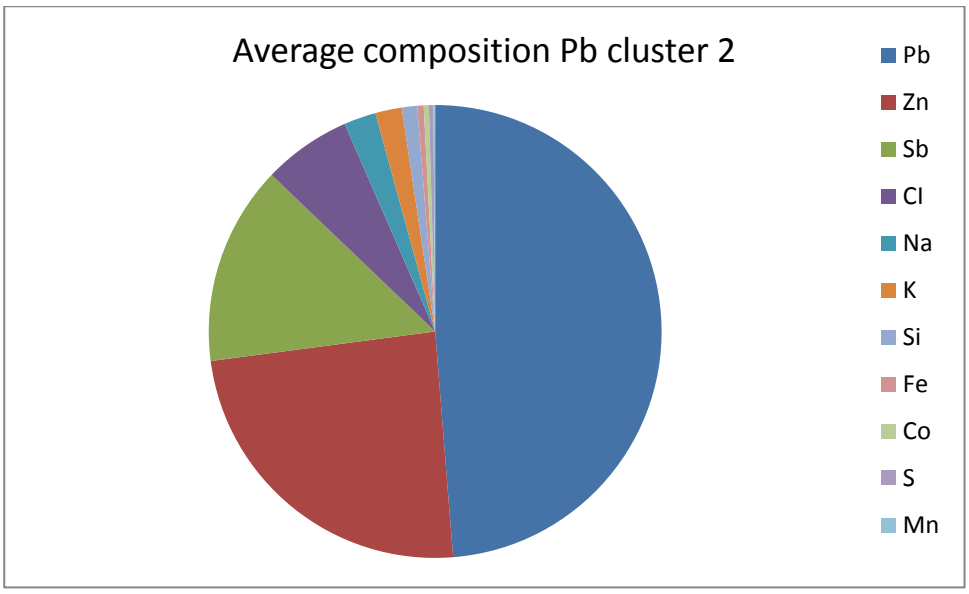

Figure 94. Composition chart, cluster 2.

Pb content in cluster 2 was below 50% on average although it was still by far the dominant component. This cluster had a high Zn content and a substantial Sb content, which was the feature which most differed from the other two clusters. Cl content by mass was similar to 1A and 1B, and Cl is present in most spectra in this group. While the size of the primary particles was quite similar to clusters 1A and 1B, the size of the agglomerates was considerably smaller in cluster 2. None of these spectra came from the Newcastle datasets, although that does not mean that no cluster 2 particles would be found at that site.

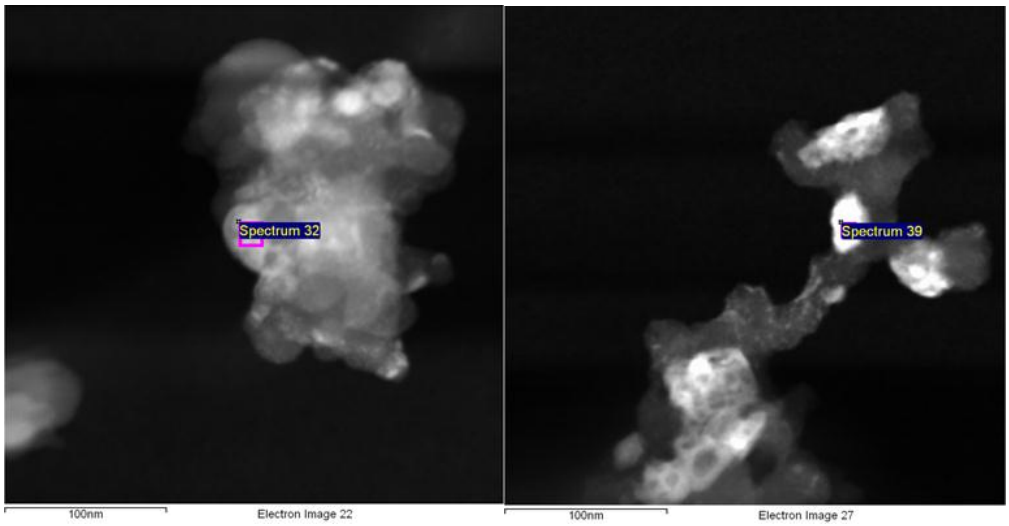

Figure 96. Examples of Pb particles from cluster 1A.

Both particles illustrated in *Figure 96* show the tendency of cluster 1A Pb particles to have irregular shapes and form multiple inclusions in a host material. Since there was no Si in the Pb-dominated particle types, this material is most likely to be carbonaceous.

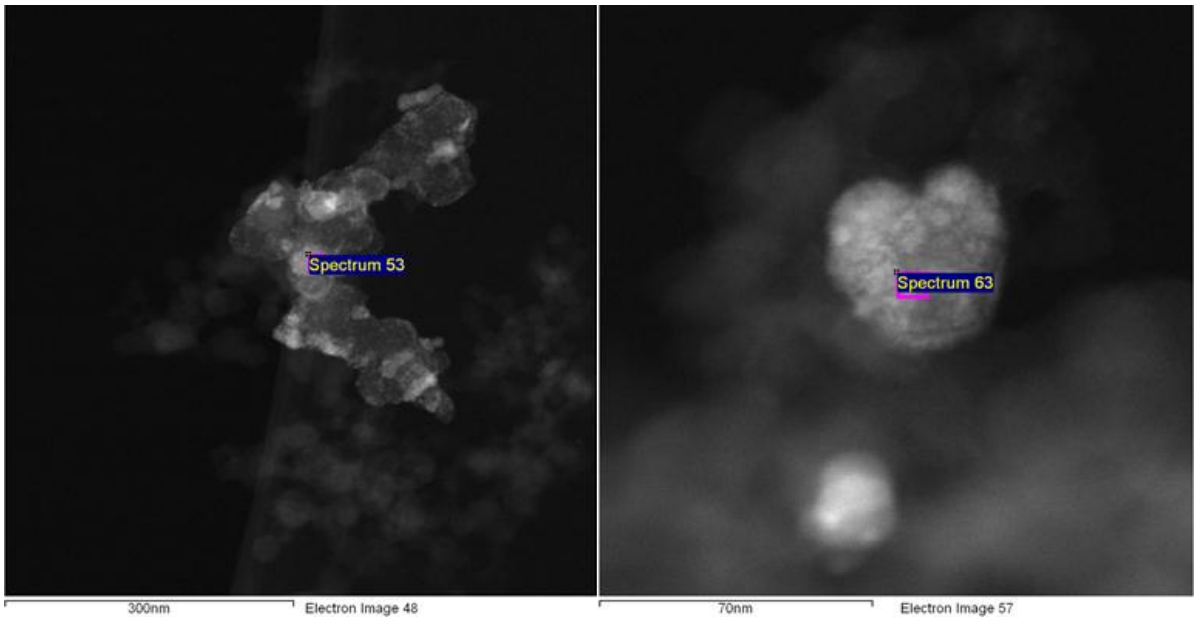

Figure 97. HAADF images of examples of Pb particles from cluster 1B.

Spectrum 53 (left) in *Figure 97* showed a very similar morphology to the cluster 1A particles in *Figure 96*. This particle was high in Zn, more similar to the 1A type. Spectrum 63 (right) showed an alternative form, of an irregular agglomerate of very small primary particles adhering to a carbon soot aggregate. This particle was high in Cl as well as Zn.

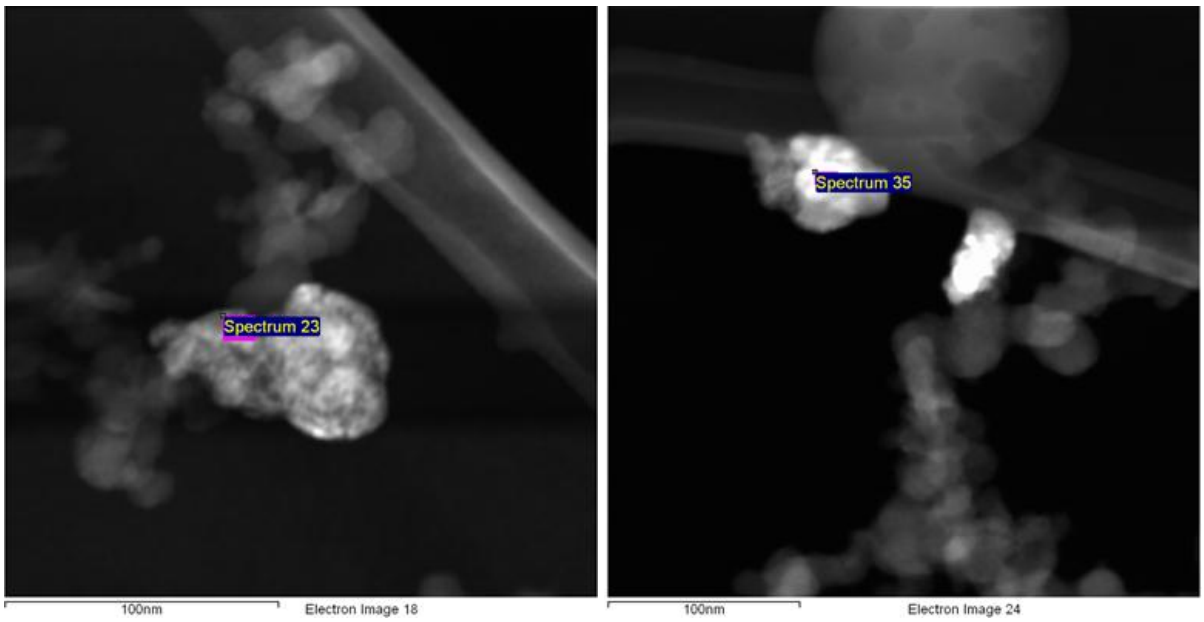

Figure 98. HAADF images of examples of cluster 2 Pb particles.

Particles in cluster 2 were also associated with other materials which appeared to be carbon soot. However, these were in the form of agglomerated nanoparticles which adhered to the outside of the soot particles rather than forming inclusions (*Figure 98*). Some of the particles which were particularly rich in Sb (35-40% by weight) also appeared as agglomerates which did not associate with soot agglomerates (*Figure 99*). This may indicate that their source does not also emit large quantities of carbon.

Figure 99. Non-adhered Pb agglomerates rich in Sb.

The particles in *Figure 99* were smaller than was normal in the other clusters and the primary constituents were very small nanoparticles, well below 10 nm in diameter.

Since the withdrawal of tetra-ethyl lead as an anti-knocking additive in fuel, isotopic analysis of Pb in atmospheric particulate matter has confirmed that industrial sources are gradually becoming more prominent compared to traffic, although emissions from gasoline vehicles remain important as Pb is a trace constituent even in unleaded fuel (Noble et al., 2008). Pb has also been associated in small particles with brake wear emissions by Saffari et al (Saffari et al., 2013). The high level of Sb in cluster 2 might indicate this as a potential source as Sb is a well-established tracer for brake wear emissions. The absence of Ba and Cu suggest the opposite, however, and there are other potential sources of Pb-Sb particles. The Pb-Sb combination also occurs in various alloys (generically known as white metal, though this refers to a wide range of alloy compositions) used in bearings. However, these alloys are generally rich in Sn and contain Cu, which are not present in cluster 2.

Tolocka et al. (2005) have also used the combination of Pb, Sb and Cd as a marker for incinerator emissions (Tolocka et al., 2005). $ZnCl_2$ is also reported to be a marker for this source and would agree with our findings that both Zn and Cl are common constituents of Pb-bearing particles. Emissions of Pb and Zn have previously been found to be important components of <50 nm and <100 nm particles emitted from waste-to-energy plants (Cernuschi et al., 2012). However, given that emissions from modern waste incinerators are quite low it is unlikely that either site would be impacted by such emissions as there are no facilities within the immediate area of either site.

Visser et al. (2014) report that the fine fraction accounts for more Pb than the coarse fraction, with vehicle exhaust, industry and secondary sulphate and wood-burning all reported as important sources (Visser et al., 2014). That result concurs with a previous work by Flament et al. (2002) which reported that most atmospheric Pb was anthropogenically sourced owing to high enrichment factors over the crust and occurred in the 400 – 900 nm size range (Flament et al., 2002). Our results from nominal D_a 320-560 nm would agree with this. Although sizing from TEM images

places the average agglomerate and particle sizes much smaller than this, a likely explanation arises from the association of Pb particles with soot agglomerates of much larger size but comparatively low density. The sizes we have determined from our TEM images would broadly be in agreement with Tolocka et al. who reported that the Pb mass concentration peaked at 150 nm D_a (Tolocka et al., 2004).

Reinard et al. (2007) reported that a class of submicron Pb-Zn-K-Na particles were associated specifically with emissions from a steelwork and could be identified in ambient samples when the wind direction at the sampling site was coming from the source. However, all three elements are present in all three particle clusters in our data. Zn is prominent but K and Na are comparatively minor constituents. Furthermore the authors reported that other combinations of these elements could not be definitively assigned to this source (Reinard et al., 2007). Ntziachristos et al. (2007) observed that roadside Pb had a broad and quite flat size distribution from 18-180 nm (Ntziachristos et al., 2007), while Lough et al. (2004) attributed submicron roadside Pb to a number of sources which included trace concentrations in gasoline, brake pads and wheel weights (Lough et al., 2004).

7.3.4 Characteristic Particle Types: Cerium Oxide

Very few Ce particles were detected by TEM. Somewhat surprisingly, these particles were actually found in Birmingham rather than Newcastle, despite the reason for sampling in Newcastle being that CeO_2 fuel additives were known to be in use by the local public transport firm. The particles we which were found broadly matched the descriptions of environmental CeO_2 previously reported as they were small, regular polyhedral nanoparticles which in some cases adhered to large soot aggregates (Park et al., 2008). Some particles were composed of Ce and O only, but there are some which are associated with other elements such as Fe and Cr which are also known to be associated with engine wear. Gantt et al. (2014) used the same instruments for sample collection at the Newcastle site (summer 2012) and determined that non-crustal Ce in bulk particulate peaks between 100-320 nm D_a, which implies that Ce particles in that environment have become associated with

soot (Gantt et al., 2014). Furthermore, the emitted particles are found to be smaller than the ambient, showing that particle growth occurs post-emission.

Figure 100. Single Ce nanoparticles associated with soot.

Element	Spectrum 68	Spectrum 70
Ce	86.33	100
Si	13.67	

Table 63. Elemental Compositions by EDX (weight %), Ce particles.

Two Ce nanoparticles collected in the nanoMOUDI Stage 7 (320-560 nm) at the Bristol Road site in Birmingham in January 2014 are illustrated in *Figure 100*. These particles were associated with the same large carbonaceous soot agglomerate and have evidently come from the same source. Spectrum 68 (left image) is a faceted nanoparticle of 11.774 nm diameter, Spectrum 70 (right image) is very similar in shape but somewhat larger, at 15.561 nm.

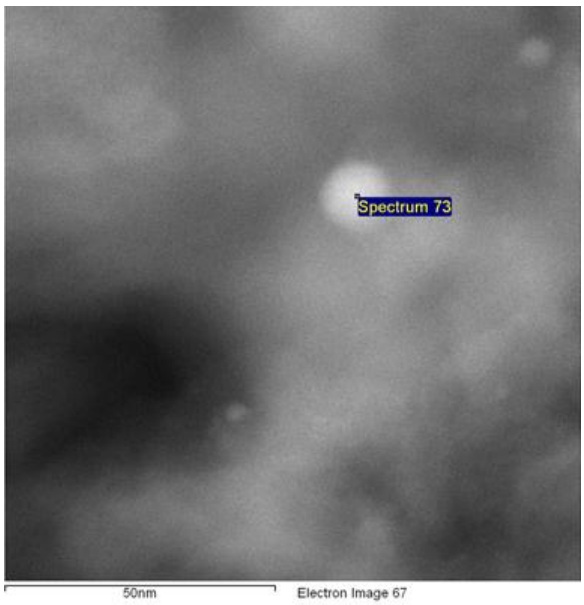

Figure 101. Ce/Fe mixed nanoparticle, associated with soot.

Element	Weight %
Ce	39.68
Fe	60.32

Table 64. Elemental Compositions by EDX (weight %), Ce/Fe particle.

Figure 101 illustrates a Ce/Fe nanoparticle of approximately comparable size (11.725 nm) to those of *Figure 100*, although the particle is more spherical in shape. In this instance Fe is present as well, such that the Ce:Fe ratio is approximately 40:60. A particle also containing Fe could still be engine-derived, as Fe is a common element in emissions from diesel engines.

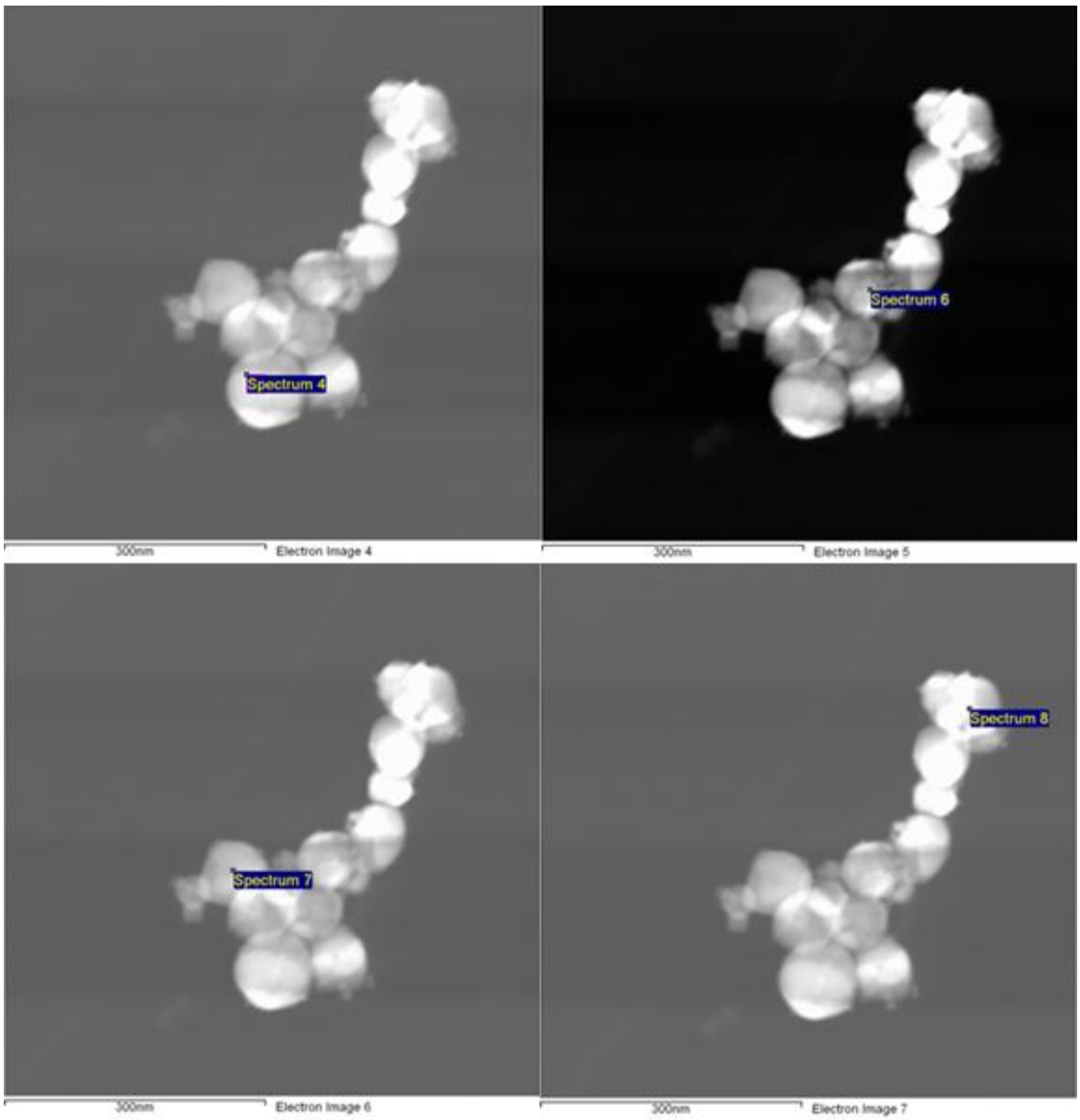

Figure 102. Ce-containing agglomerate.

Element	Spectrum 4	Spectrum 6	Spectrum 7	Spectrum 8
Ce	42.85	4.49	44.74	61.7
Fe	27.95	62.65	28.36	12.53
La	22.28	10.76	18.85	23.44
Mg	4.61	14.4	4.59	
Mn		0.98		
S		1.26	0.97	0.57
Si		0.74	0.58	0.78
Zn	2.3	4.12	1.92	0.98

Table 65. Elemental Compositions (weight %), Spectrums 4, 6, 7 & 8.

The agglomerate in *Figure 102* is highly interesting in the context of our other results. Morphologically there are clear similarities with the Fe oxide NP agglomerates which are shown in Chapter 7.3.2, but the composition is different owing to the presence of Ce and La. The morphology would suggest an origin in high-temperature combustion processes. Composition is slightly variable throughout the agglomerate, as proven by Spectrums 4-8 which are taken from different particles within the agglomerate. It may be that this particle indicates an engine origin for the Fe nano-agglomerates owing to the similarity in physical form and the presence of high levels of Ce, which are only likely to have come from a fuel additive source. Particles generated from the same process in engines not employing ceria will probably look similar in appearance but not contain Ce.

7.4 Electron Energy Loss Spectroscopy

7.4.1 Oxidation States of Fe-bearing particles

In previous studies it has generally been found that Fe (III) is the predominant oxidation state among atmospheric iron particles, although the picture is complicated because Fe participates in reactions with organic compounds which can lead to the reduction of Fe (III) (Erel et al., 1993). Fe and Mn are prone to undergo oxidation reactions during atmospheric transport and smaller particles are more likely to be found at higher oxidation states which have been found to have an average state between Fe(II) and (III) (Marris et al., 2013). A 2009 study on simulated atmospheric aging of Fe-Cr-Mn particles by Nico et al. reported that Mn in mixed metallic particles had the effect of capturing oxidative potential and passing it on to other components, leading to enhanced oxidation of Fe and Cr (Nico et al., 2009). The results presented in *Figure 18* support this contention, as a higher proportion of the Fe-Mn mixed particles are in the more oxidised states compared to the high-Fe type.

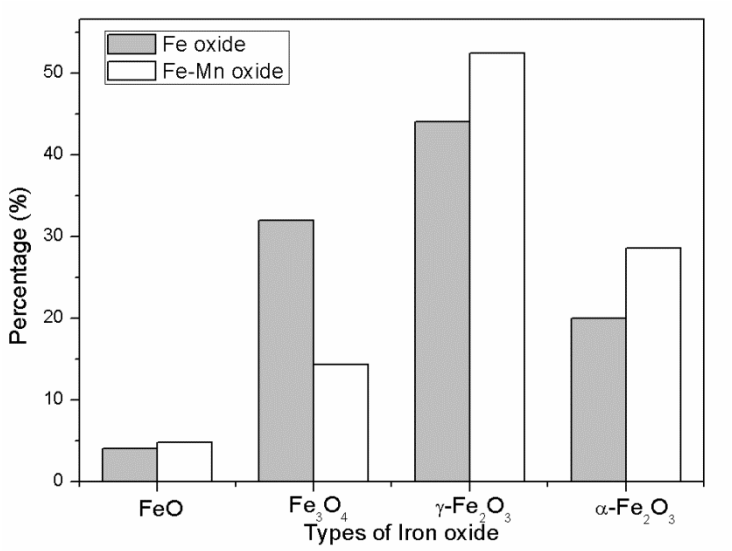

Figure 103. Percentage of total number of spectra assigned by EELS to each oxidation state, for both particle groups.

Our data confirmed the presence of Fe (II) and (III) oxides, with Fe (III) more frequently observed than Fe (II). Analysis by EELS showed that both high- and moderate-Fe groups included particles of FeO, Fe_3O_4, α-Fe_2O_3 and γ-Fe_2O_3 of which γ-Fe_2O_3 was the most numerous in both groups. FeO was much less abundant than the other forms (*Figure 103*).

Forty-six EELS spectra were collected by Dr Demie Kepaptsoglou using the SuperSTEM from two grids collected concurrently in Birmingham by the author. There were 25 spectra from Fe oxides and 21 from Fe-Mn oxides. The most frequently observed oxidation state in both composition types was γ-Fe_2O_3 which accounted for 45% of the Fe-Mn spectra and just over 50% of the Fe spectra. Fe_3O_4 accounted for a far greater proportion (> 30% compared to < 15%) of the spectra from the high-Fe group than the moderate-Fe group. α-Fe_2O_3 accounted for around 25% of each particle class – a slightly higher percentage in the moderate-Fe group and slightly lower in the high -Fe group. FeO was the least common accounting for around 5% of each particle class.

The ratio of Fe (II): Fe_{total} in our EELS data was 0.043. This is at the lower end of the ratios measured in fog and cloudwater at two sites in the Los Angeles basin by Erel et al. (1993), which varied between 0.02 and 0.55 (Erel et al., 1993). Other previous studies are also in agreement. D'Acapito et al. (2014) reported that Fe (II) was below detection limits of X-ray absorption spectroscopy (less than 5% of total Fe) in urban $PM_{2.5}$ and Fittschen et al. (2008) also found Fe (II) at similar levels across four size fractions from 15 nm to 16 µm.(d'Acapito et al., 2014; Fittschen et al., 2008).

Kukutschova et al. (2011) reported that Fe was the dominant metallic element in ultrafine brake wear particles occurring primarily as agglomerates formed from nanoparticles of 20 nm upwards. In terms of particle size and structure these features are similar to the environmental particles we describe. Nanoparticle generation was reported to be negligible when the friction interface was cold, but became highly significant at rotor temperatures above 300°C. Diffraction analysis showed the presence of Fe_3O_4 (magnetite) as well as both γ-Fe_2O_3 and α-Fe_2O_3 in these nanoparticles (Kukutschová et al., 2011).

By comparison, Liati et al. (2015) made observations of engine-derived agglomerated nanoparticles which only included Fe_3O_4, which was attributed to the short residence times of the primary particles in the high-temperature environment not allowing the slower formation of the more stable Fe_2O_3 structures (Liati et al., 2015). However, these particles also bear a morphological resemblance to the ambient particles observed in this study, opening the possibility that particles of a similar type are being sampled in the environment having undergone oxidation post-emission.

Nanoparticulate γ-Fe_2O_3 is reported to be a prominent constituent of < 500 nm diameter fly ash from coal burning (Linak et al., 2007). Reinard et al. (2007) also stated that iron is present in fly ash of all size ranges, including ultrafine ash in the form of nanoparticulate γ-Fe_2O_3. These particles are

often associated with carbonaceous soot and are assumed to have formed through the oxidation of FeS_2 during combustion (Reinard et al., 2007).

Bardelli et al. (2011) reported that the iron speciation in road dust samples collected from the Traforo del San Bernando tunnel was dominated by the Fe_3O_4 and $FeCl_3$ forms, attributed respectively to exhaust emissions and salt to prevent icing on the road. Zhang et al. (2014), analysing fine particulates in Shanghai, reported that high levels of iron oxides (principally Fe_2O_3, Fe_3O_4 and FeO(OH)) were associated with periods where emissions from iron/steel metallurgical sources were impacting on the sampling site. Using Mossbauer Spectroscopy, a study in Zakopane, Poland distinguished bulk crustal iron compounds (pyroxene, haematite and sulphides) and anthropogenically sourced ultrafines (oxides and oxyhydroxides). Urban aerosol was found to be dominated by local sources. Iron oxides and hydroxides (mostly α-Fe_2O_3 with some Fe_3O_4) were present all year round and an automotive source inferred. During winter, iron sulphides attributed to domestic coal-burning were also reported (Kopcewicz and Kopcewicz, 2001).

Oxide	**High- Fe Mean (nm)**	**High- Fe Stdev**	**N**	**Moderate- Fe mean (nm)**	**Moderate- Fe Stdev**	**N**
FeO	26.35	0.00	n=1	18.77	0.00	n=1
Fe_3O_4	26.97	20.88	n=8	20.49	1.13	n=3
γ-Fe_2O_3	32.28	22.34	n=11	22.97	7.98	n=11
α-Fe_2O_3	13.14	11.61	n=5	33.56	39.90	n=6

Table 66. Mean diameter (± s.d.) of primary spherules in iron phase particles.

	High Fe			Moderate Fe		
	Combined	BROS	NC	Combined	BROS	NC
Primary particle size (nm)	24	24.7	18.3	14.9	34.2	12.1
Cluster size (nm)	400	690	248	204	177	225
Total number 1° particles in analysed areas	225	74	151	107	25	92
Number of spectra	48	12	36	28	13	15

Table 67. Primary particle and agglomerate sizing data; combined, Birmingham (BROS) and Newcastle (NC).

As shown in *Tables 66* and *67*, there was not a clear relationship between size and oxidation state, either for the high-Fe oxide particles, or for the moderate-Fe particles which also contain Mn. Previous studies have indicated that smaller primary particles are associated with higher oxidation states, owing to the greater surface area relative to volume available to react with oxidising gases in the atmosphere (Marris et al., 2013). The small sample size, especially for FeO and Mn-alloyed Fe_3O_4, makes it difficult to draw any statistically robust conclusion from our data.

In some of the images collected at SuperSTEM it was possible to resolve the individual crystal planes within a particle (see the examples in *figures 104-106* below) and use these to make an estimation of the lattice constants, which could then be compared to literature values to determine the type of Fe oxide present.

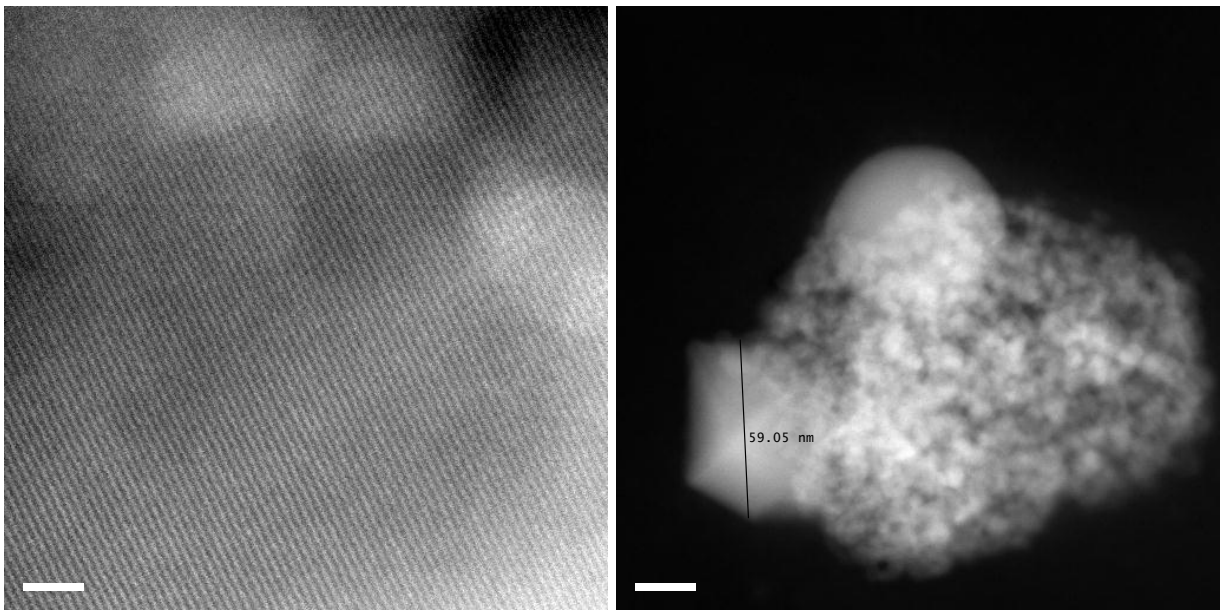

Figure 104. HAADF images from SuperSTEM showing crystal lattice in high-Fe γ-Fe_2O_3.

Lattice parameter data from Springer Materials for α-Fe_2O_3 and from Fukasawa et al. (1993) for Fe_3O_4 and γ-Fe_2O_3 was used to assign these lattice spacings to the different oxides, based simply on the nearest parameter to the mean value. Some examples were a good match for a literature value (see figure 105) but some values matched poorly, and others could not be assigned at all (*figure 106*).

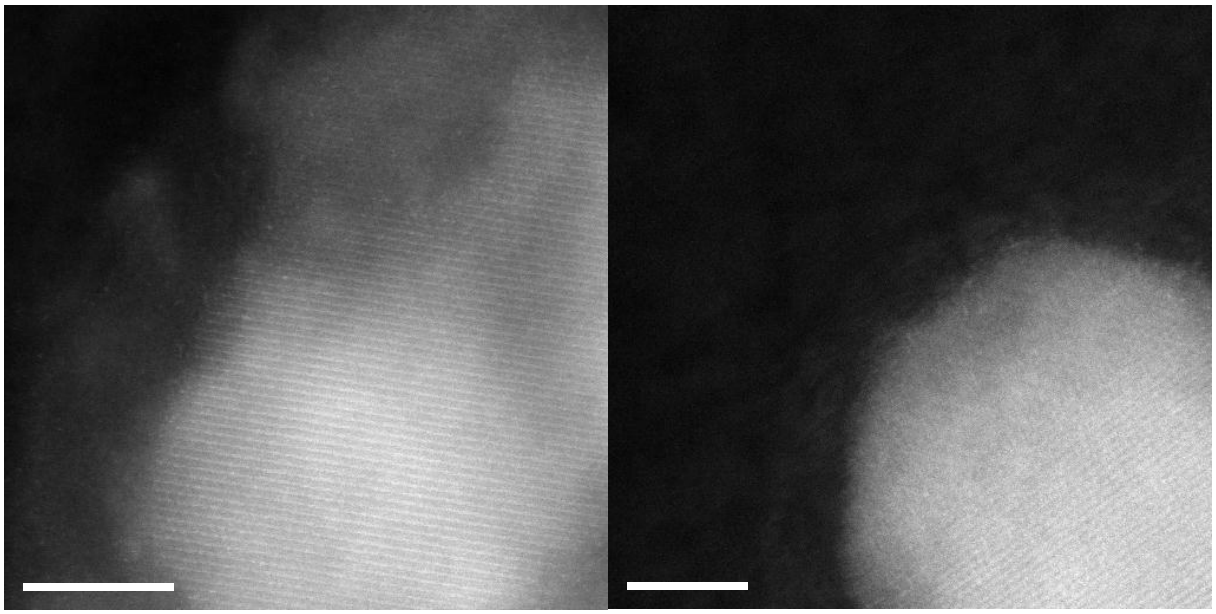

Figure 105 (l). Visible lattice, spacing 2.99 Å – corresponding to Fe1-Fe3 spacing in α-Fe_2O_3 (2.97Å).

Figure 106 (r). Visible lattice, spacing 1.38 Å – unassigned.

One potential complication arises from the changes to lattice constants depending on the replacement of iron in the lattice with minor constituents such as manganese (Fukasawa et al., 1993). Owing to the variability in composition, it was extremely difficult to predict the changes to lattice values which would apply to these particles. Furthermore there was difficulty in distinguishing the different oxides, mostly between the two forms of Fe_2O_3 but also with Fe_3O_4 to a lesser extent. Only one Fe_3O_4 particle of the moderate-Fe class was assigned from its lattice constant (see Figure 22) and the assignment from the estimated lattice constant from the image (γ-Fe_2O_3) disagreed with the EELS data (Fe_3O_4).

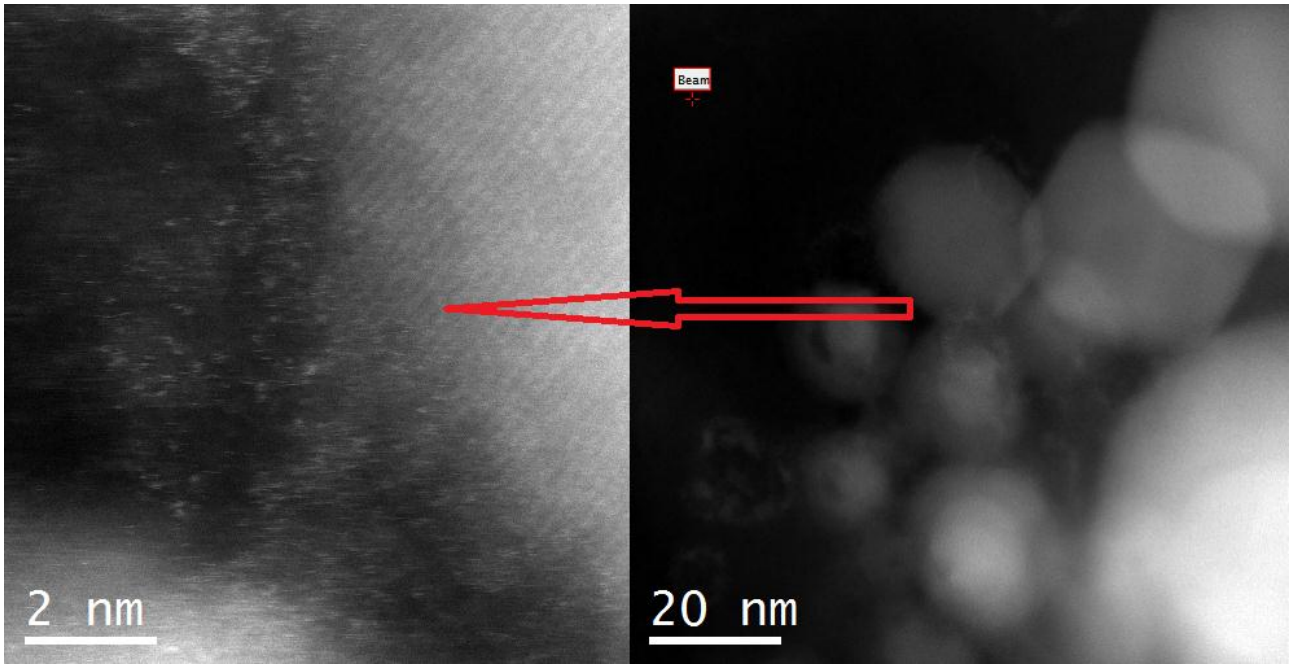

Figure 107. Fe_3O_4 Agglomerate assigned to γ-Fe_2O_3 by calculation of lattice constant.

Although an interesting experiment, the attempt to classify atmospheric iron oxide particles based on estimating the lattice spacing in the TEM images did not prove reliable, which may have resulted from the internal mixing of the particles. Spectroscopic methods such as EELS and X-ray near-edge spectroscopy (XANES) would be the best way to determine speciation in environmental samples.

7.5 Conclusions and recommendations for future work

7.5.1 Inferences about sources

Comparing the ambient particles to particles observed in previous studies, both direct from sources and in the environment, leads to an inconclusive picture concerning potential sources.

In the case of Fe, given that similar particles have been observed at two widely separated sites in which road traffic is the most important common source, it would be reasonable to assume that road traffic is the source, and the spherical/near-spherical morphology probably indicates an origin in high-temperature processes in an iron-rich environment. This seems most likely to be associated with the engine cylinder or the brakes. One factor which is likely to be important from a human health perspective is the tendency of Fe oxide nanoparticles to agglomerate in the environment forming much larger particles. This may lift the particle size from a range where lung deposition will be highly efficient to one where it is less efficient.

It is difficult to draw firm conclusions from the available Pb data. A number of sources of Pb in roadside environments are possible and the composition data we have is somewhat ambigious and cannot be easily interpreted to assign likely sources to each type. Ideally multiple samples would be collected and Pb concentration correlated with wind direction to assist in the identification of possible emission sources. Nevertheless, we have achieved an important result in identifying and describing multiple distinct types of Pb particle in the inhalable particle fraction as future studies could use the findings in conjunction with other data to assist in source assignment.

Our TEM data concerning Ce particles in the atmosphere are very sparse and although interesting on their own terms, do not offer sufficient basis for conclusions to be drawn either about sources or potential health impacts. However, a number of different types have been identified showing that Ce may be present in more than one form. Particle types identified include a small number of

particles which show Ce nanoparticles adhering to large soot agglomerates, but in one case, an example of Ce being part of a multimetallic agglomerate similar in form to the agglomerated Fe nanoparticles has been observed.

7.5.2 Priorities for further research

Further work must produce detailed physico-chemical characterisation of particles from a range of sources and compare these directly to particles in the environment with the ultimate aim of finding composition types and morphologies which can be taken as indicators of specific sources. A further step would be to investigate the chemical and physical processing these particles will undergo in the environment, as the differences between source particles and the material to which people will actually be exposed will be determined by the aging of the particles in the atmosphere.

References

Buonanno, G., Stabile, L., Avino, P., Belluso, E., 2011. Chemical, dimensional and morphological ultrafine particle characterization from a waste-to-energy plant. Waste Management 31, 2253-2262.

Cernuschi, S., Giugliano, M., Ozgen, S., Consonni, S., 2012. Number concentration and chemical composition of ultrafine and nanoparticles from WTE (waste to energy) plants. Science of the total environment 420, 319-326.

d'Acapito, F., Mazziotti Tagliani, S., Di Benedetto, F., Gianfagna, A., 2014. Local order and valence state of Fe in urban suspended particulate matter. Atmospheric Environment 99, 582-586.

Erel, Y., Pehkonen, S.O., Hoffmann, M.R., 1993. Redox chemistry of iron in fog and stratus clouds. Journal of Geophysical Research: Atmospheres 98, 18423-18434.

Fittschen, U.E.A., Meirer, F., Streli, C., Wobrauschek, P., Thiele, J., Falkenberg, G., Pepponi, G., 2008. Characterization of atmospheric aerosols using Synchroton radiation total reflection X-ray fluorescence and Fe K-edge total reflection X-ray fluorescence-X-ray absorption near-edge structure. Spectrochimica Acta Part B: Atomic Spectroscopy 63, 1489-1495.

Flament, P., Bertho, M.-L., Deboudt, K., Véron, A., Puskaric, E., 2002. European isotopic signatures for lead in atmospheric aerosols: a source apportionment based upon 206Pb/207Pb ratios. Science of The Total Environment 296, 35-57.

Fukasawa, T., Iwatsuki, M., Furukawa, M., 1993. State analysis and relationship between lattice constants and compositions including minor elements of synthetic magnetite and maghemite. Analytica Chimica Acta 281, 413-419.

Gantt, B., Hoque, S., Willis, R.D., Fahey, K.M., Delgado-Saborit, J.M., Harrison, R.M., Erdakos, G.B., Bhave, P.V., Zhang, K.M., Kovalcik, K., Pye, H.O.T., 2014. Near-Road Modeling and Measurement of Cerium-Containing Particles Generated by Nanoparticle Diesel Fuel Additive Use. Environmental Science & Technology 48, 10607-10613.

Harrison, R.M., Jones, A.M., Lawrence, R.G., 2004. Major component composition of PM10 and PM2.5 from roadside and urban background sites. Atmospheric Environment 38, 4531-4538.

Kopcewicz, B., Kopcewicz, M., 2001. Long-term measurements of iron-containing aerosols by Mössbauer spectroscopy in Poland. Atmospheric Environment 35, 3739-3747.

Kukutschová, J., Moravec, P., Tomášek, V., Matějka, V., Smolík, J., Schwarz, J., Seidlerová, J., Šafářová, K., Filip, P., 2011. On airborne nano/micro-sized wear particles released from low-metallic automotive brakes. Environmental Pollution 159, 998-1006.

Liati, A., Pandurangi, S.S., Boulouchos, K., Schreiber, D., Arroyo Rojas Dasilva, Y., 2015. Metal nanoparticles in diesel exhaust derived by in-cylinder melting of detached engine fragments. Atmospheric Environment 101, 34-40.
Linak, W.P., Yoo, J.-I., Wasson, S.J., Zhu, W., Wendt, J.O.L., Huggins, F.E., Chen, Y., Shah, N., Huffman, G.P., Gilmour, M.I., 2007. Ultrafine ash aerosols from coal combustion: Characterization and health effects. Proceedings of the Combustion Institute 31, 1929-1937.
Lough, G.C., Schauer, J.J., Park, J.-S., Shafer, M.M., DeMinter, J.T., Weinstein, J.P., 2004. Emissions of Metals Associated with Motor Vehicle Roadways. Environmental Science & Technology 39, 826-836.
Marris, H., Deboudt, K., Flament, P., Grobéty, B., Gieré, R., 2013. Fe and Mn Oxidation States by TEM-EELS in Fine-Particle Emissions from a Fe–Mn Alloy Making Plant. Environmental Science & Technology 47, 10832-10840.
Miller, A., Ahlstrand, G., Kittelson, D., Zachariah, M., 2007. The fate of metal (Fe) during diesel combustion: Morphology, chemistry, and formation pathways of nanoparticles. Combustion and Flame 149, 129-143.
Mosleh, M., Blau, P.J., Dumitrescu, D., 2004. Characteristics and morphology of wear particles from laboratory testing of disk brake materials. Wear 256, 1128-1134.
Nash, D.G., Swanson, N.B., Preston, W.T., Yelverton, T.L.B., Roberts, W.L., Wendt, J.O.L., Linak, W.P., 2012. Environmental implications of iron fuel borne catalysts and their effects on diesel particulate formation and composition. Journal of Aerosol Science.
Nico, P.S., Kumfer, B.M., Kennedy, I.M., Anastasio, C., 2009. Redox Dynamics of Mixed Metal (Mn, Cr, and Fe) Ultrafine Particles. Aerosol Science and Technology 43, 60-70.
Noble, S.R., Horstwood, M.S., Davy, P., Pashley, V., Spiro, B., Smith, S., 2008. Evolving Pb isotope signatures of London airborne particulate matter (PM 10)—constraints from on-filter and solution-mode MC-ICP-MS. Journal of Environmental Monitoring 10, 830-836.
Ntziachristos, L., Ning, Z., Geller, M.D., Sheesley, R.J., Schauer, J.J., Sioutas, C., 2007. Fine, ultrafine and nanoparticle trace element compositions near a major freeway with a high heavy-duty diesel fraction. Atmospheric Environment 41, 5684-5696.
Österle, W., Prietzel, C., Kloß, H., Dmitriev, A.I., 2010. On the role of copper in brake friction materials. Tribology International 43, 2317-2326.
Park, B., Donaldson, K., Duffin, R., Tran, L., Kelly, F., Mudway, I., Morin, J.-P., Guest, R., Jenkinson, P., Samaras, Z., Giannouli, M., Kouridis, H., Martin, P., 2008. Hazard and Risk Assessment of a Nanoparticulate Cerium Oxide-Based Diesel Fuel Additive—A Case Study. Inhalation Toxicology 20, 547-566.
Reinard, M.S., Adou, K., Martini, J.M., Johnston, M.V., 2007. Source characterization and identification by real-time single particle mass spectrometry. Atmospheric Environment 41, 9397-9409.
Saffari, A., Daher, N., Shafer, M.M., Schauer, J.J., Sioutas, C., 2013. Seasonal and spatial variation of trace elements and metals in quasi-ultrafine (PM< sub> 0.25</sub>) particles in the Los Angeles metropolitan area and characterization of their sources. Environmental Pollution 181, 14-23.
Sanderson, P., Delgado-Saborit, J.M., Harrison, R.M., 2014. A review of chemical and physical characterisation of atmospheric metallic nanoparticles. Atmospheric Environment 94, 353-365.
Thorpe, A., Harrison, R.M., 2008. Sources and properties of non-exhaust particulate matter from road traffic: A review. Science of the total environment 400, 270-282.
Tolocka, M.P., Lake, D.A., Johnston, M.V., Wexler, A.S., 2004. Number concentrations of fine and ultrafine particles containing metals. Atmospheric Environment 38, 3263-3273.
Tolocka, M.P., Lake, D.A., Johnston, M.V., Wexler, A.S., 2005. Size-resolved fine and ultrafine particle composition in Baltimore, Maryland. Journal of Geophysical Research: Atmospheres 110, D07S04.
Visser, S., Slowik, J.G., Furger, M., Zotter, P., Bukowiecki, N., Dressler, R., Flechsig, U., Appel, K., Green, D.C., Tremper, A.H., Young, D.E., Williams, P.I., Allan, J.D., Herndon, S.C., Williams, L.R., Mohr, C., Xu, L., Ng, N.L., Detournay, A., Barlow, J.F., Halios, C.H., Fleming, Z.L., Baltensperger, U., Prévôt, A.S.H., 2014. Kerb and urban increment of highly time-resolved trace elements in PM10, PM2.5 and PM1.0 winter aerosol in London during ClearfLo 2012. Atmos. Chem. Phys. Discuss. 14, 15895-15951.

CHAPTER 8: CONCLUSIONS AND SUGGESTIONS FOR FUTURE RESEARCH PRIORITES

Good progress has been made in characterising the concentrations and size distributions of several metals and ions in atmospheric particulate matter both at the bulk and single particle level in several environments, as well as in brake wear and diesel exhaust, and in investigating the relationships between different elements in these environments.

8.1 Summary of Findings

Mass-size distributions have been found to be variable at all the sites examined. In roadside environments, large coarse contributions were observed, but also submicron fine modes. A persistent feature of the data from the Birmingham Roadside site was a peak in the upper pseudo-ultrafine (100-180 nm), but this was not seen at the other sites. In the Barcelona data this specific fraction could not be separated from the rest of the ultrafine owing to the cutpoints of the instruments. It was not present at Newcastle. Background data from Birmingham showed fairly similar distributions to concurrent data from the roadside, but significant roadside increments were observed in three size ranges (100-180 nm, 320-560 nm and >1000 nm). Rural data from Harwell emphasised the importance of the coarse contribution while finer particles associated with combustion sources were far less important.

PM_{10} and $PM_{0.1}$ and/or $PM_{0.18}$ and $PM_{0.22}$ did not correlate. This is consistent with earlier studies and demonstrative of the difference in sources between large and small particles. Poor correlations were found between particulate mass data and NO_x data, but reasonably good correlations between PM_{10} calculated from nanoMOUDI data and central monitoring stations. Co-location of sampling equipment was found to be important when comparing monitoring data to impactor data; where co-location of instruments was not possible, urban background measurements were more similar at different sites than roadside measurements. MOUDI and nanoMOUDI instruments were found not to produce identical mass-size distributions in

concurrent co-located samples, indicating that there may be some differences in collection characteristics.

ICP-MS bulk concentration data for Fe and Al in the UK samples showed high variability and distributions which are not wholly consistent with previous results. V and Ni were generally found in the submicron fine mode although evidence was found for a nucleation mode of Ni, especially at roadsides. Zn was also mostly found in the submicron fine mode at the three urban sites. Concerning brake wear elements, Ba was found mostly in particles above 560 nm at all locations, while Sb distributions were incomplete, owing to low concentrations. Cu was distributed more evenly than Ba with a greater contribution from smaller particles indicative of some contribution by combustion/high temperature processes.

In Barcelona Ba, Cu, Fe and Sb were generally found to correlate well especially in coarse particles though some divergences were found in pseudo-ultrafine particles, indicating a common source in brake wear. Mg and Na were found to exhibit similar mass-size distributions indicating a common source in sea salt. V and S, commonly associated with emissions from shipping, also had similar distributions to each other. Cu:Fe percentage ratios were consistent with earlier studies and showed a change with particle size, at the roadside site. Cu/Sb ratios were approximately consistent with previous studies although Sb is present in very low levels, so relatively large variations are seen.

The soluble ion data from Birmingham was consistent with previous studies, finding that Cl^- was primarily found in the coarse mode, NO_3^- between 560-3200 nm and SO_4^{2-} mainly in the submicrometre fine mode.

By TEM, Fe was largely found in the form of complex agglomerates of primary nanoparticles. These broadly divided into high-Fe particles (Fe > 90%) and moderate-Fe particles (Fe ~ 75%) which contained Mn and Si. A number of trace constituents were found

in both classes. Factors which may impact on human health are that Fe oxide nanoparticles are highly prone to agglomeration, and that the Fe (III) state predominates, rather than the Fe (II) state. Fe (III) is less soluble and therefore less toxic in biological systems.

It was difficult to draw firm conclusions from data on Pb particles. Several different particle morphologies and compositions were observed, including irregular inclusions in non-metallic particles, and agglomerates of nanoparticles which were not associated with non-metallic particles. Cl, Sb and Zn were common constituents of Pb-bearing particles. Several sources of Pb in roadside environments are possible. The composition data is somewhat ambiguous, and cannot be easily interpreted to assign likely sources to each type although some possibilities have been discussed.

TEM data concerning Ce particles in the atmosphere were sparse and did not offer sufficient basis for conclusions to be drawn either about sources or potential health impacts. However, a number of different types were identified showing that Ce may be present in more than one form. Particle types identified include a small number of particles which showed Ce nanoparticles adhering to large soot agglomerates, but in one case, an example of Ce being part of a multi-metallic agglomerate similar in form to the agglomerated Fe nanoparticles was observed.

Evidence has been gathered (Chapter 3) to show changes in the distributions of emitted mass at varying braking forces and also differences in the distributions of elements. Al and Ni in particular were observed to behave rather differently from Fe and Cu. TEM data confirmed the dominance of abrasive-type Fe-dominated particles with angular, flake-like physical characteristics.

Future research priorities following on from this work must be to assess a greater range of pads, including semimetallic and NAO pads. Analyses of the original pad materials,

employing both ICP-MS for the bulk particulate and TEM-X-EDS for single-particle characterisation would enable comparison to the suspended wear material which would help elucidate the processes of emission and possibly explain the physic-chemical characteristics of emitted material. A wider range of braking conditions should also be tested in detail in order to develop a fuller picture of total mass distributions and elemental size distributions in brake abrasion particles. A valuable area to improve would be to employ EELS or XANES to analyse abrasion dusts for the exact chemical speciation, in particular to find out whether the Fe is present as Fe (II) or Fe (III) and determine whether the speciation of important elements is dependent on particle size and/or application pressure.

The data presented in Chapter 4 confirmed the presence of a number of metals and other inorganic components in exhaust from a EURO-5 compliant diesel engine, among which P, S, Si and Cl were common. Fe and Cr were frequently found together, so the correlation between them may be an useful indicator of engine-derived particles in roadside environments particularly when associated with Ni, as long other sources of Fe-Cr particles such as steelworking can be discounted. Other important findings are that engines making significant use of Al alloys in construction will contribute wear particles formed primarily of that material, thus providing another source of environmental Al. It was found that – under the tested conditions – Al was mostly found in fine particles rather than ultrafine. Furthermore, submicron particles included Cu. Results obtained in Barcelona and presented in Chapter 6 showed that this could be important in the environment; there were some anomalous results in Cu in $PM_{0.22}$ which did not correlate with Ba, the other favoured tracer of brake emissions. Further similar investigations covering a wider range of engine models and engine load cycles would be required to provide more comprehensive data.

8.2 Recommendations for Future Research

Future work regarding bulk particulate mass data probably needs to emphasise the simultaneous collection of multiple data types. Comparison of concurrent roadside and background data has been valuable, but the addition of particle number data and measurements of gaseous pollutants simultaneously could help to develop understanding of the relationships between different pollutants and between mass, number and volume data.

Useful mass concentration data for metals in a number of environments are now available in the literature, but a useful direction of future research on bulk concentrations would be to explore the correlations and ratios of different elements in atmospheric particulate matter, in different environments and size ranges, to explore whether these may be indicative of sources. Such a proposition may be tested by comparison of ambient data to data obtained from known sources such as brakes, tyres and engines under controlled conditions.

Further work on single-particle characterisation must aim to produce detailed physico-chemical characterisation of particles from a range of sources and compare these directly to particles in the environment with the ultimate aim of finding composition types and morphologies which can be taken as indicators of specific sources. A further step would be to investigate the chemical and physical processing these particles will undergo in the environment, as the differences between source particles and the material to which people will actually be exposed will be determined by the aging of the particles in the atmosphere. Another highly important direction of future research would be directed at assessing the biological impacts of exposure to particles produced by diesel and gasoline engines, tyre wear and brake wear with simultaneous collection of particles for chemical analysis to help determine which physical and chemical parameters are most influential in interactions with biological systems.

APPENDIX A: TABULATED TOTAL MASS CONCENTRATION DATA FROM NANOMOUDI AND MOUDI FILTERS COLLECTED AT AMBIENT MEASUREMENT SITES AND SUPPORTING AURN DATA

a. Bristol Road, Birmingham

Lower Cut/nm	BR-7-06-11	BR-10-06-11	BR-14-06-11	BR-20-06-11	BR-23-06-11	BR-27-06-11	Mean	SD
10000	8.342	3.209	4.818	2.302	2.075	1.012	3.626	2.639
5600	5.821	2.977	0.532	2.366	2.246	1.089	2.505	1.855
3200	4.330	2.651	0.995	2.761	1.702	1.535	2.329	1.191
1800	3.541	-16.791	0.866	2.512	2.032	1.359	2.062	1.039
1000	2.221	2.160	1.020	13.597	13.070	2.889	5.826	5.849
560	3.447	2.169	2.032	1.560	2.761	1.003	2.162	0.864
320	7.305	4.540	1.895	6.370	3.729	1.363	4.200	2.368
180	3.789	2.289	1.402	1.620	2.178	0.917	2.033	0.998
100	9.088	4.707	-1.205	1.972	1.715	1.020	3.700	3.322
56	2.263	1.363	5.916	1.029	1.207	0.540	2.053	1.975
32	1.843	0.724	1.955	1.222	1.035	0.532	1.218	0.580
18	3.292	2.375	3.927	0.909	1.106	1.800	2.235	1.202
10	1.689	2.443	2.821	1.059	1.509	0.557	1.680	0.844
1	-0.231	-0.094	-1.029	0.322	-1.196	-0.652	-0.480	0.582

Table 1. Mass concentrations at BROS, June 2011, in µgm^{-3}.

Lower Cut	BR-8-7-11	BR-13-7-11	BR-16-7-11	BR-19-7-11	BR-22-7-11	Mean	SD
1000	9.892	8.899	4.722	6.001	4.771	6.857	2.146
560	1.384	1.818	1.740	2.825	2.450	2.043	0.520
320	4.753	2.521	5.890	3.326	3.466	3.991	1.189
180	1.336	1.260	2.118	1.385	1.357	1.491	0.316
100	0.890	0.832	6.524	1.072	1.646	2.193	2.185
56	0.561	0.412	0.626	1.192	1.061	0.770	0.302
32	1.168	0.403	0.506	0.720	0.855	0.730	0.270
18	0.545	0.463	0.600	0.454	0.637	0.540	0.072
10	0.571	0.309	1.843	2.143	0.759	1.125	0.729
1	0.028	-0.606	0.223	0.163	-0.309	-0.100	0.313

Table 2. Mass concentrations at BROS, July 2011, in µgm^{-3}.

Lower Cut/nm	06/09/ 2011	14/09/ 2011	21/09/ 2011	28/09/ 2011	05/10/ 2011	12/10/ 2011	19/10/ 2011	26/10/ 2011	02/11/ 2011	09/11/ 2011	Mean	SD
1000	3.03	4.81	8.61	6.73	8.61	0.96	5.61	5.39	11.89	14.37	7.00	4.01
560	0.97	1.16	1.76	5.24	1.76	2.37	3.18	1.72	3.05	3.66	2.49	1.31
320	11.27	1.44	1.76	4.62	1.76	2.00	1.93	1.88	3.24	2.38	3.23	2.98
180	0.96	1.65	1.23	2.23	1.22	2.70	0.96	1.22	1.73	1.66	1.56	0.56
100	0.94	1.43	0.86	2.69	0.86	0.93	0.83	4.12	2.20	7.29	2.21	2.08
56	0.35	0.73	0.52	1.06	0.52	0.63	0.45	0.62	0.84	0.78	0.65	0.21
32	0.23	0.28	0.28	0.41	0.28	0.55	0.30	0.53	0.87	0.58	0.43	0.20
18	0.18	0.32	0.23	0.37	0.23	0.28	0.40	0.25	0.43	0.31	0.30	0.08
10	0.37	0.31	0.41	2.21	0.41	0.67	0.22	0.21	0.33	0.81	0.59	0.60
1	-0.64	-0.22	-0.31	-4.08	-0.31	0.40	0.27	-0.32	0.25	-0.03	0.31	1.30

Table 3. Mass concentrations at BROS, Autumn 2011, in µgm^{-3}.

LC/nm	21-Mar	04-Apr	11-Apr	18-Apr	25-Apr	Mean	SD	RSD
10000	8.576	3.142	1.446	1.064	5.255	3.897	3.096	79.454
5600	4.935	3.813	1.576	3.562	5.635	3.904	1.550	39.689
3200	3.858	3.56	2.91	2.417	6.382	3.825	1.535	40.136
1800	2.406	2.334	2.973	1.681	1.706	2.220	0.541	24.355
1000	2.092	2.238	2.615	1.436	2.210	2.118	0.429	20.246
560	3.232	7.465	1.538	0.948	1.130	2.863	2.727	95.254
320	5.376	3.536	1.314	1.849	3.745	3.164	1.622	51.257
180	2.18	1.624	1.077	0.796	1.372	1.410	0.531	37.668
100	3.522	2.203	1.703	1.929	2.822	2.436	0.738	30.287
56	0.725	0.752	0.617	0.345	0.479	0.584	0.171	29.348
32	0.185	0.459	0.339	0.019	-0.058	0.251	0.215	85.927
18	0.122	0.347	0.361	-0.028	-0.055	0.277	0.199	71.795
10	-0.128	0.328	0.38	-0.041	0.022	0.243	0.228	93.620
1	-0.058	1.006	0.433	1.414	-0.041	0.951	0.649	68.290
PM_{10}	28.633	29.665	17.838	16.396	25.503	23.607	6.141	26.012
$PM_{0.1}$	1.032	2.893	2.13	1.778	0.501	1.667	0.934	56.061

Table 4. BROS Spring 2013 nanoMOUDI mass concentrations in µgm^{-3}.

LC/nm	21-Mar	04-Apr	11-Apr	18-Apr	Mean	SD	RSD
18000	1.92	2.01	2.56	1.04	1.88	0.63	33.48
10000	1.28	1.04	18.41	1.92	1.41	0.45	32.13
5600	1.60	1.98	1.10	1.59	1.56	0.36	22.95
3200	2.23	5.21	3.93	1.73	3.27	1.60	48.74
1800	1.68	1.03	4.11	1.58	2.10	1.37	65.17
1000	1.45	8.43	3.43	1.27	3.65	3.34	91.51
560	1.52	5.78	1.11	0.84	2.31	2.32	100.43
320	3.90	3.61	1.64	1.81	2.74	1.18	43.07
180	2.05	2.03	1.33	1.45	1.71	0.38	21.97
100	2.68	0.89	0.02	0.25	0.96	1.21	125.59
56	2.11	2.19	1.64	1.57	1.88	0.32	16.82
1	1.02	2.82	2.82	1.34	2.00	0.96	47.97
PM_{10}	20.23	33.96	21.13	13.42	22.19	8.57	38.64
$PM_{0.1}$	5.80	5.90	4.48	3.16	4.83	1.29	26.78

Table 5. Tabulated MOUDI mass concentration data, in μgm^{-3}.

b. Elms Road, Birmingham

Lower Cut	06/09/ 2011	14/09/ 2011	21/09/ 2011	28/09/ 2011	05/10/ 2011	12/10/ 2011	19/10/ 2011	26/10/ 2011	02/11/ 2011	09/11/ 2011	Mean	SD
1000	4.70	2.97	3.67	2.98	3.67	2.86	2.98	2.59	6.23	8.18	4.08	1.81
560	1.08	0.87	1.02	5.26	1.02	1.62	1.64	1.42	4.48	3.95	2.24	1.66
320	0.94	1.18	1.93	3.08	1.93	1.18	1.90	1.37	3.67	2.21	1.94	0.87
180	0.69	0.90	0.58	1.35	0.68	0.49	0.65	1.03	5.25	1.04	1.27	1.42
100	0.67	0.72	0.54	0.60	0.54	7.76	0.50	0.61	0.81	1.23	1.40	2.25
56	0.87	0.39	0.28	0.36	0.28	0.22	0.34	0.29	0.40	1.05	0.45	0.28
32	0.47	0.35	0.27	0.43	0.28	0.30	0.41	0.27	0.52	0.28	0.36	0.09
18	0.54	0.89	0.25	0.34	0.25	0.31	0.27	0.27	0.21	0.83	0.42	0.25
10	0.45	0.40	0.29	0.36	0.29	0.25	0.22	0.33	0.20	0.43	0.32	0.09
1	-0.51	0.19	0.23	-0.98	0.23	0.31	0.28	-0.42	-0.16	-0.30	0.25	0.44

Table 6. Mass concentrations at EROS, Autumn 2011, in μgm^{-3}.

c. Harwell

Stage	Lower cut/nm	07-Dec	20-Dec	Mean	Std Dev
S5	1000	3.572	6.120	4.846	1.801
S6	560	0.313	0.382	0.348	0.049
S7	320	0.411	0.664	0.537	0.179
S8	180	0.399	0.486	0.442	0.062
S9	100	0.759	0.364	0.562	0.279
S10	56	0.220	0.265	0.242	0.032
S11	32	0.171	0.273	0.222	0.072
S12	18	0.460	0.184	0.322	0.196
S13	10	0.157	0.254	0.205	0.069
S14	1	0.079	0.052	0.065	0.019
PM_{10}		6.540	9.043	7.791	1.770
$PM_{0.1}$		1.086	1.027	1.056	0.042
AURN PM_{10}		8.506	9.670	9.088	0.823

Table 7. Mass concentrations in Harwell filter samples, μgm^{-3}

d. Newcastle

Lower Cut	12-Jan	19-Jan	26-Jan	02-Feb	09-Feb	16-Feb	23-Feb	01-Mar	08-Mar	29-Mar	05-Apr	12-Apr	19-Apr	02-May	10-May	17-May	31-May	07-Jun	13-Jun	Ar Mean	Stdev
1000	6.81	4.62	5.37	5.54	7.93	2.63	1.87	3.80	7.24	3.53	1.87	2.22	2.16	3.30	3.69	5.04	3.91	3.82	1.49	4.05	1.89
560	1.41	0.58	1.19	1.22	0.90	0.42	0.80	1.09	1.03	1.13	0.44	0.18	0.37	0.45	0.60	0.91	0.58	0.55	0.75	0.77	0.34
320	3.19	1.09	3.17	3.09	1.42	0.74	1.51	2.79	1.27	1.17	1.03	0.12	1.25	1.73	0.73	1.21	0.96	0.72	1.01	1.48	0.91
180	3.91	0.92	1.36	1.26	1.85	0.89	0.80	2.01	0.81	1.73	0.83	0.65	0.68	0.91	0.65	0.96	0.70	0.70	0.73	1.18	0.78
100	2.56	0.82	0.93	1.29	0.84	0.52	0.66	0.78	0.62	0.96	0.60	0.18	0.56	0.56	0.48	1.13	1.47	0.44	0.64	0.84	0.52
56	0.87	0.98	0.52	0.33	0.45	0.39	0.55	0.31	0.19	0.33	0.32	0.24	0.90	0.30	0.26	0.39	0.57	0.35	0.39	0.45	0.23
32	0.57	0.36	0.36	0.82	0.34	0.40	0.67	0.31	0.19	0.25	0.19	0.18	0.26	0.37	0.34	0.32	0.39	0.70	0.45	0.39	0.18
18	0.20	0.43	0.51	0.45	0.18	0.26	0.23	0.90	0.15	0.42	0.20	0.38	0.21	0.12	0.34	0.36	0.31	0.36	1.07	0.37	0.24
10	0.22	0.27	0.18	1.22	0.11	0.28	0.36	0.50	0.72	0.37	0.22	0.17	0.17	0.29	0.56	0.34	0.57	0.50	1.18	0.43	0.31
1	0.18	0.23	0.76	0.18	0.24	0.65	0.18	0.14	0.07	0.38	0.14	0.14	0.29	0.15	0.07	0.28	0.23	0.43	0.59	0.28	0.20

Table 8. NanoMOUDI mass concentration data, Newcastle µgm^{-3}.

Lower Cut	16-Feb	01-Mar	15-Mar	22-Mar	12-Apr	10-May	23-May	31-May	07-Jun	13-Jun	21-Jun	28-Jun	05-Jul	12-Jul	Mean	Stdev
18000	0.807	0.755	0.960	1.059	1.516	1.741	0.562	1.609	1.060	0.208	0.653	0.556	0.758	0.541	0.869	0.910
10000	0.299	0.227	0.312	0.265	0.747	0.328	0.156	0.732	0.635	3.336	0.249	0.186	0.241	0.088	0.293	0.540
5600	1.083	0.625	0.785	0.772	1.581	1.190	0.692	1.494	0.725	2.197	0.469	0.457	0.709	0.372	0.709	0.924
3200	1.941	1.196	2.159	1.976	3.255	2.964	2.283	3.507	1.619	1.651	1.505	1.305	2.042	1.194	2.284	2.059
1800	1.414	1.023	1.457	1.368	1.908	2.055	1.747	2.345	1.012	1.042	1.182	1.096	1.531	0.943	0.894	1.401
1000	0.965	0.872	1.931	1.189	5.433	1.168	0.984	2.358	0.753	0.654	0.847	2.427	1.734	1.276	0.647	1.549
560	0.490	0.746	1.407	0.947	3.976	0.663	0.428	2.338	0.755	1.541	1.023	1.030	0.966	0.195	0.485	1.133
320	1.577	1.605	2.262	2.112	4.412	1.504	0.790	4.122	1.592	0.156	1.334	1.243	1.221	1.639	0.876	1.763
180	0.216	0.281	0.321	0.204	0.317	0.128	0.151	0.719	0.139	-0.002	1.054	0.164	0.206	0.229	0.168	0.286
1	0.712	0.841	0.637	0.957	0.432	0.387	1.094	0.510	1.323	0.499	0.473	n/a	n/a	0.414	0.714	0.690

Table 9. MOUDI mass concentration data, Newcastle µgm^{-3}.

e. Barcelona

i. Roadside site

Lower cut/ nm	09/05/ 2013	13/05/ 2013	16/05/ 2013	21/05/ 2013	27/05/ 2013	03/06/ 2013	Mean	Stdev
18000	1.662	4.555	1.815	1.724	1.678	1.576	2.169	1.172
10000	0.962	0.672	0.605	1.307	0.881	0.945	0.895	0.249
5600	1.427	1.371	0.879	1.254	1.408	1.051	1.232	0.222
3200	7.344	2.475	1.641	2.009	1.869	2.019	2.893	2.198
1800	6.309	1.888	1.293	1.685	1.611	1.421	2.368	1.942
1000	1.414	1.495	0.852	0.964	1.005	1.059	1.131	0.260
560	0.562	1.326	0.445	0.775	0.496	0.906	0.752	0.332
320	2.084	2.602	1.488	1.646	1.729	2.790	2.056	0.536
180	1.756	1.906	1.155	1.241	1.299	1.950	1.551	0.359
56	2.136	2.513	1.805	1.996	2.016	2.721	2.198	0.348
1	0.811	1.190	0.917	1.211	1.541	1.400	1.178	0.278
PM_{10}	23.843	16.765	10.474	12.780	12.974	15.317	15.359	6.473
$PM_{0.18}$	2.946	3.703	2.722	3.207	3.557	4.120	3.376	0.625

Table 10. Total PM mass concentrations at the roadside site, in μgm^{-3}.

Lower Cut/ nm	09/05/ 2013	13/05/ 2013	16/05/ 2013	21/05/ 2013	27/05/ 2013	05/06/ 2013	11/06/ 2013	Mean	Stdev
21500	2.514	1.037	0.855	0.277	1.999	1.743	1.334	1.394	0.754
12000	1.033	0.659	0.395	0.271	1.361	0.745	0.517	0.712	0.379
6700	1.718	0.833	0.724	0.612	1.625	1.318	0.932	1.109	0.444
3800	4.375	2.035	1.440	0.599	2.718	2.906	1.845	2.274	1.208
2200	3.107	1.778	1.470	1.226	1.984	2.018	1.414	1.857	0.626
1200	0.588	4.215	1.039	0.681	1.125	1.547	0.963	1.451	1.258
670	2.493	4.277	1.983	0.733	1.779	4.792	4.544	2.943	1.588
380	0.610	0.248	0.120	0.559	0.359	0.301	3.390	0.798	1.155
220	1.981	2.939	0.571	0.878	0.419	0.639	1.989	1.345	0.961
1	3.119	2.969	4.336	3.439	2.588	3.003	2.415	3.124	0.632
PM_{12}	17.991	19.296	11.682	8.727	12.597	16.524	17.492	14.901	7.873
$PM_{0.22}$	3.119	2.969	4.336	3.439	2.588	3.003	2.415	3.124	0.632

Table 11. Mass concentrations at background site, total PM, in μgm^{-3}.

f. Supporting AURN Data

i. Birmingham Tyburn Roadside

PM_{10} NO_x and temperature data from the Birmingham Tyburn Roadside AURN station was used to compare with nanoMOUDI and MOUDI data from BROS.

Tyburn Rd	BR-7-6-11	BR-10-6-11	BR-14-6-11	BR-20-6-11	BR-23-6-11	BR-27-6-11	Mean	SD	%SD
PM_{10}	20	16	17	DATA UNAVAILABLE			18	2	11
NO_x	70	78	78	68	69	106	78	14	18
T / ˚C	11	12	14	15	16	15	14	2	13

Table 12. June 2011 AURN data, Tyburn Rd, Birmingham. PM_{10} and NO_x in μgm^{-3}

Tyburn Rd	BR-27-6-11	BR-8-7-11	BR-13-7-11	BR-16-7-11	BR-19-7-11	BR-22-7-11	Mean	SD	%SD
PM_{10}	DATA UNAVAILABLE					14	14	n/a	n/a
NO_x	106	69	108	42	132	87	91	32	35
T / ˚C	15	15	14	15	14	13	14	1	5

Table 13. July 2011 AURN data, Tyburn Rd, Birmingham. PM_{10} and NO_x in μgm^{-3}

Tyburn Rd	06/09/2011	14/09/2011	21/09/2011	28/09/2011	05/10/2011	12/10/2011	19/10/2011	26/10/2011	02/11/2011	09/11/2011	Mean	SD	%SD
PM_{10}	15	17	19	34	13	21	19	23	43	38	24	10	43
NO_x	46	102	85	133	53	114	102	176	126	119	106	38	36
T / ˚C	15	13	13	15	14	11	10	11	10	9	12	2	19

Table 14. Autumn 2011 AURN data, Tyburn Rd, Birmingham. PM_{10} and NO_x in μgm^{-3}

Tyburn Rd	21/03/2013	04/04/2013	11/04/2013	18/04/2013	25/04/2013	Mean	SD	%SD
PM_{10}	28	36	24	24	17	26	7	26
NO_x	68	112	85	84	104	91	17	19
T / ˚C	1	4	10	9	7	6	4	61

Table 15. Spring 2013 AURN data, Tyburn Rd, Birmingham. PM_{10} and NO_x in μgm^{-3}

ii. Birmingham Tyburn

PM_{10} NO_x and temperature data from the Birmingham Tyburn AURN station was used to compare with nanoMOUDI and MOUDI data from EROS.

Tyburn	06/09/ 2011	14/09/ 2011	21/09/ 2011	28/09/ 2011	05/10/ 2011	12/10/ 2011	19/10/ 2011	26/10/ 2011	02/11/ 2011	09/11/ 2011	Mean	SD	%SD
PM_{10}	15	15	20	32	14	22	18	19	37	30	22	8	36
NO_x	25	49	49	77	25	63	43	102	57	58	55	23	42
T / ˚C	15	13	13	15	14	11	10	11	10	9	12	2	19

Table 16. Autumn 2011 AURN data, Tyburn, Birmingham. PM_{10} and NO_x in μgm^{-3}

iii. Harwell

PM_{10} NO_x and temperature from the Harwell AURN station for the period of the nanoMOUDI sampling, December 2011.

Harwell	07-Dec	21-Dec	Mean	SD	%SD
PM_{10}	9	10	9	1	115
NO_x	5	3	4	1	64
T / ˚C	5	8	7	2	168

Table 17. December 2012 AURN data, Harwell. PM_{10} and NO_x in μgm^{-3}

iv. Newcastle Centre

PM_{10} NO_x and temperature data from the Birmingham Tyburn AURN station was used to compare with nanoMOUDI and MOUDI data from Newcastle.

NC	**12/01/ 2012**	**19/01/ 2012**	**26/01/ 2012**	**02/02/ 2012**	**09/02/ 2012**	**16/02/ 2012**	**23/02/ 2012**	**01/03/ 2012**	**08/03/ 2012**	**29/03/ 2012**	**05/04/ 2012**	**12/04/ 2012**	**19/04/ 2012**	
PM_{10}	31	13	23	23	27	11	15	23	20	20	10	17	16	
NO_x	129	50	81	77	55	31	35	55	32	35	37	39	41	
T / ˚C	2	6	3	0	4	7	9	6	8	7	8	6	7	
	02/05/ 2012	**10/05/ 2012**	**17/05/ 2012**	**31/05/ 2012**	**07/06/ 2012**	**13/06/ 2012**	**21/06/ 2012**	**28/06/ 2012**	**05/07/ 2012**	**12/07/ 2012**	**19/07/ 2012**	**Mean**	**SD**	**%SD**
PM_{10}	14	13	22	11	12	10	12	13	12	8	8	16	6	39
NO_x	36	32	40	34	35	35	39	45	40	41	38	46	22	47
T / ˚C	7	8	9	11	11	13	14	16	14	14	16	9	4	51

Table 18. Autumn 2011 AURN data, Tyburn, Birmingham. PM_{10} and NO_x in μgm^{-3}

APPENDIX B: TABULATED ICP-MS METAL CONCENTRATION DATA AND SOLUBLE ION CONCENTRATION DATA

Presented in the following section are the ICP-MS and anion chromatography results for mass concentrations of metal and soluble ions in the UK sites, from acid digests of nanoMOUDI filter samples. These have been converted from solution concentrations into airborne concentrations.

Eight sets of samples are shown for Bristol Road, Birmingham. Five sets are available for Elms Road, Birmingham. Two sets were collected at Harwell and both were extracted for ICP-MS analysis. Seven sets of samples are available for the Newcastle site.

Mass concentration data for five sets of soluble ion samples collected in Birmingham are presented.

Elemental data for those elements discussed in the analysis of the Barcelona data are included. This only represents those elements discussed in Chapter 6, although more elements than this were collected.

1. **Bristol Road Samples**
    a. **Al**

Low Cutpoint / nm	BR-26-7-11	BR-6-9-11	BR-28-9-11	BR-5-10-11	BR-12-10-11	BR-19-10-11	BR-2-11-11	BR-9-11-11	Mean	Std Dev	%Std Dev	Median
1000	5.07	1.07	20.38	22.98	11.29	15.44	19.46	2.14	12.23	8.64	70.68	13.37
560	3.15	1.24	1.69	3.87	2.67	6.29	3.41	3.76	3.26	1.55	47.42	3.28
320	1.11	0.47	2.92	2.65	3.44	3.12	2.91	3.42	2.51	1.11	44.10	2.92
180	0.95	0.65	3.04	4.47	8.35	1.85	2.64	3.34	3.16	2.44	77.32	2.84
100	0.93	2.59	2.81	1.32	3.25	7.47	3.36	3.67	3.18	1.99	62.61	3.03
56	1.21	0.84	3.25	2.42	5.33	5.82	3.25	3.91	3.25	1.77	54.53	3.25
32	0.87	0.00	2.05	0.85	0.73	11.11	2.99	5.31	2.99	3.69	123.50	1.46
18	23.22	0.76	2.13	1.76	5.36	2.85	2.57	2.46	5.14	7.42	144.48	2.52
10	2.20	7.05	2.42	5.21	2.26	2.19	2.62	3.18	3.39	1.79	52.76	2.52
1	5.85	5.39	31.84	42.84	47.70	103.80	28.58	84.50	43.81	34.98	79.83	37.34
PM_{10} (ng/m^3)	21.35	20.07	72.53	88.36	90.40	159.94	71.79	31.19	69.45	46.62	67.13	72.16
$PM_{0.1}$ (ng/m^3)	10.12	14.05	41.70	53.07	61.39	125.77	40.01	14.85	45.12	37.75	83.67	40.85

Table 1. BROS Al mass concentration data, ngm^{-3}.

b. Ba

Low Cutpoint / nm	BR-26-7-11	BR-6-9-11	BR-28-9-11	BR-5-10-11	BR-12-10-11	BR-19-10-11	BR-2-11-11	BR-9-11-11	Mean	Std Dev	%Std Dev	Median
1000	0.34	0.05	7.22	2.24	6.12	4.50	13.55	<0.011	4.86	4.71	96.98	4.50
560	0.52	0.08	0.57	0.23	0.86	1.26	0.10	0.41	0.50	0.40	80.08	0.47
320	0.07	0.01	0.46	0.16	0.56	0.25	0.16	0.05	0.22	0.20	91.75	0.16
180	0.03	<0.011	0.41	0.06	0.06	0.04	0.02	0.01	0.09	0.14	159.67	0.04
100	0.01	0.09	0.13	<0.022	< 0.022	<0.022	0.05	<0.011	0.07	0.05	75.07	0.07
56	0.01	0.02	<0.022	<0.022	< 0.022	<0.022	0.04	<0.011	0.02	0.01	66.92	0.02
32	<0.01	0.00	0.06	<0.022	< 0.022	0.03	<0.022	0.02	0.03	0.03	95.76	0.02
18	0.02	<0.011	0.03	<0.022	< 0.022	<0.022	<0.022	<0.011	0.02	0.01	23.30	0.02
10	0.06	0.02	<0.022	0.03	< 0.022	0.06	0.12	<0.011	0.06	0.04	65.57	0.06
1	0.05	<0.011	0.09	0.09	< 0.022	0.03	0.03	<0.011	0.06	0.03	51.22	0.05
PM_{10} (ng/m^3)	1.11	0.27	8.97	2.80	7.60	6.16	14.06	0.49	5.18	4.90	94.60	4.48
$PM_{0.1}$ (ng/m^3)	0.15	0.04	0.19	0.11	0.00	0.11	0.19	0.02	0.10	0.07	72.71	0.11

Table 2. Ba mass concentration data, BROS (ngm^{-3}).

c. Ce

Low Cutpoint / nm	BR-26-7-11	BR-6-9-11	BR-28-9-11	BR-5-10-11	BR-12-10-11	BR-19-10-11	BR-2-11-11	BR-9-11-11	Mean	Std Dev	%Std Dev	Median
1000	0.10	<0.011	<0.022	0.05	0.04	0.04	0.04	<0.011	0.05	0.03	49.36	0.04
560	0.14	<0.011	<0.022	<0.022	< 0.022	0.02	<0.022	<0.011	0.08	0.08	102.49	0.08
320	0.13	<0.011	<0.022	<0.022	< 0.022	<0.022	<0.022	<0.011	0.13	n/a	n/a	0.13
180	0.12	<0.011	<0.022	<0.022	< 0.022	<0.022	<0.022	<0.011	0.12	n/a	n/a	0.12
100	0.12	<0.011	<0.022	<0.022	< 0.022	<0.022	<0.022	<0.011	0.12	n/a	n/a	0.12
56	0.11	<0.011	<0.022	<0.022	< 0.022	<0.022	<0.022	<0.011	0.11	n/a	n/a	0.11
32	0.12	0.00	<0.022	<0.022	< 0.022	<0.022	<0.022	<0.011	0.06	0.08	141.42	0.06
18	0.12	<0.011	<0.022	<0.022	< 0.022	<0.022	<0.022	<0.011	0.12	n/a	n/a	0.12
10	0.13	<0.011	<0.022	<0.022	< 0.022	<0.022	<0.022	<0.011	0.13	n/a	n/a	0.13
1	0.16	<0.011	0.07	<0.022	< 0.022	<0.022	<0.022	<0.011	0.11	0.06	57.34	0.11
PM_{10} (ng/m^3)	1.23	0.00	0.07	0.05	0.04	0.06	0.04	0.00	0.19	0.42	227.57	0.04
$PM_{0.1}$ (ng/m^3)	0.62	0.00	0.07	0.00	0.00	0.00	0.00	0.00	0.09	0.22	253.43	0.00

Table 3. Ce mass concentration data, BROS, (ngm^{-3}).

d. Cu

Low Cutpoint / nm	BR-26-7-11	BR-6-9-11	BR-28-9-11	BR-5-10-11	BR-12-10-11	BR-19-10-11	BR-2-11-11	BR-9-11-11	Mean	Std Dev	%Std Dev	Median
1000	0.81	0.13	14.97	3.03	9.18	9.42	13.73	0.04	6.41	6.17	96.21	6.10
560	1.06	0.40	2.10	0.48	1.81	2.98	0.12	0.58	1.19	1.00	84.27	0.82
320	0.17	0.03	1.01	0.32	1.23	0.61	0.27	0.13	0.47	0.44	93.10	0.30
180	1.11	0.04	0.82	0.12	0.50	0.07	<0.044	0.09	0.39	0.43	108.73	0.12
100	0.16	0.91	0.24	<0.022	0.13	0.04	0.06	0.10	0.23	0.30	129.53	0.13
56	0.10	0.03	0.18	<0.022	0.20	0.06	0.10	0.03	0.10	0.07	70.16	0.10
32	0.00	0.00	0.22	<0.022	0.06	<0.022	0.18	0.09	0.09	0.09	99.17	0.08
18	0.89	0.14	0.15	<0.022	0.25	0.04	0.05	0.00	0.22	0.31	141.12	0.14
10	0.11	0.02	0.16	0.04	0.26	0.17	<0.044	0.02	0.11	0.09	79.72	0.11
1	0.05	0.25	0.45	0.19	0.42	0.41	0.35	0.17	0.28	0.14	50.32	0.35
PM_{10} (ng/m^3)	4.44	1.96	20.31	4.19	14.03	13.79	14.86	1.26	9.35	7.20	76.97	9.12
$PM_{0.1}$ (ng/m^3)	1.14	0.44	1.17	0.23	1.19	0.68	0.68	0.32	0.73	0.39	53.70	0.68

Table 4. Cu mass concentration data, BROS, (ngm^{-3}).

e. Fe

Low Cutpoint / nm	BR-26-7-11	BR-6-9-11	BR-28-9-11	BR-5-10-11	BR-12-10-11	BR-19-10-11	BR-2-11-11	BR-9-11-11	Mean	Std Dev	%Std Dev	Median
1000	17.79	13.91	270.44	209.53	250.89	194.49	153.82	1.08	138.99	111.76	80.41	174.16
560	25.56	24.62	28.62	241.78	67.67	92.98	1.84	9.89	61.62	78.82	127.91	27.09
320	3.81	9.29	241.11	309.78	58.09	20.18	1.56	1.50	80.66	123.02	152.50	14.73
180	0.78	14.93	133.22	53.78	231.33	9.47	0.83	0.49	55.60	84.29	151.59	12.20
100	0.77	28.92	54.09	13.22	127.13	9.10	0.70	0.50	29.31	43.61	148.82	11.16
56	1.06	8.91	65.93	44.91	676.89	37.93	0.80	0.34	104.60	232.54	222.32	23.42
32	0.25	0.00	91.18	33.82	24.82	19.25	0.70	2.25	21.53	31.03	144.09	10.75
18	0.76	7.61	37.53	111.00	38.64	108.91	0.60	0.40	38.18	47.03	123.16	22.57
10	0.82	6.20	18.13	72.89	354.89	61.62	0.78	0.87	64.53	120.78	187.18	12.17
1	1.86	13.92	53.27	85.78	173.27	40.09	1.53	0.74	46.31	59.61	128.72	27.01
PM_{10} (ng/m^3)	53.45	128.32	993.53	1176.49	2003.62	594.02	163.16	18.06	641.33	706.54	110.17	378.59
$PM_{0.1}$ (ng/m^3)	4.74	36.64	266.04	348.40	1268.51	267.81	4.41	4.61	275.15	425.74	154.73	151.34

Table 5. Fe mass concentration data, BROS, (ngm^{-3}).

f. Ni

Low Cutpoint / nm	BR-26-7-11	BR-6-9-11	BR-28-9-11	BR-5-10-11	BR-12-10-11	BR-19-10-11	BR-2-11-11	BR-9-11-11	Mean	Std Dev	%Std Dev	Median
1000	0.25	0.16	1.59	0.35	0.42	0.30	0.67	0.15	0.49	0.48	98.00	0.32
560	0.19	0.20	0.13	0.46	0.34	0.83	0.41	0.47	0.38	0.22	58.56	0.38
320	0.21	0.08	0.78	0.96	0.36	0.25	0.40	0.51	0.44	0.30	66.75	0.38
180	0.42	0.11	0.66	1.44	1.24	0.11	0.44	0.12	0.57	0.52	91.71	0.43
100	0.15	0.18	0.66	0.10	0.51	0.13	0.28	0.59	0.32	0.23	69.77	0.23
56	0.19	0.10	0.50	0.15	1.33	0.31	0.46	0.10	0.39	0.41	104.01	0.25
32	0.15	0.00	0.63	0.15	0.30	0.11	0.59	1.33	0.41	0.44	106.96	0.23
18	0.22	0.07	0.23	0.27	0.68	0.62	0.25	0.41	0.34	0.21	61.56	0.26
10	0.13	0.11	0.54	1.25	2.84	0.14	0.14	0.57	0.72	0.94	131.78	0.34
1	0.10	0.08	0.18	0.53	2.12	0.40	0.32	0.07	0.48	0.69	143.95	0.32
PM_{10} (ng/m^3)	2.02	1.09	5.90	5.68	10.16	3.19	3.94	4.32	4.54	2.81	61.86	4.13
$PM_{0.1}$ (ng/m^3)	0.80	0.37	2.07	2.36	7.28	1.58	1.75	2.48	2.34	2.13	91.01	1.91

Table 6. Ni mass concentration data, BROS, (ngm^{-3}).

g. Sb

Low Cutpoint / nm	BR-26-7-11	BR-6-9-11	BR-28-9-11	BR-5-10-11	BR-12-10-11	BR-19-10-11	BR-2-11-11	BR-9-11-11	Mean	Std Dev	%Std Dev	Median
1000	0.06	0.011	<0.022	0.23	1.02	0.61	1.99	<0.011	0.65	0.76	116.00	0.42
560	0.11	0.012	<0.022	0.05	0.19	0.30	<0.022	0.11	0.13	0.10	79.81	0.11
320	0.03	<0.011	0.04	0.06	0.29	0.12	0.16	0.04	0.10	0.09	89.92	0.06
180	<0.01	<0.011	<0.022	<0.022	0.12	0.02	<0.022	<0.011	0.07	0.07	94.09	0.07
100	<0.01	0.02	<0.022	<0.022	< 0.022	<0.022	0.05	<0.011	0.03	0.02	70.56	0.03
56	<0.01	<0.011	<0.022	<0.022	< 0.022	<0.022	<0.022	<0.011	n/a	n/a	n/a	n/a
32	<0.01	<0.011	<0.022	<0.022	< 0.022	<0.022	<0.022	<0.011	n/a	n/a	n/a	n/a
18	<0.01	<0.011	<0.022	<0.022	< 0.022	<0.022	<0.022	<0.011	n/a	n/a	n/a	n/a
10	<0.01	<0.011	<0.022	<0.022	< 0.022	<0.022	<0.022	<0.011	n/a	n/a	n/a	n/a
1	<0.01	<0.011	<0.022	<0.022	< 0.022	<0.022	<0.022	<0.011	n/a	n/a	n/a	n/a
PM_{10} (ng/m^3)	0.20	0.04	0.04	0.34	1.61	1.05	2.19	0.15	0.70	0.82	117.29	0.27
$PM_{0.1}$ (ng/m^3)	0.00	0.00	0.00	0.00	0.00	0.00	0.00	0.00	0.00	0.00	n/a	0.00

Table 7. Sb mass concentration data, BROS, (ngm^{-3}).

h. Sr

Low Cutpoint / nm	BR-26-7-11	BR-6-9-11	BR-28-9-11	BR-5-10-11	BR-12-10-11	BR-19-10-11	BR-2-11-11	BR-9-11-11	Mean	Std Dev	%Std Dev	Median
1000	0.07	0.03	0.74	0.52	0.40	0.56	5.44	<0.011	1.11	1.93	173.64	0.52
560	0.07	0.04	0.04	0.04	0.04	0.10	0.03	0.09	0.06	0.03	51.68	0.04
320	<0.011	<0.011	0.03	<0.022	0.02	0.02	0.06	0.02	0.03	0.02	50.16	0.02
180	<0.011	<0.011	0.02	<0.022	< 0.022	<0.022	<0.022	<0.011	0.02	n/a	n/a	0.02
100	<0.011	0.07	<0.022	<0.022	< 0.022	<0.022	<0.022	<0.011	0.07	n/a	n/a	0.07
56	<0.011	<0.011	<0.022	<0.022	< 0.022	<0.022	<0.022	<0.011	n/a	n/a	n/a	n/a
32	<0.011	<0.012	<0.022	<0.022	< 0.022	<0.022	<0.022	<0.011	n/a	n/a	n/a	n/a
18	0.04	<0.011	<0.022	<0.022	< 0.022	<0.022	<0.022	<0.011	0.04	n/a	n/a	0.04
10	0.03	<0.011	<0.022	<0.022	< 0.022	<0.022	<0.022	<0.011	0.03	n/a	n/a	0.03
1	0.04	<0.011	<0.022	<0.022	< 0.022	<0.022	<0.022	<0.011	0.04	n/a	n/a	0.04
PM_{10} (ng/m^3)	0.26	0.13	0.83	0.56	0.47	0.68	5.52	0.11	1.07	1.82	169.61	0.51
$PM_{0.1}$ (ng/m^3)	0.11	0.00	0.00	0.00	0.00	0.00	0.00	0.00	0.01	0.04	282.84	0.00

Table 8. Sr mass concentration data, BROS, (ngm^{-3}).

i. V

Low Cutpoint / nm	BR-26-7-11	BR-6-9-11	BR-28-9-11	BR-5-10-11	BR-12-10-11	BR-19-10-11	BR-2-11-11	BR-9-11-11	Mean	Std Dev	%Std Dev	Median
1000	< 0.022	< 0.022	0.55	0.13	0.15	0.21	0.19	<0.022	0.25	0.17	69.76	0.19
560	0.03	< 0.022	0.16	0.10	0.11	0.25	<0.044	0.08	0.12	0.07	61.32	0.11
320	< 0.022	< 0.022	0.49	0.14	0.18	0.19	<0.044	0.04	0.21	0.17	80.84	0.18
180	< 0.022	< 0.022	0.56	0.06	0.17	0.06	<0.044	<0.022	0.21	0.23	108.99	0.12
100	< 0.022	0.025	<0.044	<0.044	0.06	<0.044	<0.044	<0.022	0.04	0.02	57.63	0.04
56	< 0.022	< 0.022	<0.044	<0.044	0.16	<0.044	<0.044	<0.022	0.16	n/a	n/a	0.16
32	< 0.022	< 0.023	0.05	<0.044	< 0.044	<0.044	<0.044	<0.022	0.05	n/a	n/a	0.05
18	< 0.022	< 0.022	<0.044	0.05	< 0.044	<0.044	<0.044	<0.022	0.05	n/a	n/a	0.05
10	< 0.022	< 0.022	<0.044	0.06	0.07	<0.044	<0.044	<0.022	0.07	0.01	16.64	0.07
1	< 0.022	< 0.022	<0.044	<0.044	< 0.044	<0.044	<0.044	<0.022	n/a	n/a	n/a	n/a
PM_{10} (ng/m^3)	0.03	0.02	1.81	0.54	0.92	0.72	0.19	0.11	0.54	0.61	112.22	0.37
$PM_{0.1}$ (ng/m^3)	0.00	0.00	0.05	0.11	0.24	0.00	0.00	0.00	0.05	0.08	171.52	0.00

Table 9. V mass concentration data, BROS, (ngm^{-3})

.

j. Zn

Low Cutpoint / nm	BR-26-7-11	BR-6-9-11	BR-28-9-11	BR-5-10-11	BR-12-10-11	BR-19-10-11	BR-2-11-11	BR-9-11-11	Mean	Std Dev	%Std Dev	Median
1000	0.65	0.37	14.85	1.43	5.28	4.96	16.99	0.52	5.63	6.66	118.34	3.20
560	1.07	0.71	2.44	0.29	2.54	6.36	2.34	2.51	2.28	1.88	82.27	2.39
320	0.18	<0.022	2.42	1.59	2.32	1.59	2.66	1.38	1.73	0.84	48.55	1.59
180	3.07	<0.022	2.28	6.79	4.99	0.19	0.68	0.78	2.68	2.46	91.69	2.28
100	0.15	0.95	2.13	<0.044	1.30	0.08	1.67	2.93	1.32	1.03	78.68	1.30
56	0.12	<0.022	0.81	<0.044	0.92	<0.044	2.13	0.46	0.88	0.76	85.97	0.81
32	0.37	0.00	0.58	<0.044	0.08	<0.044	1.72	2.42	0.86	0.99	114.32	0.48
18	0.70	<0.022	<0.044	<0.044	1.24	0.73	4.09	0.12	1.38	1.57	113.78	0.73
10	0.20	0.20	0.72	2.71	1.88	<0.044	0.51	1.95	1.17	1.00	85.71	0.72
1	0.20	<0.022	0.39	<0.044	1.33	0.33	1.64	0.53	0.74	0.59	80.74	0.39
PM_{10} (ng/m^3)	6.70	2.23	26.63	12.82	21.86	14.24	34.42	13.62	16.56	10.55	63.69	13.93
$PM_{0.1}$ (ng/m^3)	1.58	0.20	2.51	2.71	5.44	1.06	10.07	5.49	3.63	3.23	88.81	2.61

Table 10. Zn mass concentration data, BROS, (ngm^{-3}).

2. Elms Road Samples

a. Al

Low Cutpoint / nm	ER-28-9-11	ER-5-10-11	ER-12-10-11	ER-19-10-11	ER-2-11-11	Mean	SD	%SD
1000	2.04	9.82	5.04	23.96	0.57	8.28	9.45	114.04
560	1.25	35.80	3.50	9.68	3.88	10.82	14.31	132.22
320	2.10	4.65	3.47	9.37	3.19	4.56	2.84	62.28
180	2.11	10.37	2.99	4.30	2.15	4.39	3.46	78.95
100	2.08	33.02	2.32	4.29	0.63	8.47	13.79	162.83
56	1.49	13.38	3.04	22.82	0.64	8.27	9.61	116.14
32	1.57	1.80	2.22	2.42	0.72	1.75	0.66	37.97
18	1.64	9.87	3.05	5.89	1.11	4.31	3.62	83.91
10	1.82	16.90	3.73	8.45	0.64	6.31	6.63	105.02
1	6.50	48.09	38.79	52.04	0.77	29.24	23.95	81.90
PM_{10} (ng/m^3)	22.61	183.70	68.15	143.22	14.30	86.40	74.66	86.41
$PM_{0.1}$ (ng/m^3)	13.03	90.04	50.83	91.63	3.24	49.75	41.50	83.42

Table 11. Al mass concentration data, EROS, (ngm^{-3}).

b. Ba

Low Cutpoint / nm	ER-28-9-11	ER-5-10-11	ER-12-10-11	ER-19-10-11	ER-2-11-11	Mean	SD	%SD
1000	0.091	0.28	1.16	1.07	0.02	0.53	0.55	104.46
560	<0.022	0.19	0.60	0.25	0.12	0.19	0.21	115.42
320	0.036	0.13	0.11	0.17	0.05	0.10	0.06	55.89
180	<0.022	<0.022	< 0.022	<0.022	0.06	0.06	n/a	n/a
100	<0.022	0.04	< 0.022	<0.022	0.05	0.05	0.01	13.42
56	<0.022	<0.022	< 0.022	<0.022	0.02	0.02	n/a	n/a
32	<0.022	<0.022	< 0.022	<0.022	0.02	0.02	n/a	n/a
18	<0.022	<0.022	< 0.022	<0.022	0.04	0.04	n/a	n/a
10	0.024	<0.022	< 0.022	<0.022	0.02	0.02	0.00	12.01
1	<0.022	0.14	< 0.022	<0.022	0.05	0.09	0.06	65.61
PM_{10} (ng/m^3)	0.15	0.78	1.87	1.49	0.45	0.95	0.72	75.61
$PM_{0.1}$ (ng/m^3)	0.02	0.14	0.00	0.00	0.15	0.06	0.07	120.75

Table 12. Ba mass concentration data, EROS, (ngm^{-3}).

c. Cu

Low Cutpoint / nm	ER-28-9-11	ER-5-10-11	ER-12-10-11	ER-19-10-11	ER-2-11-11	Mean	SD	%SD
1000	0.36	0.57	2.50	2.51	0.03	1.20	1.21	101.61
560	0.12	8.34	2.11	0.70	3.89	1.57	3.31	210.86
320	0.53	0.18	0.94	0.45	0.17	0.45	0.32	69.60
180	0.38	0.04	0.36	<0.022	0.22	0.25	0.16	64.05
100	0.58	0.07	1.94	<0.022	0.12	0.68	0.87	128.53
56	0.17	0.04	0.16	0.03	0.04	0.09	0.07	79.92
32	0.17	0.07	0.15	<0.022	0.18	0.14	0.05	37.12
18	0.20	0.05	0.20	0.06	0.42	0.19	0.15	79.49
10	0.17	<0.022	0.17	0.03	0.06	0.11	0.08	68.81
1	0.44	0.30	0.54	0.33	0.08	0.27	0.17	63.31
PM_{10} (ng/m^3)	3.13	9.65	9.06	3.78	5.21	6.17	3.01	48.86
$PM_{0.1}$ (ng/m^3)	1.16	0.46	1.21	0.12	0.78	0.75	0.46	62.04

Table 13. Cu mass concentration data, EROS, (ngm^{-3}).

d. Fe

Low Cutpoint / nm	ER-28-9-11	ER-5-10-11	ER-12-10-11	ER-19-10-11	ER-2-11-11	Mean	SD	%SD
1000	99.29	87.22	113.47	57.36	0.25	71.52	44.88	62.76
560	1.59	53.91	196.93	15.49	5.78	54.74	82.13	150.04
320	289.11	22.96	908.00	9.72	1.09	246.17	389.12	158.07
180	460.22	61.11	261.11	3.26	3.99	157.94	199.39	126.24
100	866.67	18.17	109.38	4.61	4.20	200.60	374.91	186.89
56	166.58	9.61	204.87	5.53	55.97	88.51	91.93	103.86
32	110.29	6.91	61.87	2.80	0.94	36.56	48.38	132.33
18	143.64	99.36	84.76	5.03	100.88	86.73	50.69	58.44
10	60.16	25.24	36.44	12.90	133.00	53.55	47.70	89.08
1	199.76	50.47	440.22	15.86	137.56	168.77	168.07	99.59
PM_{10} (ng/m^3)	2397.30	434.96	2417.04	132.56	443.66	1165.11	1140.77	97.91
$PM_{0.1}$ (ng/m^3)	680.42	191.59	828.16	42.13	428.35	434.13	327.28	75.39

Table 14. Fe mass concentration data, EROS, (ngm^{-3}).

e. Ni

Low Cutpoint / nm	ER-28-9-11	ER-5-10-11	ER-12-10-11	ER-19-10-11	ER-2-11-11	Mean	SD	%SD
1000	0.24	0.25	0.22	0.17	0.09	0.19	0.07	33.93
560	<0.022	1.19	0.45	0.11	0.14	0.47	0.50	105.79
320	0.72	0.16	1.49	1.02	0.30	0.74	0.54	73.30
180	1.29	0.32	0.48	0.06	0.81	0.59	0.48	80.38
100	1.90	0.12	0.20	0.12	0.04	0.48	0.80	166.76
56	0.35	0.45	0.34	0.17	0.27	0.31	0.10	33.16
32	0.26	0.14	0.15	0.16	0.08	0.16	0.06	40.13
18	0.43	0.32	0.26	0.14	0.33	0.30	0.11	36.40
10	0.18	0.15	0.12	0.10	0.35	0.18	0.10	55.65
1	0.47	0.13	0.69	7.65	0.36	0.32	3.24	1015.79
PM_{10} (ng/m^3)	5.83	3.23	4.40	2.04	2.77	3.66	1.49	40.78
$PM_{0.1}$ (ng/m^3)	1.69	1.19	1.56	0.56	1.39	1.28	0.44	34.72

Table 16. Ni mass concentration data, EROS, (ngm^{-3}).

f. Sb

Low Cutpoint / nm	ER-28-9-11	ER-5-10-11	ER-12-10-11	ER-19-10-11	ER-2-11-11	Mean	SD	%SD
1000	<0.022	0.04	0.20	0.18	<0.011	0.14	0.09	61.45
560	<0.022	0.05	0.23	0.09	0.33	0.21	0.13	62.81
320	0.04	0.04	0.19	0.10	0.03	0.08	0.07	84.62
180	<0.022	<0.022	< 0.022	<0.022	<0.011	n/a	n/a	n/a
100	<0.022	<0.022	< 0.022	<0.022	<0.011	n/a	n/a	n/a
56	<0.022	<0.022	< 0.022	<0.022	<0.011	n/a	n/a	n/a
32	<0.022	<0.022	< 0.022	<0.022	<0.011	n/a	n/a	n/a
18	<0.022	<0.022	< 0.022	<0.022	<0.011	n/a	n/a	n/a
10	<0.022	<0.022	< 0.022	<0.022	<0.011	n/a	n/a	n/a
1	<0.022	<0.022	< 0.022	<0.022	<0.011	n/a	n/a	n/a
PM_{10} (ng/m^3)	0.04	0.13	0.62	0.36	0.36	0.30	0.23	75.03
$PM_{0.1}$ (ng/m^3)	0.00	0.00	0.00	0.00	0.00	0.00	0.00	n/a

Table 17. Sb mass concentration data, EROS, (ngm^{-3}).

g. Sr

Low Cutpoint / nm	ER-28-9-11	ER-5-10-11	ER-12-10-11	ER-19-10-11	ER-2-11-11	Mean	SD	%SD
1000	<0.022	0.13	0.19	0.33	0.56	0.30	0.19	63.83
560	<0.022	0.05	0.04	0.04	1.20	0.62	0.58	93.51
320	<0.022	<0.022	< 0.022	0.03	0.03	0.03	0.00	7.73
180	<0.022	<0.022	< 0.022	<0.022	<0.011	n/a	n/a	n/a
100	<0.022	<0.022	< 0.022	<0.022	0.01	0.01	n/a	n/a
56	<0.022	<0.022	< 0.022	<0.022	<0.011	n/a	n/a	n/a
32	<0.022	<0.022	< 0.022	<0.022	0.01	0.01	n/a	n/a
18	<0.022	<0.022	< 0.022	<0.022	0.03	0.03	n/a	n/a
10	<0.022	<0.022	< 0.022	<0.022	<0.011	n/a	n/a	n/a
1	<0.022	<0.022	< 0.022	<0.022	<0.011	n/a	n/a	n/a
PM_{10} (ng/m^3)	0.00	0.18	0.23	0.39	1.84	0.53	0.75	141.13
$PM_{0.1}$ (ng/m^3)	0.00	0.00	0.00	0.00	0.04	0.01	0.02	223.61

Table 18. Sr mass concentration data, EROS, (ngm^{-3}).

h. V

Low Cutpoint / nm	ER-28-9-11	ER-5-10-11	ER-12-10-11	ER-19-10-11	ER-2-11-11	Mean	SD	%SD
1000	0.08	0.06	0.09	0.12	<0.022	0.09	0.02	27.83
560	<0.044	0.10	0.17	0.11	0.09	0.10	0.04	36.47
320	0.27	0.09	0.32	0.15	<0.022	0.21	0.11	50.45
180	0.40	0.05	0.06	<0.044	<0.022	0.17	0.20	119.55
100	0.65	0.05	< 0.044	<0.044	<0.022	0.35	0.42	122.33
56	0.13	0.05	0.05	<0.044	<0.022	0.08	0.05	59.11
32	0.08	0.05	< 0.044	<0.044	<0.022	0.06	0.02	36.08
18	0.11	0.06	< 0.044	<0.044	0.04	0.07	0.04	49.65
10	0.05	0.05	0.05	<0.044	0.06	0.05	0.01	11.23
1	0.15	<0.044	0.08	<0.044	0.05	0.10	0.05	52.46
PM_{10} (ng/m^3)	1.91	0.57	0.82	0.38	0.24	0.78	0.67	85.03
$PM_{0.1}$ (ng/m^3)	0.52	0.21	0.18	0.00	0.15	0.21	0.19	89.25

Table 19. V mass concentration data, EROS, (ngm^{-3}).

i. Zn

Low Cutpoint / nm	ER-28-9-11	ER-5-10-11	ER-12-10-11	ER-19-10-11	ER-2-11-11	Mean	SD	%SD
1000	0.35	1.02	2.98	2.45	0.76	1.51	1.14	75.41
560	<0.044	9.74	3.46	0.99	10.59	5.79	4.71	81.25
320	0.68	0.51	2.35	4.12	1.45	1.82	1.48	81.01
180	1.20	0.44	0.81	<0.044	5.56	2.00	2.39	119.37
100	0.31	0.59	0.14	<0.044	0.30	0.33	0.19	55.61
56	<0.044	0.39	0.05	0.49	<0.022	0.31	0.23	74.55
32	<0.044	<0.044	0.13	0.10	0.38	0.20	0.15	74.95
18	<0.044	0.13	0.19	0.23	0.43	0.25	0.13	52.38
10	<0.044	<0.044	0.16	<0.044	0.02	0.09	0.10	110.76
1	<0.044	0.80	0.34	<0.044	<0.022	0.80	0.33	40.46
PM_{10} (ng/m^3)	2.53	13.63	10.62	8.39	19.49	10.93	6.28	57.43
$PM_{0.1}$ (ng/m^3)	0.00	1.33	0.88	0.82	0.83	0.77	0.48	62.23

Table 20. Zn mass concentration data, EROS, (ngm^{-3}).

3. Harwell Samples

a. Al

Lower cutpoint/nm	HW-7-12-11	HW-21-12-11	Mean	SD	%SD
1000	0.56	1.92	1.24	0.96	77.71
560	2.28	0.87	1.57	1.00	63.40
320	0.93	0.56	0.75	0.26	34.67
180	0.87	0.70	0.79	0.12	14.97
100	0.69	0.68	0.68	0.01	1.38
56	0.64	0.41	0.53	0.17	31.83
32	0.52	0.44	0.48	0.05	11.16
18	0.97	0.49	0.73	0.34	46.63
10	0.62	0.48	0.55	0.10	17.97
1	4.79	18.21	11.50	9.49	82.56
PM_{10}	12.86	24.76	18.81	8.41	44.72
$PM_{0.1}$	7.53	20.03	13.78	8.83	64.10

Table 21. Harwell Al concentrations, in ngm^{-3}.

b. Ba

Lower cutpoint/nm	HW-7-12-11	HW-21-12-11	Mean	SD	%SD
1000	0.03	0.10	0.06	0.05	82.79
560	0.04	0.01	0.02	0.02	102.96
320	0.05	0.03	0.04	0.01	25.64
180	0.02	0.08	0.05	0.05	94.81
100	0.05	0.07	0.06	0.02	29.12
56	0.01	0.01	0.01	0.01	64.78
32	<0.006	0.01	0.01	n/a	n/a
18	0.02	0.02	0.02	0.00	23.58
10	<0.006	0.01	0.01	n/a	n/a
1	<0.006	0.01	0.01	n/a	n/a
PM_{10}	0.21	0.36	0.28	0.11	38.03
$PM_{0.1}$	0.03	0.07	0.05	0.02	48.93

Table 22. Harwell Ba concentrations, in ngm^{-3}.

c. Ce

Lower cutpoint/nm	HW-7-12-11	HW-21-12-11	Mean	SD	%SD
1000	<0.006	0.01	0.01	n/a	n/a
560	0.01	<0.006	0.01	n/a	n/a
320	<0.006	0.01	0.01	n/a	n/a
180	0.01	0.03	0.02	0.02	88.96
100	0.04	0.01	0.03	0.02	72.15
56	0.01	0.01	0.01	0.00	4.58
32	0.01	0.01	0.01	0.00	3.69
18	0.01	<0.006	0.01	n/a	n/a
10	0.01	0.01	0.01	0.00	18.81
1	<0.006	0.01	0.01	n/a	n/a
PM_{10}	0.09	0.09	0.09	0.00	1.82
$PM_{0.1}$	0.03	0.03	0.03	0.00	1.99

Table 23. Harwell Ce concentrations, in ngm^{-3}.

d. Cu

Lower cutpoint/nm	HW-7-12-11	HW-21-12-11	Mean	SD	%SD
1000	0.19	0.52	0.35	0.23	65.78
560	0.54	0.25	0.40	0.21	52.63
320	0.40	0.65	0.53	0.18	34.12
180	0.60	3.10	1.85	1.77	95.88
100	0.95	2.69	1.82	1.23	67.84
56	0.56	0.53	0.54	0.02	4.55
32	0.27	0.43	0.35	0.12	33.23
18	0.78	0.39	0.58	0.27	47.22
10	0.34	0.36	0.35	0.01	2.27
1	0.24	0.50	0.37	0.18	48.20
PM_{10}	4.87	9.41	7.14	3.21	44.98
$PM_{0.1}$	2.19	2.20	2.20	0.00	0.17

Table 24. Harwell Cu concentrations, in ngm^{-3}.

e. Fe

Lower cutpoint/nm	HW-7-12-11	HW-21-12-11	Mean	SD	%SD
1000	9.04	6.50	7.77	1.80	23.15
560	8.72	0.40	4.56	5.88	129.13
320	18.16	0.89	9.52	12.21	128.27
180	19.73	0.72	10.23	13.45	131.51
100	10.87	2.44	6.65	5.97	89.66
56	9.32	2.88	6.10	4.56	74.75
32	4.60	3.50	4.05	0.78	19.15
18	4.08	2.77	3.43	0.93	27.05
10	5.45	0.78	3.11	3.30	106.09
1	5.79	1.16	3.48	3.28	94.32
PM_{10}	95.76	22.01	58.89	52.15	88.56
$PM_{0.1}$	29.24	11.08	20.16	12.84	63.70

Table 25. Harwell Fe concentrations, in ngm^{-3}.

f. Ni

Lower cutpoint/nm	HW-7-12-11	HW-21-12-11	Mean	SD	%SD
1000	0.07	0.34	0.20	0.20	96.37
560	0.09	0.21	0.15	0.08	54.09
320	0.37	0.06	0.22	0.22	99.77
180	0.10	0.12	0.11	0.01	13.38
100	0.19	0.09	0.14	0.07	52.47
56	0.20	0.05	0.13	0.10	81.01
32	0.04	0.06	0.05	0.01	22.80
18	0.41	0.20	0.30	0.14	47.43
10	0.04	0.03	0.04	0.01	17.53
1	0.06	0.02	0.04	0.03	73.52
PM_{10}	1.58	1.20	1.39	0.27	19.39
$PM_{0.1}$	0.76	0.37	0.56	0.27	48.44

Table 26. Harwell Ni concentrations, in ngm^{-3}.

g. Sb

Lower cutpoint/nm	HW-7-12-11	HW-21-12-11	Mean	SD	%SD
1000	0.01	0.02	0.01	0.01	55.55
560	0.02	<0.006	0.02	n/a	n/a
320	0.06	0.02	0.04	0.03	84.24
180	0.02	0.01	0.02	0.01	42.47
100	<0.006	0.02	0.02	n/a	n/a
56	<0.006	<0.006	n/a	n/a	n/a
32	<0.006	<0.006	n/a	n/a	n/a
18	<0.006	<0.006	n/a	n/a	n/a
10	<0.006	<0.006	n/a	n/a	n/a
1	<0.006	<0.006	n/a	n/a	n/a
PM_{10}	0.11	0.06	0.09	0.03	38.31
$PM_{0.1}$	<0.006	0.00	0.00	n/a	n/a

Table 27. Harwell Sb concentrations, in ngm^{-3}.

h. Sr

Lower cutpoint/nm	HW-7-12-11	HW-21-12-11	Mean	SD	%SD
1000	0.03	0.30	0.17	0.19	111.84
560	0.04	0.01	0.03	0.02	66.78
320	0.03	0.06	0.04	0.02	57.77
180	0.04	0.23	0.14	0.14	101.13
100	0.09	0.18	0.14	0.07	48.50
56	0.04	0.01	0.03	0.02	77.95
32	0.01	0.03	0.02	0.01	38.20
18	0.05	0.01	0.03	0.03	89.23
10	0.01	0.03	0.02	0.01	53.11
1	0.01	0.02	0.02	0.01	56.87
PM_{10}	0.36	0.90	0.63	0.38	60.08
$PM_{0.1}$	0.13	0.10	0.12	0.02	16.36

Table 28. Harwell Sr concentrations, in ngm^{-3}.

i. V

Lower cutpoint/nm	HW-7-12-11	HW-21-12-11	Mean	SD	%SD
1000	<0.011	0.02	0.02	n/a	n/a
560	<0.011	<0.011	n/a	n/a	n/a
320	0.03	0.03	0.03	0.00	3.71
180	0.01	<0.011	0.01	n/a	n/a
100	<0.011	<0.011	n/a	n/a	n/a
56	<0.011	<0.011	n/a	n/a	n/a
32	<0.011	<0.011	n/a	n/a	n/a
18	<0.011	<0.011	n/a	n/a	n/a
10	<0.011	<0.011	n/a	n/a	n/a
1	<0.011	<0.011	n/a	n/a	n/a
PM_{10}	0.04	0.05	0.04	0.01	11.86
$PM_{0.1}$	<0.011	<0.011	n/a	n/a	n/a

Table 29. Harwell V concentrations, in ngm^{-3}.

j. Zn

Lower cutpoint/nm	HW-7-12-11	HW-21-12-11	Mean	SD	%SD
1000	0.22	1.64	0.93	1.01	108.54
560	0.55	0.99	0.77	0.31	40.63
320	1.63	0.65	1.14	0.70	61.28
180	0.44	2.35	1.39	1.35	97.22
100	1.15	2.04	1.59	0.63	39.21
56	1.16	0.23	0.69	0.65	94.18
32	0.12	0.27	0.20	0.10	53.02
18	1.96	0.18	1.07	1.26	117.47
10	0.15	0.23	0.19	0.06	31.86
1	0.07	0.20	0.14	0.09	65.79
PM_{10}	7.44	8.77	8.11	0.94	11.61
$PM_{0.1}$	3.46	1.12	2.29	1.66	72.47

Table 30. Harwell Zn concentrations, in ngm^{-3}.

4. Newcastle Samples

a. Al

LC / nm	26/01/2012	02/02/2012	23/02/2012	08/03/2012	29/03/2012	10/05/2012	17/05/2012	Mean	SD	RSD
1000	19.07	5.40	2.70	9.82	4.08	4.71	10.25	8.00	5.66	70.66
560	2.44	4.86	1.62	35.80	1.86	2.67	1.80	7.29	12.62	173.04
320	7.06	2.86	2.15	4.65	1.22	1.31	3.23	3.21	2.07	64.47
180	7.47	3.68	2.00	10.37	2.31	2.60	3.49	4.56	3.15	69.14
100	6.61	9.67	2.47	33.02	1.48	3.28	1.83	8.34	11.28	135.29
56	10.57	6.33	3.74	13.38	1.70	4.49	6.44	6.66	4.05	60.77
32	10.22	10.84	1.81	1.80	3.51	1.42	3.84	4.77	4.04	84.58
18	6.06	4.66	9.12	9.87	3.33	4.25	1.76	5.58	2.98	53.49
10	6.72	3.63	2.61	16.90	0.97	2.90	1.92	5.09	5.51	108.16
1	111.56	31.19	19.23	48.09	19.39	7.35	17.29	23.76	35.60	149.86
PM_{10}	57.15	77.72	44.76	173.88	39.84	30.26	41.60	66.46	49.77	74.89
$PM_{0.1}$	33.57	56.66	36.51	90.04	28.90	20.41	31.25	42.47	23.72	55.85

Table 31. Newcastle Al concentrations, in ngm^{-3}.

b. Ba

LC / nm	26/01/2012	02/02/2012	23/02/2012	08/03/2012	29/03/2012	10/05/2012	17/05/2012	Mean	SD	RSD
1000	0.87	0.34	0.14	2.17	0.18	0.44	0.59	0.68	0.71	104.47
560	0.08	0.16	0.09	0.08	0.07	0.01	0.09	0.08	0.04	50.14
320	0.09	0.04	0.18	0.01	0.03	0.05	0.05	0.06	0.06	90.59
180	0.11	0.07	0.04	0.04	<0.01	<0.011	0.06	0.06	0.03	43.81
100	<0.011	0.12	0.07	0.07	0.06	0.02	0.05	0.06	0.03	50.96
56	<0.011	0.02	0.07	<0.01	0.01	0.02	0.04	0.03	0.02	74.81
32	0.02	0.07	0.03	<0.01	<0.01	0.02	0.01	0.03	0.03	84.75
18	0.05	0.02	0.04	<0.01	<0.01	<0.011	<0.01	0.03	0.02	50.90
10	0.01	0.02	0.04	<0.01	<0.01	0.02	<0.01	0.02	0.01	50.66
1	0.12	0.03	0.15	0.03	<0.01	0.01	0.02	0.06	0.06	99.34
PM_{10}	0.48	0.53	0.70	0.23	0.34	0.15	0.32	0.40	0.19	47.71
$PM_{0.1}$	0.20	0.15	0.32	0.03	0.01	0.08	0.07	0.12	0.11	89.44

Table 32. Newcastle Ba concentrations, in ngm^{-3}.

c. Cu

LC / nm	26/01/2012	02/02/2012	23/02/2012	08/03/2012	29/03/2012	10/05/2012	17/05/2012	Mean	SD	RSD
1000	1.66	0.93	0.24	1.83	0.24	0.43	2.28	1.09	0.84	76.88
560	0.23	0.78	0.18	0.12	0.12	0.14	0.25	0.26	0.24	90.86
320	0.38	0.34	0.22	0.14	0.10	0.10	0.69	0.28	0.21	74.79
180	1.43	0.27	0.15	0.16	0.10	0.06	0.24	0.35	0.48	139.80
100	0.09	0.58	0.18	0.09	0.07	0.14	0.17	0.19	0.17	92.09
56	0.26	0.26	0.31	0.07	0.07	0.17	0.09	0.17	0.10	57.47
32	0.30	0.56	0.10	0.05	0.07	0.07	0.14	0.18	0.18	99.87
18	0.19	0.20	0.23	0.07	0.09	0.03	0.41	0.18	0.13	71.93
10	0.24	0.10	0.06	0.10	0.13	0.12	0.22	0.14	0.07	48.07
1	1.59	0.28	0.67	0.21	0.25	0.16	0.44	0.51	0.50	98.10
PM_{10}	4.70	3.37	2.10	1.02	1.26	0.99	2.65	2.30	1.39	60.27
$PM_{0.1}$	2.58	1.41	1.37	0.50	0.62	0.55	1.30	1.19	0.73	61.73

Table 33. Newcastle Cu concentrations, in ngm^{-3}.

d. Fe

LC / nm	26/01/ 2012	02/02/ 2012	23/02/ 2012	08/03/ 2012	29/03/ 2012	10/05/ 2012	17/05/ 2012	Mean	SD	%SD	Mean (excluding17-5)	SD	%SD
1000	44.12	18.51	4.36	102.99	118.33	27.47	201.89	73.95	70.88	95.85	52.63	47.02	89.33
560	5.65	19.96	4.66	11.13	24.12	9.39	161.44	33.76	56.76	168.10	12.48	7.88	63.13
320	2.83	33.60	6.93	143.56	50.51	22.91	970.67	175.86	353.69	201.12	43.39	52.10	120.08
180	2.00	20.89	7.63	164.11	24.06	19.67	192.44	61.54	80.54	130.87	39.73	61.53	154.88
100	1.57	7.08	5.89	119.33	17.06	24.12	151.11	46.60	61.69	132.41	29.18	44.93	154.00
56	16.18	6.38	2.82	16.20	16.20	19.32	66.84	20.56	21.28	103.48	12.85	6.60	51.38
32	10.58	13.00	10.34	12.00	36.97	11.71	152.78	35.34	52.65	149.00	15.77	10.43	66.17
18	8.14	3.09	2.36	28.51	226.44	22.83	373.33	94.96	146.60	154.38	48.56	87.80	180.79
10	5.37	13.27	9.99	58.13	214.56	7.94	113.89	60.45	78.71	130.21	51.54	82.27	159.61
1	8.17	29.76	31.42	100.37	197.44	48.32	703.22	159.81	248.02	155.19	69.25	70.09	101.22
PM_{10}	60.49	147.02	82.04	653.34	925.69	186.22	2885.73	705.79	1015.79	143.92	342.47	359.65	105.02
$PM_{0.1}$	48.43	65.49	56.93	215.21	691.61	110.13	1410.07	371.13	511.66	137.87	197.97	249.60	126.08

Table 34. Newcastle Fe concentrations, in ngm^{-3}.

e. Ni

LC / nm	26/01/2012	02/02/2012	23/02/2012	08/03/2012	29/03/2012	10/05/2012	17/05/2012	Mean	SD	RSD
1000	0.21	0.19	0.11	0.28	0.23	0.19	0.67	0.27	0.19	69.75
560	0.09	0.53	0.16	0.07	0.20	0.44	0.78	0.32	0.27	82.31
320	0.10	0.16	0.22	0.75	0.11	0.15	3.18	0.67	1.13	169.39
180	0.58	0.16	0.10	0.41	0.51	0.19	0.66	0.37	0.22	59.68
100	0.14	0.62	0.12	0.47	0.42	0.16	0.89	0.40	0.29	72.02
56	0.37	0.10	0.33	0.08	0.04	0.12	0.27	0.19	0.13	70.44
32	0.60	0.70	0.33	0.05	0.08	0.10	0.52	0.34	0.27	80.36
18	0.66	0.72	0.13	0.08	0.36	0.16	1.29	0.49	0.44	89.88
10	0.18	0.82	0.31	0.70	0.46	0.21	0.42	0.44	0.24	54.32
1	0.29	0.12	0.13	0.20	0.28	0.22	2.50	0.53	0.87	162.41
PM_{10}	3.01	3.93	1.83	2.81	2.69	1.76	10.53	3.79	3.06	80.69
$PM_{0.1}$	2.10	2.45	1.23	1.11	1.22	0.81	5.00	1.99	1.45	72.86

Table 35. Newcastle Ni concentrations, in ngm^{-3}.

f. Sb

LC / nm	26/01/2012	02/02/2012	23/02/2012	08/03/2012	29/03/2012	10/05/2012	17/05/2012	Mean	SD	RSD
1000	0.17	0.04	0.02	0.23	0.02	0.05	0.10	0.09	0.08	90.05
560	0.01	0.03	0.02	0.02	0.02	<0.011	0.02	0.02	0.01	36.29
320	0.03	0.05	0.10	<0.01	0.02	<0.011	0.02	0.04	0.03	79.26
180	<0.011	0.08	<0.01	0.02	<0.011	<0.011	0.02	0.04	0.04	87.59
100	<0.011	0.12	0.04	<0.011	<0.011	<0.011	<0.011	0.08	0.05	65.18
56	<0.011	<0.011	<0.011	<0.011	<0.011	<0.011	<0.011	n/a	n/a	n/a
32	<0.011	<0.011	<0.011	<0.011	<0.011	<0.011	<0.011	n/a	n/a	n/a
18	<0.011	<0.011	<0.011	<0.011	<0.011	<0.011	<0.011	n/a	n/a	n/a
10	<0.011	<0.011	<0.011	<0.011	<0.011	<0.011	<0.011	n/a	n/a	n/a
1	<0.011	<0.011	0.02	<0.011	<0.011	<0.011	<0.011	n/a	n/a	n/a
PM_{10}	0.05	0.28	0.18	0.04	0.06	0.00	0.05	0.09	0.10	105.62
$PM_{0.1}$	<0.011	<0.011	0.02	<0.011	<0.011	<0.011	<0.011	0.02	n/a	n/a

Table 36. Newcastle Sb concentrations, in ngm^{-3}.

g. Sr

LC / nm	26/01/2012	02/02/2012	23/02/2012	08/03/2012	29/03/2012	10/05/2012	17/05/2012	Mean	SD	RSD
1000	0.42	0.14	0.05	0.23	0.09	0.21	0.23	0.20	0.12	61.93
560	0.02	0.05	0.02	0.02	0.02	<0.011	0.02	0.03	0.01	55.73
320	0.05	0.02	0.02	<0.011	<0.01	0.02	0.011	0.02	0.01	58.72
180	0.17	0.02	0.02	0.02	<0.01	<0.011	0.011	0.05	0.07	145.11
100	<0.011	0.09	0.02	<0.011	<0.01	0.02	<0.011	0.04	0.04	93.52
56	<0.011	0.02	0.06	<0.011	0.014	0.02	<0.011	0.03	0.02	67.04
32	<0.011	0.04	0.02	<0.011	<0.011	<0.011	<0.011	0.03	0.02	54.22
18	0.02	0.02	0.05	<0.011	<0.011	<0.011	<0.011	0.03	0.02	59.84
10	0.02	<0.011	<0.011	<0.011	<0.011	0.02	<0.011	0.02	0.00	8.37
1	0.15	0.01	0.10	<0.011	<0.011	<0.011	<0.011	0.08	0.07	81.15
PM_{10}	0.42	0.27	0.30	0.04	0.12	0.07	0.04	0.18	0.15	83.73
$PM_{0.1}$	0.18	0.09	0.22	0.00	0.014	0.03	<0.011	0.09	0.09	101.32

Table 37. Newcastle Sr concentrations, in ngm^{-3}.

h. V

LC / nm	26/01/2012	02/02/2012	23/02/2012	08/03/2012	29/03/2012	10/05/2012	17/05/2012	Mean	SD	RSD
1000	0.155	0.025	<0.022	0.139	0.033	0.029	0.188	0.095	0.074	77.89
560	<0.022	0.028	<0.022	<0.022	<0.022	<0.022	0.081	0.054	0.038	69.52
320	0.024	0.050	0.063	0.022	<0.022	<0.022	0.558	0.143	0.232	162.21
180	<0.022	0.044	<0.022	0.041	<0.022	<0.022	0.152	0.079	0.063	79.93
100	<0.022	0.027	<0.022	0.023	<0.022	<0.022	0.087	0.046	0.036	78.39
56	<0.022	<0.022	<0.022	<0.022	<0.022	<0.022	0.037	0.037	n/a	n/a
32	<0.022	<0.022	<0.022	<0.022	<0.022	<0.022	0.086	0.086	n/a	n/a
18	<0.022	<0.022	<0.022	<0.022	0.037	<0.022	0.181	0.109	0.102	93.25
10	<0.022	<0.022	<0.022	<0.022	0.027	<0.022	0.069	0.048	0.030	63.14
1	0.024	<0.022	0.042	<0.022	0.033	0.030	0.277	0.081	0.110	135.35
PM_{10}	0.048	0.149	0.104	0.086	0.130	0.030	1.528	0.296	0.545	183.83
$PM_{0.1}$	0.024	<0.022	0.042	<0.022	0.096	0.030	0.651	0.168	0.271	160.86

Table 38. Newcastle V concentrations, in ngm^{-3}.

i. Zn

LC / nm	26/01/2012	02/02/2012	23/02/2012	08/03/2012	29/03/2012	10/05/2012	17/05/2012	Mean	SD	RSD
1000	4.49	4.19	2.78	3.52	0.68	2.28	2.97	2.98	1.28	42.86
560	1.23	4.58	0.98	0.39	0.93	1.41	1.94	1.64	1.38	84.33
320	2.42	2.04	1.52	1.94	0.30	0.43	0.48	1.30	0.88	67.70
180	12.96	1.81	0.96	2.24	2.99	0.67	0.45	3.15	4.42	139.97
100	15.80	49.51	1.30	1.47	1.83	0.88	2.60	3.98	5.82	146.16
56	4.46	1.97	3.81	0.06	0.17	0.81	0.41	1.67	1.81	108.28
32	3.57	5.04	1.65	0.11	0.44	0.39	>0.022	1.87	2.01	107.96
18	3.46	3.71	1.78	>0.022	0.40	0.37	0.42	1.69	1.56	92.63
10	1.71	3.24	1.05	2.58	1.03	1.47	0.42	1.64	0.97	59.25
1	7.76	0.45	1.59	>0.022	0.35	0.18	0.27	1.77	2.98	168.70
PM10	53.37	72.35	14.64	8.79	9.12	6.61	7.00	24.55	26.86	109.40
PM0.1	20.97	14.41	9.88	2.75	2.39	3.21	1.53	7.88	7.49	95.09

Table 39. Newcastle Zn concentrations, in ngm^{-3}.

5. BROS Soluble Ions

a. Chloride

Lower Cut/nm	24-Mar	04-Apr	11-Apr	18-Apr	25-Apr	16-May	Mean
10000	0.014	0.155	0.011	0.162	0.259	0.090	0.115
5600	1.008	0.037	0.002	0.207	0.296	0.122	0.279
3200	0.701	0.019	0.015	0.281	0.548	0.141	0.284
1800	0.297	0.011	0.013	0.253	0.386	0.162	0.187
1000	0.093	0.009	0.000	0.207	0.278	0.114	0.117
560	0.077	0.002	0.015	0.096	0.108	0.114	0.069
320	0.068	0.022	0.001	0.079	0.281	0.109	0.093
180	0.008	0.016	0.001	0.089	0.081	0.065	0.043
100	0.041	0.000	0.002	0.093	0.138	0.070	0.057
56	0.000	0.022	0.000	0.090	0.127	0.064	0.051
32	0.018	0.002	0.043	0.066	0.073	0.090	0.049
18	0.000	0.021	0.000	0.081	0.067	0.164	0.055
10	0.002	0.006	0.011	0.099	0.072	0.069	0.043
1	0.005	0.000	0.001	0.083	0.333	0.071	0.082
PM_{10}	3.122	0.119	0.105	1.725	2.788	1.356	1.536
$PM_{0.1}$	0.291	0.052	0.055	0.419	0.672	0.459	0.325

Table 40. Chloride ion concentrations in μgm^{-3}.

b. Nitrate

Lower Cut/nm	24-Mar	04-Apr	11-Apr	18-Apr	25-Apr	16-May	Mean
10000	0.000	0.046	0.010	0.120	0.135	0.075	0.064
5600	0.252	0.057	0.001	0.193	0.214	0.099	0.136
3200	0.477	0.052	0.039	0.351	0.366	0.108	0.232
1800	0.452	0.078	0.052	0.336	0.429	0.148	0.249
1000	0.445	0.118	0.088	0.322	0.378	0.202	0.259
560	0.383	0.591	0.063	0.156	0.201	0.145	0.256
320	0.305	0.283	0.070	0.149	0.147	0.222	0.196
180	0.120	0.116	0.014	0.195	0.171	0.032	0.108
100	0.220	0.098	0.023	0.126	0.136	0.120	0.121
56	0.104	0.039	0.000	0.164	0.111	0.074	0.082
32	0.159	0.036	0.001	0.158	0.073	0.076	0.084
18	0.183	0.043	0.000	0.209	0.097	0.067	0.100
10	0.078	0.037	0.005	0.189	0.116	0.001	0.071
1	0.115	0.037	0.006	0.172	0.207	0.030	0.095
PM_{10}	4.101	1.584	0.362	2.723	2.647	2.072	2.248
$PM_{0.1}$	0.907	0.193	0.012	0.893	0.604	0.496	0.518

Table 41. Nitrate ion concentrations in μgm^{-3}.

c. Sulphate

Lower Cut/nm	24-Mar	04-Apr	11-Apr	18-Apr	25-Apr	16-May	Mean
10000	0.009	0.001	0.010	0.127	0.572	0.068	0.131
5600	0.044	0.074	0.028	0.154	0.383	0.074	0.126
3200	0.060	0.214	0.058	0.216	0.400	0.084	0.172
1800	0.042	0.286	0.342	0.209	0.354	0.091	0.221
1000	0.038	0.396	0.010	0.251	0.315	0.129	0.190
560	0.230	2.145	0.293	0.558	0.498	0.293	0.670
320	0.311	0.097	0.091	1.101	2.526	0.339	0.744
180	0.180	0.045	0.049	0.421	0.847	0.091	0.272
100	0.129	0.026	0.117	0.368	0.852	0.097	0.265
56	0.011	0.024	0.058	0.071	0.173	0.066	0.067
32	0.007	0.146	0.058	0.103	0.057	0.066	0.073
18	0.000	0.073	0.026	0.025	0.030	0.115	0.045
10	0.011	0.009	0.000	0.036	0.039	0.065	0.027
1	0.000	0.100	0.050	0.032	0.960	0.063	0.201
PM_{10}	1.871	3.634	1.179	3.545	7.435	1.576	3.207
$PM_{0.1}$	0.299	0.352	0.192	0.267	1.259	0.376	0.457

Table 42. Sulphate ion concentrations in μgm^{-3}.

6. Barcelona – Roadside Site

Lower cut	09/05/ 2013	13/05/ 2013	16/05/ 2013	21/05/ 2013	27/05/ 2013	03/06/ 2013	Mean	Stdev	%Stdev
18000	1.22	2.33	1.76	2.34	1.60	1.78	1.84	0.43	23.64
10000	0.81	1.12	0.73	1.74	0.64	0.91	0.99	0.40	40.53
5600	1.56	2.05	1.45	2.16	1.99	1.41	1.77	0.33	18.83
3200	2.30	3.08	2.02	3.03	2.96	2.51	2.65	0.44	16.62
1800	1.35	1.77	1.57	1.82	1.79	0.02	1.39	0.70	50.10
1000	0.61	1.00	0.69	0.84	0.74	0.79	0.78	0.14	17.47
560	0.35	0.53	0.47	0.53	0.45	0.47	0.47	0.06	13.77
320	0.38	0.43	0.35	0.48	0.45	0.47	0.43	0.05	12.14
180	0.20	0.24	0.19	0.20	0.21	0.23	0.21	0.02	8.84
56	0.25	0.44	0.28	0.29	0.36	0.28	0.32	0.07	21.97
1	0.23	0.29	0.19	0.24	0.30	0.19	0.24	0.05	19.67
PM_{10}	7.22	9.82	7.21	9.59	9.26	6.37	8.25	1.48	17.97
$PM_{0.18}$	0.48	0.73	0.47	0.53	0.66	0.48	0.56	0.11	20.12

Table 43. Ba concentrations in ng m^{-3}, Roadside site.

Lower cut	09/05/ 2013	13/05/ 2013	16/05/ 2013	21/05/ 2013	27/05/ 2013	03/06/ 2013	Mean	Stdev	%Stdev
18000	2.71	5.58	4.03	4.05	3.47	3.24	3.85	0.99	25.67
10000	1.51	1.63	1.46	2.72	1.29	1.67	1.71	0.51	29.87
5600	3.02	4.23	3.16	4.37	4.13	3.16	3.68	0.63	17.03
3200	5.23	6.69	4.51	6.50	6.89	5.52	5.89	0.95	16.09
1800	2.92	4.09	3.48	4.18	4.27	0.18	3.19	1.56	49.03
1000	1.44	2.41	1.54	1.93	2.01	1.73	1.84	0.36	19.28
560	0.96	1.45	1.12	1.43	1.40	1.10	1.24	0.21	16.84
320	1.04	1.59	1.05	1.66	1.33	1.48	1.36	0.27	19.69
180	0.81	1.13	0.86	0.84	1.14	0.75	0.92	0.17	18.39
56	1.15	1.64	1.18	1.46	1.91	1.10	1.41	0.32	22.91
1	0.86	0.97	0.48	0.54	1.08	0.83	0.79	0.24	29.78
PM_{10}	17.43	24.20	17.39	22.91	24.17	15.86	20.33	3.83	18.85
$PM_{0.18}$	2.01	2.60	1.67	2.00	2.99	1.94	2.20	0.49	22.43

Table 44. Cu concentrations in ng m^{-3}, Roadside site.

Lower cut	09/05/ 2013	13/05/ 2013	16/05/ 2013	21/05/ 2013	27/05/ 2013	03/06/ 2013	Mean	Stdev	%Stdev
18000	64.06	91.50	97.44	83.06	68.88	80.03	80.83	12.80	15.84
10000	35.98	34.19	39.94	58.29	24.65	37.98	38.51	11.05	28.71
5600	83.29	105.16	99.65	92.25	94.01	65.77	90.02	13.97	15.52
3200	155.99	188.46	144.59	134.45	140.59	116.86	146.82	24.14	16.44
1800	97.39	112.70	119.22	81.23	80.21	0.73	81.91	42.83	52.29
1000	40.88	62.73	44.78	35.53	30.37	32.55	41.14	11.84	28.78
560	23.29	33.21	24.54	24.44	17.42	19.13	23.67	5.52	23.30
320	21.79	49.79	24.19	24.09	19.09	20.94	26.65	11.50	43.17
180	12.25	14.24	10.27	9.77	7.98	9.22	10.62	2.26	21.30
56	11.34	22.16	10.65	11.70	13.86	8.90	13.10	4.72	36.02
1	14.60	18.34	10.21	10.30	10.75	6.95	11.86	4.00	33.74
PM_{10}	460.83	606.80	488.09	423.77	414.28	281.04	445.80	106.36	23.86
$PM_{0.18}$	25.94	40.50	20.86	22.00	24.61	15.85	24.96	8.38	33.58

Table 45. Fe concentrations in ng m^{-3}, Roadside site.

Lower cut	09/05/ 2013	13/05/ 2013	16/05/ 2013	21/05/ 2013	27/05/ 2013	03/06/ 2013	Mean	Stdev	%Stdev
18000	0.25	0.40	0.33	0.35	0.33	0.34	0.33	0.05	13.84
10000	0.14	0.12	0.12	0.21	0.10	0.15	0.14	0.04	31.24
5600	0.34	0.44	0.37	0.46	0.47	0.34	0.40	0.06	14.74
3200	0.63	0.72	0.51	0.68	0.79	0.63	0.66	0.10	15.82
1800	0.35	0.39	0.38	0.41	0.44	0.00	0.33	0.18	55.45
1000	0.16	0.23	0.15	0.20	0.16	0.20	0.18	0.03	17.66
560	0.09	0.12	0.09	0.12	0.10	0.13	0.11	0.02	16.27
320	0.11	0.19	0.12	0.13	0.13	0.28	0.16	0.07	41.41
180	0.09	0.15	0.06	0.08	0.06	0.21	0.11	0.06	59.71
56	0.00	0.20	0.06	0.12	0.07	0.28	0.12	0.09	76.99
1	0.00	0.06	0.04	0.06	0.06	0.11	0.06	0.03	45.24
PM_{10}	1.77	2.50	1.78	2.27	2.29	2.17	2.13	0.29	13.73
$PM_{0.18}$	0.00	0.26	0.10	0.18	0.14	0.39	0.18	0.14	75.96

Table 46. Sb concentrations in ng m^{-3}, Roadside site.

Lower cut	09/05/ 2013	13/05/ 2013	16/05/ 2013	21/05/ 2013	27/05/ 2013	03/06/ 2013	Mean	Stdev	%Stdev
18000	0.28	0.58	0.43	0.51	0.33	0.20	0.39	0.14	36.84
10000	0.16	0.24	0.07	0.35	0.20	0.20	0.20	0.10	50.94
5600	0.37	0.57	0.33	0.45	0.55	0.39	0.44	0.10	23.55
3200	0.71	1.00	0.65	0.64	0.99	0.43	0.74	0.25	33.56
1800	0.49	0.32	0.51	0.64	0.72	0.00	0.45	0.29	64.07
1000	0.21	0.36	0.05	0.23	0.22	0.29	0.23	0.11	50.43
560	0.16	0.26	0.16	0.22	0.21	0.20	0.20	0.04	17.75
320	0.32	0.36	0.27	0.24	0.29	0.39	0.31	0.06	20.54
180	0.25	0.28	0.19	0.16	0.16	0.31	0.23	0.07	30.60
56	0.12	0.45	0.28	0.22	0.31	0.46	0.31	0.11	34.58
1	0.07	0.25	0.17	0.17	0.20	0.33	0.20	0.07	34.03
PM_{10}	2.70	3.84	2.60	2.97	3.67	2.80	3.10	0.53	16.99
$PM_{0.18}$	0.19	0.69	0.44	0.39	0.52	0.79	0.50	0.22	42.76

Table 47. Roadside Sn concentrations in ng m^{-3}.

Lower cut	09/05/ 2013	13/05/ 2013	16/05/ 2013	21/05/ 2013	27/05/ 2013	03/06/ 2013	Mean	Stdev	%Stdev
18000	0.10	0.16	0.13	0.12	0.11	0.49	0.18	0.15	83.05
10000	0.05	0.04	0.04	0.08	0.04	0.23	0.08	0.08	103.68
5600	0.11	0.14	0.12	0.14	0.14	0.20	0.14	0.03	22.56
3200	0.20	0.24	0.17	0.21	0.25	0.26	0.22	0.04	16.40
1800	0.13	0.14	0.13	0.14	0.15	0.07	0.13	0.03	26.61
1000	0.06	0.08	0.05	0.07	0.06	0.11	0.07	0.02	31.48
560	0.04	0.05	0.03	0.06	0.04	0.08	0.05	0.02	33.16
320	0.05	0.24	0.04	0.07	0.07	0.10	0.09	0.08	83.91
180	0.04	0.06	0.03	0.05	0.04	0.08	0.05	0.02	35.67
56	0.00	0.08	0.03	0.04	0.04	0.10	0.05	0.03	61.78
1	0.00	0.04	0.03	0.03	0.03	0.03	0.03	0.01	21.95
PM_{10}	0.62	1.09	0.62	0.82	0.82	1.01	0.83	0.20	23.55
$PM_{0.18}$	0.00	0.13	0.06	0.07	0.08	0.13	0.08	0.05	62.61

Table 48. Roadside Mo concentrations in ng m^{-3}.

Lower cut	09/05/ 2013	13/05/ 2013	16/05/ 2013	21/05/ 2013	27/05/ 2013	03/06/ 2013	Mean	Stdev	%Stdev
18000	1.96	7.36	3.58	3.34	3.26	3.20	3.78	1.84	48.71
10000	1.75	2.19	1.40	3.03	1.90	2.01	2.05	0.55	26.95
5600	2.13	3.08	1.97	3.04	2.96	2.58	2.63	0.48	18.35
3200	2.99	5.77	3.66	3.66	3.99	4.79	4.14	0.99	23.82
1800	3.08	7.14	4.35	3.56	4.60	0.47	3.87	2.18	56.36
1000	4.60	12.03	7.48	6.64	7.59	9.82	8.03	2.58	32.20
560	1.88	4.53	2.84	5.00	2.65	2.79	3.28	1.21	36.85
320	2.01	4.70	3.54	3.67	4.81	3.68	3.73	1.01	27.09
180	1.89	2.94	2.25	2.19	3.03	2.30	2.43	0.45	18.54
56	2.04	4.23	2.77	3.06	3.86	2.39	3.06	0.85	27.65
1	1.04	1.38	0.86	1.35	5.86	1.21	1.95	1.93	98.83
PM_{10}	21.68	45.81	29.71	32.17	39.35	30.03	33.12	8.40	25.36
$PM_{0.18}$	3.08	5.61	3.62	4.40	9.72	3.60	5.01	2.47	49.34

Table 49. Roadside Zn concentrations in ng m^{-3}.

Lower cut	09/05/ 2013	13/05/ 2013	16/05/ 2013	21/05/ 2013	27/05/ 2013	03/06/ 2013	Mean	Stdev	%Stdev
nm									
18000	25.65	40.54	19.01	25.67	21.73	16.75	24.89	8.45	33.95
10000	8.62	32.38	4.95	20.18	7.55	8.00	13.61	10.62	77.99
5600	22.62	26.65	10.62	17.47	17.09	10.27	17.45	6.48	37.11
3200	49.25	32.04	20.99	27.05	33.63	21.12	30.68	10.52	34.30
1800	32.85	22.54	15.75	21.07	22.09	0.49	19.13	10.69	55.87
1000	16.79	11.89	8.09	10.25	10.38	7.69	10.85	3.30	30.44
560	2.63	3.51	1.79	3.62	3.05	2.04	2.77	0.76	27.26
320	2.08	3.31	1.72	2.68	8.08	2.09	3.33	2.40	71.96
180	1.65	2.50	1.57	2.80	2.52	1.47	2.08	0.58	28.02
56	3.13	6.72	2.02	3.94	4.63	2.17	3.77	1.76	46.78
	1.97	2.75	1.67	2.38	4.55	1.48	2.47	1.12	45.39
PM_{10}	132.97	111.91	64.22	91.26	106.02	48.83	92.54	31.32	33.85
$PM_{0.18}$	5.10	9.47	3.68	6.32	9.17	3.65	6.23	2.59	41.58

Table 50. Roadside Mg concentrations, ngm^{-3}.

Lower cut	09/05/ 2013	13/05/ 2013	16/05/ 2013	21/05/ 2013	27/05/ 2013	03/06/ 2013	Mean	Stdev	%Stdev
nm									
18000	154.09	298.13	132.97	85.76	136.69	47.55	142.53	85.69	60.12
10000	43.01	22.37	25.46	33.06	37.82	23.45	30.86	8.45	27.38
5600	135.46	62.53	67.00	82.72	96.37	44.12	81.37	31.94	39.26
3200	373.01	176.34	163.47	172.41	229.21	126.62	206.84	87.80	42.45
1800	259.80	159.28	123.96	169.61	161.90	9.64	147.36	81.25	55.13
1000	137.18	78.00	66.97	71.02	87.36	58.80	83.22	28.16	33.84
560	30.12	21.79	15.99	26.23	34.13	20.05	24.72	6.73	27.24
320	22.68	32.27	25.76	31.47	42.02	22.00	29.37	7.55	25.71
180	16.30	21.00	14.57	18.58	39.25	21.19	21.82	8.93	40.92
56	47.42	37.65	28.00	49.68	61.94	33.78	43.08	12.34	28.65
	7.20	8.67	21.11	9.30	30.25	12.49	14.84	9.05	61.00
PM_{10}	1029.17	597.52	526.82	631.02	782.45	348.69	652.61	232.53	35.63
$PM_{0.18}$	54.62	46.31	49.11	58.98	92.19	46.28	57.91	17.52	30.25

Table 51. Roadside Na concentrations, ngm^{-3}.

Lower cut	09/05/ 2013	13/05/ 2013	16/05/ 2013	21/05/ 2013	27/05/ 2013	03/06/ 2013	Mean	Stdev	%Stdev
18000	52.86	229.43	33.73	124.12	38.20	58.67	89.50	75.91	84.82
10000	30.81	325.96	14.81	158.37	27.62	35.27	98.81	123.23	124.72
5600	55.84	179.93	15.75	80.33	36.38	27.37	65.93	60.31	91.46
3200	28.75	98.08	14.18	47.48	35.59	30.66	42.46	29.30	69.02
1800	21.09	52.81	11.72	27.43	28.94	1.45	23.91	17.52	73.27
1000	15.97	39.75	10.04	21.24	22.22	10.72	19.99	10.94	54.71
560	14.35	31.56	9.58	21.00	17.63	9.02	17.19	8.42	48.95
320	11.86	31.41	6.77	16.76	19.66	8.69	15.86	9.02	56.89
180	12.99	34.94	6.14	16.84	18.65	10.00	16.59	10.07	60.67
56	31.74	74.71	13.27	42.42	36.49	13.66	35.38	22.68	64.10
	39.44	33.03	8.57	19.42	52.42	8.95	26.97	17.66	65.49
PM_{10}	232.03	576.23	96.02	292.92	267.97	120.52	264.28	172.14	65.14
$PM_{0.18}$	71.18	107.74	21.84	61.84	88.90	22.61	62.36	34.83	55.85

Table 52. Roadside Al concentrations, ngm^{-3}.

Lower cut	09/05/ 2013	13/05/ 2013	16/05/ 2013	21/05/ 2013	27/05/ 2013	03/06/ 2013	Mean	Stdev	%Stdev
nm									
18000	101.82	198.79	86.20	126.59	121.05	117.19	125.27	38.90	31.05
10000	66.25	83.07	45.59	115.35	76.74	67.06	75.68	23.23	30.70
5600	71.64	128.75	52.55	108.10	109.32	77.52	91.31	28.59	31.31
3200	82.35	130.09	62.18	107.19	115.61	102.34	99.96	24.28	24.29
1800	55.69	86.63	45.47	64.00	84.10	8.92	57.47	28.66	49.87
1000	42.08	71.64	30.29	49.43	54.99	30.89	46.55	15.74	33.81
560	35.33	61.10	19.66	50.48	39.45	18.55	37.43	16.80	44.89
320	28.75	63.07	19.84	37.23	65.90	23.62	39.74	20.06	50.48
180	34.77	69.73	19.04	45.10	51.98	28.68	41.55	18.07	43.50
56	65.41	127.52	33.04	98.67	82.17	31.89	73.12	37.58	51.39
1	32.45	55.42	19.80	33.71	95.31	15.99	42.11	29.50	70.05
PM_{10}	448.48	793.94	301.86	593.91	698.82	338.40	529.24	198.82	37.57
$PM_{0.18}$	97.87	182.94	52.84	132.38	177.48	47.88	115.23	59.13	51.32

Table 53. Roadside Ca concentrations, ngm^{-3}.

7. Barcelona – Background Site

Lower Cut/ nm	09/05/ 2013	13/05/ 2013	16/05/ 2013	21/05/ 2013	27/05/ 2013	05/06/ 2013	11/06/ 2013	18/06/ 2013	Mean	St dev	%St dev
21500	0.71	0.82	0.65	0.19	0.86	0.75	0.97	0.77	0.72	0.23	32.66
12000	0.43	0.58	0.58	0.29	0.65	0.28	0.42	0.57	0.48	0.14	29.69
6700	0.55	0.67	0.67	0.27	0.77	0.61	0.83	0.69	0.63	0.17	26.65
3800	0.92	1.03	0.74	0.31	0.07	1.06	1.28	1.06	0.81	0.42	51.74
2200	0.16	0.82	0.55	0.56	0.60	0.74	0.76	0.70	0.61	0.21	33.82
1200	0.12	0.55	0.45	0.46	0.44	0.42	0.54	0.83	0.48	0.19	40.90
670	0.25	0.34	0.53	0.53	0.34	0.41	0.68	3.23	0.79	1.00	126.31
380	0.29	0.27	0.23	0.31	0.24	0.18	0.15	0.36	0.25	0.07	26.44
220	0.39	0.23	0.20	0.38	0.18	0.15	0.14	0.65	0.29	0.17	59.92
1	0.79	0.94	0.97	0.72	0.88	0.63	0.78	0.82	0.82	0.11	13.83

Table 54. Ba concentrations in ng m^{-3}, Background site.

Lower Cut/ nm	09/05/ 2013	13/05/ 2013	16/05/ 2013	21/05/ 2013	27/05/ 2013	05/06/ 2013	11/06/ 2013	18/06/ 2013	Mean	Stdev	%Stdev
21500	1.42	1.68	1.45	0.98	1.79	1.24	1.48	1.02	1.38	0.29	21.14
12000	0.79	1.01	0.75	0.99	1.08	0.54	0.74	0.90	0.85	0.18	20.92
6700	0.97	1.77	1.50	1.18	1.68	1.24	1.45	1.04	1.36	0.29	21.59
3800	1.99	2.55	2.01	1.04	0.21	2.13	2.33	1.66	1.74	0.77	44.07
2200	0.41	2.16	1.55	1.32	1.70	1.53	1.59	1.21	1.43	0.50	35.05
1200	0.57	1.72	1.49	1.28	1.24	1.16	1.16	1.01	1.20	0.34	28.11
670	1.22	1.79	1.79	1.06	1.60	1.24	1.65	1.52	1.48	0.28	18.66
380	0.72	0.94	1.02	0.91	1.04	0.59	0.47	0.49	0.77	0.23	30.27
220	1.20	1.03	0.74	1.04	0.98	0.42	0.49	0.62	0.82	0.29	35.00
1	2.66	5.30	11.03	7.27	4.45	2.59	2.50	3.51	4.91	2.97	60.39

Table 55. Cu concentrations in ng m^{-3}, Background site.

Lower Cut/ nm	09/05/ 2013	13/05/ 2013	16/05/ 2013	21/05/ 2013	27/05/ 2013	05/06/ 2013	11/06/ 2013	18/06/ 2013	Mean	Stdev	%Stdev
21500	35.35	40.06	23.81	4.98	43.84	37.90	48.48	33.09	33.44	13.65	40.83
12000	16.72	22.60	12.38	9.89	38.31	11.75	19.13	31.60	20.30	10.11	49.81
6700	23.71	30.96	25.90	11.36	43.07	38.63	40.48	34.65	31.10	10.50	33.77
3800	38.99	48.85	33.23	11.26	0.77	50.00	61.30	42.88	35.91	20.42	56.86
2200	6.60	39.76	24.11	17.01	28.82	32.21	33.91	25.79	26.02	10.42	40.02
1200	4.88	25.86	17.13	18.92	15.92	17.50	23.99	18.77	17.87	6.28	35.16
670	25.46	32.17	22.66	22.24	17.16	19.79	29.05	12.01	22.57	6.45	28.58
380	10.57	8.92	8.14	11.38	8.61	6.49	6.11	5.75	8.24	2.06	24.99
220	15.77	8.65	9.47	14.88	6.41	4.21	5.30	4.88	8.70	4.48	51.49
1	38.69	47.68	45.46	32.93	40.70	29.54	34.59	30.25	37.48	6.80	18.15

Table 56. Fe concentrations in ng m^{-3}, Background site.

Lower Cut/ nm	09/05/ 2013	13/05/ 2013	16/05/ 2013	21/05/ 2013	27/05/ 2013	05/06/ 2013	11/06/ 2013	18/06/ 2013	Mean	Stdev	%Stdev
21500	0.09	0.16	0.06	0.05	0.14	0.13	0.23	0.10	0.12	0.06	48.40
12000	0.04	0.09	0.00	0.06	0.08	0.05	0.09	0.06	0.06	0.03	51.29
6700	0.07	0.07	0.08	0.04	0.14	0.13	0.21	0.09	0.10	0.05	51.50
3800	0.17	0.18	0.15	0.00	0.00	0.24	0.25	0.14	0.14	0.10	67.68
2200	0.03	0.13	0.08	0.00	0.11	0.15	0.27	0.09	0.11	0.08	75.84
1200	0.00	0.09	0.06	0.00	0.08	0.10	0.19	0.07	0.07	0.06	82.99
670	0.19	0.12	0.12	0.00	0.10	0.29	0.54	0.10	0.18	0.17	91.73
380	0.00	0.00	0.00	0.00	0.05	0.03	0.09	0.02	0.02	0.03	135.16
220	0.09	0.00	0.06	0.00	0.04	0.04	0.12	0.03	0.05	0.04	88.94
1	0.24	0.22	0.39	0.22	0.27	0.28	0.72	0.18	0.31	0.17	55.17

Table 57. Sb concentrations in ng m^{-3}, Background site.

Lower Cut	09/05/ 2013	13/05/ 2013	16/05/ 2013	21/05/ 2013	27/05/ 2013	05/06/ 2013	11/06/ 2013	18/06/ 2013	Mean	Stdev	%Stdev
21500	0.09	0.18	0.23	0.09	0.21	0.05	0.11	0.07	0.13	0.07	54.24
12000	0.08	0.23	0.05	0.05	0.02	-0.03	0.03	0.17	0.07	0.09	116.19
6700	0.05	0.25	0.00	0.15	0.36	0.10	0.16	0.10	0.15	0.11	77.54
3800	0.09	0.19	0.08	0.15	-0.02	0.20	0.22	0.15	0.13	0.08	57.97
2200	-0.08	0.11	-0.10	0.21	0.20	0.13	0.19	0.06	0.09	0.12	136.40
1200	0.17	0.25	0.17	0.17	0.13	0.04	0.18	0.15	0.16	0.06	37.00
670	1.22	0.78	0.50	0.00	0.86	1.82	2.94	1.20	1.17	0.90	76.91
380	-0.05	0.18	0.05	0.05	0.05	0.03	0.10	-0.01	0.05	0.07	141.14
220	0.14	0.05	0.10	0.12	0.18	0.17	0.25	0.11	0.14	0.06	42.14
1	1.94	0.94	2.42	1.37	1.76	2.07	2.32	1.20	1.75	0.54	30.70

Table 58. V concentrations in ng m^{-3}, Background site.

Lower Cut	09/05/ 2013	13/05/ 2013	16/05/ 2013	21/05/ 2013	27/05/ 2013	05/06/ 2013	11/06/ 2013	18/06/ 2013	Mean	Stdev	%Stdev
21500	38.92	25.98	28.15	33.07	29.86	16.38	17.49	26.68	27.07	7.49	27.67
12000	18.17	19.60	20.28	19.95	19.26	10.89	8.66	11.28	16.01	4.85	30.28
6700	25.17	25.06	22.17	60.86	27.43	12.98	15.85	18.20	25.96	14.96	57.62
3800	66.57	49.61	39.85	29.53	0.98	26.97	33.81	47.06	36.80	19.30	52.44
2200	11.14	45.18	33.30	23.52	36.40	27.33	30.20	39.90	30.87	10.55	34.17
1200	19.18	57.99	32.92	23.13	35.67	26.82	32.32	37.81	33.23	11.84	35.63
670	169.17	255.76	152.33	25.05	125.36	200.30	264.89	176.47	171.17	76.18	44.51
380	14.06	17.55	18.63	30.86	17.34	13.25	12.07	13.81	17.20	6.00	34.90
220	46.30	31.96	35.14	22.43	25.96	31.23	31.98	32.54	32.19	7.00	21.75
1	129.15	111.84	197.83	200.34	103.38	108.65	132.62	129.65	139.18	38.50	27.66

Table 59. S concentrations in ng m^{-3}, Background site.

Lower Cut	09/05/ 2013	13/05/ 2013	16/05/ 2013	21/05/ 2013	27/05/ 2013	05/06/ 2013	11/06/ 2013	18/06/ 2013	Mean	Stdev	%Stdev
21500	265.27	61.41	118.38	44.23	141.52	60.81	56.47	159.48	113.45	75.12	66.21
12000	39.61	29.05	33.57	24.11	31.03	19.61	13.38	28.04	27.30	8.21	30.07
6700	126.82	60.65	75.12	49.03	95.60	45.42	48.07	90.16	73.86	28.81	39.00
3800	563.19	234.14	227.40	95.02	8.07	148.22	225.44	340.52	230.25	167.94	72.94
2200	83.08	197.27	201.17	96.41	208.09	125.66	192.26	275.70	172.45	65.16	37.78
1200	13.34	153.85	156.16	70.95	139.76	84.19	132.06	186.41	117.09	56.57	48.31
670	66.84	42.31	55.10	50.57	48.81	33.04	35.80	44.60	47.13	10.84	23.01
380	19.46	24.34	23.17	41.90	18.22	13.17	8.76	16.90	20.74	9.93	47.88
220	234.33	35.59	39.42	39.88	20.86	15.20	9.18	12.65	50.89	75.13	147.65
1	21.87	26.32	35.29	43.95	26.44	20.93	15.19	26.07	27.01	8.95	33.13

Table 60. Na concentrations in ng m^{-3}, Background site.

Lower Cut	09/05/ 2013	13/05/ 2013	16/05/ 2013	21/05/ 2013	27/05/ 2013	05/06/ 2013	11/06/ 2013	18/06/ 2013	Mean	Stdev	%Stdev
21500	39.34	13.12	26.65	3.20	26.32	17.15	17.57	27.31	20.48	11.55	56.39
12000	12.40	6.88	20.17	3.61	12.21	5.92	5.98	10.51	9.60	5.72	59.61
6700	20.17	9.98	16.96	6.83	18.23	9.91	13.88	17.43	13.71	4.97	36.29
3800	68.94	30.82	29.71	11.19	1.40	23.51	34.81	46.52	28.63	21.37	74.66
2200	9.98	25.04	24.39	12.57	27.05	17.11	25.98	34.36	20.31	6.99	34.45
1200	1.38	19.09	19.13	11.10	16.24	10.54	17.31	20.78	13.54	6.41	47.31
670	6.35	4.18	7.64	9.32	4.66	3.60	4.88	8.66	5.80	2.07	35.65
380	2.09	2.23	3.04	9.27	2.41	2.02	1.21	2.28	3.18	2.74	86.06
220	29.42	2.22	3.88	8.96	1.83	1.91	1.04	2.43	7.04	10.23	145.32
1	6.45	6.03	8.84	8.91	8.56	4.11	5.31	4.03	6.89	1.91	27.73

Table 61. Mg concentrations in ng m^{-3}, Background site.

Lower Cut	09/05/ 2013	13/05/ 2013	16/05/ 2013	21/05/ 2013	27/05/ 2013	05/06/ 2013	11/06/ 2013	18/06/ 2013	Mean	Stdev	%Stdev
21500	59.76	27.90	136.34	20.70	51.84	90.49	44.13	46.38	59.69	37.48	62.80
12000	72.21	22.08	236.26	21.47	42.78	45.16	20.98	43.73	63.08	72.08	114.26
6700	42.14	23.86	107.97	20.92	39.09	39.85	36.94	40.35	43.89	27.09	61.73
3800	33.49	27.05	54.95	25.24	5.66	45.65	39.46	41.06	34.07	15.04	44.14
2200	5.11	20.72	31.81	22.82	22.46	29.06	22.40	34.80	23.65	9.07	38.37
1200	7.85	23.68	32.72	25.71	19.96	36.87	12.13	21.91	22.60	9.65	42.69
670	12.91	13.08	25.01	32.56	19.03	21.81	10.46	19.31	19.27	7.29	37.85
380	8.86	11.59	19.67	23.80	13.24	17.47	5.67	23.19	15.44	6.66	43.12
220	17.21	11.61	18.73	23.71	10.58	19.91	5.27	19.56	15.82	6.09	38.51
1	182.46	40.36	213.70	103.28	50.57	30.20	22.60	23.00	83.27	75.87	91.11

Table 62. Al concentrations in ng m^{-3}, Background site.

Lower Cut	09/05/ 2013	13/05/ 2013	16/05/ 2013	21/05/ 2013	27/05/ 2013	05/06/ 2013	11/06/ 2013	18/06/ 2013	Mean	Stdev	%Stdev
21500	94.69	107.69	124.83	58.41	187.38	139.67	123.31	121.30	119.66	36.93	30.86
12000	52.95	63.98	77.89	64.59	130.09	70.13	48.56	84.50	74.09	25.54	34.47
6700	59.37	78.80	75.02	68.38	133.06	91.82	95.57	93.28	86.91	22.61	26.01
3800	88.77	103.23	92.18	58.17	43.90	124.00	124.29	108.09	92.83	29.07	31.31
2200	17.42	68.47	72.43	64.47	89.82	77.22	69.93	80.43	67.52	21.74	32.20
1200	20.06	47.15	65.15	82.05	45.60	53.40	36.51	47.50	49.68	18.44	37.11
670	26.67	27.08	64.56	110.73	57.24	47.17	28.14	32.59	49.27	28.80	58.45
380	28.66	32.49	55.24	76.17	42.09	33.53	21.69	47.10	42.12	17.41	41.33
220	40.19	27.93	54.40	83.88	49.72	40.14	28.75	33.62	44.83	18.34	40.90
1	40.77	47.36	76.27	71.39	92.56	46.02	41.47	36.96	56.60	20.57	36.34

Table 63. Ca concentrations in ng m^{-3}, Background site.

Lower Cut	09/05/ 2013	13/05/ 2013	16/05/ 2013	21/05/ 2013	27/05/ 2013	05/06/ 2013	11/06/ 2013	18/06/ 2013	Mean	Stdev	%Stdev
21500	0.71	0.27	0.05	0.29	0.39	0.36	0.55	0.14	0.35	0.21	61.69
12000	0.18	0.23	0.17	0.07	0.21	0.12	0.23	0.79	0.25	0.23	90.59
6700	0.17	0.11	0.08	0.50	0.51	1.37	0.23	0.83	0.47	0.44	93.14
3800	0.28	0.12	0.20	0.09	0.02	0.27	0.25	0.29	0.19	0.10	53.96
2200	0.17	0.50	0.22	0.00	0.42	0.12	0.10	0.36	0.24	0.17	73.91
1200	0.22	0.21	0.07	0.02	0.03	0.26	0.32	0.52	0.21	0.17	82.08
670	2.09	2.46	1.25	0.07	0.85	1.15	2.05	0.75	1.34	0.81	60.66
380	0.51	0.21	0.08	0.00	0.16	0.16	0.14	0.16	0.18	0.15	83.62
220	0.32	0.28	0.45	0.15	0.33	0.17	0.30	0.23	0.28	0.10	34.08
1	1.37	1.06	1.29	0.63	1.14	1.14	1.46	0.70	1.10	0.30	27.15

Table 64. Ni concentrations in ng m^{-3}, Background site.

APPENDIX C - CORRELATION TABLES FOR MASS CONCENTRATION DATA.

1. Concurrent Bristol Rd/Elms Rd samples.

	BR S5	BR S6	BR S7	BR S8	BR S9	BR S10	BR S11	BR S12	BR S13	BR PM_{10}	BR $PM_{0.1}$
ER S5	0.61	0.05	0.03	0.00	0.41	0.03	0.23	0.02	0.00	0.64	0.02
ER S6	0.29	0.77	0.00	0.22	0.27	0.70	0.40	0.43	0.49	0.70	0.80
ER S7	0.46	0.53	0.02	0.05	0.05	0.46	0.37	0.49	0.19	0.44	0.46
ER S8	0.23	0.07	0.00	0.02	0.01	0.20	0.62	0.35	0.00	0.19	0.14
ER S9	0.22	0.00	0.02	0.54	0.02	0.00	0.07	0.00	0.00	0.09	0.04
ER S10	0.15	0.00	0.29	0.04	0.35	0.00	0.00	0.02	0.00	0.41	0.00
ER S11	0.00	0.06	0.33	0.00	0.06	0.03	0.05	0.27	0.02	0.07	0.08
ER S12	0.01	0.02	0.01	0.00	0.19	0.02	0.04	0.01	0.00	0.05	0.01
ER S13	0.00	0.02	0.26	0.02	0.17	0.00	0.15	0.22	0.05	0.09	0.01
ER PM_{10}	0.29	0.33	0.00	0.31	0.22	0.36	0.69	0.29	0.10	0.53	0.44
ER $PM_{0.1}$	0.02	0.01	0.17	0.01	0.16	0.00	0.04	0.02	0.00	0.13	0.01

Table 1. Correlation Coefficients (R^2 values) for concurrent Bristol Rd/Elms Rd mass concentration data.

2. Bristol Road Correlations, NanoMOUDI data.

	S5	S6	S7	S8	S9	S10	S11	S12	S13	PM_{10}	$PM_{0.1}$	Soot (32-180)	Nuc (0-32)	AURN PM_{10}	AURN NO_x	AURN T
S5	1.00	0.00	0.08	0.12	0.17	0.01	0.06	0.02	0.00	0.60	0.02	0.19	0.02	0.06	0.04	0.21
S6	0.00	1.00	0.01	0.19	0.03	0.01	0.03	0.02	0.01	0.10	0.02	0.04	0.03	0.24	0.03	0.02
S7	0.08	0.01	1.00	0.15	0.12	0.00	0.04	0.02	0.04	0.27	0.01	0.11	0.02	0.00	0.23	0.00
S8	0.12	0.19	0.15	1.00	0.38	0.06	0.22	0.19	0.19	0.37	0.18	0.50	0.20	0.03	0.01	0.02
S9	0.17	0.03	0.12	0.38	1.00	0.00	0.02	0.03	0.04	0.34	0.01	0.71	0.04	0.08	0.00	0.07
S10	0.01	0.01	0.00	0.06	0.00	1.00	0.57	0.67	0.45	0.08	0.86	0.22	0.68	0.01	0.01	0.01
S11	0.06	0.03	0.04	0.22	0.02	0.57	1.00	0.67	0.39	0.28	0.73	0.36	0.58	0.00	0.03	0.09
S12	0.02	0.02	0.02	0.19	0.03	0.67	0.67	1.00	0.45	0.11	0.85	0.37	0.84	0.04	0.05	0.06
S13	0.00	0.01	0.04	0.19	0.04	0.45	0.39	0.45	1.00	0.07	0.67	0.29	0.75	0.01	0.01	0.15
PM_{10}	0.60	0.10	0.27	0.37	0.34	0.08	0.28	0.11	0.07	1.00	0.14	0.48	0.12	0.16	0.04	0.04
$PM_{0.1}$	0.02	0.02	0.01	0.18	0.01	0.86	0.73	0.85	0.67	0.14	1.00	0.37	0.93	0.01	0.03	0.05
Soot (32-180)	0.19	0.04	0.11	0.50	0.71	0.22	0.36	0.37	0.29	0.48	0.37	1.00	0.39	0.03	0.01	0.02
Nuc (0-32)	0.02	0.03	0.02	0.20	0.04	0.68	0.58	0.84	0.75	0.12	0.93	0.39	1.00	0.01	0.04	0.06
AURN PM_{10}	0.06	0.24	0.00	0.03	0.08	0.01	0.00	0.04	0.01	0.16	0.01	0.03	0.01	1.00	0.27	0.16
AURN NO_x	0.04	0.03	0.23	0.01	0.00	0.01	0.03	0.05	0.01	0.04	0.03	0.01	0.04	0.27	1.00	0.03
AURN T	0.21	0.02	0.00	0.02	0.07	0.01	0.09	0.06	0.15	0.04	0.05	0.02	0.06	0.16	0.03	1.00

Table 2. Correlation Matrix, nanoMOUDI mass concentrations and AURN data, Bristol Road (Birmingham Roadside Site).

3. Elms Road Correlations, NanoMOUDI data

	S5	S6	S7	S8	S9	S10	S11	S12	S13	PM_{10}	$PM_{0.1}$	Soot (32-180)	Nuc (0-32)	AURN PM_{10}	AURN NO_x	AURN T
S5	1.00	0.23	0.16	0.19	0.78	0.61	0.03	0.14	0.06	0.67	0.30	0.75	0.13	0.30	0.04	0.12
S6	0.23	1.00	0.71	0.35	0.23	0.05	0.20	0.00	0.00	0.72	0.00	0.18	0.00	0.88	0.14	0.02
S7	0.16	0.71	1.00	0.59	0.08	0.00	0.21	0.11	0.16	0.65	0.08	0.03	0.13	0.73	0.03	0.02
S8	0.19	0.35	0.59	1.00	0.10	0.00	0.40	0.05	0.16	0.59	0.04	0.06	0.08	0.53	0.02	0.10
S9	0.78	0.23	0.08	0.10	1.00	0.64	0.00	0.42	0.24	0.54	0.47	0.83	0.40	0.23	0.00	0.11
S10	0.61	0.05	0.00	0.00	0.64	1.00	0.02	0.42	0.51	0.22	0.75	0.90	0.49	0.03	0.06	0.00
S11	0.03	0.20	0.21	0.40	0.00	0.02	1.00	0.01	0.01	0.23	0.01	0.08	0.01	0.15	0.04	0.02
S12	0.14	0.00	0.11	0.05	0.42	0.42	0.01	1.00	0.59	0.02	0.83	0.41	0.97	0.01	0.02	0.00
S13	0.06	0.00	0.16	0.16	0.24	0.51	0.01	0.59	1.00	0.00	0.63	0.37	0.75	0.04	0.00	0.19
PM_{10}	0.67	0.72	0.65	0.59	0.54	0.22	0.23	0.02	0.00	1.00	0.06	0.47	0.01	0.78	0.01	0.09
$PM_{0.1}$	0.30	0.00	0.08	0.04	0.47	0.75	0.01	0.83	0.63	0.06	1.00	0.66	0.85	0.00	0.12	0.00
Soot (32-180)	0.75	0.18	0.03	0.06	0.83	0.90	0.08	0.41	0.37	0.47	0.66	1.00	0.44	0.15	0.02	0.02
Nuc (0-32)	0.13	0.00	0.13	0.08	0.40	0.49	0.01	0.97	0.75	0.01	0.85	0.44	1.00	0.02	0.02	0.01
AURN PM_{10}	0.30	0.88	0.73	0.53	0.23	0.03	0.15	0.01	0.04	0.78	0.00	0.15	0.02	1.00	0.18	0.12
AURN NO_x	0.04	0.14	0.03	0.02	0.00	0.06	0.04	0.02	0.00	0.01	0.12	0.02	0.02	0.18	1.00	0.12
AURN T	0.12	0.02	0.02	0.10	0.11	0.00	0.02	0.00	0.19	0.09	0.00	0.02	0.01	0.12	0.12	1.00

Table 3. Correlation Matrix, nanoMOUDI mass concentrations and AURN data, Elms Road (Birmingham Background Site).

4. Newcastle Correlations, nanoMOUDI data.

	S5	S6	S7	S8	S9	S10	S11	S12	S13	PM_{10}	$PM_{0.1}$	Soot (32-180)	Nuc (0-32)	AURN PM_{10}	AURN NO_x	AURN T
S5	1.00	0.42	0.21	0.28	0.26	0.01	0.01	0.07	0.00	0.68	0.01	0.17	0.04	0.57	0.28	0.28
S6	0.42	1.00	0.63	0.50	0.46	0.00	0.10	0.04	0.07	0.80	0.11	0.33	0.07	0.59	0.45	0.21
S7	0.21	0.63	1.00	0.45	0.39	0.04	0.15	0.03	0.02	0.66	0.10	0.36	0.03	0.48	0.65	0.45
S8	0.28	0.50	0.45	1.00	0.62	0.10	0.03	0.00	0.04	0.65	0.00	0.49	0.02	0.62	0.72	0.30
S9	0.26	0.46	0.39	0.62	1.00	0.21	0.12	0.01	0.00	0.64	0.05	0.87	0.00	0.35	0.63	0.14
S10	0.01	0.00	0.04	0.10	0.21	1.00	0.02	0.01	0.11	0.07	0.05	0.45	0.04	0.02	0.19	0.03
S11	0.01	0.10	0.15	0.03	0.12	0.02	1.00	0.01	0.20	0.12	0.37	0.28	0.11	0.01	0.13	0.02
S12	0.07	0.04	0.03	0.00	0.01	0.01	0.01	1.00	0.28	0.00	0.52	0.01	0.74	0.00	0.00	0.05
S13	0.00	0.07	0.02	0.04	0.00	0.11	0.20	0.28	1.00	0.02	0.48	0.00	0.63	0.02	0.01	0.04
PM_{10}	0.68	0.80	0.66	0.65	0.64	0.07	0.12	0.00	0.02	1.00	0.07	0.53	0.01	0.70	0.70	0.37
$PM_{0.1}$	0.01	0.11	0.10	0.00	0.05	0.05	0.37	0.52	0.48	0.07	1.00	0.14	0.77	0.00	0.05	0.01
Soot (32-180)	0.17	0.33	0.36	0.49	0.87	0.45	0.28	0.01	0.00	0.53	0.14	1.00	0.00	0.24	0.62	0.12
Nuc (0-32)	0.04	0.07	0.03	0.02	0.00	0.04	0.11	0.74	0.63	0.01	0.77	0.00	1.00	0.03	0.00	0.06
AURN PM_{10}	0.57	0.59	0.48	0.62	0.35	0.02	0.01	0.00	0.02	0.70	0.00	0.24	0.03	1.00	0.57	0.52
AURN NO_x	0.28	0.45	0.65	0.72	0.63	0.19	0.13	0.00	0.01	0.70	0.05	0.62	0.00	0.57	1.00	0.50
AURN T	0.28	0.21	0.45	0.30	0.14	0.03	0.02	0.05	0.04	0.37	0.01	0.12	0.06	0.52	0.50	1.00

Table 4. Correlation Matrix, nanoMOUDI mass concentrations and AURN data, Newcastle Civic Centre.

5. Newcastle MOUDI Correlations

	S1	S2	S3	S4	S5	S6	S7	S8	S9	S12	PM_{10}	$PM_{0.18}$	AURN PM_{10}	AURN NO_x	AURN T
S1	1.00	0.07	0.05	0.65	0.55	0.22	0.22	0.54	0.04	0.03	0.47	0.00	0.34	0.20	0.25
S2	0.07	1.00	0.68	0.00	0.01	0.00	0.09	0.04	0.06	0.04	0.05	0.00	0.00	0.00	0.00
S3	0.05	0.68	1.00	0.28	0.17	0.08	0.36	0.06	0.03	0.13	0.41	0.00	0.19	0.06	0.10
S4	0.65	0.00	0.28	1.00	0.78	0.28	0.37	0.44	0.02	0.08	0.67	0.00	0.40	0.24	0.23
S5	0.55	0.01	0.17	0.78	1.00	0.24	0.26	0.40	0.06	0.07	0.53	0.02	0.32	0.11	0.31
S6	0.22	0.00	0.08	0.28	0.24	1.00	0.76	0.61	0.01	0.13	0.66	0.14	0.86	0.78	0.05
S7	0.22	0.09	0.36	0.37	0.26	0.76	1.00	0.60	0.06	0.13	0.88	0.05	0.82	0.63	0.06
S8	0.54	0.04	0.06	0.44	0.40	0.61	0.60	1.00	0.15	0.07	0.75	0.00	0.69	0.46	0.17
S9	0.04	0.06	0.03	0.02	0.06	0.01	0.06	0.15	1.00	0.10	0.05	0.02	0.01	0.00	0.00
S12	0.03	0.04	0.13	0.08	0.07	0.13	0.13	0.07	0.10	1.00	0.13	1.00	0.12	0.15	0.00
PM_{10}	0.47	0.05	0.41	0.67	0.53	0.66	0.88	0.75	0.05	0.13	1.00	0.02	0.81	0.52	0.19
$PM_{0.18}$	0.00	0.00	0.00	0.00	0.02	0.14	0.05	0.00	0.02	1.00	0.02	1.00	0.02	0.09	0.10
AURN PM_{10}	0.34	0.00	0.19	0.40	0.32	0.86	0.82	0.69	0.01	0.12	0.81	0.02	1.00	0.80	0.19
AURN NO_x	0.20	0.00	0.06	0.24	0.11	0.78	0.63	0.46	0.00	0.15	0.52	0.09	0.80	1.00	0.07
AURN T	0.25	0.00	0.10	0.23	0.31	0.05	0.06	0.17	0.00	0.00	0.19	0.10	0.19	0.07	1.00

Table 5. Correlation Matrix, MOUDI mass concentrations and AURN data, Newcastle Civic Centre.

6. Barcelona Roadside Correlations, MOUDI

	Inlet	**1**	**2**	**3**	**4**	**5**	**6**	**7**	**8**	**9+10**	**Backup**	**PM_{10}**	**$PM_{0.18}$**
Inlet	1.00	0.21	0.08	0.01	0.02	0.43	0.68	0.20	0.19	0.15	0.00	0.01	0.07
1	0.21	1.00	0.09	0.02	0.02	0.03	0.01	0.02	0.02	0.00	0.04	0.01	0.01
2	0.08	0.09	1.00	0.25	0.26	0.44	0.05	0.02	0.07	0.01	0.02	0.36	0.02
3	0.01	0.02	0.25	1.00	1.00	0.39	0.03	0.01	0.13	0.00	0.39	0.87	0.11
4	0.02	0.02	0.26	1.00	1.00	0.36	0.04	0.00	0.10	0.00	0.39	0.83	0.14
5	0.43	0.03	0.44	0.39	0.36	1.00	0.36	0.37	0.57	0.25	0.07	0.67	0.04
6	0.68	0.01	0.05	0.03	0.04	0.36	1.00	0.57	0.46	0.57	0.05	0.03	0.39
7	0.20	0.02	0.02	0.01	0.00	0.37	0.57	1.00	0.93	0.97	0.06	0.20	0.63
8	0.19	0.02	0.07	0.13	0.10	0.57	0.46	0.93	1.00	0.84	0.00	0.44	0.41
9+10	0.15	0.00	0.01	0.00	0.00	0.25	0.57	0.97	0.84	1.00	0.13	0.12	0.75
Backup	0.00	0.04	0.02	0.39	0.39	0.07	0.05	0.06	0.00	0.13	1.00	0.18	0.61
PM_{10}	0.01	0.01	0.36	0.87	0.83	0.67	0.03	0.20	0.44	0.12	0.18	1.00	0.00
$PM_{0.18}$	0.07	0.01	0.02	0.11	0.14	0.04	0.39	0.63	0.41	0.75	0.61	0.00	1.00

Table 6. Correlation Matrix, MOUDI mass concentrations, Barcelona Roadside site.

7. Barcelona Background Correlations, MOUDI

	Inlet	**1**	**2**	**3**	**4**	**5**	**6**	**7**	**8**	**9**	**PM_{12}**	**$PM_{0.22}$**
Inlet	1.00	0.72	0.93	0.93	0.78	0.03	0.07	0.00	0.00	0.20	0.29	0.20
1	0.72	1.00	0.84	0.58	0.47	0.00	0.00	0.04	0.01	0.26	0.08	0.26
2	0.93	0.84	1.00	0.83	0.73	0.06	0.01	0.01	0.01	0.20	0.12	0.20
3	0.93	0.58	0.83	1.00	0.93	0.01	0.08	0.01	0.03	0.11	0.37	0.11
4	0.78	0.47	0.73	0.93	1.00	0.01	0.01	0.06	0.04	0.03	0.26	0.03
5	0.03	0.00	0.06	0.01	0.01	1.00	0.25	0.06	0.38	0.02	0.26	0.02
6	0.07	0.00	0.01	0.08	0.01	0.25	1.00	0.15	0.23	0.22	0.69	0.22
7	0.00	0.04	0.01	0.01	0.06	0.06	0.15	1.00	0.10	0.29	0.08	0.29
8	0.00	0.01	0.01	0.03	0.04	0.38	0.23	0.10	1.00	0.11	0.57	0.11
9	0.20	0.26	0.20	0.11	0.03	0.02	0.22	0.29	0.11	1.00	0.24	1.00
PM_{12}	0.29	0.08	0.12	0.37	0.26	0.26	0.69	0.08	0.57	0.24	1.00	0.24
$PM_{0.22}$	0.20	0.26	0.20	0.11	0.03	0.02	0.22	0.29	0.11	1.00	0.24	1.00

Table 7. Correlation Matrix, MOUDI mass concentrations, Barcelona Background site.

APPENDIX D – CORRELATION TABLES OF AMBIENT CHEMICAL DATA

1. Birmingham Roadside Data

B'ham Roadside PM_{10}	Al	Ba	Ce	Cu	Fe	Ni	Sb	Sr	V	Zn
Al	1.00	0.22	0.14	0.33	0.24	0.12	0.21	0.02	0.22	0.12
Ba	0.22	1.00	0.09	0.74	0.08	0.15	0.61	0.65	0.20	0.88
Ce	0.14	0.09	1.00	0.05	0.09	0.12	0.05	0.03	0.09	0.12
Cu	0.33	0.74	0.05	1.00	0.21	0.22	0.24	0.18	0.62	0.63
Fe	0.24	0.08	0.09	0.21	1.00	0.81	0.07	0.04	0.41	0.09
Ni	0.12	0.15	0.12	0.22	0.81	1.00	0.14	0.00	0.34	0.26
Sb	0.21	0.61	0.05	0.24	0.07	0.14	1.00	0.56	0.00	0.46
Sr	0.02	0.65	0.03	0.18	0.04	0.00	0.56	1.00	0.01	0.57
V	0.22	0.20	0.09	0.62	0.41	0.34	0.00	0.01	1.00	0.23
Zn	0.12	0.88	0.12	0.63	0.09	0.26	0.46	0.57	0.23	1.00

Table 1. Elemental Correlation Matrix, Birmingham Roadside PM_{10}.

B'ham Roadside $PM_{0.1}$	Al	Ba	Ce	Cu	Fe	Ni	Sb	Sr	V	Zn
Al	1.00	0.01	0.15	0.00	0.14	0.06	N/A	0.14	0.04	0.01
Ba	0.01	1.00	0.09	0.06	0.21	0.24	N/A	0.06	0.17	0.02
Ce	0.15	0.09	1.00	0.22	0.07	0.09	N/A	0.99	0.06	0.08
Cu	0.00	0.06	0.22	1.00	0.18	0.13	N/A	0.18	0.12	0.00
Fe	0.14	0.21	0.07	0.18	1.00	0.87	N/A	0.07	0.92	0.01
Ni	0.06	0.24	0.09	0.13	0.87	1.00	N/A	0.09	0.84	0.13
Sb	N/A	N/A	N/A	N/A	N/A	N/A	N/A	N/A	N/A	N/A
Sr	0.14	0.06	0.99	0.18	0.07	0.09	N/A	1.00	0.06	0.07
V	0.04	0.17	0.06	0.12	0.92	0.84	N/A	0.06	1.00	0.02
Zn	0.01	0.02	0.08	0.00	0.01	0.13	N/A	0.07	0.02	1.00

Table 2. Elemental Correlation Matrix, Birmingham Roadside $PM_{0.1}$.

2. Birmingham Background Data

B'ham Background PM_{10}	Al	Ba	Cu	Fe	Ni	Sb	Sr	V	Zn
Al	1.00	0.16	0.21	0.28	0.25	0.01	0.19	0.15	0.00
Ba	0.16	1.00	0.18	0.00	0.11	0.67	0.06	0.16	0.00
Cu	0.21	0.18	1.00	0.00	0.00	0.12	0.02	0.10	0.18
Fe	0.28	0.00	0.00	1.00	0.84	0.01	0.22	0.62	0.32
Ni	0.25	0.11	0.00	0.84	1.00	0.09	0.24	0.87	0.38
Sb	0.01	0.67	0.12	0.01	0.09	1.00	0.06	0.25	0.13
Sr	0.19	0.06	0.02	0.22	0.24	0.06	1.00	0.36	0.66
V	0.15	0.16	0.10	0.62	0.87	0.25	0.36	1.00	0.67
Zn	0.00	0.00	0.18	0.32	0.38	0.13	0.66	0.67	1.00

Table 3. Elemental Correlation Matrix, Birmingham Background PM_{10}.

B'ham Background $PM_{0.1}$	Al	Ba	Cu	Fe	Ni	Sb	Sr	V	Zn
Al	1.00	0.04	0.49	0.40	0.54	N/A	0.39	0.30	0.40
Ba	0.04	1.00	0.03	0.08	0.01	N/A	0.43	0.00	0.21
Cu	0.49	0.03	1.00	0.98	0.90	N/A	0.00	0.47	0.26
Fe	0.40	0.08	0.98	1.00	0.79	N/A	0.00	0.35	0.23
Ni	0.54	0.01	0.90	0.79	1.00	N/A	0.02	0.61	0.19
Sb	N/A	N/A	N/A	N/A	N/A	N/A	N/A	N/A	N/A
Sr	0.39	0.43	0.00	0.00	0.02	N/A	1.00	0.03	0.00
V	0.30	0.00	0.47	0.35	0.61	N/A	0.03	1.00	0.48
Zn	0.40	0.21	0.26	0.23	0.19	N/A	0.00	0.48	1.00

Table 4. Elemental Correlation Matrix, Birmingham Background $PM_{0.1}$.

3. Newcastle Data

Newcastle PM_{10}	Al	Ba	Ce	Cu	Fe	Ni	Sb	Sr	V	Zn
Al	1.00	0.00	0.41	0.13	0.08	0.03	0.02	0.09	0.09	0.12
Ba	0.00	1.00	0.11	0.29	0.10	0.02	0.57	0.60	0.02	0.24
Ce	0.41	0.11	1.00	0.15	0.00	0.02	0.02	0.14	0.04	0.05
Cu	0.13	0.29	0.15	1.00	0.01	0.06	0.12	0.62	0.01	0.62
Fe	0.08	0.10	0.00	0.01	1.00	0.85	0.08	0.34	0.91	0.19
Ni	0.03	0.02	0.02	0.06	0.85	1.00	0.00	0.12	0.96	0.01
Sb	0.02	0.57	0.02	0.12	0.08	0.00	1.00	0.21	0.01	0.42
Sr	0.09	0.60	0.14	0.62	0.34	0.12	0.21	1.00	0.17	0.51
V	0.09	0.02	0.04	0.01	0.91	0.96	0.01	0.17	1.00	0.07
Zn	0.12	0.24	0.05	0.62	0.19	0.01	0.42	0.51	0.07	1.00

Table 5. Elemental Correlation Matrix, Newcastle PM_{10}.

Newcastle $PM_{0.1}$	Al	Ba	Ce	Cu	Fe	Ni	Sb	Sr	V	Zn
Al	1.00	0.04	0.10	0.45	0.15	0.00	0.05	0.15	0.10	0.50
Ba	0.04	1.00	0.14	0.38	0.23	0.01	0.64	0.90	0.06	0.43
Ce	0.10	0.14	1.00	0.17	0.02	0.07	0.03	0.14	0.05	0.09
Cu	0.45	0.38	0.17	1.00	0.03	0.12	0.01	0.52	0.00	0.77
Fe	0.15	0.23	0.02	0.03	1.00	0.58	0.07	0.33	0.88	0.33
Ni	0.00	0.01	0.07	0.12	0.58	1.00	0.05	0.04	0.79	0.00
Sb	0.05	0.64	0.03	0.01	0.07	0.05	1.00	0.46	0.02	0.01
Sr	0.15	0.90	0.14	0.52	0.33	0.04	0.46	1.00	0.15	0.63
V	0.10	0.06	0.05	0.00	0.88	0.79	0.02	0.15	1.00	0.17
Zn	0.50	0.43	0.09	0.77	0.33	0.00	0.01	0.63	0.17	1.00

Table 6. Elemental Correlation Matrix, Newcastle $PM_{0.1}$.

4. Barcelona Data

BTR PM_{10}	Ba	Cu	Fe	Sb	Sn	Mo	Zn	Mg	Na	Al	Ca
Ba	1.00	0.96	0.31	0.53	0.61	0.11	0.55	0.23	0.04	0.63	0.84
Cu	0.96	1.00	0.25	0.58	0.74	0.13	0.63	0.23	0.04	0.59	0.89
Fe	0.31	0.25	1.00	0.02	0.20	0.00	0.21	0.31	0.09	0.51	0.29
Sb	0.53	0.58	0.02	1.00	0.71	0.76	0.75	0.00	0.10	0.53	0.64
Sn	0.61	0.74	0.20	0.71	1.00	0.40	0.84	0.16	0.00	0.66	0.87
Mo	0.11	0.13	0.00	0.76	0.40	1.00	0.51	0.03	0.30	0.34	0.25
Zn	0.55	0.63	0.21	0.75	0.84	0.51	1.00	0.01	0.08	0.55	0.63
Mg	0.23	0.23	0.31	0.00	0.16	0.03	0.01	1.00	0.81	0.34	0.37
Na	0.04	0.04	0.09	0.10	0.00	0.30	0.08	0.81	1.00	0.03	0.07
Al	0.63	0.59	0.51	0.53	0.66	0.34	0.55	0.34	0.03	1.00	0.80
Ca	0.84	0.89	0.29	0.64	0.87	0.25	0.63	0.37	0.07	0.80	1.00

Table 7. Elemental Correlation Matrix, Barcelona Roadside PM_{10}.

BTR $PM_{0.1}$	Ba	Cu	Fe	Sb	Sn	Mo	Zn	Mg	Na	Al	Ca
Ba	1.00	0.76	0.65	0.04	0.14	0.23	0.52	0.92	0.12	0.74	0.83
Cu	0.76	1.00	0.28	0.00	0.06	0.08	0.83	0.84	0.50	0.66	0.76
Fe	0.65	0.28	1.00	0.01	0.00	0.03	0.06	0.57	0.01	0.72	0.55
Sb	0.04	0.00	0.01	1.00	0.88	0.86	0.00	0.00	0.09	0.03	0.01
Sn	0.14	0.06	0.00	0.88	1.00	0.95	0.04	0.02	0.03	0.00	0.00
Mo	0.23	0.08	0.03	0.86	0.95	1.00	0.06	0.08	0.03	0.00	0.03
Zn	0.52	0.83	0.06	0.00	0.04	0.06	1.00	0.61	0.76	0.33	0.54
Mg	0.92	0.84	0.57	0.00	0.02	0.08	0.61	1.00	0.28	0.87	0.97
Na	0.12	0.50	0.01	0.09	0.03	0.03	0.76	0.28	1.00	0.15	0.28
Al	0.74	0.66	0.72	0.03	0.00	0.00	0.33	0.87	0.15	1.00	0.90
Ca	0.83	0.76	0.55	0.01	0.00	0.03	0.54	0.97	0.28	0.90	1.00

Table 8. Elemental Correlation Matrix, Barcelona Roadside $PM_{0.18}$.

BBS PM_{12}	Ba	Cu	Fe	Sb	V	S	Na	Mg	Al	Ca	Ni
Ba	1.00	0.03	0.05	0.02	0.00	0.14	0.15	0.21	0.04	0.01	0.02
Cu	0.03	1.00	0.02	0.06	0.16	0.12	0.02	0.03	0.33	0.21	0.09
Fe	0.05	0.02	1.00	0.46	0.28	0.66	0.00	0.00	0.12	0.15	0.49
Sb	0.02	0.06	0.46	1.00	0.94	0.17	0.01	0.00	0.09	0.08	0.32
V	0.00	0.16	0.28	0.94	1.00	0.04	0.03	0.01	0.10	0.07	0.28
S	0.14	0.12	0.66	0.17	0.04	1.00	0.17	0.17	0.00	0.23	0.32
Na	0.15	0.02	0.00	0.01	0.03	0.17	1.00	0.96	0.06	0.55	0.21
Mg	0.21	0.03	0.00	0.00	0.01	0.17	0.96	1.00	0.07	0.48	0.17
Al	0.04	0.33	0.12	0.09	0.10	0.00	0.06	0.07	1.00	0.04	0.05
Ca	0.01	0.21	0.15	0.08	0.07	0.23	0.55	0.48	0.04	1.00	0.69
Ni	0.02	0.09	0.49	0.32	0.28	0.32	0.21	0.17	0.05	0.69	1.00

Table 9. Elemental Correlation Matrix, Barcelona Background PM_{12}.

BBS $PM_{0.22}$	Ba	Cu	Fe	Sb	V	S	Na	Mg	Al	Ca	Ni
Ba	1.00	0.31	0.75	0.00	0.01	0.01	0.03	0.18	0.11	0.12	0.03
Cu	0.31	1.00	0.27	0.01	0.01	0.62	0.62	0.53	0.38	0.37	0.03
Fe	0.75	0.27	1.00	0.00	0.00	0.00	0.02	0.26	0.19	0.14	0.14
Sb	0.00	0.01	0.00	1.00	0.45	0.00	0.20	0.00	0.01	0.01	0.43
V	0.01	0.01	0.00	0.45	1.00	0.04	0.08	0.02	0.16	0.02	0.54
S	0.01	0.62	0.00	0.00	0.04	1.00	0.61	0.36	0.39	0.10	0.06
Na	0.03	0.62	0.02	0.20	0.08	0.61	1.00	0.50	0.19	0.33	0.40
Mg	0.18	0.53	0.26	0.00	0.02	0.36	0.50	1.00	0.36	0.74	0.00
Al	0.11	0.38	0.19	0.01	0.16	0.39	0.19	0.36	1.00	0.08	0.07
Ca	0.12	0.37	0.14	0.01	0.02	0.10	0.33	0.74	0.08	1.00	0.01
Ni	0.03	0.03	0.14	0.43	0.54	0.06	0.40	0.00	0.07	0.01	1.00

Table 10. Elemental Correlation Matrix, Barcelona Background $PM_{0.22}$.